2019

# Intense terahertz light-quantum quench and control of superconductivity

Xu Yang
*Iowa State University*

**Intense terahertz light-quantum quench and control of superconductivity**

by

**Xu Yang**

A dissertation submitted to the graduate faculty

in partial fulfillment of the requirements for the degree of

DOCTOR OF PHILOSOPHY

Major: Condensed Matter Physics

Program of Study Committee:
Jigang Wang, Major Professor
Peter Orth
Rebecca Flint
Kirill Tuchin
Patricia Thiel

The student author, whose presentation of the scholarship herein was approved by the program of study committee, is solely responsible for the content of this dissertation. The Graduate College will ensure this dissertation is globally accessible and will not permit alterations after a degree is conferred.

Iowa State University

Ames, Iowa

2019

## DEDICATION

I would like to dedicate this thesis to my parents, Haiyan Zhang and Zeqing Yang for their support during my PhD study.

# TABLE OF CONTENTS

**Page**

# LIST OF TABLES

# LIST OF FIGURES

# ACKNOWLEDGEMENTS

I would like to take this opportunity to express my gratitude to those who helped me during my PhD study. First and foremost, I cannot thank my advisor Dr. Jigang Wang too much for his insightful guidance, patience and support from all respects. I spent five wonderful years in the group and really enjoyed this journey of discoveries. Second, my research cannot be done without our excellent collaborators. We get strong theory support from Dr. Martin Mootz, Dr. Ilias Perakis at University of Alabama-Birmingham and Dr. Peter Orth at Iowa State University. Marvelous data are taken on high quality samples from Dr. Chang-Beom Eom's group at University of Wisconsin-Madison, Dr. Xinyu Liu at University of Notre Dame , and Dr. Paul Canfield's group at Iowa State University. I really appreciate the guidance from my committee members: Dr. Peter Orth, Dr. Rebecca Flint, Dr. Kirill Tuchin and Dr. Patricia Thiel. I would additionally like to thank Dr. Liang Luo for his guidance at the initial stages of my research and Chirag Vaswani for his assistance in my later experiment. Zhaoyu Liu, Di Chen, Richard Kim, Dr. Jong-Mok Park from our group and many others throughout department never hesitate to provide their help, which I would always be grateful to.

This work was supported by Army Research office under Army Research office award W911NF-15-1-0135 (THz spectroscopy) and U.S. Department of Energy (DOE), Office of Basic Energy Science, Division of Materials Sciences and Engineering at the Ames Laboratory under contract number DE-AC02-07CH11358. The Ames Laboratory is operated for the DOE by Iowa State University. The document number assigned to this thesis/dissertation is IS-T3244.

## ABSTRACT

This thesis summarizes my PhD work on intense Terahertz (THz) light-quantum quench and control of superconductivity. BCS superconductor $Nb_3Sn$ and iron based superconductor $Ba(Fe_{1-x}Co_x)_2As_2$ are studied by intense THz/optical pump/-weak THz probe ultrafast spectroscopy. I design and develop the experiment setup that reaches the strongest THz pump reported so far in similar tabletop configurations. Single cycle THz pulses up to MV/cm peak E field open up a new regime to explore the quantum dynamics and emergent phase in condensed matter system, including superconducting (SC) condensate, topological Dirac fermions, exciton phase transition, quantum coherence in perovskite solar cell and 2D materials.

# CHAPTER 1. OVERVIEW

Ultrafast spectroscopy is a powerful tool to study non-equilibrium dynamics of condensed matter system. Ultra-intense, very short laser pulse not only provide necessary fast time resolution, but also serves as seed to access a broad spectra from X-ray to infrared by nonlinear process. Together with laser scanning techniques, ultrafast spectroscopy opens up a new regime to resolve quantum dynamics in the complex materials by a multi-color–temporal/spatial resolved fashion.

Light-matter interaction from X-ray to mid-infrared wavelength has been extensively explored in the last few decades, thanks to the development of modern photonics and electronics. However, their Terahertz dynamics are rarely reported due to lack of efficient Terahertz radiation source. Many interesting phenomena lie in the Terahertz band, such as rotational energy of molecules, lattice vibrations in solids, intra-band transitions in semiconductors, and superconductivity. It is not until recently that single cycle Terahertz pulse with peak E field up to MV/cm is accessible via tilted phase front matching technique by tabletop ultrafast laser system.

With both pump and probe in Terahertz regime, laser heating from excessive photon energy is minimized for narrowly gapped, strongly correlated system, like superconductivity (SC). On the other hand, electric field, rather than photon energy is the dominant factor in light-matter interaction, serving as a new tuning knob to actively control material properties at ultrafast time scales.

In Chapter 2, we introduce basic principles of ultrafast laser spectroscopy, Terahertz detection and generation techniques. Our experiment setup and data analysis method are described in details, especially the effort to generate intense Terahertz pulse at MV/cm peak E field. In Chapter 3, we reveal a post-quench, pre-thermalization gapless state hidden underneath SC dome in $Nb_3Sn$ superconductor induced by non-thermal, non-adiabatic Terahertz quench. In Chapter 4, thermal nature of optical pumping is demonstrated by applying 1.55eV fs photoexcitation, in comparison

to non-thermal Terahertz quench. For the first time we observe quantum-limit energy transfer, i.e. one photon breaks one Cooper pairs despite their large energy mismatch. In Chapter 5, we studied Terahertz dynamics of pair breaking process in iron pnictide superconductor system, and discovered a photo-induced excitonic state within electron-hole pockets. In Chapter 6, we demonstrate the first gapless superconductivity state and forbidden pseudo spin mode in BCS superconductor, by engineering Terahertz driven nonlinear current. Last chapter is a brief summary of my PhD work and outlook for future research.

# CHAPTER 2. INTRODUCTION

In this section, we give a brief introduction to fundamental principles of ultrafast spectroscopy and Terahertz science (1), which is used to drive our experiment setup. Optical design, data taking scheme and analysis method are also described in the following section.

## 2.1 Principle of Lasers

The shortest time resolution ever reached so far is by ultrafast lasers. The word "laser" is short for "light amplification by stimulated emission of radiation". A laser consists of three parts: gain medium, pumping energy and cavity to provide positive feedback, as shown in Figure 2.3. The gain medium is used to generate and amplify stimulated emission, energized by pumping source, like electric current or light. Selective optical modes interferes constructively within the laser cavity and output through one cavity mirror with less reflectivity. Since the first laser demonstration by Dr Theodore H. Maiman in 1963, laser has been widely used in scientific research, industry manufacturing, telecommunication, etc., making a huge impact on people's everyday life.

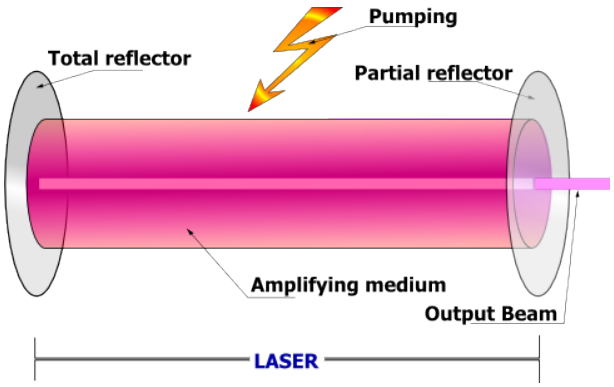


Figure 2.1 A simple design of Laser consists of cavity mirrors, gain medium and external pumping.

### 2.1.1 Einstein AB Coefficient

The concept of "stimulated radiation" was established along with the development of quantum mechanics. First discovery to the quantum world is Planck's formula to describe black body radiation:

$$I(\omega)d\omega = \frac{\hbar\omega^3 d\omega}{\pi^2 c^2 (e^{\hbar/kT} - 1)}. \tag{2.1}$$

where $I(\omega)$ stands for intensity of the angular frequency distribution in the small interval $d\omega$, $\hbar$ is Planck constant, $k$ is Boltzmann's constant, $T$ is the equilibrium temperature and $c$ is the velocity of light in vacuum. For the first time it brings about the concept of "quantum" when describing microscopic behaviors of electrons, photons, etc.

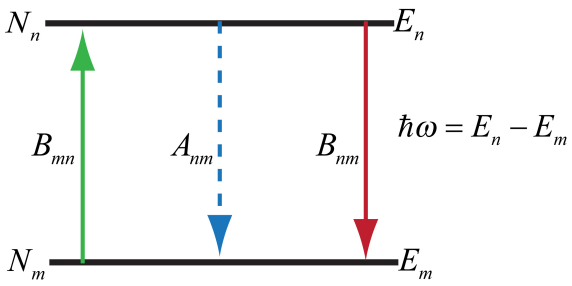


Figure 2.2 Einstein AB coefficient for two-level system.

Second big success is Bohr's model for hydrogen atom. Based on these two discoveries, Einstein realized that three types of processes should be included in the black body radiation: spontaneous emission ($A_{nm}$), stimulated absorption ($B_{mn}$) and stimulated emission ($B_{nm}$). The probability of electron transition for these processes are named as Einstein AB coefficients. For static two-level system in Figure 2.4, number of photon emitted equals the number of absorbed photons:

$$N_m B_{mn} I(\omega) = N_n B_{nm} I(\omega) + N_n A_{nm} \tag{2.2}$$

At thermal equilibrium, relative populations on two levels separated by an energy $\hbar\omega$ at temperature T, $N_n/N_m = exp(-\hbar\omega/kT)$, is applied to Equation 2.2, one gets:

$$I(\omega) = \frac{A_{nm}}{B_{mn} e^{\hbar\omega/kT} - B_{nm}} \tag{2.3}$$

This is exactly the same form of Planck black body radiation formula (Equation 2.1). Comparing these two formulas leads to:

$$A_{nm}/B_{nm} = \hbar\omega^3/\pi^2c^3; B_{nm} = B_{mn} \tag{2.4}$$

In stimulated emission, a twin photon is generated when a photon with energy $\hbar\omega$ passes through an excited atom, with the same excitation energy level. This new photon has the same energy, propagation direction, polarization state and phase. Light is amplified at optical gain of two in this elementary process.

Overall light amplification is realized when stimulated emission surpasses light absorption in the medium. This is achieved by population inversion as $N_n > N_m$. After replacing $A_{nm}$, $B_{mn}$ in Equation 2.2, one can get:

$$B_{nm}I(\omega)(N_m - N_n) = N_n\frac{\hbar\omega^3}{pi^2c^3}B_{nm} > 0 \tag{2.5}$$

when $N_m > N_n$. It is easy to see that population inversion can never be satisfied In two-level system.

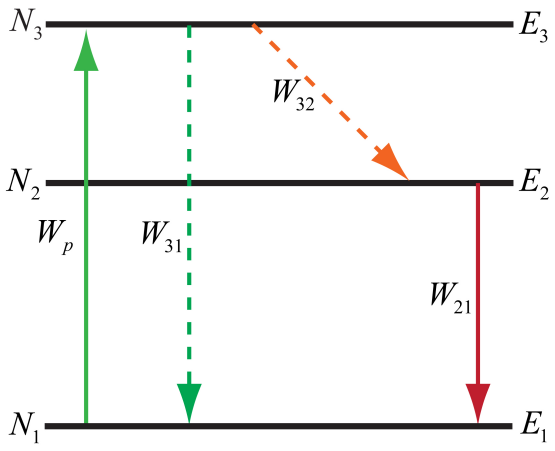


Figure 2.3 Population inversion in three-level system.

### 2.1.2 Population Inversion

Fortunately, real materials have complicated many quantum states and two-level systems are rare in nature. Three-level system can be used as gain medium to realize population inversion, as shown in Figure 2.5. Electrons at level 1 are excited to level 3 by optical pumping, whose rate is denoted by $W_p$. Electrons at level 3 can decay to either level 1 at rate $W_{31}$ or level 2 at $W_{32}$. $W_{31}$ is the combined decay rate of stimulated $W_p$ (as discussed above, $B_{nm} = B_{mn}$) and spontaneous emission $W_{31}^{sp}$, which gives:

$$W_{13} = W_p + W_{13}^{sp} > W_p \tag{2.6}$$

Rate equations can be easily derived to model the dynamical process as:

$$\begin{aligned} \frac{dN_3}{dt} &= W_p N_1 - W_{32} N_3 - W_{31} N_3 \\ \frac{dN_2}{dt} &= W_{32} N_3 - W_{21} N_2 \\ N &= N_1 + N_2 + N_3 \end{aligned} \tag{2.7}$$

At static state, time derivative of particle population at each state vanishes and we can get:

$$\frac{N_2}{N_1} \approx \frac{W_p}{W_{21}}(1 - \frac{W_{31}}{W_{32}}) \tag{2.8}$$

From equation above, we can see that efficient population inversion $N_2/N_1 >> 1$ requires:

$$W_{31} << W_{32} \qquad W_{21} << W_p \tag{2.9}$$

and in strong pumping regime, it is reasonable to assume:

$$W_{21} << W_{32} \qquad W_{31} << W_p \tag{2.10}$$

Under such assumptions of Equation 2.9, $(1 - \frac{W_{31}}{W_{32}}) \approx 1$, and we have:

$$\Delta N = N_1 - N_2 \approx N_2(\frac{W_{21}}{W_p} - 1) = N\frac{W_p}{W_p + W_{21}}(\frac{W_{21}}{W_p} - 1) < 0 \tag{2.11}$$

Equation 2.9 indicates that most of electrons decay to level 2 instead of level 1. Equation 2.10 shows that strong pump and metastable middle level 2 are favorable for light amplification. Under

these conditions, excited electrons accumulate at level 2 and population inversion is established between level 1 and 2.

The light intensity propagating along z axis through gain medium can be described by Lambert-Beer's law:

$$\frac{dI(z)}{dz} = -I(z)\Delta N\sigma_{12} \tag{2.12}$$

where $\sigma_{12}$ is the stimulated-emission cross-section of the transition. Then light intensity increases as propagates through gain medium.

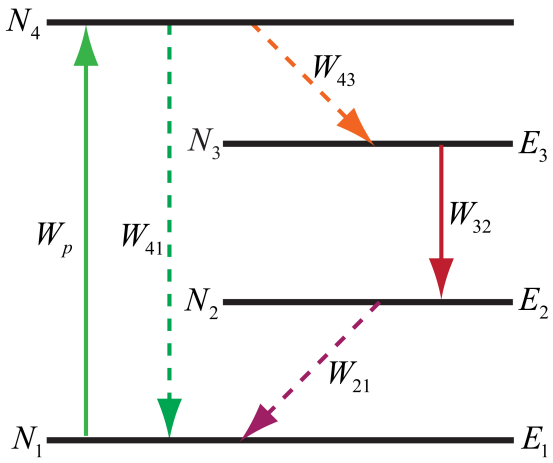


Figure 2.4 Four-level system.

More efficient gain medium used in laser proves to be four-level system, as shown in Figure 2.4. In this case, population inversion is achieved between level 3 and 2, by assuming $W_{43} >> W_{41}$, $W_{21} >> W_{32}$, $W_{21} \approx W_{43}$. Electrons at ground state get excited to level 4 by optical pumping and quickly decay to level 3, whose lifetime is much longer. Since level 2 is empty at beginning, any electrons at level 3 will lead to population inversion. De-excited electrons transfer to level 2 through stimulated emission, quickly relax to level 1 and pumped to highest energy. Similarly, rate

equations can be worked out in four-level system:

$$\begin{aligned}
\frac{dN_4}{dt} &= W_p N_1 - W_{43} N_3 - W_{41} N_4 \\
\frac{dN_3}{dt} &= W_{43} N_4 - W_{32} N_3 \\
\frac{dN_2}{dt} &= W_{32} N_3 - W_{21} N_2 \\
N &= N_1 + N_2 + N_3
\end{aligned} \tag{2.13}$$

By assuming strong pumping condition $W_p >> W_{32}$, we get:

$$\Delta N \approx N(\frac{W_p}{W_p + W_{43}}) \tag{2.14}$$

Surprisingly, simple rate equations accurately describes the electronics structures and dynamical quantum behavior of gain medium. Four-level model mimics chromium ion dissolved in alumina (ruby) very well, which is the gain medium in Ti-Sapphire ultrafast laser, light source of our experiment setup.

### 2.1.3 Cavity Mode

Coherent stimulated light emission interferes constructively between two high-reflectivity mirrors, which forms a Fabry-Perot (FP) resonator. Laser beam, with well defined wavelength, photon coherence and directionality, comes out from less reflective side of FP cavity.

Longitude mode inside FP cavity at length L must satisfy standing wave condition:

$$m\lambda = 2L, \qquad m \in N^+. \tag{2.15}$$

There exists finite number of modes, as long as grain is greater than loss. Laser emission is the summation of all these modes. Detailed calculation of cavity parameter and latitude mode can be found in somewhere else (1).

## 2.2 Generation of Ultrashort Pulse

### 2.2.1 Propagation of Ultrashort Pulse

Laser design discussed in last section can only generate continuous wave, which cannot be used to resolve ultrafast phenomena. Only short pulse can provide much needed time resolution. From Fourier transformation, we know that wave bandwidth and temporal length has the relation:

$$\Delta t \Delta \omega \geq \frac{1}{2} \tag{2.16}$$

Equality to 1/2 is reached only by Gaussian wave, which is also called transform-limited wave:

$$E_y = Re(E_0 exp(-\Gamma t^2 + i\omega_0 t)). \tag{2.17}$$

And frequency spectrum is:

$$E_0(\omega) = E_0 exp(-\frac{-(\omega - \omega_0)^2}{4\Gamma}). \tag{2.18}$$

From the relation, we can see that ultra-broad bandwidth is required to generate ultra-short pulse.

However, transform-limited waveform may be distorted when pulse propagates through dispersive medium. First type of distortion is called optical chirp, when a quadratic time dependence is added to the original phase term:

$$E_y = Re(E_0 exp(-\Gamma t^2 + i(\omega_0 t - at^2))). \tag{2.19}$$

Instantaneous frequency is:

$$\omega(t) = \frac{\partial \Phi}{\partial t} = \omega_0 + \alpha t \tag{2.20}$$

So the leading edge is blue shifted compared to trailing edge.

Second factor is group velocity dispersion. Gaussian wave propagating a distance x in a dispersive medium can be expressed as:

$$E_0(\omega, x) = E_0 \cdot exp(-\frac{-(\omega - \omega_0)^2}{4\Gamma}) exp[-ik(\omega)x]. \tag{2.21}$$

where $k(\omega)$ is frequency dependent wave vector:

$$k(\omega) = k(\omega_0) + k'(\omega - \omega_0) + \frac{1}{2}k''(\omega - \omega_0)^2 \tag{2.22}$$

Wave spectrum is modified:

$$E_0(\omega, x) = E_0 \cdot exp(-ik(\omega_0)x - ik'(\omega - \omega_0) - (\frac{1}{4\Gamma} + \frac{i}{2}k'')(\omega - \omega_0)^2). \tag{2.23}$$

Temporal E field oscillation can be obtained by applying Fourier transformation:

$$E_0(\omega, x) = E_0\sqrt{\frac{\Gamma(x)}{\pi}} \cdot exp[i\omega_0(t - \frac{x}{v_\phi(\omega_0)})] \cdot exp[-\Gamma(x)(t - \frac{x}{v_g(\omega_0)})^2]. \tag{2.24}$$

where

$$v_\phi(\omega_0) = (\frac{\omega}{k})_{\omega_0} \qquad v_g(\omega_0) = (\frac{d\omega}{dk})_{\omega_0} \qquad \frac{1}{\Gamma(x)} = \frac{1}{\Gamma} + 2ik''x \tag{2.25}$$

The phase velocity $v_\phi$ measures the propagating speed of plane wave components, group velocity $v_g$ is the speed of wave envelope, either delayed or advanced phase velocity. Clearly the wave is broadened temporally since $\Gamma(x) > \Gamma$. After working out some math, the last term in Equation 2.21 is:

$$exp[-\frac{\Gamma}{1 + \xi^2x^2}(t - \frac{x}{v_g})^2 + i\frac{\Gamma\xi x}{1 + \xi^2x^2}(t - \frac{x}{v_g})^2] \tag{2.26}$$

where $\xi = 2\Gamma k''$. First term shows that pulse undergoes broadening under group velocity dispersion $k''$. Second term is in the same form of optical chirp described by Equation 2.16.

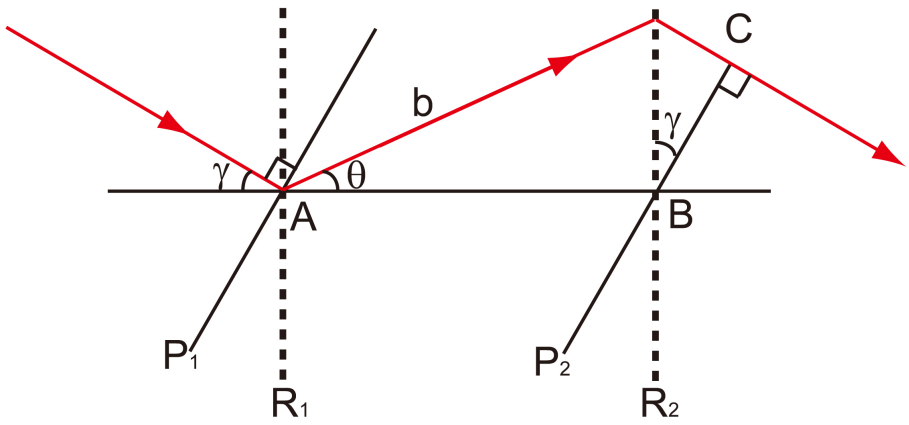


Figure 2.5 Grating pair to change group dispersion.

In order to compress pulse duration of distorted wave, a pair of gratings can be used to compensate group velocity dispersion. Dispersion induced by two gratings have opposite sign, which

implies the parallel grating orientation. The diffraction due to grating is:

$$d(\sin\gamma + \sin\theta) = \lambda \tag{2.27}$$

After some simple derivation, group delay along trajectory ABC is:

$$t = \frac{b}{c}(1 + \sin\theta\sin\gamma) \tag{2.28}$$

and dispersion parameter can be expresses by:

$$\begin{aligned} D &= \frac{1}{b}\frac{dt}{d\lambda} = \frac{\lambda}{cd^2}[1 - (\frac{\lambda}{d} - \sin\gamma)^2]^{-1} \\ k'' &= -\frac{\lambda^3}{2\pi 2c^2d^2}[1 - (\frac{\lambda}{d} - \sin\gamma)^2]^{-1} \end{aligned} \tag{2.29}$$

So a pair of gratings are able to compensate either positive or negative group dispersion by choosing right parameters.

### 2.2.2 Mode-Lock and Gain Broadening

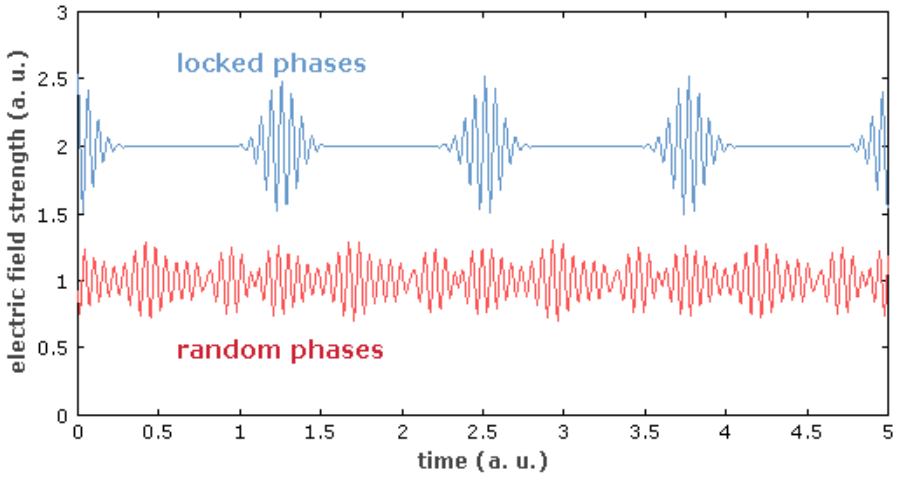


Figure 2.6 Comparison between optical modes with random phases and fixed phase (mode-lock).

As we discussed in Section 2.2.3, laser cavity is able to support many longitude modes whose net gain $g > 0$, i.e. difference between light amplification and cavity loss should be greater than zero.

Bandwidth of one mode is clearly not enough to generate fs ultrashort pulse. The technique to have constructive interference between different modes and couple them together is called "mode-lock" (ML). The most important criteria for ML is to lock phase of each cavity mode, otherwise random phase could smear out the interference features, as shown in Figure 2.6. There are two main mode-locking methods developed so far: passive mode-locking by inserting a saturable absorbing medium into cavity, or active mode-locking from an external modulation at frequency $\Omega$ of either cavity loss (by inserting an acoustic-optical crystal) or gain of amplifying medium.

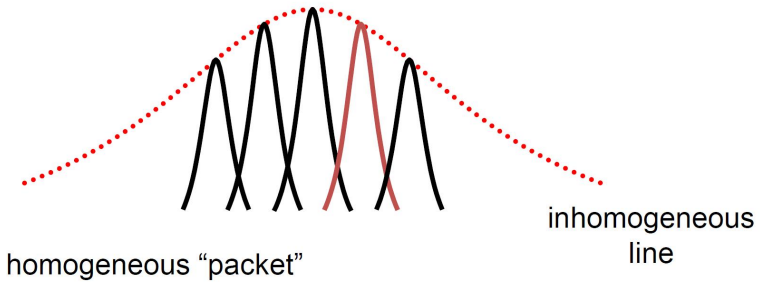


Figure 2.7 Homogeneous and inhomogeneous gain broadening effect.

Another important concept is gain ($g(\omega)$) broadening, which can be categorized into two types: homogeneous and inhomogeneous (1).

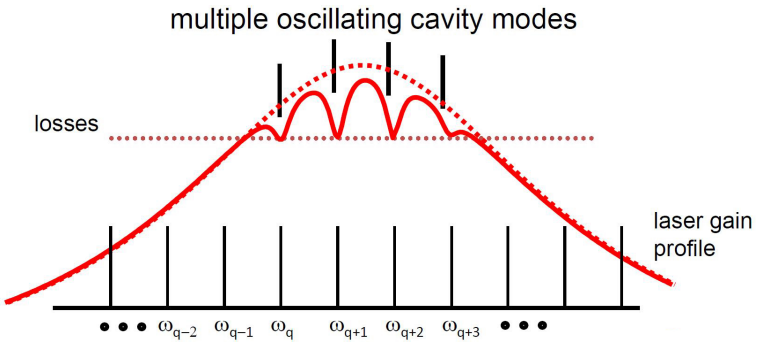


Figure 2.8 Inhomogeneous saturation and hole burning effect.

Inhomogeneous broadening is an increase in the linewidth of an atomic transition determined by wavelength. Two main factors for inhomogenenous broadening are Doppler effect and lattice

defects. At the frequency of cavity mode emission, a hole is burned upon gain spectrum $g(\omega)$ and laser emission from different modes could survive simultaneously. Ultrashort pulse can be generated when phase between different modes are locked together.

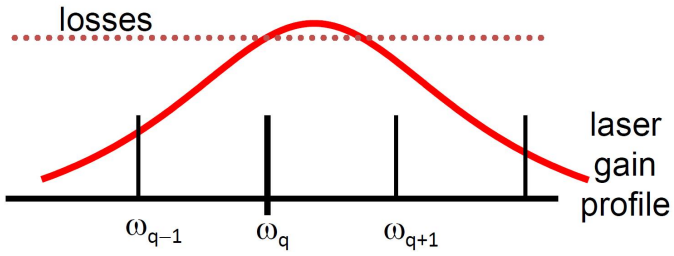


Figure 2.9 Homogeneous saturation.

Homogeneous broadening, on the other hand, refers to effects which increase the optical linewidth of an electronic transition equally for all radiating or absorbing atoms, ions or molecules. The spectral shape of the transition cross sections of all involved atoms are the same. Common reasons include finite lifetimes of the energy levels and molecule collision.

Homogeneous saturation refers to the case when the lineshape of the gain spectrum is not modified by pumping. Since inverted population $\Delta N$ is consumed by laser emission, system undergoes continuous drop of gain spectrum until only one longitude mode in the center survives when gain compensate the loss (as shown in Figure 2.9). Clearly this situation of single mode survival is not favorable for ultrashort pulse generation.

### 2.2.3 Ti-sapphire Oscillator-Amplifier System

The ultrafast laser used in our experiment is commercial Ti-sapphire Oscillator-Amplifier system from Spectra-Physics. The gain medium is Ti-doped sapphire crystal which has very broad emission spectrum from 600-1100nm, ideal for short pulse generation. As we mentioned above, the energy level can be model as four-level system.

A Millennia laser consist of two laser diodes which can supply 10 W of 532 nm power as optical pump for Tsunami oscillator. The oscillator generates 30fs pulse at 78MHz repetition rate, which provide seed light for further amplification by Spitfire amplifier. The Tsunami laser head contains

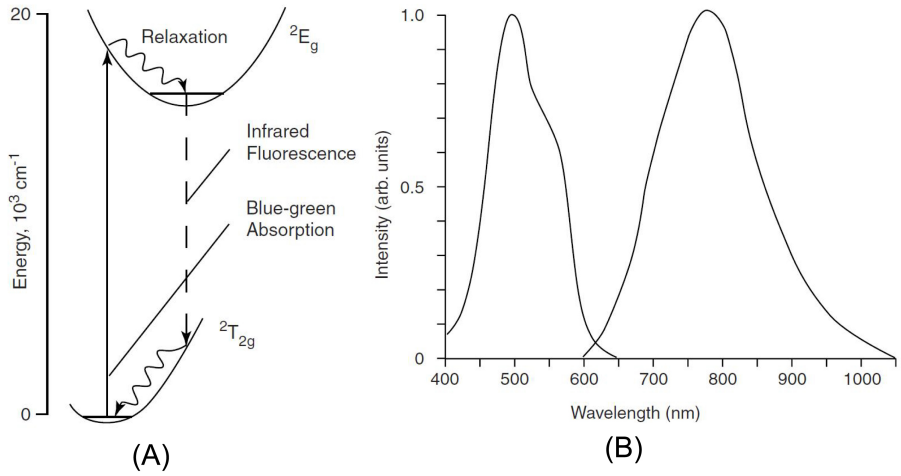


Figure 2.10 (A): Absorption and emission spectra of Ti:sapphire. (B): Energy level structure of Ti3+ in sapphire.

the Ti:sapphire rod and the optics that form the resonator cavity. Elements include pump beam mirrors (M), rod focusing mirrors (M), an output coupler (OC), a high reflector (HR), beam folding mirrors, dispersion control elements (Pr), acoustic modulator (AOM) for mode locking and other tuning elements. The laser design is shown below (2).

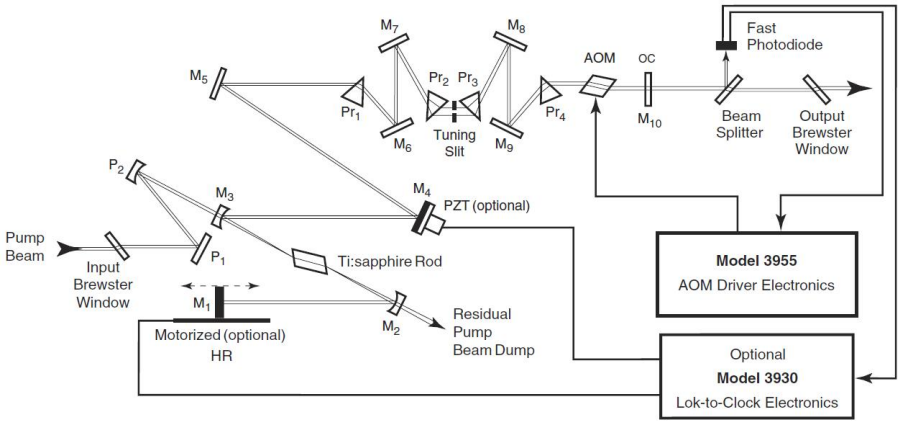


Figure 2.11 Configuration of Tsunami Oscillator.

Laser pulse from oscillator is further amplified by regenerate amplifier to 3mJ pulse energy, 35fs duration, 1KHz repetition rate and 800nm center wavelength. The maximum output energy of a solid-state amplifier is normally limited by the optical damage threshold of the crystalline material

used in the system. This limitation is circumvented by using "chirped pulse amplification". Optical seed pulse is first stretched temporally to reduce its peak power by a pair of gratings, then gets amplified, and finally recompressed by a second grating pair to a width close to its original duration. It consists of Faraday rotator (FI), aperture (A), mirrors (M), concave mirrors (CM) and Pockels cell to select pulse. The configuration is shown in Figure.

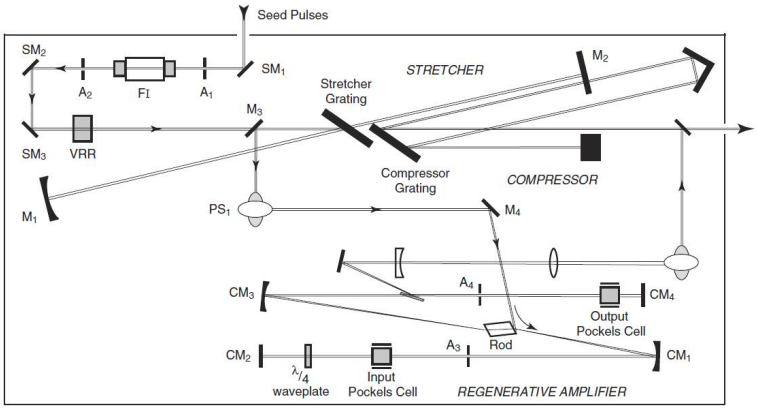


Figure 2.12 Configuration of Spitfire laser amplifier.

## 2.3 Terahertz generation and detection technique

Very bright ultrafast laser pulse opens the door to a broadband wavelength by nonlinear optics. Figure 2.13 presents the accessible spectrum output from optical parametric amplifier (OPA) driven by Ti-sapphire ultrafast laser. In this section, we will focus on generation and detection techniques of Terahertz (THz) wave.

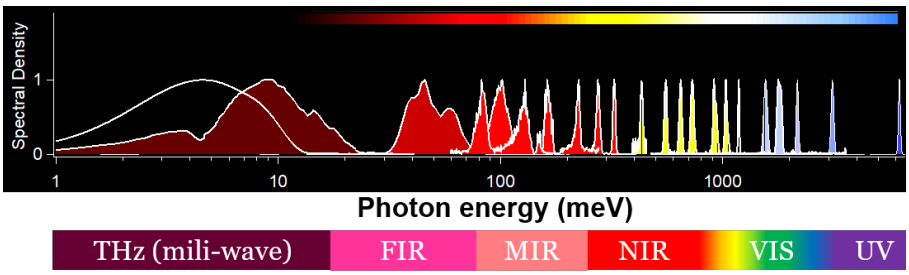


Figure 2.13 Available spectrum from non-linear process by ultrafast laser.

### 2.3.1 Introduction to THz radiation

THz refers to the electromagnetic (EM) wave from 0.1-10THz right between microwave and infrared band. A simple conversion of 1THz electromagnetic wave is:

$$1THz \sim 300\mu m \sim 4.1meV \sim 1ps \sim 48K \tag{2.30}$$

EM spectrum at THz band remains unexplored until the recent two decades along with advances in ultrafast lasers. THz science has demonstrated great potential in applications like safe imaging, high speed computation, space exploration, spectrum analysis etc. (3).

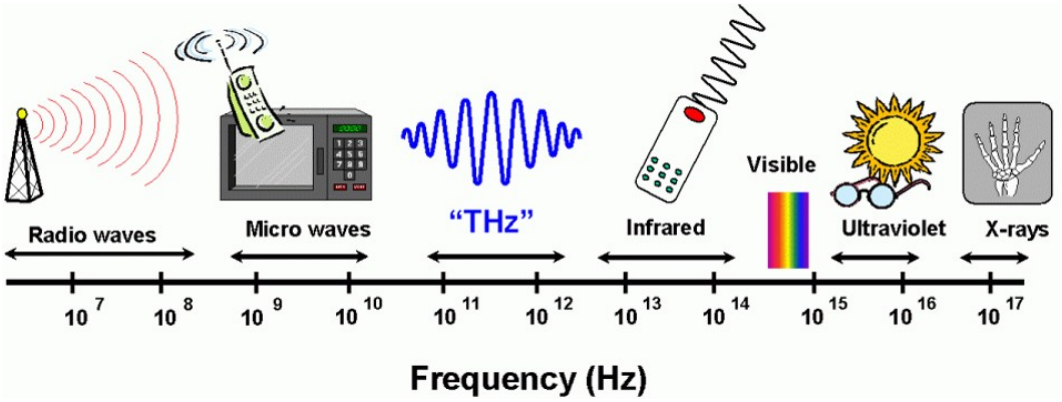


Figure 2.14 THz and adjacent electromagnetic radiation

For material science, many important phenomenon lie in THz band, such as lattice vibration, spin precession, cooper pairs in superconductor. THz wave provides an effective tool to probe and control these processes resonantly. Large E field of intense THz wave is also able to accelerate carriers in semiconductor and induce insulator-metal transition in VO2 compound (4).

### 2.3.2 THz Generation by Optical Rectification

For the past years, a few approaches have been developed to generate and detect THz radiations, such as quantum-cascade lasers (QCLs) (1), photoconductive antennas (PCAs) (2), optical rectification (OR) (3), free electron lasers (FELs) (4), bolometers, pyroelectric detectors, etc. Here we focus on THz generation by optical rectification in ZnTe non-linear crystal.

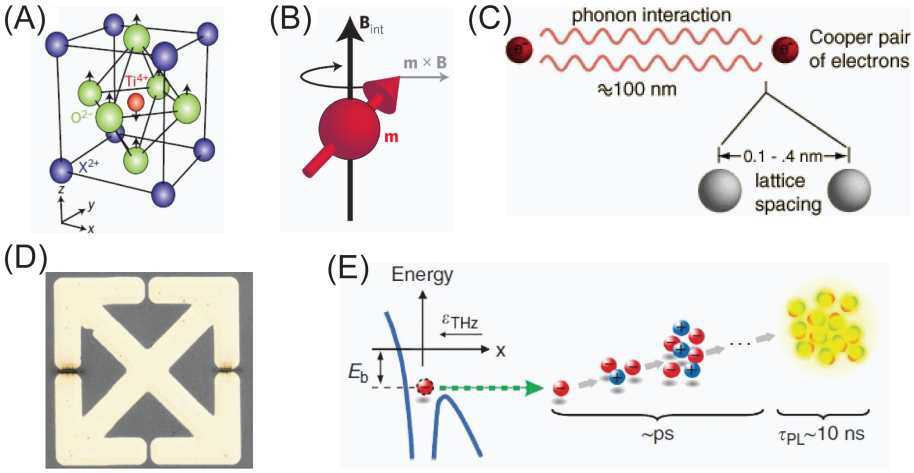


Figure 2.15 THz control of materials. Resonant control: (A) Lattice vibration of $SrTiO_3$, (B) spin precession in $SmFeO_3$, (C) Cooper pairs in superconductor; Non-resonant control: (D) Insulator-metal phase transition in $VO_2$, (E) Impact ionization in narrow bandgap semiconductor.

Nonlinear polarization induced by optical rectification is:

$$P_i^{(2)}(0) = \sum_{j,k} \epsilon_0 \chi_{ijk}^{(2)}(0, \omega, -\omega) E_j(\omega) E_k^*(\omega) \tag{2.31}$$

among which i, j, k are indices for the Cartesian components of fields, $\chi_{ijk}^{(2)}$ is the second-order nonlinear susceptibility tensor element for the crystal system. Many of the tensor components are zero due to crystal symmetry. For ZnTe, Equation can be simplified to:

$$\begin{pmatrix} P_x \\ P_y \\ P_z \end{pmatrix} = 4\epsilon_0 d_{14} E_0^2 \sin\theta \begin{pmatrix} \cos\theta \sin\theta \\ \cos\theta \cos\theta \\ \sin\theta \sin\phi \cos\phi \end{pmatrix} \tag{2.32}$$

So intensity of THz radiation is:

$$I_{THz}(\theta, \phi) \propto |P|^2 = 4\epsilon_0^2 d_{14}^2 E_0^4 \sin^2\theta (4\cos^2\theta + \sin^2\theta \sin^2(2\phi)) \tag{2.33}$$

Strongest radiation is obtained when laser polarization lies in 110 plane, which gives $\sin^2 2\phi = 1 \quad \phi = \frac{\pi}{4}, \frac{3\pi}{4}$. Then THz intensity is written as:

$$I_{THz}(\theta) = \frac{3}{4} I_{THz}^{max} \sin^2\theta (4 - 3\sin^2\theta) \tag{2.34}$$

when $I_{THz}^{max}$ is reached at $\theta = \sin^{-1}\sqrt{\frac{2}{3}} = 41.8°$. In experiment, laser polarization is aligned $[\bar{1}11]$, while generated THz emission has the same polarization.

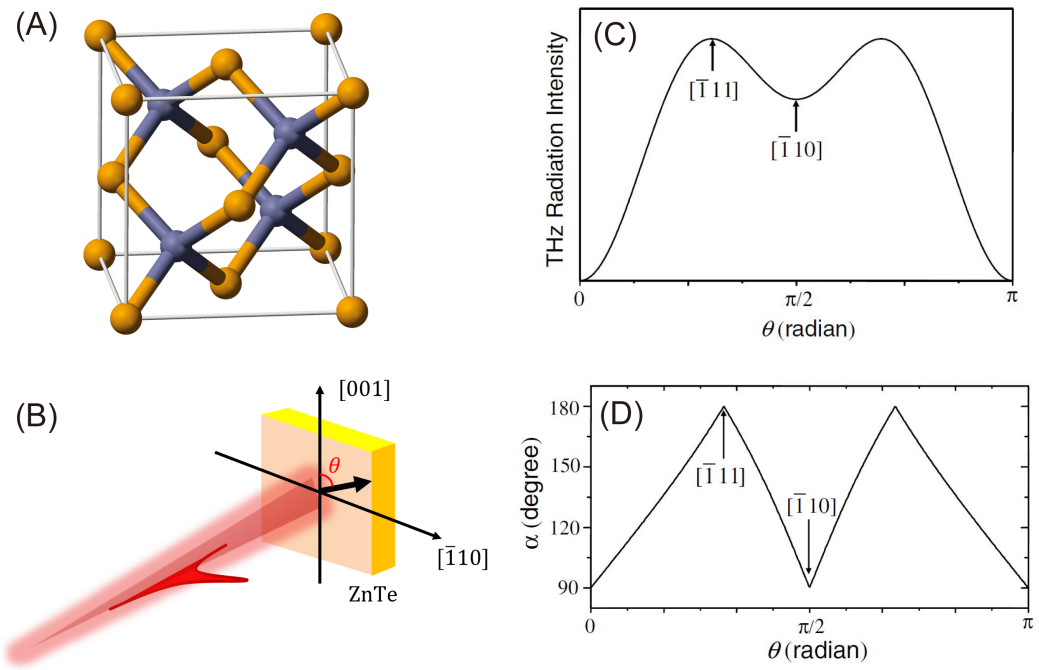


Figure 2.16 (A) ZnTe crystal structure; (B) Laser polarization in 110 plan; (C) (D) amplitude and polarization of THz E field. $\alpha$ is THz polarization in the coordination of (B) with respect to [001].

### 2.3.3 Free-Space Electro-Optic Sampling

THz E field oscillation can be sampled by a second laser pulse in time domain through Pockels effect, which refers to non-linear process when optical index of material is modulated by applied electric field. It has the expression of second-order nonlinearity:

$$P_i^{(2)}(\omega) = 2\sum_{j,k} \epsilon_0 \chi_{ijk}^{(2)}(\omega,\omega,0) E_j(\omega) E_k(0) = \sum_j \epsilon_0 \chi_{ij}^{(2)}(\omega) E_j(\omega) \tag{2.35}$$

where $\chi_{ij}(\omega) = 2\sum_k \chi_{ijk}^{(2)}(\omega,\omega,0)E_k(0)$ is the field induced susceptibility tensor. Sampling beam polarization is rotated by crystal birefringence and picked up by optics shown in Figure 2.17.

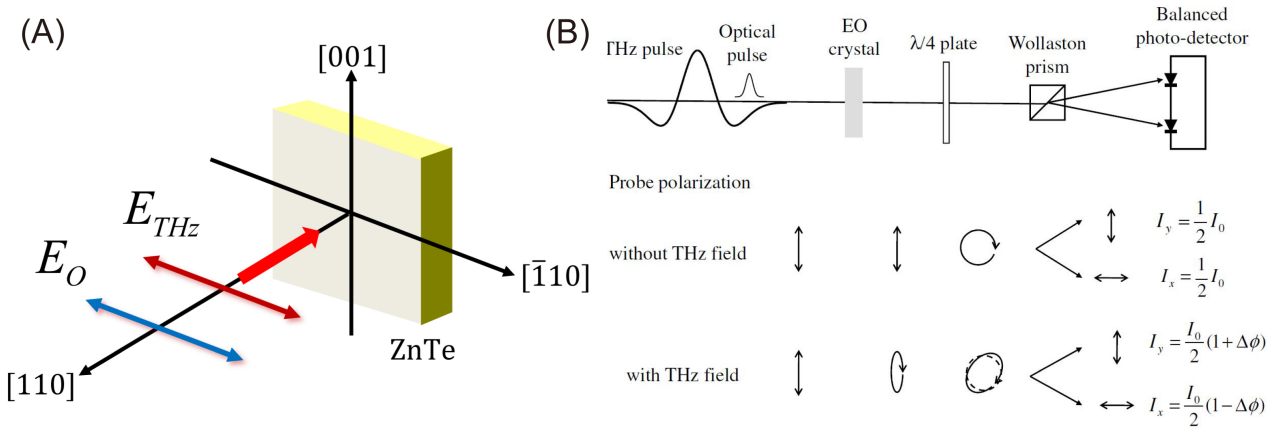


Figure 2.17 (A) Polarization of incident THz and optical light; (B) Optics to read out polarization state change of sampling beam.

Then we calculate relation between $E_{THz}$ and optical signal size from balance detector. The matrix for Equation is :

$$\begin{pmatrix} P_x \\ P_y \\ P_z \end{pmatrix} = 4\epsilon_0 d_{14} \begin{pmatrix} 0 & 0 & 0 & 1 & 0 & 0 \\ 0 & 0 & 0 & 0 & 1 & 0 \\ 0 & 0 & 0 & 0 & 0 & 1 \end{pmatrix} \begin{pmatrix} E_{O,x}E_{THz,x} \\ E_{O,y}E_{THz,t} \\ E_{O,z}E_{THz,z} \\ E_{O,y}E_{THz,z} + E_{O,z}E_{THz,y} \\ E_{O,z}E_{THz,x} + E_{O,x}E_{THz,z} \\ E_{O,x}E_{THz,y} + E_{O,y}E_{THz,x} \end{pmatrix} \tag{2.36}$$

$$= -4\epsilon_0 d_{14} E_O E_{THz} \boldsymbol{e_z} \perp \boldsymbol{E_O}$$

where

$$\boldsymbol{E_O} = \frac{E_O}{\sqrt{2}} \begin{pmatrix} 1 \\ -1 \\ 0 \end{pmatrix}; \quad \boldsymbol{E_{THz}} = \frac{E_{THz}}{\sqrt{2}} \begin{pmatrix} 1 \\ -1 \\ 0 \end{pmatrix}. \tag{2.37}$$

The non-linear P is orthogonal to incident optical beam, indicating the polarization is transformed from linear to elliptical shape after transmitting through ZnTe crystal in presence of THz E field.

The differential phase retardation $\Delta\phi$ can be calculated as:

$$\Delta\phi = (n_y - n_x)\frac{\omega L}{c} = \frac{\omega L}{c} n_O^3 r_{41} E_{THz} \tag{2.38}$$

in which $n_O$ is the refractive index at optical frequency and $r_{41}$ is the non-linear coefficient for EO sampling. Intensity of two beams by Wollaston prism, under small rotation approximation, is:

$$\begin{aligned} I_x &= \frac{I_0}{2}(1 - \sin\Delta\phi) \approx \frac{I_0}{2}(1 - \Delta\phi) \\ I_y &= \frac{I_0}{2}(1 + \sin\Delta\phi) \approx \frac{I_0}{2}(1 + \Delta\phi) \end{aligned} \tag{2.39}$$

Signal from balanced detector can be written as:

$$I_s = I_y - I_x = I_0\Delta\phi = \frac{I_0\omega L}{c} n_O^3 r_{41} E_{THz} \propto E_{THz} \tag{2.40}$$

We could use a much shorter optical sampling pulse to measure the real time E field oscillation. In this way, not only the amplitude, but also phase of THz wave is determined accurately. Spectrum after Fourier transformation $\tilde{T}$ is complex, containing both amplitude and phase information. From $\tilde{T}$, optical response from film materials can be extracted according to Fresnel equations. The setup is called "THz-TDS", in short for "THz time domain spectroscopy".

### 2.3.4 Generation of Intense THz Wave

From the equation above, we can see that efficient THz generation has several requirements: large non-linear coefficient, high saturation fluence, high transmission and phase matching between THz and optical light. ZnTe's ability to generate intense THz pulse is limited by its small non-linear coefficient ($d_{14} = 4pm/V$) and low saturation fluence.

Free electron laser emission covers spectrum from millimeter wave to X-ray, however access to such large facility is quite limited. $LiNbO_3$ is another option for THz generation with large electro-optic coefficient $d_{33} = 27pm/V$. But it is inefficient for conventional co-linear optical rectification scheme due to large index mismatch between 800nm group and THz phase index, which are $n_O = 2.3$, $n_T = 5.2$ respectively.

An ingenious way to circumvent the velocity mismatching is to use Cherenkov radiation. It refers to electromagnetic radiation emitted from a charged particle moving through a dielectric

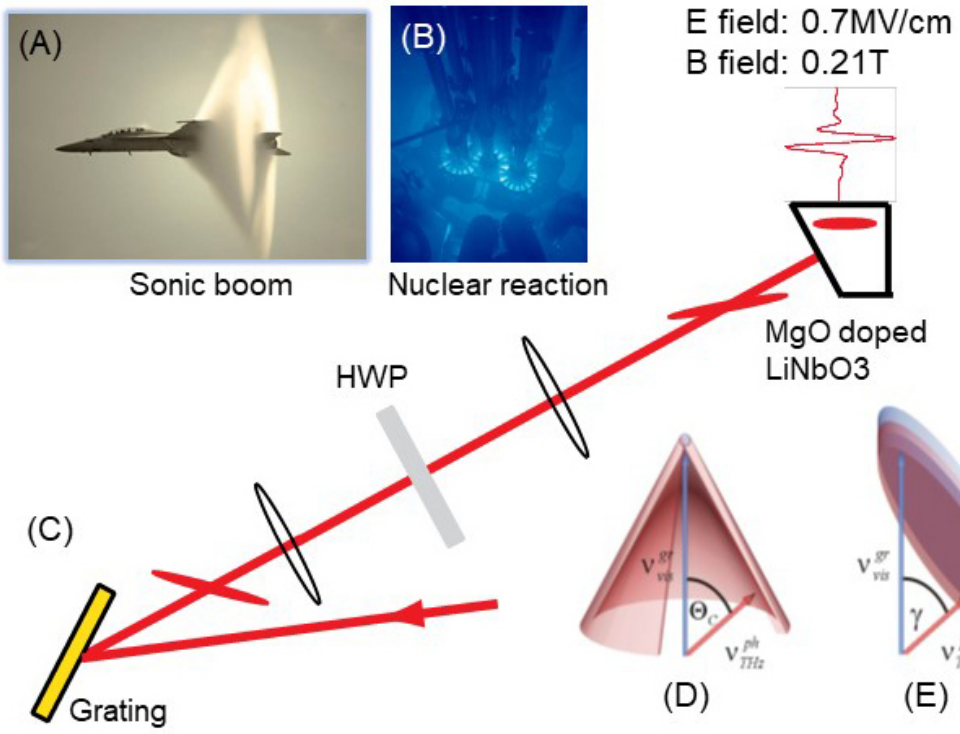


Figure 2.18 (A) Sonic boom; (B) Blue light radiation by electron Charenkov radiation in nuclear plan; (C) THz generation by tilted phase front in MgO doped $LiNbO_3$ crystal; Cherenkov radiation of a particle in (D) and plan wave in (E).

medium at a speed greater than the phase velocity of light in that medium. Two famous examples are the sonic boom around ultrasonic jet, and the blue light emission by electrons with velocity greater than light in cooling water. Radiation propagates along the conical surface at angle $\theta_c$:

$$\theta_c = \arccos(\frac{v_p}{v_g}) \tag{2.41}$$

which compensate the velocity mismatch between electron and light. Similarly, the phase front of optical light can be steered to $\theta_c$ as

$$\theta_c = \arccos(\frac{v_p}{v_g}) = \arccos(\frac{n_O}{n_{THz}}) = 64^\circ \tag{2.42}$$

by grating dispersion (Figure 2.18). Each spectral component on the tilted wave front, in analogy to electron, radiates THz when propagating inside $LiNbO_3$ crystal. Sum over whole spectrum will

lead to constructive interference on one side and destructive interference on the other side, which satisfies phase matching condition for optical rectification.

In experiment, $LiNbO_3$ is doped with MgO to increase the breakdown fluence. Crystal is cut in 64° angle prism shape. Intense THz pulse, with peak E field up to 0.9MV/cm, B field as large as 0.2T, exits the angled crystal plane and gets focused at sample position.

## 2.4 Ultrafast Spectroscopy

The access to ultrashort pulse makes it possible to study ultrafast dynamics in materials. This section gives a brief introduction to ultrafast science and spectroscopy.

### 2.4.1 History of Ultrafast Science

The ultrafast science can be dated back to an argument by punters in a bar: does galloping horse ever lifts all four feet completely off the ground during gait? This interesting question, which is clearly beyond the capability of human eyes, caught attention of Leland Stanford, the industrialist and horseman. He commissioned Eadweard Muybridge, a professional photographer, to find a method to resolve this argument (5).

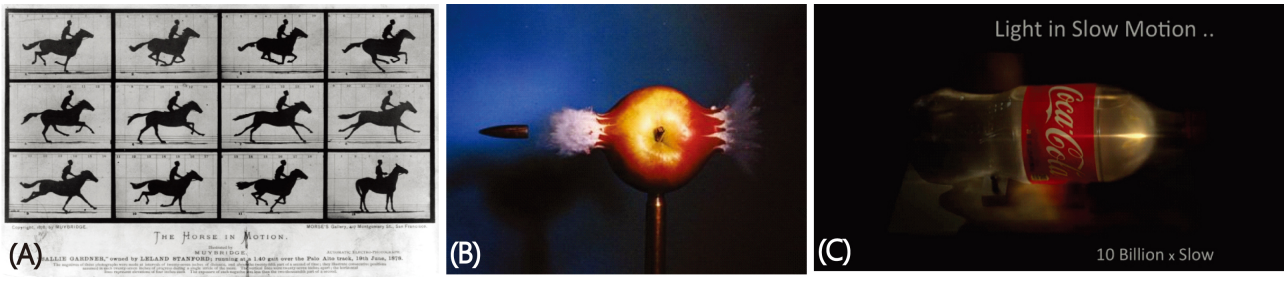


Figure 2.19 (A): Bar bet: Galloping horse ever lifts all four feet completely off the ground during the gait? (1878) 1/2000s per frame. (B): How to Make Applesauce at MIT (1964) 1/1 million s per frame. (C): Ultrashort laser pulse shot through bottle of water (2013) 1/1 trillion s per frame.

At Stanford's farm in Palo Alto, Eadweard placed the 24 cameras, 27 inches apart along a track parallel to the horse's path. Shutters of cameras were controlled by trip wires triggered by the

horse's legs. The photographs were taken in succession one twenty-fifth of a second apart, with the shutter speeds less than 1/2000 s. Finally he was able to make a short movie from 16 frames of such pictures . As shown in Figure 2.19, one picture clearly shows all four feet in air for a galloping horse. There were also rumors that Stanford had a large bet riding on the outcome of this study.

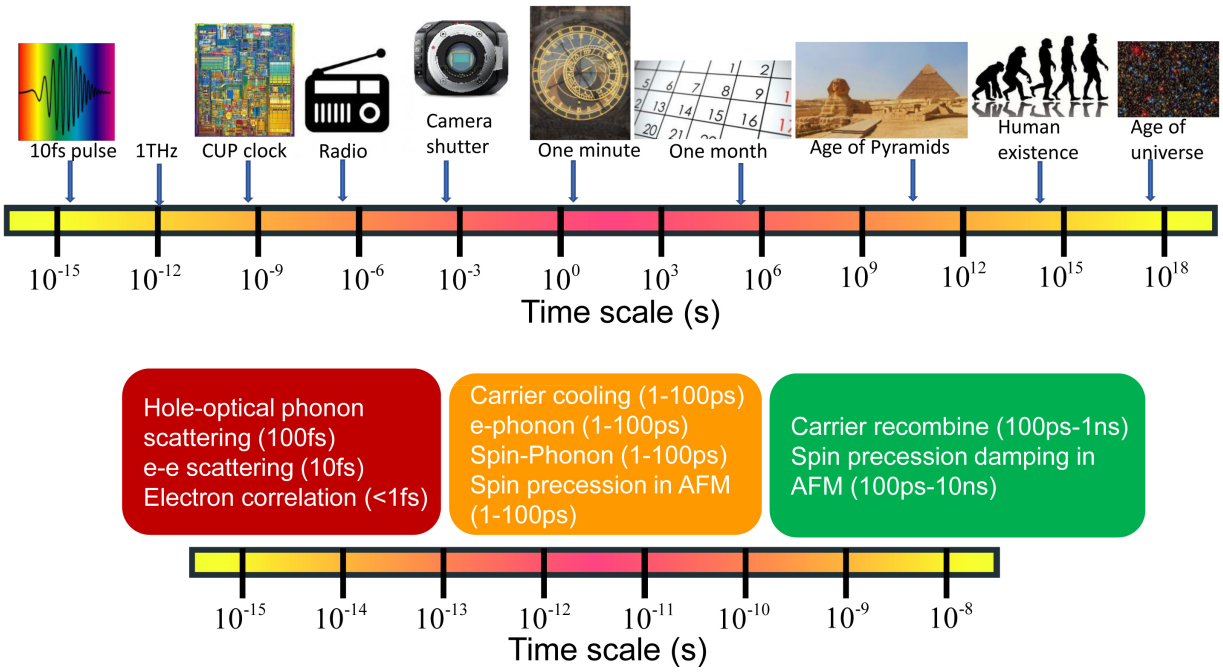


Figure 2.20 Time scale of everything

However, the pursuit of speed never stops. Among all these achievement, the most famous one might be a picture which captures the moment when bullet flew through an apple, shot by Professor Harold Edgerton, also known as Papa flash at MIT. (5). He invented short duration electronic flash and pushed high speed photography to 1/million second per frame. Nowadays technique is able to reach 1/trillion second per frame, making it possible to shoot a movie of light transmitting through water (6).

Figure 2.20 shows the time scale we have ever studied so far, from the shortest optical pulse to the clock rate of CPU, life expand of human and the age of universe. The physical process in

condensed matter is from fs to ns. We will need probe at fs duration to captures the fast interaction of electrons, holes, spins, phonons etc, which is realized by the ultrafast lasers.

### 2.4.2 Ultrafast Pump-Probe Spectroscopy

The essential tool to study ultrafast phenomenon is femtosecond laser, which has fs time resolution and extremely high peak intensity due to compressed energy into a very short time window. Laser beam is split into two paths: strong side is normally used as optical pump and weak one as probe. Laser pulse with very high peak intensity is able to excite many kinds of phenomena such as ionization, lattice vibration, phase transition, transient currents and polarization etc. Specific process can be isolated by selecting pump-probe wavelength and their distinct time scales. Optical properties of materials are modified accordingly like magnetization, polarization, conductivity, permittivity, non-linear dielectric constant. Pump induced change is captured by probe at a later time, from which we can peek into the ultrafast microscopic physical process inside the complex material systems.

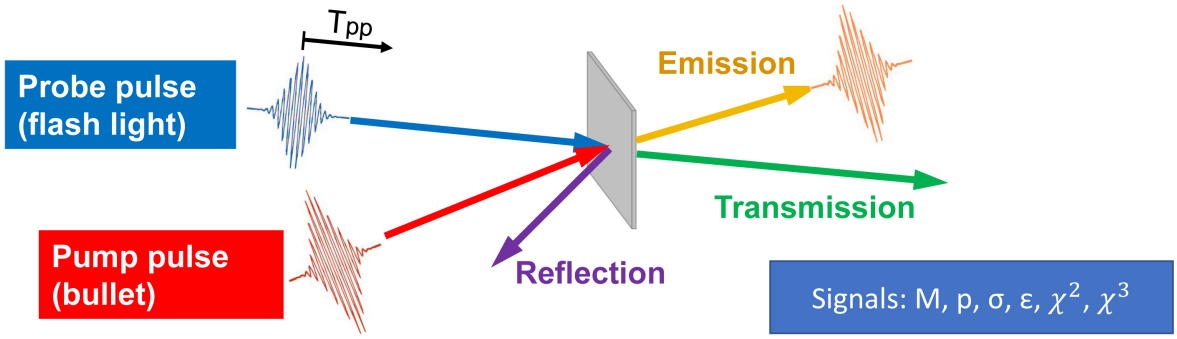


Figure 2.21 Schematic for ultrafast pump-probe measurement.

The scheme of ultrafast pump-probe measurement is plotted in Figure 2.21. Optical delay between pump and probe is $t_{pp}$. We can understand pump-probe measurement in analogy to high-speed photography in Figure 2.19(B): optical pump→bullet , probe→flash light, detector→camera, apple→ materials we are interested in.

## 2.5 THz pump-THz probe spectroscopy

### 2.5.1 Experiment setup

For time resolved ultrafast THz pump-THz probe measurement, a Ti-Sapphire amplifier with pule energy at 3mJ, pulse duration at 40fs, 1KHz repetition rate and 800nm center wavelength was split into three paths: pump, probe and sampling (Figure 2.22).

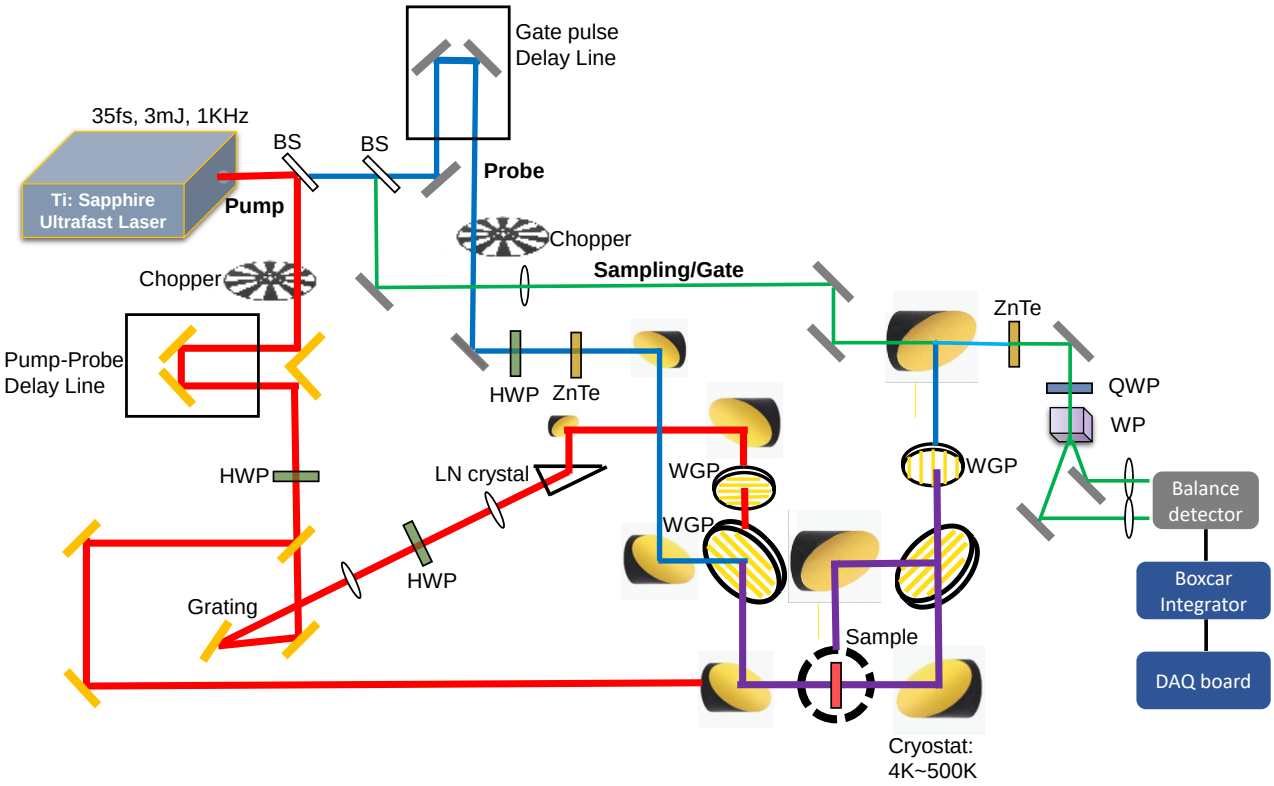


Figure 2.22 Experimental setup of THz pump-THz probe spectroscopy. BS: beam splitter; HWP: half wave plate; AL: achromatic lens; LN: MgO doped $LiNbO_3$; WGP: wire grid polarizer; QWP: quarter wave plate; WP: Wollaston prism

The intense THz pump pulses were generated by the tilted-pulse-front phase matching method through 1.3% MgO doped LiNbO3 crystal, of which experimental scheme follows (7). The weak THz probe pulses were generated by optical rectification and detected by free space electro-optic

sampling through 1mm thick (110) ZnTe crystal. Pump and probe THz pulse with orthogonal polarizations was combined by a wire grid polarizer in collinear geometry and focused on sample at normal incidence. Two extra wire grid polarizers were placed before the beam combiner to purify pump THz polarization. By rotating the first wire grid polarizer, we were able to tune pump THz E field continuously. Specifically speaking, 800nm beam from amplifier was s-polarized, perpendicular to the sheet. Pump THz E-field was parallel to 800nm polarization, while probe E-field was perpendicular to 800nm. Spot size of pump and probe on sample were 1.2mm, 0.8mm respectively. After sample, pump THz pulse was blocked by another wire grid polarizer and transmitted probe THz E field was sampled by 800nm pulse. The output signal from balanced detector was integrated by Boxcar and sent to DAQ board together with the chopper synchronization signal.

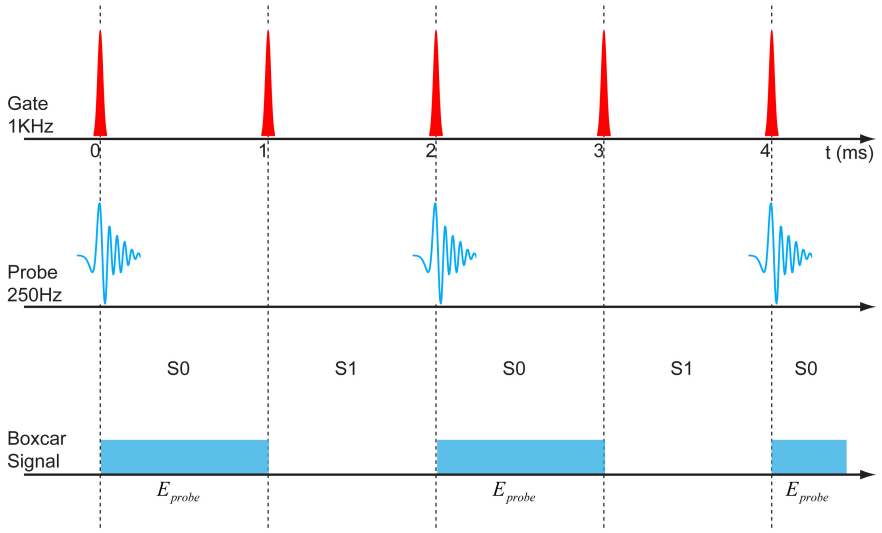


Figure 2.23 Experimental setup of THz pump-THz probe spectroscopy. Temporal pulse sequence of static THz transmission measurement.

Our data taking scheme is well described by Shimano's paper (8) except for different chopping frequency. For static THz transmission measurement without pump, probe pulses were chopped by 500Hz and transmitted probe E field is obtained by subtracting adjacent pulse signal.

$$E_t = S0 - S1. \tag{2.43}$$

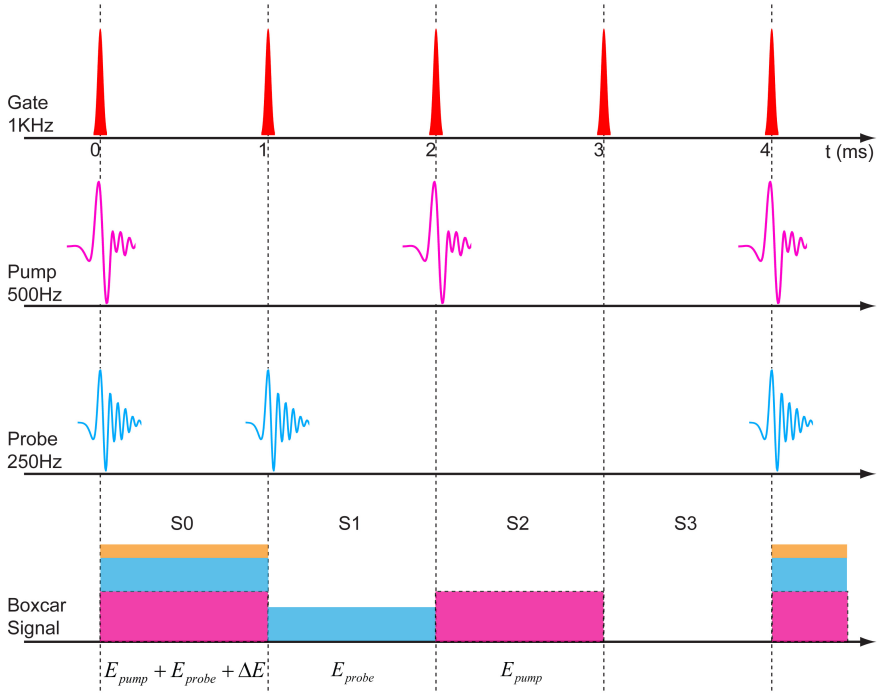


Figure 2.24 Temporal pulse sequence of pump induced probe transmitted THz E field change measurement.

For pump induced probe E field change measurement, pump and probe pulses were chopped at 500Hz and 250Hz simultaneously. One period of pulses consists of 4 channels: pump on probe on, pump off probe on, pump on probe off, pump off probe off. By subtracting the pump leakage from the signal, transmitted probe E field change induced by pump $\Delta E$ is:

$$\Delta E = (S0 - S2) + (S1 - S3). \tag{2.44}$$

### 2.5.2 Complex conductivity extraction:

Optical conductivity was calculated from complex transmission $\tilde{t}(\omega)$ by comparing transmitted E field through film sample to reference. The index of vacuum is assumed to be 1.

For reference, according to Fresnel equation, the complex transmission $\tilde{t}_{ref}$ is:

$$\tilde{t}_{ref} = \frac{E_{out}^{ref}}{E_{in}} = \frac{4n_{sub}}{(1+n_{sub})^2}\frac{e^{i\beta_{sub}}}{e^{i\beta_{sub}^{ref}}}. \tag{2.45}$$

where $\beta_{sub} = \frac{2\pi}{\lambda_0} n_{sub} d_{sub}$, $\beta_{air}^{ref} = \frac{2\pi}{\lambda_0} d_{sub}$ and $E_{in}$ is the incident THz E field.

For a thin film sample on a substrate, coherent light propagation must be considered (9). According to transfer matrix, the complex transmission $\tilde{t}_s$ is:

$$\tilde{t}_s = \frac{E_{out}^s}{E_{in}} = \frac{2n_{sub}}{(1+n_{sub})} \frac{e^{i\beta_{sub}}}{e^{i\beta_{air}^s}} \frac{2}{(1+n_{sub})\cos\beta_s - (n_s + \frac{n_{sub}}{n_s}) i \sin\beta_s}. \tag{2.46}$$

where $\beta_s = \frac{2\pi}{\lambda_0} n_s d_s$, $\beta_{air}^s = \frac{2\pi}{\lambda_0}(d_{sub} + d_s)$. By compared the transmitted THz E field through sample and reference, measured complex transmission in experiment $\tilde{t}_{exp}$ is:

$$\tilde{t}_{exp} = \frac{E_{out}^s}{E_{out}^{ref}} = \frac{\tilde{t}_s}{\tilde{t}_{ref}} = \frac{1+n_{sub}}{(1+n_{sub})\cos\beta_s - (n_s + \frac{n_{sub}}{n_s}) i \sin\beta_s} \times e^{-i\frac{2\pi}{\lambda_0}(d_s + \delta d_{ref})}. \tag{2.47}$$

Here $\delta d_{ref}$ is the phase correction due to small different thickness between sample substrate and reference. Take the corrected transmission as:

$$\tilde{t}_{cor} = \tilde{t}_{exp} \times e^{i\frac{2\pi}{\lambda_0}(d_s + \delta d_{ref})}. \tag{2.48}$$

Then we shall have:

$$\tilde{t}_{cor} = \frac{1+n_{sub}}{(1+n_{sub})\cos\beta_s - (n_s + \frac{n_{sub}}{n_s}) i \sin\beta_s} \tag{2.49}$$

In the thin film limit, $\beta_s << 1$:

$$\cos\beta_s \sim 1, \sin\beta_s \sim \beta_s. \tag{2.50}$$

. Then the complex dielectric coefficient of sample is:

$$\tilde{\epsilon} = n_s^2 = (1+n_{sub}) \left(1 - \frac{1}{\tilde{t}_{cor}}\right) \frac{c}{i \cdot 2\pi \cdot d_s \cdot f} - n_{sub}. \tag{2.51}$$

And complex conductivity is:

$$\tilde{\sigma} = \frac{i\omega}{4\pi}(1 - \tilde{\epsilon}). \tag{2.52}$$

In our measurement of $Nb_3Sn$, the phase correction is chosen to make $\sigma_1$, $\sigma_2$ all positive either with or without pump, which is less than 1% of substrate thickness.

## 2.6 Introduction to superconductivity

### 2.6.1 General properties

Superconductivity is a quantum mechanical phenomenon of vanishing electrical resistance and expulsion of magnetic flux fields in certain materials, when cooled below a characteristic critical temperature $T_c$ (10). It is characterized by Meissner effect, the complete ejection of magnetic field from interior, even for field in an originally normal sample. It CANNOT be explained by perfect conductivity, which would tend to trap flux in. According to BCS theory of superconductivity, such exotic behavior is the result of electron pairing (Cooper pair) condensation to a single macroscopic quantum state.

The existence of such reversible Meissner effect implies that superconductivity will be destroyed by a critical magnetic field $H_c$, which is related thermodynamcially to the free-energy difference between normal and superconducting states in zero field, the so called condensation energy of the superconducting state (12). That is:

$$\frac{H_c^2(T)}{8\pi} = f_n(T) - f_s(T) \tag{2.53}$$

where $f_n$ and $f_s$ are the Helmholtz free energies per unit volume in the respective phases in zero field. $H_c(T)$ drops as temperature increases and vanishes above $T_c$.

Depending on the manner on which penetration occurs at increasing field for cylindrical shaped samples with their axes parallel to the applied magnetic field, there are two clearly distinguishable types of superconductors.

Type I Below a critical field $H_c(T)$ that increases as T falls below $T_c$, there is no penetration of flux. When applied field exceeds $H_c(T)$ , the entire specimen reverts to the normal state and the field penetrates perfectly.

Type II Below a lower critical field $H_{c1}(T)$ there is no penetration of flux, when the applied field exceeds an upper critical field $H_{c2}(T) > H_{c1}(T)$, the entire specimen reverts to the normal state and field penetrates perfectly. When applied field strength is between $H_{c1}(T)$ and $H_{c2}(T)$, there is partial penetration of flux, and the sample develops a rather complicated microscopic structure, i.e.

vortex states of both normal and superconducting regions known as mixed state. The magnetization curve corresponding to Type I and II superconductor behavior is shown in Figure 2.25.

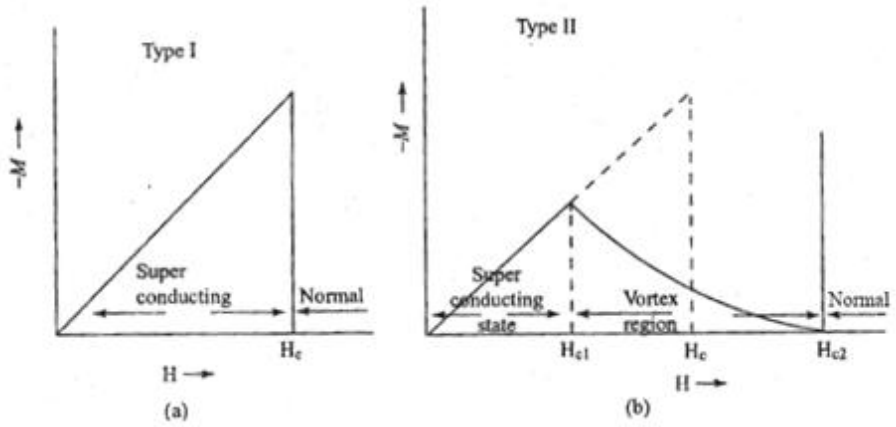


Figure 2.25 Magnetization of Type I and II superconductor vs applied magnetic field (11).

Above $Tc$, superconductivity resistivity has the form of normal metals, described by $\rho(T) = \rho_0 + BT^5$, in which the constant term arises from impurity and defect scattering, and the term in $T^5$ arises from phonon scattering. Below $T_c$, resistivity drops abruptly to zero and current can flow in a superconductor with no discernible dissipation of energy. However, if the current exceeds a critical value, the superconducting state will be destroyed (Silsbee effect). The size of this critical current also depends on the material nature and geometry of the specimen, and related to whether the magnetic field produced by the current exceeds the critical field at the surface of superconductor. A superconductor well below its transition temperature will also respond without dissipation to an AC electric field provided that the frequency is not too large above the SC correlation energy gap $\Delta/\hbar$.

Electron gas model predicts that good electrical conductors are also good conductors of heat, since conduction electrons transport entropy as well as electric charge. Superconductors, contrary to this, are poor thermal conductors, indicating that those electrons in the persistent current carry no entropy.

For traditional superconductors, metal to superconductivity transition establishes an energy gap $\Delta$ at orders of $kT_c$, between ground state and quasi-particle excitation of the system. However,

this energy gap is different from band gap formed by periodic crystal structure. The origin of this superconducting gap $\Delta$ are explained by BCS theory of superconductor.

### 2.6.2 London equation

F. London and H. London first proposed a quantitative way to explain the fundamental fact that a metal in superconducting state permits no magnetic field in its interior. First we write the equation for acceleration of superconducting current density $\boldsymbol{J}_s$ in presence of an external field E as:

$$\frac{d}{dt}\frac{m}{N_s e^2}\boldsymbol{J}_s = \boldsymbol{E} \tag{2.54}$$

where $N_s$ is the superfluid particle density, which can be taken as equal to the particle density in the normal state N, assuming all carriers condensed into Cooper pairs. In addition, using Maxwell's equation, this relation can be written as:

$$\frac{d}{dt}(\nabla \times \frac{m}{N_s e^2}\boldsymbol{J}_s + \frac{\boldsymbol{B}}{c}) = 0 \tag{2.55}$$

Flux expulsion, or Meissner effect, is accounted for by assuming not only the time derivative in the precious equation, but the function in bracket itself is zero $\nabla \times \frac{m}{N_s e^2}\boldsymbol{J}_s + \frac{\boldsymbol{B}}{c} = 0$. With Maxwell's equation $\boldsymbol{B} = \nabla \times \boldsymbol{A}$, this expression reduces to:

$$\boldsymbol{J}_s = -\frac{m}{N_s e^2}\boldsymbol{A} \tag{2.56}$$

Using Maxwell's equation $\nabla \times \boldsymbol{B} = \frac{4\pi}{c}\boldsymbol{J}_s$, we can obtain the magnetic field $\boldsymbol{B}$ as:

$$\nabla^2 \boldsymbol{B} = \frac{4\pi N_s e^2}{mc^2}\boldsymbol{B} = \frac{\boldsymbol{B}}{\lambda_L^2} \tag{2.57}$$

with London penetration depth defined by:

$$\lambda_L = (\frac{mc^2}{4\pi N_s e^2})^{1/2} = \frac{c}{\omega_p} \tag{2.58}$$

where $\omega_p$ is plasma frequency. As this equation describes the spatial variation of B, $\lambda_L$ characterizes the exponential decay of the electromagnetic field. For normal metals, ski depth $\delta_0$ is inversely proportional to $\omega^{-1/2}$, while London penetration depth is frequency independent. Temperature

dependence of $\lambda_L$ follows the condensate density $N_s(T)$. For time-varying fields, Eq. 2.55 gives $1/\omega$ dependence of imaginary part of conductivity as:

$$\sigma_2(\omega) = \frac{N_s e^2}{m\omega} == \frac{c^2}{4\pi\lambda_L\omega} \tag{2.59}$$

Through Kramers-Kronig relation, the real part of the conductivity is given by:

$$\sigma_1(\omega) = \frac{\pi}{2}\frac{N_s e^2}{m}\delta(0) = \frac{c^2}{8\lambda_L^2}\delta(\omega = 0) \tag{2.60}$$

### 2.6.3 BCS theory of superconductivity

The most successful theory to explain superconductivity is proposed by Bardeen, Cooper and Schrieffer in 1957, which is called BCS theory in short. The key idea of superconductivity is electron pair condensation. Below certain critical Tc, two electrons with opposite momentum and spin are coupled and form a cooper pairs under phonon mediated-attractive potential. This weak attraction leads to a ground state separated from excited states by an energy gap $\Delta$. However, Fermi sea is not stable to electron pair, and Cooper pairs condense into a single macroscopic quantum state without dissipation at DC.

The penetration depth and coherence length emerge as natural consequences of the BCS theory. The London equation is obtained from magnetic fields that vary slowly in space. Thus the central phenomenon in superconductivity, the Meissner effect, is obtained in a natural way. Superconducting transition temperature $T_c$ can be obtained by the material characteristic electron-lattice attractive interaction potential U and electron density of orbitals $D(\epsilon_F)$ of one spin at Fermi level. Magnetic flux through a superconducting ring is quantized and effective unit of charge 2e rather than e, as a consequence of electron paring. The quantum signature of superconductivity, Josephson junction, is also well explained by this theory.

### 2.6.4 Electrodynamics of superconducting state

There are several different length scales which play important roles and their relative magnitude determines the nature of superconducting state, and also the response to electromagnetic fields (13).

The first scale is London penetration depth:

$$\lambda_L = \frac{c}{\omega_p} \tag{2.61}$$

determined through plasma frequency $\omega_p$ by the parameters of metallic state and derived from Meissner effect. The second length scale is the correlation length:

$$\xi = \frac{\hbar v_F}{\pi \Delta} \tag{2.62}$$

describing, crudely speaking the spatial extension of Cooper pairs at 0K. Here the $v_F$ is Fermi velocity and $\Delta$ is SC order parameter. The third length scale is the mean free path of uncondensed electrons:

$$l = v_F \tau \tag{2.63}$$

set by the impurities and lattice imperfections at low temperature. $\tau$ is the time between two scattering events. Depending on the relative magnitude of their ratios, various types of superconductors are observed. The local limit is where $l << \xi, \lambda$. More commonly it is referred to as the dirty limit $l/\xi \to 0$. In the opposite, so-called clean limit is when $l/\xi \to \infty$. It is also necessary to distinguish the following two cases: Pippard or anomalous limit, defined by $\lambda << \xi, l$ (Type I superconductor), and the London limit for which $\xi << \lambda, l$ (Type II superconductor).

The spectral weight associated with excitation is conserved by going from normal to broken symmetry states. While we have to integrate the real part of the normal state conductivity spectrum $\sigma_1^n(\omega)$, in the superconducting phase there are two contributions: one from collective mode of the Cooper pairs $\sigma_1^{coll}(\omega)$, and one from the single $\sigma_1^{sp}(\omega)$:

$$\int_{-\infty}^{+\infty} [\sigma_1^{coll}(\omega) + \sigma_1^{sp}(\omega)] d\omega = \int_{-\infty}^{+\infty} \sigma_1^n(\omega) d\omega = \frac{\pi}{2} \frac{Ne^2}{m} \tag{2.64}$$

assuming that all the normal carriers condense. Because of the difference in coherence factors for the superconducting and density wave ground states, the conservation of spectral weight has different consequences. Spectral weight A is removed from integral upon going through superconducting transition:

$$\int_{-\infty}^{+\infty} [\sigma_1^n(\omega) - \sigma_1^s(\omega)] d\omega = A \frac{Ne^2}{m} \tag{2.65}$$

where $\sigma_1^n(\omega)$ and $\sigma_1^s(\omega)$ are conductivity spectra at normal and superconducting state. Comparing Eq 2.58 and Eq 2.59 leads to:

$$\lambda = \frac{c}{\sqrt{8A}} \tag{2.66}$$

connecting the penetration depth $\lambda$ to the missing spectral weight A. This relationship is expected to hold also at finite temperatures and for various values of the mean free path and coherence length – as long as the arguments leading to the transition rate apply. In the limit of long relaxation time $\tau$, the entire Drude spectral weight of normal carriers collapses in the collective mode, giving

$$\sigma_1(\omega = 0) = \frac{\pi N_s e^2}{2m}\delta(\omega = 0) \tag{2.67}$$

### 2.6.5 Introduction to Anderson pseudo spin formalism

In BCS ground state, two electrons $+k\uparrow$ and $-k\downarrow$ form a cooper pair $(+k\uparrow, -k\downarrow)$, whose ground state wave function can be expressed in Anderson pseudo spin formalism:

$$|\Psi_{BCS}\rangle = \prod_k (u_k |00\rangle_k + v_k |11\rangle_k \tag{2.68}$$

where $|11\rangle_k$ and $|00\rangle_k$ stands for Anderson pseudo spin up and down. And BCS Hamiltonian as:

$$H_{BCS} = 2\sum_k \vec{b_k} \cdot \vec{\sigma_k} \tag{2.69}$$

where $\vec{\sigma_k} = (\sigma_k^x, \sigma_k^y, \sigma_k^z)$ is the Anderson pseudo spin and $\vec{b_k} = (-\Delta', -\Delta", \epsilon_k)$ is the pseudo magnetic field whose z component is band dispersion measured from Fermi energy. Then complex order parameter of superconductor is:

$$\Delta = \Delta' + \Delta" = U\sum_k (\sigma_k^x + \sigma_k^y) \tag{2.70}$$

where U is the pairing interaction potential.

In equilibrium, pseudo spin at each k is aligned along pseudo magnetic field direction. Time evolution of pseudo spin is described by Bloch equation:

$$\frac{\partial}{\partial t}\vec{\sigma_k} = 2\vec{b_k} \times \vec{\sigma_k} \tag{2.71}$$

So order parameter dynamics can be represented by motion of pseudo spin. For spatially homogeneous monochromatic electro magnetic wave $E\exp(i\omega t)$ applied on superconductor, the z component of $\vec{b_k}$ in the nonlinear regime is:

$$\begin{aligned}\frac{\epsilon_{k-eA(t)}+\epsilon_{k-eA(t)}}{2} &= \epsilon_k + \frac{e^2}{2}\sum_{i,j}\frac{\partial^2\epsilon_k}{\partial k_i \partial k_j}A_i(t)A_j(t) + O(A^4) \\ &= \epsilon_k - \frac{e^2}{2}\sum_{i,j}\frac{\partial^2\epsilon_k}{\partial k_i \partial k_j}\frac{E_i(t)E_j(t)}{\omega^2} + O(E^4)\end{aligned} \tag{2.72}$$

which has additional frequency components at $2\omega$ and $4\omega$. Accordingly, pseudo spin, or order parameter, is oscillating at $2\omega$ and $4\omega$ under such magnetic field.

# CHAPTER 3. TERAHERTZ LIGHT-QUANTUM-TUNING OF A METASTABLE CORRELATED PHASE HIDDEN BY SUPERCONDUCTIVITY

## 3.1 Introduction

"Sudden" quantum quench and prethermalization have emerged as a cross-cutting theme for discovering emergent states of matter, such as quantum criticality and generalized Gibbs ensembles of cold atoms, quark-gluon plasmas, or metastable phases in the early universe (14; 15; 16). Yet this remains challenging in electron matter (17; 18; 19; 20; 21), especially superconductors (SC), despite recent progress (8; 22; 23; 24; 25). The grand open question of what is hidden underneath the "SC dome" occurring in several quantum materials appears to be universal (26), yet the new, even thermodynamically forbidden states have been unexplored. Here we reveal a long-lived, hidden gapless quantum phase of prethermalized quasi-particles following single-cycle, resonant terahertz quench of the $Nb_3Sn$ SC gap above a critical fluence. Its conductivity is characterized by a sharp coherent peak and a vanishing scattering rate that decreases almost linearly at low frequency, most pronounced around full depletion of the SC condensate, and is absent for high frequency pump. Above pump threshold, such quantum behaviors with memory persist as an unusual prethermalization plateau, without relaxation to normal or SC thermal states for order of magnitude longer than the quasi-particle and energy relaxation times. Switching to this metastable "quantum fluid" state signals dynamic quench of coupled SC and charge-density-wave-like orders and reveals a more complex organization principle beneath SC.

Exotic states in correlated materials have been discovered by using traditional tuning methods such as chemical substitution and applied pressure or magnetic fields. These methods correspond to slow changes of parameters g in the Hamiltonian H(g) and mostly access states of thermodynamic equilibrium, as illustrated in Figure 3.1a. The availability of single-cycle, intense terahertz (THz)

pulses (red arrow) now opens fascinating possibilities for non-thermal and non-adiabatic quench of Hamiltonians, in analogy to "parameter quenches" below megahertz frequency scales in ultracold atoms. During post-quench, pre-thermalization time evolution, the system can reach persisting, quasi-steady plateau states far-from-equilibrium. Such states are inaccessible to adiabatic tuning and optical pumping methods. In the latter case, the induced heating and dissipation couple excited quasi-particles with, e.g., thermal baths of hot phonons. When applied to correlated materials with competing orders, THz quench of the dominant SC phase without heating of other degrees of freedom allows to investigate the possibility of obtaining new pre-thermalized quantum states and preempted "hidden" orders beneath SC. The latter have not yet been observed despite recent exciting observations in THz–driven dynamics, e.g., collective modes (22; 23) excited by relatively weak SC quench and light-enhanced SC in cuprates (24; 25). Strong THz SC quench, one order of magnitude higher than in Ref. (8; 22; 23) is desired for driving phase transitions (4; 27) which have been scarce so far in SC materials. Prior studies indicate photoinduced, spatially inhomogeneous SC/metallic phases due to, e.g., dirty limit samples and below–threshold THz fields used (8; 28).

## 3.2 Sample preparation

A nearly single-crystal $Nb_3Sn$ film 20nm thick with a critical temperature of $T_c$ ~16K was grown by magnetron sputtering on a 1mm $Al_2O_3(100)$ substrate. It was grown by co-sputtering of Nb and Sn at high temperatures. Nb and Sn targets were current-regulated at 0.33A and 0.1A respectively in 3 mtorr of Ar, positioned 15.5cm from the substrate. Base pressure was $9.4 \times 10^{-8}$ mtorr. The $10 \times 10 \times 1$mm R-plane sapphire substrate was exposed to a SiC-coated graphite heating element above, and exposed to Nb and Sn flux from below. Deposited material was heated directly by the radiation, which largely passed through the sapphire. Film temperature during growth is estimated at $1020°C$ by measuring film temperature on thick films grown under similar conditions. Temperatures were measured with an optical pyrometer.

## 3.3 Static Terahertz Electrodynamics of Superconductor $Nb_3Sn$

Here we present evidence of a quantum-quench, phase transition to a gapless, prethermalization plateau state $|\psi_{Plateau}\rangle$ in a $Nb_3Sn$ superconductor. Sub-picosecond, single-cycle THz fields up to 620 kilovolt/cm (Figure 3.1b) non-adiabatically excite quasiparticles (QPs) without excessive heating, using central frequency $\hbar\omega$=4 meV (Figure 3.1c) in the vicinity of twice the QP excitation gap, $2\Delta_{SC}$ ~5.1 meV at 4.1 K. Such *non-thermal* depletion of the SC condensate is implemented on time scales comparable to SC gap fluctuation times $\hbar/2\Delta_{SC}$ ≈0.8ps, which leads to a distinct THz light-tuned hidden quantum phase in a nearly single-crystal $Nb_3Sn$ film of 20nm thick on 1mm $Al_2O_3(100)$ substrate. The sample exhibits a SC transition at $T_c$ ~16 K and an electronic instability or martensitic transition around $T_M$ ~47 K (supplementary). This has been attributed to optical phonon condensation ("dimerization" of Nb atoms) (29), possibly driven by a Van Hove singularity-like electronic density-of-states and by strong electron-phonon interaction (33; 30; 34; 32; 31; 35) The equilibrium frequency-dependent complex conductivities $\sigma_1(\omega, T)$ and $\sigma_2(\omega, T)$ measure the dissipative and inductive responses respectively, Figure 3.1d and 1e. Specifically, the equilibrium 4.1 K traces exhibit a large, $1/\omega$ response in $\sigma_2$ from the SC condensate and zero conductivity in $\sigma_1$ below $2\Delta_{SC}$. These change in the normal state, 16 K traces, in both $\sigma_2(\omega)$, which gradually decreases at low frequency, and in $\sigma_1(\omega)$, which shows no gap. The above behaviors also show that our sample is much cleaner compared to those in prior THz studies (8; 28) (supplementary).

## 3.4 Terahertz Induced Hidden Phase in Pump-probe Measurement

We characterize the nonequilibrium post-quench states by measuring the complex conductivity $(\sigma_1(\omega, \Delta t_{pp}),\ \sigma_2(\omega, \Delta t_{pp}))$ as a function of pump-probe delay $\Delta t_{pp}$, shown in Figure 3.1f. This is obtained by first constructing a two-time THz pump and THz probe map of the induced THz probe field transmission through the excited sample, $\Delta E(t_{gate}, \Delta t_{pp})$, by scanning both gating pulse delay $t_{gate}$ and $\Delta t_{pp}$. The top panel of Figure 3.1f shows an example of raw data at 4.1K for $E_{THz}$ =120 kV/cm. The time-dependent dielectric response functions are then retrieved at each $\Delta t_{pp}$ via Fourier transformation along the $t_{gate}$ axis (methods and supplementary). The low

frequency spectra $\Delta\sigma_2(\omega) = \Delta n_s e^2/m\omega$ reflect the pump-induced change in superfluid density $\Delta n_s/n_s$ (solid circle). The peak of the differential THz field change $\Delta E/E_0$ (inset, red line), normalized by the transmission through the unexcited sample $E_0$ (black line), closely follows the above-obtained $\Delta n_s/n_s$, in both dynamics and magnitude. This indicates that the $\Delta E/E_0$, under this condition, originates from condensate quench and recovery.

Figure 3.2 demonstrates distinct post-quench states and two regimes by tuning, via $E_{THz}$, the "distance" from the equilibrium SC state $|\psi_{SC}\rangle$. The red arrows in Figure 3.2a mark (1) a *partial* quench regime at fields $E_{\#1-\#3}$ =47, 120 and 155 kV/cm, respectively; (2) a *full* quench regime at $E_{\#4-\#6}$ =256, 446 and 620 kV/cm, respectively, at T=4.1K. We see a clear suppression of $n_s$ with nonlinear dependence on the quench field, demonstrated by the $\Delta E/E_0$ at $\Delta t_{pp}$ =12ps long after the pump pulse is gone. Figure 3.2b corroborates this conclusion: the $1/\omega$ divergence in $\sigma_2(\omega, \Delta t_{pp})$ (solid circles, lower panel) gradually decreases in the first regime, and disappears in the second regime indicative of a full depletion of the SC condensate. Non-thermal QP populations have been predicted to induce a first-order SC to normal state phase transition in BCS superconductors (36). Quantum quenching of the BCS pairing interaction also induces a non-thermal transition to a *gapless coherent* state (16). While the latter differs from the normal state, the two have indistinguishable THz conductivities (37). In our experiment, we observe a distinctly different non-equilibrium $\sigma_1(\omega)$ (Figure 3.2b, upper panel) of post-quench states (solid circles) which display, remarkably, coherent QP transport manifesting as a sharp increase towards zero frequency and larger integrated spectral weight, by ~10%, near $E_F$ (1-10 meV). Note that $\sigma_2(\omega)$ (lower panel) nearly coincide with those of equilibrium thermal states at various temperatures (gray diamonds), except for a sharp upturn at very low frequency, most pronounced for $E_{\#4-\#6}$ marked by the arrows. The $\sigma_2$ cusp clearly cannot be accounted for by the residual condensate seen, e.g., in the $E_{\#4}$ vs. 15K trace. Rather, it correlates with the sharp $\sigma_1$ peak as dictated by the Kramers-Kronig relation. Most strikingly, the coherent peak and the additional spectral weight in $\sigma_1(\omega)$ persist into the full SC quench regime at $E_{\#4-\#6}$ (solid blue, red and purple circles). Moreover, as shown in Figure 3.2c, they disappear for 35fs pump pulses at 1.55 eV (at threshold fluence

$4\mu J/cm^2$, black lines), unlike (38; 21), or when quenching above $T_c$ (620kV/cm and T=18K, red lines). These features are also clearly distinct from observations of an inhomogeneous SC state (Figure A3, supplementary) and the predictions of the above standard BCS quench model (16; 37). This shows that the observed, THz light-tuned quantum phase is unique and cannot be accessed by any other tuning methods above.

The sharp peak in the conductivity in Figure 3.2b indicates a narrow linewidth proportional to the effective scattering rate $1/\tau(\omega)$, i.e., the imaginary part of the self–energy $\Sigma_2(\omega)$ (Figure A4-A5, supplementary). A remarkable feature is seen in Figure 3.2d: $1/\tau(\omega)$ decreases towards zero almost linearly with $\omega$ at $\omega \to 0$, at the expense of scattering above $2\Delta_{SC}$. This is seen for both full ($E_{\#5}$, red solid circle) and partial ($E_{\#2}$, yellow green solid circle) SC quench. In comparison, Figure 3.2e shows that, in equilibrium, $1/\tau(\omega)$ at $T > T_c$ (18K, gray circles) remains fairly constant and converges to the elastic impurity scattering $1/\tau_{imp} \sim 7.7\,\text{meV} \sim 2\Delta_{SC}$, while for $T < T_c$ the $1/\tau(\omega)$ spectra clearly reveal zero scattering below $2\Delta_{SC}$. Following THz quantum quench, *vanishing* $1/\tau(\omega)$ at $\omega \to 0$ is significantly lower than the $1/\tau_{imp}$, smallest scattering rate in the gapless normal state. Therefore we conclude that the THz light-quantum-tuning scheme reveals the emergence of a *gapless, non-Fermi-liquid "quantum fluid"*.

Figure 3.3 reveals a *photoexcitation threshold* for relaxation slowdown, i.e., prethermalized plateau temporal behavior, at $E_{th}$ ~256 kV/cm, corresponding to a transition to the persisting $|\psi_{Plateau}\rangle$ phase. This is clearly seen in the detailed pump–fluence–dependence of $\Delta E/E_0$ as a function of time delay, shown here on a logarithmic scale at $T$=4.1 K. At low quench field, $E_{THz} < E_{th}$, we observe a smooth, ps condensate recovery with a relaxation time $\tau^{\text{fast}}$ ~0.6ns. This is typical for SC recovery due to QP decay, as seen, e.g., in the 27 kV/cm (magenta line) and 120 kV/cm (purple line) traces in Figure 3.3a. This is corroborated by the detailed time evolution of $\Delta\sigma_2$ up to 1000 ps (inset) shown for $E_{\#2}$. In contrast, at high quench fields $E_{THz} > E_{th}$, a much longer *many-ns* quasi-steady temporal regime emerges and dominates the out–of–equilibrium dynamics. This is witnessed, e.g., by an order of magnitude longer relaxation time $\tau^{\text{slow}}$ ~7 ns in the 445 kV/cm (red line) and 620kV/cm (black line) traces. The post-quench, non–equilibrium

$\sigma_2(\omega)$ (Figure 3.3c) completely loses the $1/\omega$ divergence already at $\Delta t_{pp} = 12$ ps (black) compared to $\Delta t_{pp}$=-10ps (gray). The emergent gapless state persists at very long time delays, e.g., 500ps (red) and 1000ps (blue), with very little recovery to the initial SC state (inset). Note that $\sigma_1(\omega)$ of the gapless quantum state still displays the coherent peak (Figure 3.2b) distinct from the normal states. In addition, the dynamics are markedly faster above $T_c$. For normal state quench at 620 kV/cm and $T$=18K, $\sigma_2(\omega)$ has mostly recovered to its ground state behavior in the 1000 ps trace in Figure 3.3d, consistent with a short $\Delta E/E_0$ decay constant ~0.6 ns (inset). This energy relaxation $\tau^{\text{th}}$ is comparable to the thermalization time observed for optical pump (Figure 3.2c). Figure 3.3b illustrates the characteristic timescales extracted from the above experimental data and distinguishes their different physical origins. Clearly, both the energy relaxation and QP decay times are much shorter than the lifetime of the prethermalized plateau state.

To highlight the correlation physics in the gapless $|\psi_{Plateau}\rangle$, we compare in Figure 3e the $1/\tau(\omega)$ at $T = 4.1$ K (solid red circles) vs. $T = 18$ K (gray circles) for various time delays $\Delta t_{pp}$=12 ps, 500 ps and 1000 ps, at $E_{\#6}$=620 kV/cm. Interestingly, besides their different $\omega$ dependence discussed above, the $1/\tau(\omega)$ spectra of these post-quench states exhibit a sharp isosbestic point at a frequency $\omega_c \sim 2\Delta_{SC}$. This frequency marks the crossing from suppressed to enhanced scattering and exhibits very little shift for a wide range of time delays measured up to 1000 ps (vertical dashed line). The formation of an isosbestic point *as function of time delay* represents a hallmark for correlated state build-up and signifies a memory of hidden correlation gaps that manifests as transient spectral weight transfer from higher to lower frequencies. Such a salient feature in the prethermalization plateau state underpins a very weak time dependence of spectral redistribution, e.g., the 1000 ps $1/\tau(\omega)$ spectra retain memory of a nearly linear frequency dependence and the emergent correlation gap with no apparent relaxation to either normal (gray circles) or initial SC state behavior (gray rectangles) (lower panel). This is in contrast to the 18 K quench, which lead to largely frequency-independent $1/\tau(\omega)$ (Figure 3.3e), *always larger* than the impurity scattering $1/\tau_{imp}$, and to full relaxation before 1000 ps.

### 3.5 Theoretical Simulation of Hidden Phase

The observation of additional spectral weight near $E_F$ in the hidden $|\psi_{Plateau}\rangle$, as compared to the normal state (Figure 3.2b), indicates that the condensate $n_s\delta(\omega)$ at $\omega = 0$ did not come exclusively from spectral weight at $\omega \leq 2\Delta_{SC}$ but also involved a larger competing gap $\Delta_W > \Delta_{SC}$. Ref. (30) introduced a mean field model to predict the coexistence of a charge-density-wave (CDW)-like order and SC in the ground state of $Nb_3Sn$, which is driven by strong electron-phonon coupling. This coexistence results in a correlation energy gap that varies between different regions in k-space (30). Here we use this model to demonstrate the emergence of additional gapless excitations following decrease of $\Delta_W(t)$ that accompanies THz quench of $\Delta_{SC}(t)$. A $\sigma_1$ peak at low frequencies is then formed by transferring spectral weight from higher frequencies (supplementary). Even a relatively small (~10%) laser–induced decrease from equilibrium of $\Delta_W(t)$ in a low–T transient state with $\Delta_{SC} = 0$ leads to a coherent peak in $\sigma_1(\omega)$, Figure 3.4a-4c, and a partially–gapped Fermi surface with regions of gapless excitations (shaded area), Figure 4d-4f. For example, for $\Delta_W(t) = 0.8\,\Delta_{W,0}$ (Figure 3.4c) and $0.9\,\Delta_{W,0}$ (Figure 3.4b), $\sigma_1$ develops a sharp peak at low frequencies (Figure 3.4e-4f) that is absent for the equilibrium $\Delta_{W,0} \sim 40$meV (32) (Figure 3.4d). The emergence of such peak when ($\Delta_W(t) < \Delta_{W,0}$, $\Delta_{SC}(t)$=0) in a transient state is consistent with our experimental observation (Figure 3.2b). This calculation suggests that our observed additional spectral weight and low-frequency coherent peak could arise from a THz-quench-induced decrease in a competing order parameter. The latter accompanies the quench of the SC gap, beyond the thermodynamic restriction, and changes the partial k–dependent Fermi surface gapping (Figure 3.4a-4c). .

A THz ultrafast quench of low energy $\Delta_{SC}$ with simultaneous decrease in high energy $\Delta_W$ can arise from coherent/nonthermal quench dynamics (green circles, Figure 3b) due to, e.g., THz excitation of short duration (to be discussed elsewhere). Over timescales longer than relaxation due to inelastic scattering, the above ultrafast k-dependent change of the electronic correlation gap creates a nonthermal "initial condition" that can access different regions of the free energy landscape (39). To illustrate how a long-lived prethermalized state may emerge and get trapped for a long

time after the coherent temporal regime (Figure 3.3b), a simple free energy calculation based on the mean–field model of Ref.(30) (methods), shown in Figs. 3.4g–4i, compares the dependence on $\Delta_W$ for three cases: (1) $\Delta_{SC} = \Delta_{SC,4K}$ (Figure 3.4g) as in the equilibrium state below $T_c$. The free energy minimum is then located at $\Delta_W = \Delta_{W,0}$ and corresponds to an equilibrium homogeneous phase characterized by a two–component k-dependent order parameter (30). (2) $\Delta_{SC,18K} = 0$ (Figure 3.4h) describes the thermal normal state showing an increase in the equilibrium $\Delta_W$ (red dash line) due to the reduction of the competing SC order. (30). We expect such landscape following quenching of $\Delta_{SC}$ via high energy, optical pumping (Figure 3.2c). (3) $\Delta_{SC} = 0$ while $T(t) < T_c$ (Figure 3.4i), achieved via nonthermal THz light–induced dynamics, changes the free–energy landscape, e.g. from Figure 3.4g to Figure 3.4i that differs from the thermal normal state (Figure 3.4h). Within the model of Ref. (30) (methods), a sharp local minimum then develops at $\Delta_W \sim 0$ (blue arrow), which as seen in Figure 3.4f is accompanied by a sharp peak in $\sigma_1(\omega \to 0)$. Additional couplings to acoustic phonons (29; 33) and the details of the bandstructure influence such metastable states with reduced lattice distortion/dimerization (35). The THz-laser-quantum tuning "suddenly" brings the system in an excited state with $\Delta_{SC}$=0 and initiates coherent/anharmonic motion of $\Delta_W(t)$ that can access such free energy local minima for sufficient pump fluence and then get trapped there due to damping of the coherent motion prior to returning to the global minimum. Such simultaneously suppressed $\Delta_W$ and SC order parameters, going beyond the thermodynamic self-consistency limitation (30), is consistent with our observation of a long–lived (metastable) phase above threshold. THz light-quantum-quench and prethermalization of competing orders revealed may be extended to access hidden density-wave phases and quantum criticality under the SC dome in High–Tc materials.

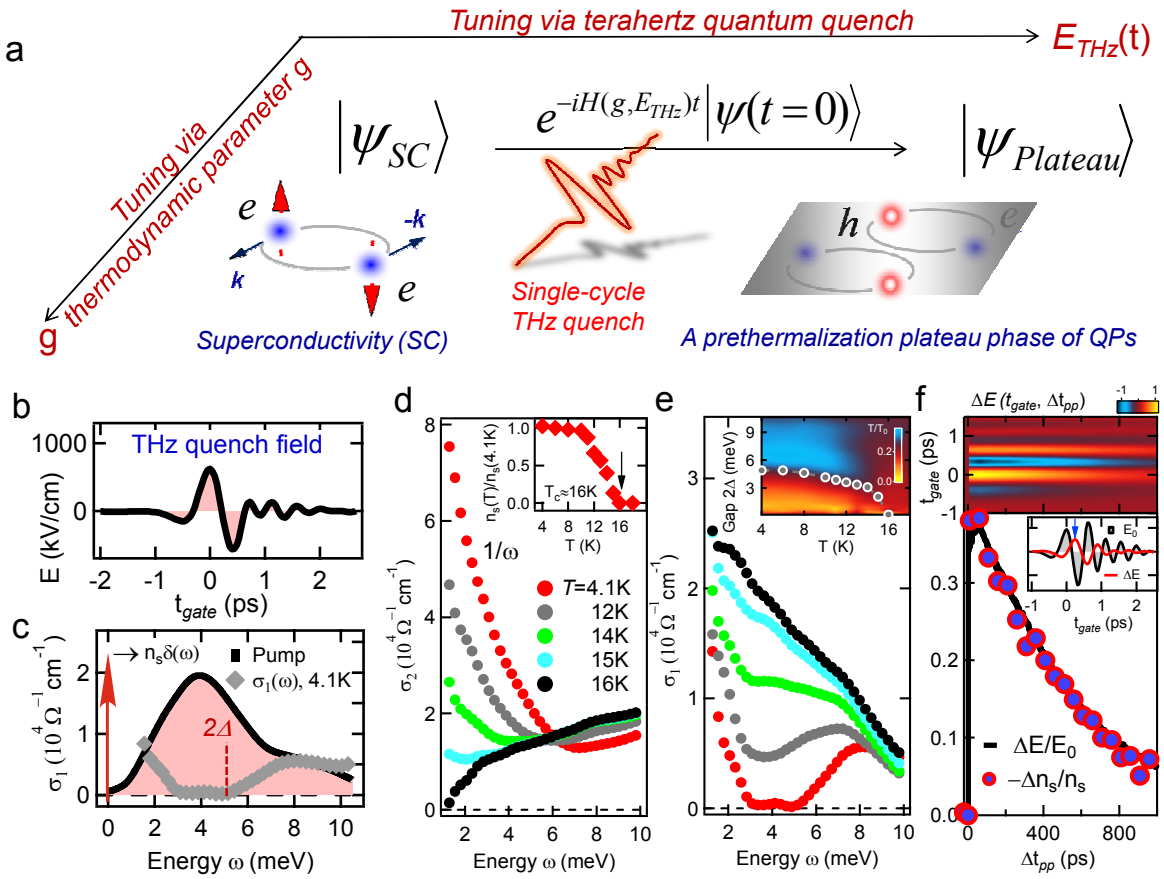


Figure 3.1 (**a**) Schematic of out-of-equilibrium quantum tuning scheme, via non-thermal quenching of the SC order $|\psi_{SC}\rangle$, for discovery of a hidden phase marked as $|\psi_{B-phase}\rangle$. (**b**) A typical, single–cycle THz quench electric field in time domain. (**c**): Quench field spectrum (shaded black) with central frequency well within the $2\Delta_{SC}$ gap shown by $\sigma_1(\omega)$ (gray diamond) at 4.1K. $\sigma_1(\omega)$ at zero frequency is marked by red arrow and is proportional to superfluid density $n_s$. The complex conductivity is shown as (**d**) $\sigma_2(\omega)$, (**e**) $\sigma_1(\omega)$. Insets: (d) $n_s$ and (e) 2D false color plot of static transmission spectrum overlaid by extracted $\Delta_{SC}$ gap at different temperatures. (**f**) A 2D false color plot of THz pump–induced change, under peak pump field $E_{THz}$ =120kV/cm, in THz probe E—field, $\Delta E(t_{gate}, \Delta t_{pp})$. The normalized temporal profile of $\Delta E/E_0$, measured at $t_{gate} = -0.08ps$ (inset, red line), closely follows the dynamic superfluid density change $\Delta n_s/n_s$.

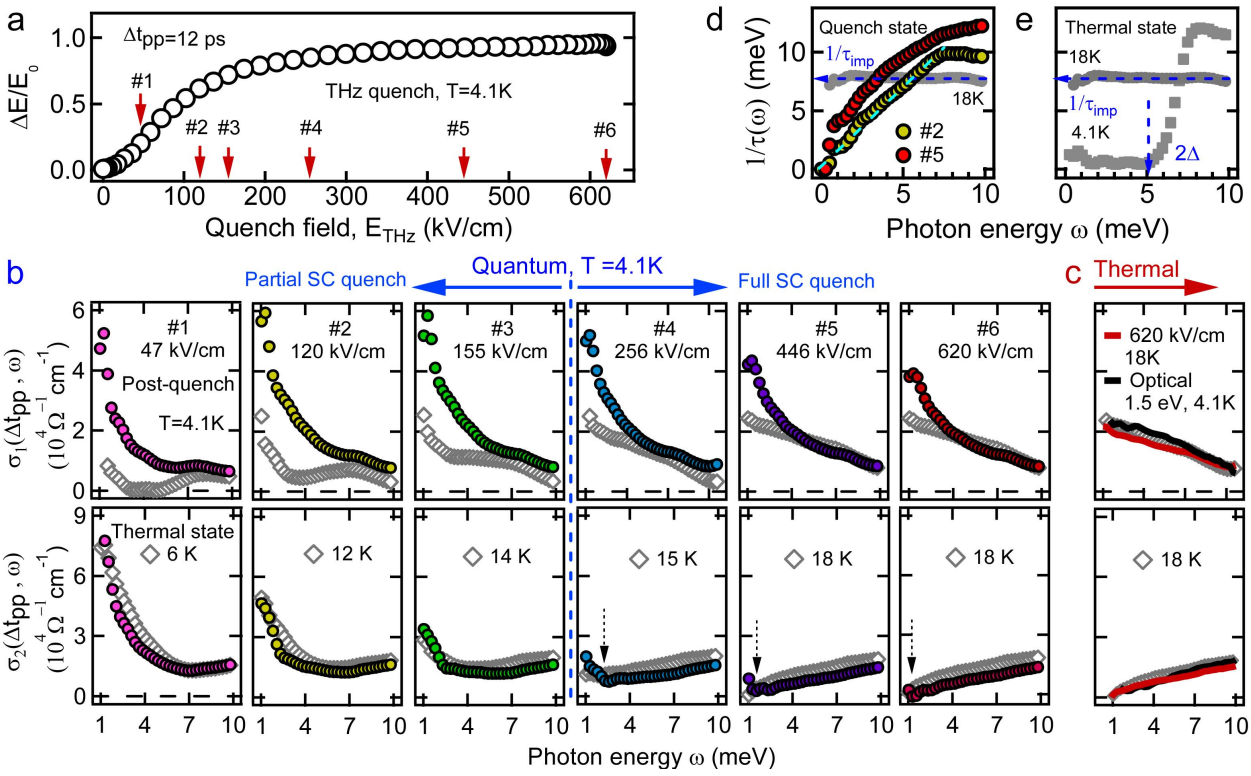


Figure 3.2 The distinct spectral features of the gapless quantum state differ from both normal metallic states and thermal behaviors. (**a**) Nonlinear pump-field dependence of peak-peak probe E-field transmission change $-\Delta E/E_0$ for fields up to 620kV/cm. (**b**) THz response functions, expressed as $\sigma_1$ and $\sigma_2$, of the post-quench states (solid circles) at various pump E fields marked in (a), corresponding to partial ($E_{\#1-\#3}$) and full ($E_{\#4-\#6}$)) SC order quench. Shown together are the equilibrium responses $\sigma_1$ at various temperatures from 6K to 18K (gray diamond) that give nearly identical $\sigma_2$ to the non-equilibrium state, except the onset of a sharp upturn at very low frequencies, marked by arrows, consistent with the diverging-like $\sigma_1$ by the Kramers-Kronig relation. (**c**): The post quench state conductivities at initial T=18K above $T_c$ for $E_{\#6}$ pumping (red line) and at T=4.1K below $T_c$ but for optical pumping at 1.55 eV (black line). (**d**): Frequency-dependent scattering rate $1/\tau(\omega)$ for the post-quench states pumped by $E_{\#2}$ and $E_{\#5}$ compared to the normal state result that converges to $1/\tau_{imp}$ (gray circle). (**e**): $1/\tau(\omega)$ for the equilibrium SC (4.1K) and normal (18K) states as marked.

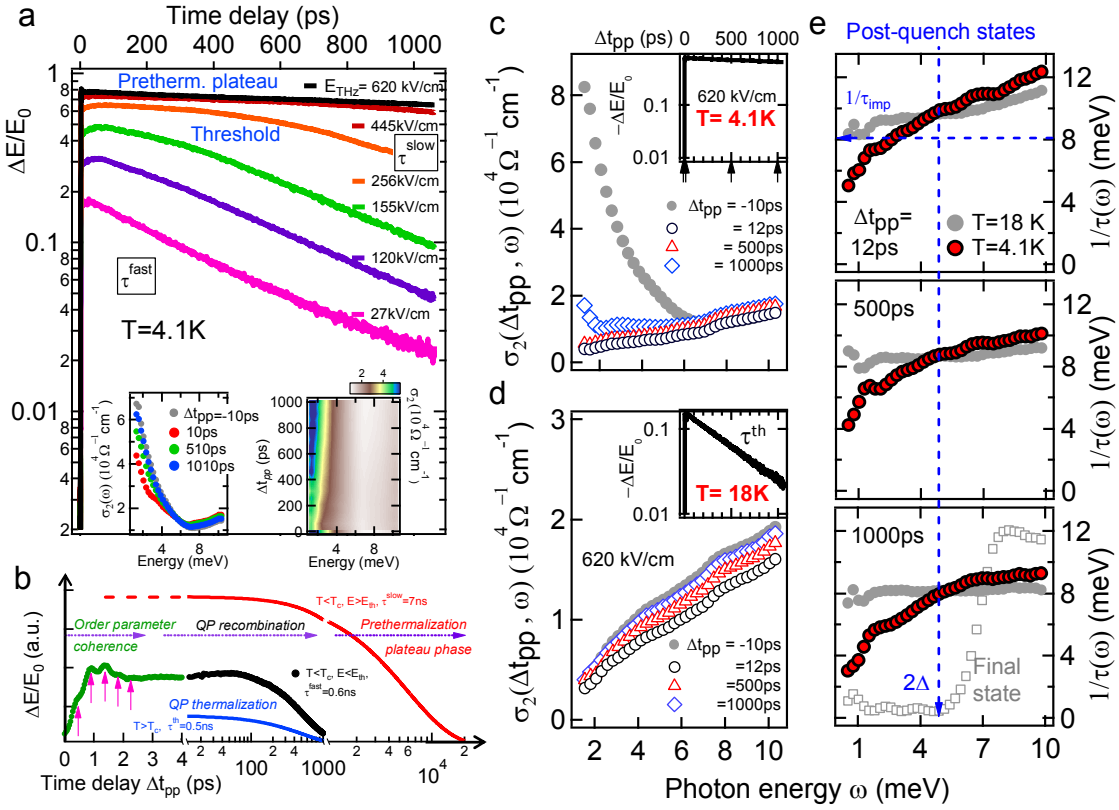


Figure 3.3 The persisting, prethermalized plateau state with non-thermal characteristics and long-lived memory. (**a**) Temporal dynamics of $-\Delta E/E_0$ at different quench field $E_{THz}$ shows a clear transition between two different decay profiles, marked as $\tau^{fast}$ and $\tau^{slow}$ at the threshold field $E_{th}$. Inset: THz response $\sigma_2$ as a function of time delay, with representative traces for time delays $\Delta t_{pp}$= -10ps, 12ps, 500ps, 1ns at $E_{THz}$ =120kV/cm at 4.1K. (**b**):An illustration of the characteristic timescales extracted from the data in (a)-(d) which range from SC order parameter coherence (green), QP decay (black) and thermalization (blue) to post-quench prethermalization above the threshold (red). (**c**): $\sigma_2$ of the post-quench state for various time delays $\Delta t_{pp}$= -10ps, 12ps, 500ps, 1ns at $E_{THz}$=620kV/cm at 4.1K. Inset: $-\Delta E/E_0$ dynamics. (**d**): The same spectral-temporal characteristics as (b) but for the normal state at 18K. (**e**): A comparison of $1/\tau(\omega)$ corresponding to (b) and (c) at the given time delays. Shown together is the final SC state after relaxation (gray square).

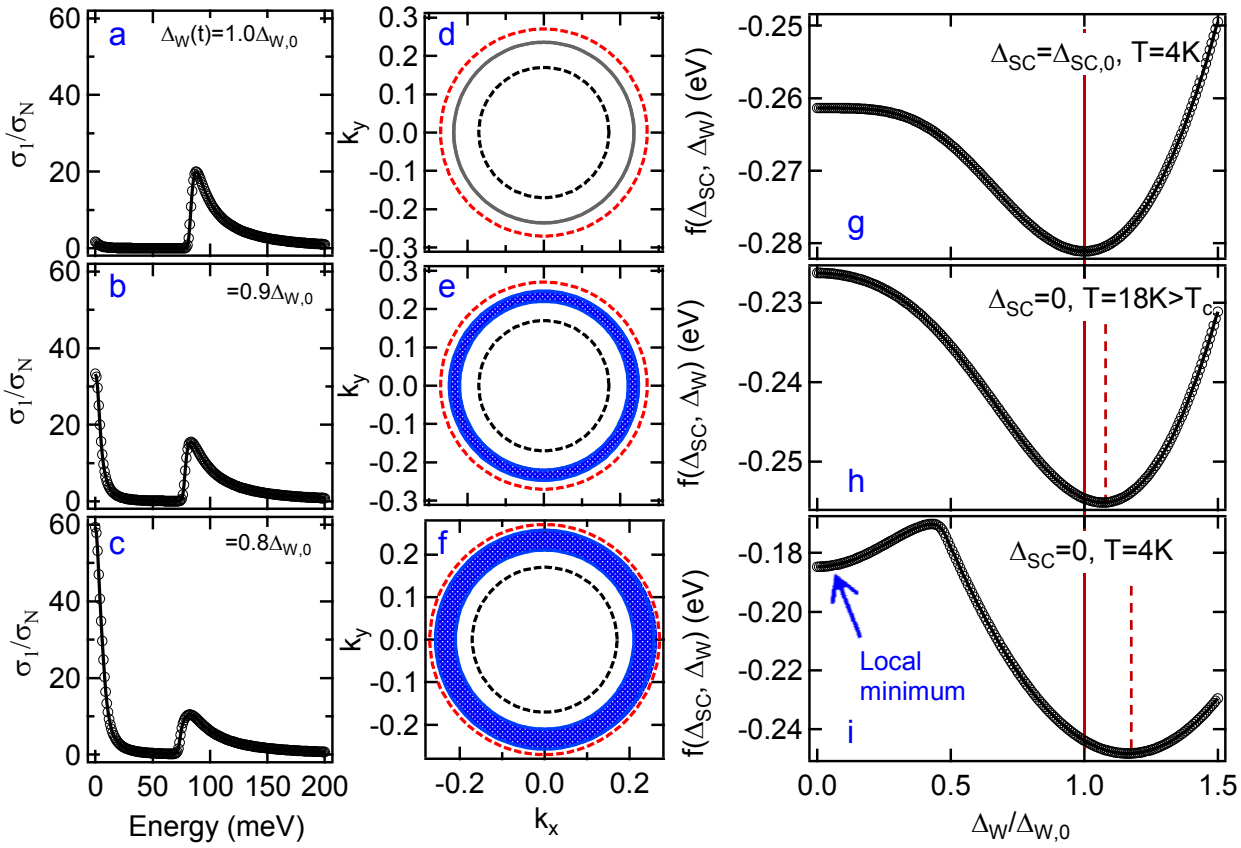


Figure 3.4 Predictions of theoretical model for the hidden gapless quantum state with extraordinary conductivity. (**a**–**f**) Simulation of the conductivity (a-c) and Fermi surface (d-f) with the reduced gap $\Delta_W$ as discussed in the main text. A and D: $\Delta_W/\Delta_{W,0}$=1; B and E: 0.9; C and F: 0.8. Red and black dash lines illustrate the $e$ and $h$ pockets. Blue shaded areas highlight the regions of gapless excitations. (**g**–**i**) Free–energy density for the model Hamiltonian (supplementary) as function of the CDW-like order parameter $\Delta_W$. (**g**) $\Delta_{SC} = \Delta_{SC,4K}$ for equilibrium state below $T_c$; (**h**) $\Delta_{SC,18K} = 0$ describes the thermal normal state showing an increase in the equilibrium $\Delta_W$ (red dash line); (**i**) $\Delta_{SC} = 0$ while $T(t) < T_c$ describes a pre-thermalized gapless state following THz quench of the SC gap with minimal heating that cannot be realized in equilibrium.

# CHAPTER 4. TERAHERTZ ELECTRODYNAMICS OF COEXISTING ORDERS AND ULTRAFAST QUANTUM ENERGY TRANSFER IN $Nb_3Sn$ SUPERCONDUCTOR

In this chapter, we compare the equilibrium and optically induced THz electrodynamics of a moderately clean $Nb_3Sn$ superconductor (SC) to understand and control the THz conductivity from co-existing electronic orders. For high frequency pump, we observe an photo-induced enhancement in the quasi–particle (QP) conductivity, which persists up to an additional critical temperature, well above the SC transition, with a corresponding electronic gap and absent for low frequency pump. In the SC state, the fluence dependence of Cooper pair breaking, together with an analytic model, reveals, remarkably, a "one photon–to–one pair" non-resonant energy transfer despite the large energy mismatch, i.e., the rest of photon energy transferring to phonons rather than creating additional QPs. Such a *quantum limit* energy transfer to QPs, which we attribute in part to strong electron–phonon coupling, is at least one order of magnitude smaller than in previously studied SCs.

## 4.1 Introduction

The competition and interference between SC and other co-existing electronic instabilities appears to be universal in quantum materials and controls ordering tendencies, possibly at ultrafast time scales. How to exploit these co-existing orders as a control knob to understand and achieve ultrafast manipulation of materials properties is an outstanding challenge. Answering these questions has been proved difficult not only in the more sophisticated quantum materials (17; 19; 46) but also in some well-established systems such as A15 superconductors (30; 47; 33; 34; 48; 49). $Nb_3Sn$, as a paradigmatic example, exhibits an electronic instability or martensitic transition above a superconducting one, which has been described to optical phonon condensation ("dimerization" of

Nb atoms) (29), possibly driven by a Van Hove singularity (VHS)-like electronic density-of-states peaked at $\sim E_F$ and by strong electron-phonon interaction (33; 30; 34; 32; 50; 48). Consequently, the order parameters competing with SC likely exhibit multiple components, both lattice and electronic, whose exact origin is still debated, e.g., from the apparent splitting of the three-fold degenerate $\Gamma_{12}$ band to an additional electronic or charge-density-wave(CDW)-like contribution seen in tunneling (32; 51; 49) and Raman spectroscopy experiments (52). Independent of its precise origin, the associated, partial Fermi surface gapping, $\Delta_W \gg \Delta_{SC}$ below the martensitic anomaly affects the electronic states near $E_F$ differently from the SC one (30) and, thereby, opens an unexplored opportunity for ultrafast manipulation of THz conductivity in A15 compounds.

THz spectroscopy is a powerful tool for *quantitative* studies of SC states both in– and out–of–equilibrium. Arising from energy scales in the vicinity of SC gaps $\Delta_{SC}$ of few meV, THz electrodynamics, characterized by the complex optical conductivity response function $\tilde{\sigma} = \sigma_1(\omega) + i\sigma_2(\omega)$, is a direct measure of both inductivity of SC condensate and dissipation of QPs. Such THz measurements allow access to the key properties of the broken symmetry states, including, e.g., the SC/QP density, SC gap and complex optical self-energy. Prior THz studies of SC samples mostly revealed "conventional" features consistent with the deep impurity limit, $\hbar/\tau_{imp} \gg 2\Delta_{SC}$ (53; 53; 54; 8). In addition, the spectral-temporal dynamics of the order parameters out-of-equilibrium represent a powerful tool to study the role of correlations and co-existing orders. The time resolution can follow Cooper pair breaking dynamics while the time-resolved THz spectra can track possible spectral weight transfer to the Fermi surface from both the condensate peak $n_s\delta(\omega)$ and from any competing correlation electronic gap $\Delta_W \gg \Delta_{SC}$. These salient features have never been studied in A15 superconductors and the interesting comparisons are absent with prior ultrafast THz dynamics, e.g., in $MgB_2$ and NbN superconductors, which don't exhibit co-existing electronic gaps (53; 54; 8) and in the cuprates, which exhibit much more complex gap structure (55).

In this Letter, we present the equilibrium and optically-induced, ultrafast THz electrodynamics of a moderately clean $Nb_3Sn$ SC with mean free path comparable to the coherence length. We find that the non-equilibrium THz conductivity after fs optical pump excitation ($\sim$1.55eV) gains

an additional spectral weight that, strikingly, persists far above the superconducting $T_C$. This is opposite to the case of a low frequency pump pulse (∼4meV), which gives rise to a reduced THz conductivity above $T_C$. We interpret the distinction as evidence for softening of a coexisting, electronic order $\Delta_W$ below the martensitic transition. Furthermore, we observe a rapid, SC pair breaking process consistent with strong electron-phonon coupling. This, together with an analytic model, reveals a remarkable quantum limit of energy transfer, i.e., one high energy photon breaks only one low energy Cooper pair, with the rest of photon energy transferring to phonons rather than creating additional QPs. Such minimal transfer of photon energy $\hbar\omega$ to QPs, $2\Delta_{SC}/\hbar\omega$=0.33%, is at least one order of magnitude lower than previously measured in other superconductors (53; 54; 56).

## 4.2 Method: Optical Pump-THz Probe Ultrafast Spectroscopy

A $Nb_3Sn$ film 20nm thick was grown by magnetron sputtering on a 1mm $Al_2O_3$(R-plane) substrate by co-sputtering of Nb and Sn at high temperatures. The optical pump and THz probe spectroscopy technique is implemented by using three pulses (77): optical pump $E_{op}$, THz probe $E_{THz}$ by optical rectification, and optical gating pulse at time $t_{gate}$ for electro-optic sampling. The setup was driven by a 1 kHz Ti:Sapphire regenerative amplifier with 35 fs duration at 800 nm center wavelength. The transmitted electrical field is in the coherent limit, and all multiple reflections at interfaces have been treated to deconvolve the complex THz conductivity, for both equilibrium and non-equilibrium states at pump-probe delay $\Delta t_{pp}$.

### 4.3 Terahertz Electrodynamics of Superconductivity

The equilibrium time-domain THz transmission field and complex electrodynamic response are shown in Figs.4.1(a) and 1(b)-1(c), respectively, as a function of temperature. The 4.1 K traces exhibit a diverging $1/\omega$ response in $\sigma_2$, arising from reactive SC condensate, and a dissipationless conductivity, witnessed in $\sigma_1$ below $2\Delta_{SC}$ =5.1 meV. A finite $\sigma_1$ peak at the lowest frequencies <3 meV originates from intraband absorption of the thermally excited Bogoliubons. The above distinct conductivity features diminish when approaching $T_c$, as seen in the 10-15 K measurements shown in Figs.4.2(b)-2(c). As seen in the 16 K and 18 K traces, the normal state exhibits a gradually decreasing $\sigma_2(\omega)$ at low frequencies and a Drude spectral shape of $\sigma_1(\omega)$ without gap. The relatively narrow linewidth of $\sigma_1(\omega)$ indicates a much smaller impurity scattering rate $\hbar/\tau \sim$7 meV than in previous THz studies (53; 54; 8). Our sample shows an order of magnitude larger ratio $l/\xi \sim$1 of mean free path over coherence length, determined by $\pi\tau\Delta/\hbar$ in $Nb_3Sn$, indicative of a cleaner SC state.

We now extract the optical self energy $\Sigma(\omega, T)$ using an extended Drude model (57), which provides information complementary to $\widetilde{\sigma}(\omega)$ that is more relevant for characterizing impurity scattering and correlation. Figs.4.1(d) and 1(e) present the complex $\Sigma(\omega, T)$ in terms of the frequency-dependent momentum scattering rate $1/\tau(\omega)$ and mass renormalization $m^*(\omega)/m_0$, which relate to the imaginary and real parts of the self-energy, respectively. We emphasize three key observations in the SC state. First, the $1/\tau(\omega)$ spectra in Fig.4.1(d) clearly reveal the SC gap opening, which suppresses the scattering rate below $2\Delta_{SC}$ and reduces it to zero at 4.1K. Second, sharp impurity peaks, commonly seen in dirty limit SC samples at $2\Delta_{SC}$ (57), are absent in $1/\tau(\omega)$ and replaced by a broad cusp in $m^*(\omega)/m_0$ above $2\Delta_{SC}$. Third, $m^*(\omega)/m_0$ in the SC state as $\omega \to$0 reflects $n/n_s$, i.e., the ratio between the electron density $n$ and the superfluid density $n_s$. Here, $n/n_s(4.1K) = m^*(\omega = 0, 4.1K)/m_0 \sim$1.34 indicates that ∼75% of the electrons participate in superfluidity, consistent with the superfluid density ratio (∼70%) obtained from the optical sum rule $\int_{0+}^{\infty}(\sigma_1^n(\omega) - \sigma_1^s(\omega))\, d\omega = \frac{\pi}{2}\frac{n_s e^2}{m}$. This measured $n_s/n$ is ∼6 times larger than in superconducting Pb (57).

Fig.4.2 demonstrates a previously-unestablished feature in the non-equilibrium THz dynamics that underpin a coexisting order in the normal state of $Nb_3Sn$. The measured THz fields are shown in the time domain in Fig. 4.2(a), including the pump induced change, $\Delta E(t)$, after a fixed pump-probe delay $\Delta\tau_{pp}$=10 ps (red) and the transmitted field through the unexcited sample, $E0(t)$ (black). In Fig.4.2(b) we record the photoinduced THz field peak-to-peak amplitude as a function of temperature from 4K to 70K. Two transitions are visible. As expected in a SC, the photoinduced signal drops significantly at $T_C$ ~16K. Unlike in a conventional SC however, the signal persists into the normal state and completely diminishes only at a much higher temperature $T_M$ ~47 K (inset). Intriguingly, the latter transition in the THz field amplitude coincides with the martensitic anomaly that has been associated with the structural-electronic instabilities (33; 30; 34; 32; 50; 48; 29). Fig.4.2(b) reveals its order parameter with a critical temperature $T_M$.

Importantly, the coexisting $T_M$ order above SC suggests the possibility to optically control the low-energy THz conductivity response by tuning the pump between the optical and THz frequency range with respect to its correlation gap $\Delta_C$. We start with the normal state at 18K slightly above $T_C$. The non-equilibrium $\sigma_1(\omega)$ data is shown in Fig. 4.2(c) for 1.55eV (black) and 4meV (red) pump photon energy. After 1.55eV pump excitation (black), the low frequency conductivity $\sigma_1(\omega)$ gains an additional spectral weight over its equilibrium (no pump) values (gray circles), which is responsible for the non-vanishing, pump-induced signals $\Delta E_{THz}$ in the normal state below $T_M$ shown in Fig. 4.2(b). This pump-induced enhancement is consistent with softening of the correlation gap that develops at the $T_M$ transition, which can arise from $\Gamma_{12}$ phonon condensation (dimerization) and/or electronic VHSs, by optical excitation with frequency $\hbar\omega_{op} \gg \Delta_W$. Such softening gives rise to spectral weight transfer to the Fermi surface from high energies above $\Delta_W$. Intriguingly, by changing the pump photon energy to 4 meV, i.e., $\hbar\omega_{THz} \ll \Delta_W$, we observe pump-reduced instead of pump-enhanced low frequency conductivity (red). This opposite behavior serves as a clear indication that photoexcitation at sufficiently low frequencies fails to quench the $\Delta_W$ gap and, instead, heats up the gapless electronic Fermi sea portion and also the lattice via electron-lattice coupling. Therefore, the observed difference between low and high pump frequencies

demonstrates control of the transient THz conductivity by pump photoexcitation above (electronic gap melting) and below (gapless Fermi sea/lattice heating) the correlation gap $\Delta_W$. In addition, we argue that the distinct difference by tuning pump photoexcitation implies the additional electronic instability of the martensitic anomaly, beyond the structural one. Without such new degree of freedom below $T_M$, THz heating of QPs would thermalize quickly together with lattice at $\Delta t_{pp}$=10 ps, the measured, pump-probe delay (Fig. 4.2(b)). Such an elevated lattice temperature would also tend to enhance, instead of reduce, the THz conductivity by reducing the $\Gamma_{12}$ band splitting. Note that this normal state photoexcitation behavior is absent in previously studied NbN and $MgB_2$ that don't have co-existing electronic gaps (53; 53; 54).

Next we turn our attention to the non-equilibrium cooper pair breaking (CPB) responses in the superconducting state after fs optical excitation. For $\hbar\omega_{op} >> 2\Delta_{SC}$, CPB processes can be driven by multiple interactions of the condensate with photoexcited electrons and QPs or with high frequency phonons (HFPs). Previous works have shown that the majority of the absorbed photon energy subsequently transfers to the phonon reservoir during the fs excitation and then continues to deplete the SC condensate (53; 54; 56). Figs. 4.3(a) and 3(b) plot the non-equilibrium THz conductivity $\sigma_1(\omega)$ and $\sigma_2(\omega)$ of $Nb_3Sn$, for various fluences of 1.55eV pump photoexcitation at $T$=4.1 K. We observe very similar spectral shapes to those seen for various temperatures in equilibrium (Fig. 4.1). Photo-induced QPs gradually close the SC gap $2\Delta_{SC}$. At the same time, the low frequency $1/\omega$ divergence in $\sigma_2$ diminishes with increasing pump fluence $I_{pump}$. Both features disappear simultaneously above $4\mu J/cm^2$. The thermalized gap $\Delta_{SC}(I_{pump})$ and the superfluid density $n_s$, readily obtained from our transient THz spectra and shown in Figs. 4.3(c) and 3(d), quickly diminish as $I_{pump}$ approaches $4\mu J/cm^2$. An elevated elecron/lattice transient temperature $T^*$ established after the pump can be extracted by fitting the data. As shown in the inset, $T^* \rightarrow T_c$ at the quenching fluence $\sim 4\mu J/cm^2$. Therefore, conductivity at $\Delta t_{pp}$=10 ps for $T<T_C$ is consistent with previous $T^*$ non-equilibrium superconductivity models (36; 57; 58).

## 4.4 Quantum-limit Energy Transfer

Finally, we track the early time evolution prior to the establishment of a T* quasi-equilibrium temperature regime, which results from transient pair breaking pathways due to scattering with HFPs and hot QPs. The experimentally–observed ultrafast THz signals, which reflect the photoexcited QP density $n$(t), are presented in Fig. 4.4(a) for various pump fluences. They show faster CPB with increasing pump fluence during the first 4 ps. In order to reveal the microscopic energy transfer among various reservoirs, we model the CPB kinetics based on the widely used, Rothwarf-Taylor (RT) model (59) that is extensively discussed in (58). Here the QP and HFP densities, $n$(t) and $N$(t), are described by two coupled differential equations (59; 58; 53; 54). The rise of $n$(t) in time originates from the CPB process preceding to the QP relaxation, which can be described by the analytical expression (58):

$$n(t) = \frac{\beta}{R}[-\frac{1}{4} - \frac{1}{2\tau} + \frac{1}{\tau}\frac{1}{1 - Kexp(-t\beta/\tau)}], \tag{4.1}$$

where K and $\tau$ are dimensionless parameters determined by the initial conditions: $K = ((\tau/2)/(4Rn_0/\beta+1)-1)/((\tau/2)/(4Rn_0/\beta+1)+1))$and $\frac{1}{\tau} = \sqrt{1/4 + 2R/\beta(n_0 + 2N_0)}$. Here, $\beta$ is the CPB probability by absorption of HFP and $R$ is the bare QP bi-molecular decay rate. $n_0$ and $N_0$ are the initial QP and HFP densities immediately after fs photoexcitation. $\beta$ and $R$ are independent of the fluence for weak excitations, when $n_0$ is much smaller than the material–dependent value $\beta/R$. Fig. 4.4(a) presents the best fits, which show a very good agreement with the data. The fitting parameters $\tau/\beta$ and K are extracted as the function of fluence and plotted in Figs. 4.4(b) and (c) respectively.

Further quantitative information can be obtained by plotting $\tau/\beta$ and K versus the absorbed energy density $\Omega$. Here $\Omega$ at $I_q$=4.02$\mu$J/$cm^2$ is equal to the SC condensate energy U=4757mJ/mol (60). Denoting the portion of the absorbed energy that initially goes into QP excitation as p, we have $n_0$=p$\Omega/\Delta$ and $N_0$=(1-p)$\Omega/2\Delta$ created by fs photoexcitation. The best fit to the extracted $\tau/\beta$ and K data, obtained by minimizing the mean-square error (MSE) of the parameter set $\{p, R, \beta\}$, is achieved for p=0.2$\pm$0.1%, which gives the values of $\beta^{-1} = 1.0 \pm 0.1$ ps and R = 105.5 $\pm$ 10 ps$^{-1}$ unit cell$^{-1}$. We further plot the MSE of the above fitting as function of p in Fig. 4.4d by only

fitting $\{R, \beta\}$ for each fixed p. Intriguingly, a strong deviation from the minimum error starts at a very small p$\sim$0.33% that coincides with $2\Delta_{SC}/\hbar\omega$, as marked (dashed arrow) in Fig. 4.4(d). The merely 0.33% portion of absorbed photon energy $\hbar\omega$ that excites QPs reveals a "quantum" energy transfer process where one high energy photon, $\hbar\omega$=1.55 eV, breaks only one pair, $2\Delta_{SC}$ =5.1 meV, with rest of the energy going into exciting phonons during the initial relaxation regime of the QP cascading process (inset, Fig. 4.4(d)). The good agreement between data and simulations, seen in Figs. 4.3 and 4.4, validate this claim, which implies that a photoelectron-phonon relaxation pathway dominates over the photoelectron-SC interactions. This effect is much more pronounced in $Nb_3Sn$ than in other superconductors, where the measured photon energy transfer to QPs is at least one order of magnitude smaller during the early relaxation times: 0.33% here vs. $MgB_2$ (p$\sim$6%) (53), NbN (p$\sim$9%) (54) and cuprates (p$\sim$10%) (56).

The applicability of the analytic RT model for reaching the above conclusion is well justified by the following condition satisfied by our data:$n_0 = p\Omega/\Delta \simeq 1 \times 10^{-4} \ll \beta/R = 1 \times 10^{-2}$, where $\beta/R = \frac{N(0)^2\pi\omega_D^3}{18v\Delta_{SC}}$(58). Here $\omega_D$ is the phonon cutoff frequency, N(0) is the electronic density of states per unit cell at the Fermi level and $v$ is the number of atoms per unit cell. We used the values $v$=8, $\Delta_{SC}$=2.55 meV, N(0)=11.4 states(spin cell eV)$^{-1}$ (61) and $\omega_D$=6.9 THz (62). In addition, the value of electron-phonon coupling constant $\lambda$ can be determined from the relation $R = \frac{8\pi v\lambda\Delta_{SC}^2}{\hbar N(0)\omega_D^2}$. We obtain $\lambda \approx 2.0$, which agrees very well with previous estimates of $\lambda \approx$1.8$\pm$0.15 (63) and is 2 times larger than in the previously studied NbN. In addition, a much higher phonon-pair scattering probability $\beta \sim 1\text{ps}^{-1}$ seen in $Nb_3Sn$ as compared to $MgB_2$ ($\beta$=1/15 ps$^{-1}$) (53) and NbN ($\beta$=1/6 ps$^{-1}$) (54). This conclusion is consistent with our observation of much faster CPB dynamics, Fig. 4.4(a), and a minimal initial energy transfer to QPs (p), Fig. 4.4(d). We attribute the much higher $\beta$ to a much larger density of states $N(0)/v$ due to the bandstructure in $Nb_3Sn$ (1.425) (61) as compared to NbN (0.44) (64) and $MgB_2$ (0.23) (65; 66).

## 4.5 Summary and Outlook

In summary, the THz electrodynamics of $Nb_3Sn$ demonstrate control of the THz conductivity by tuning pump photoexcitation and provide additional evidence for the presence of an electronic order below the martensitic anomaly. Our results demonstrate a "one photon–one pair" quantum energy transfer, much pronounced than previously studied superconductors, which we attribute in part to strong electron–phonon coupling. This points the opportunity to probe and manipulate complex materials by harnessing the ultrafast THz electrodynamics of strongly coupled orders.

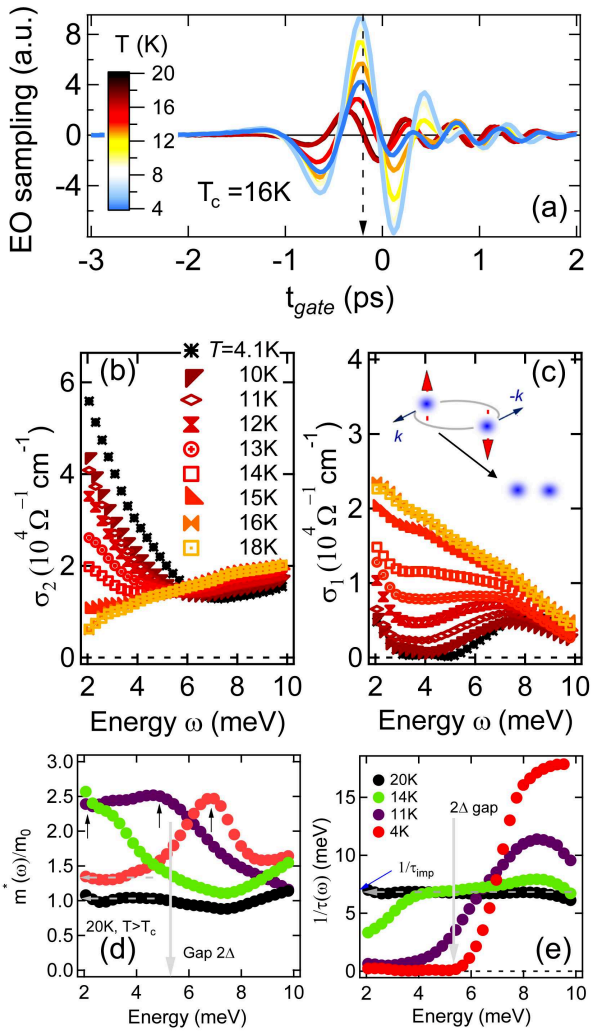


Figure 4.1 THz probe transmitted field $E_{probe}$ as function of gate delay time $t_{gate}$ for the thermal equilibrium state from 4K to 20K. (b), (c) Temperature dependence of imaginary and real parts of the conductivity, $\sigma_1(\omega)$ and $\sigma_2(\omega)$. Inset to (b): schematic of Cooper pair breaking. (d) Mass renormalization $m^*/m$ and (e) momentum scattering rate $1/\tau$ spectra calculated from $\sigma_1(\omega)$ and $\sigma_2(\omega)$ in (a), (b). Grey solid line denotes $2\Delta_{SC}$ gap at 4.1K. Dashed lines mark the asymptotic $m^*/m$ and $1/\tau$ towards zero frequency.

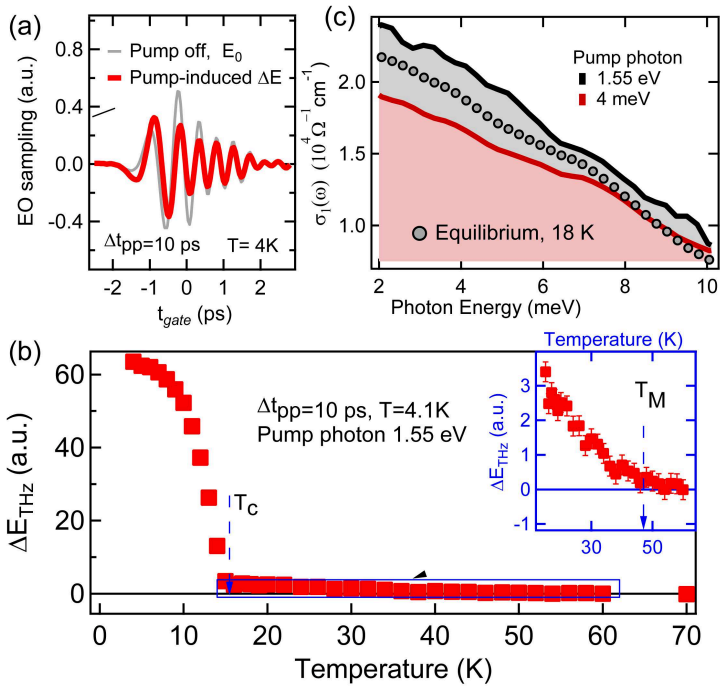


Figure 4.2 (a) Transmitted $E_{probe}$ through unpumped $Nb_3Sn$ film (gray) and pump induced change $\Delta E_{probe}$ (red). (b) Temperature dependence of peak-to-peak $\Delta E_{probe}$ at $4.02\mu J/cm^2$. $\Delta E_{probe}$ above $T_c$ is magnified in inset to (b) and critical temperature $T_M$ is marked by blue dashed line. (c) $\sigma_1(\omega)$ after 1.55eV (black), 4meV (red) pump photo-excitation compared to equilibrium (gray circle) at 18K.

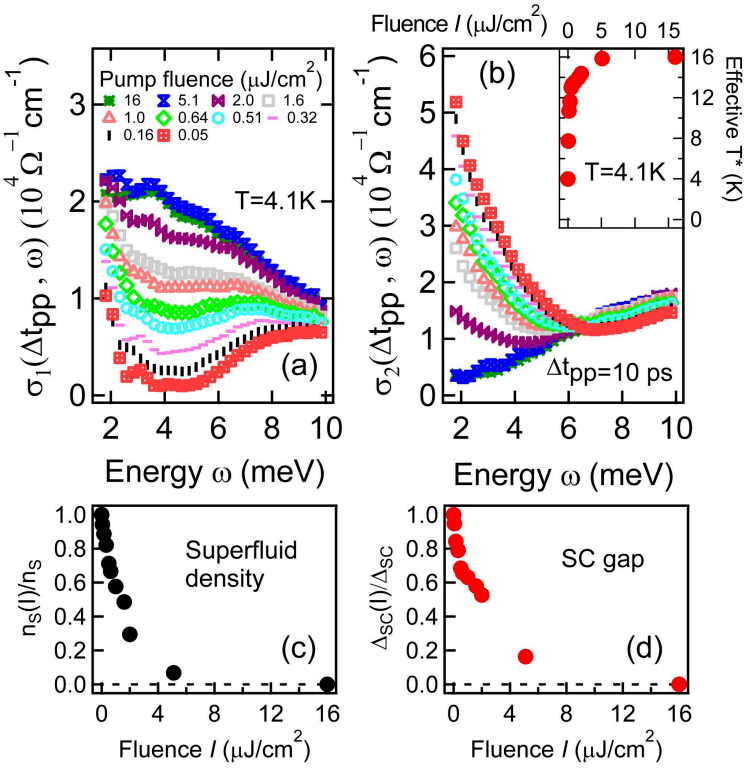


Figure 4.3 (a), (b) Non-equilibrium $\sigma_1(\omega)$ and $\sigma_2(\omega)$ at pump-probe delay $t_{pp}$=10ps for optical-pump fluences 0.05-16$\mu J/cm^2$. Inset to (b) shows effective temperature T* at various fluences. (c), (d) Fluence dependence of superfluid density $n_s$ and SC gap $\Delta_{SC}$.

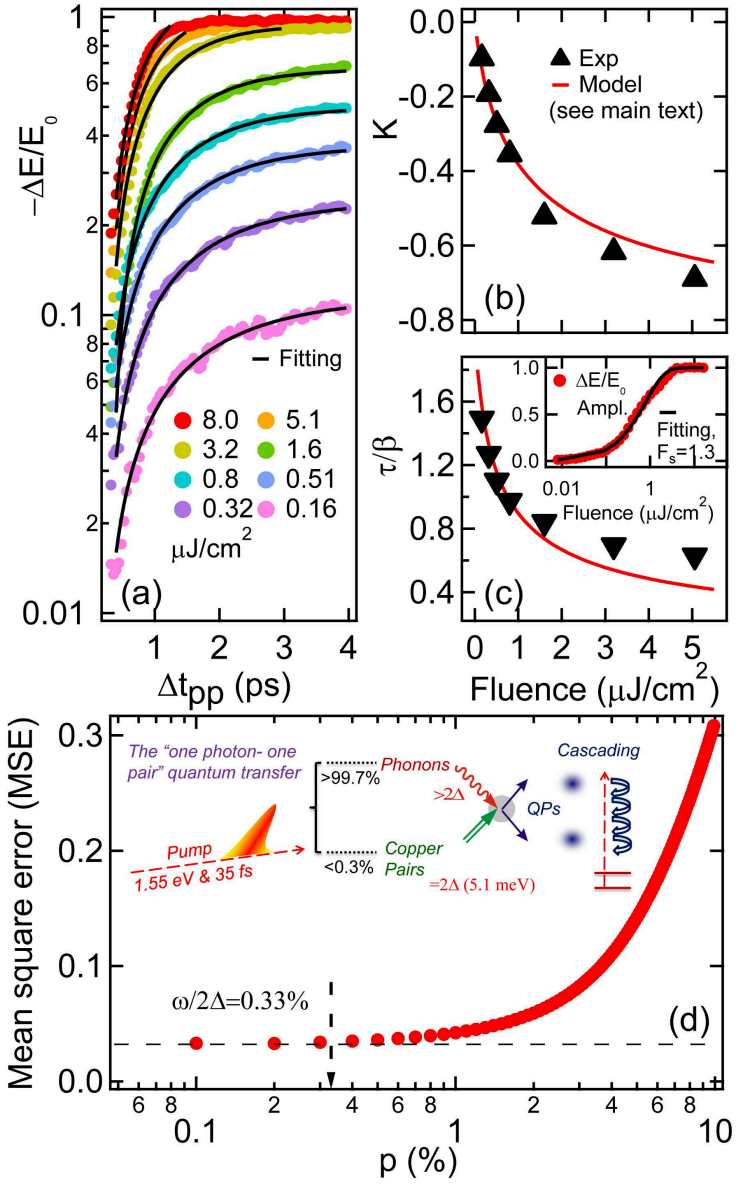


Figure 4.4 (a) Pump-probe dynamics measured in experiment (dots) and fitted by RT model (black line). (b), (c) Fluence dependence of RT model parameters K and $\xi/\eta$ (black triangle) and fitting curve (red line). (d) Fitting MSE vs. QP energy absorption percentage p. Inset to (c) shows fluence dependence of pump induced $\Delta E$ fitted by a saturation curve $(1 - exp(-I/F_s))$. Inset to (d) shows the schematics of microscopic CPB by 1.55eV photon.

# CHAPTER 5. NON-EQUILIBRIUM PAIR BREAKING IN $Ba(Fe_{1-x}Co_x)_2As_2$ SUPERCONDUCTORS: EVIDENCE FOR FORMATION OF PHOTO-INDUCED EXCITONIC STATE

Ultrafast THz spectroscopy reveals an unusual out-of-equilibrium Cooper pair dynamics driven by fs optical quench of superconductivity (SC) in iron pnictides. Following the standard picosecond SC quench via hot–phonon scattering, a second, abnormally slow (many 100's of ps), SC quench regime is observed prior to condensate recovery. This two–step pair breaking dynamics critically depends on doping and temperature, displays a nonlinear pump fluence dependence, and is observed in both single crystal and thin film samples with the uniform excitation. Using density matrix equations of motion, we argue that the build–up of excitonic ($e$–$h$) inter–pocket correlation, due to residual interactions among photoexcited quasiparticles (QP), quenches SC in a correlated QP state.

## 5.1 Introduction

Ultrafast optical tailoring of transient quantum states provides a new way to discover, design, and control exotic correlated materials phases. Recent examples include, among others, quantum femtosecond magnetism (18) and laser-induced superconductivity (25). This strategic approach is implemented by non–thermal separation, within a certain time window, of distinct coupled orders. The latter are strongly intertwined in equilibrium, but respond differently to strong fs photoexcitation (19; 20). Iron-arsenide based superconductors (FeSCs) (68) are well–suited for such non–equilibrium control, as their properties are determined by competing SC, spin density wave (SDW), nematic and structural orders (69). Here we address two open issues: (i) how to use non-equilibrium SC pairing/pair breaking to distinguish between the two bosonic channels,

i.e., phonon and magnetic, that determine the SC properties, (ii) how instabilities in two different correlation channels, i.e., Cooper and excitonic, can lead to controllable transient states.

Ultrafast THz spectroscopy is well–suited for disentangling strongly–coupled excitations. In SCs, this can be achieved by directly probing out-of-equilibrium Cooper pairs and their dynamics following strong pump photoexcitation. By tuning the THz probe frequency in the vicinity of the SC gaps $2\Delta_{SC}$ of few meV, low-frequency THz electrodynamics can be used to directly measure the time evolution of a SC condensate. The latter is "suddenly" driven away from equilibrium, by fs optical excitation here, as illustrated in Fig.5.1(a). Previous ultrafast studies showed that the SC dynamic following high-frequency optical pump mostly comes from its interactions with hot phonons (58; 55). In FeSCs, SDW ($e$–$h$) channel (72) in additional to phonons should play an important role with distinct ultrafast SC dynamics. This has never been observed due in part to the fact that the dynamics in the SC states has been measured only in the optical high frequency region (71) and THz dynamics in resonance with the SC gap have been extremely scarce so far.

Photogeneration of non-equilibrium states in quantum materials with competing SC and density wave orders, such as the FeSCs, provides an opportunity to elucidate the role of $e$–$h$ channels in high–$T_c$ superconductivity. In equilibrium, the SDW phase of FeSCs shows a spontaneous coherence emerging from nested $e$-like and $h$-like Fermi sea pockets, with transition to a $(0, \pi)/(\pi, 0)$ spin-striped state (73; 74). Following QP photoexcitation in these $e$ and $h$ pockets, which can melt the SDW order (72), excitonic correlation can build–up due to the residual inter–pocket interaction (illustrated in Figure 5.1(b)). Such incoherent dynamics is well–documented in semiconductors, where dephasing of excitonic polarization or relaxation of photoexcited $e$–$h$ plasma is followed by formation of a transient state of correlated $e$ and $h$ QPs (75; 86).

In this letter, we present an ultrafast THz spectroscopy investigation of the non-equilibrium dynamics of the SC order in $Ba(Fe_{1-x}Co_x)_2As_2$. We find that Cooper pair breaking subsequent to strong fs optical excitation follows an unusual two-step temporal profile. In particular, the usual phonon scattering channel ($\tau_{Fast}$) is distinguished from an additional, suprisingly slow SC quench ($\tau_{Slow}$). This long-lived, pre-bottleneck dynamics lasts for many 100's of ps under strong

pumping prior to SC recovery. The pump fluence dependence of the SC quench differs between the under- and overdoped regimes with different SDW coherence. Such never-before-seen pair–breaking dynamics, together with quantum kinetic modeling, provide first evidence for the formation of an emergent correlated state of QP $e$–$h$ pairs, out-of-equilibrium, competing with SC, which is driven by excitonic correlation of the disconnected Fermi sea pockets.

## 5.2 Sample Preparation and Experiment Setup

The samples are single-crystalline $Ba(Fe_{1-x}Co_x)_2As_2$ with cobalt substitutions of $x$=0.047 and 0.1. In the underdoped sample ($x$=0.047), long-range SDW and structural phase transitions appear at $T_N$=48 K and $T_S$ =66 K, respectively (74). These phase transitions are *absent* in the overdoped sample ($x$=0.100). Both samples exhibit a SC transition at $T_C \sim 17$ K. Our optical pump–THz probe reflectivity spectroscopy setup is described in detail elsewhere (77; 78; 79). The opaque sample is mounted at $45^o$ to incident light and cooled to T=4.1 K.

## 5.3 Non-equilibrium Dynamics of Pair Breaking

We start with the equilibrium THz measurements of the static SC order and energy gap. The typical static THz reflection spectra, $R(T)$, of $Ba(Fe_{0.953}Co_{0.047})_2As_2$ are shown in Figure 5.1(c). We compare temperatures $T$=4.1 K (red diamonds) and 18 K (black rectangles), below and above the SC transition respectively. These spectra are obtained through Fourier transform of the measured time domain THz field traces, e.g., the red-line curve in the inset of Figure 5.1(d). They are normalized by the normal state 20 K trace. The ratio $R(4.1\,K)/R(20\,K)$ in the measured spectral range of 1–11 meV exhibits the characteristic SC profile. The distinct upward cusp with maximum at ~5 meV reflects the SC energy gap $2\Delta_{SC}$. In contrast, $R(18\,K)/R(20\,K) \sim 1$ has a featureless spectral shape. The measured spectra are reproduced well by the Mattis-Bardeen (MB) theory. In the low-$\omega/T$ limit, the ratio can be expressed as $1 + 4\sqrt{\omega/(\pi\sigma_{1N})}$, where $\sigma_{1N}$ is the normal state conductivity.

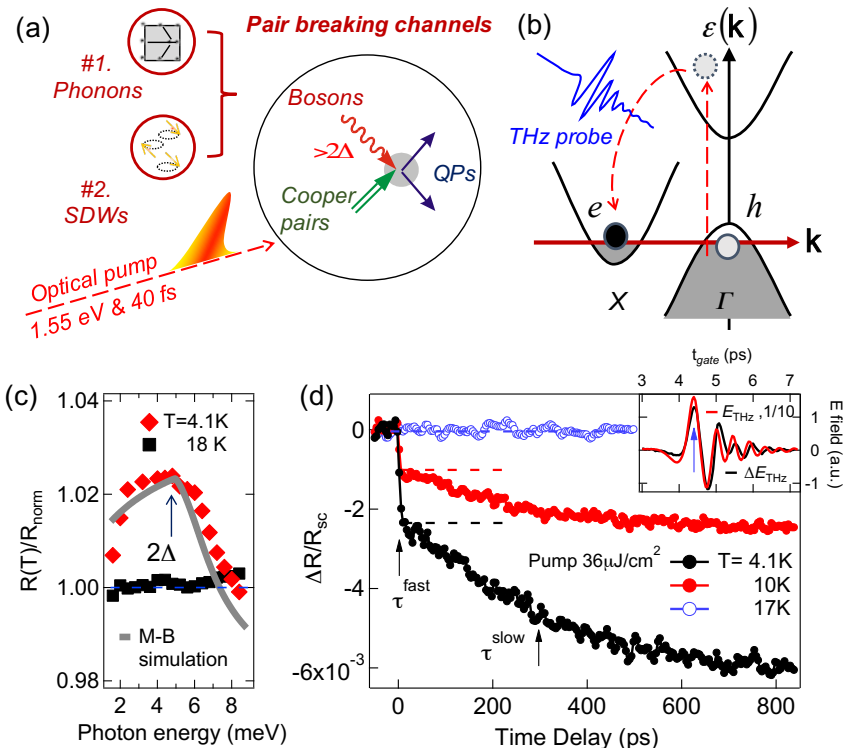


Figure 5.1 **Schematics of SC pair breaking channels** (a), and interband transitions, (b), after fs pump photoexcitation. (c): Static THz reflectivity spectra, normalized to the normal state spectra at 20 K, for underdoped $x = 0.047$ sample, at 4.1 K and 18 K. Grey line shows the result of the Mattis-Bardeen theory. (d) Ultrafast THz dynamics for the above underdoped sample. Inset: The measured time–dependent THz field transients, with gate-time (blue arrow) $t_{gate}$=4.4 ps, at $T$=4.1K.

The ultrafast THz differential reflectivity $\Delta R/R_{SC}$ in the underdoped compound is shown in Figure 5.1(d) for three different temperatures, 4.1 K, 10 K and 17 K. The pump fluence and photon energy are set to 40 $\mu J/cm^2$ and 1.55 eV, respectively. The transient signals are given by the difference of the time-dependent THz fields in the photo-excited (pump on, back line, inset) and unexcited (pump off) states (red line, inset). $\Delta R/R_{SC}$ is then obtained as $[(E_{THz} + \Delta E_{THz})^2 - E_{THz}^2]/E_{THz}^2$. The $\Delta R/R_{SC}$ dynamics fixed at $t_{gate}$ = 4.4 ps (blue arrow, inset) is recorded as function of pump–probe delay. Figure 5.1(d) demonstrates a distinct two-step temporal profile of pair–breaking dynamics. The initial sub-ps SC gap decrease ($\tau_{\text{Fast}}$) is followed by a further very

slow decrease that continues for an unusually long time ~800 ps ($\tau_{\text{Slow}}$). The strong temperature dependence in Figure 5.1(d) coincides with the SC transition, i.e., the transient signals quickly decrease, as seen in the 4.1 K (black) and 10 K traces (red), and diminish at T≈$T_C$ ≈ 17 K (blue).

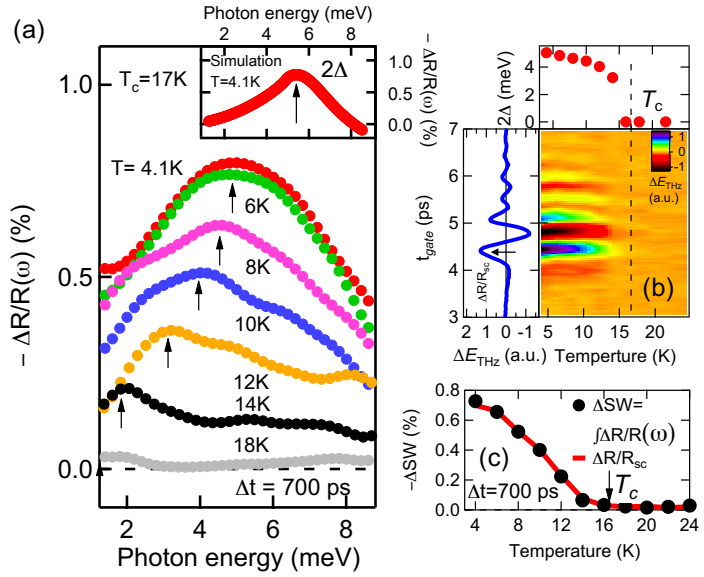


Figure 5.2 (a) THz differential reflectivity spectra (dots) for the $x$=0.047 sample at 700 ps. The cusp peak marked by black arrows reflects $2\Delta_{SC}$. Inset shows the MB simulation (see text). (b) Temperature–dependent ΔE/E THz transients. Left panel: ΔE/E transient at 4.1 K. Top panel: temperature dependence of $2\Delta_{SC}$. (d) Temperature dependence of the integrated spectral weight and peak transient amplitude.

We now present transient $\Delta R/R_{SC}$ spectra that further point to non-equilibrium pair–breaking as the origin of the pump-induced THz signals. Figure 5.2(a) shows the temperature–dependent low frequency, ~1–9 meV, differential reflectivity spectra of the underdoped $x = 0.047$ sample at a fixed long time delay of 700 ps. These spectra are obtained from the Fourier transform of the time-domain THz raw data (Figure 5.2(b)). We note three distinct features: (1) The negative low frequency change $\Delta R/R_{SC}$ <0 indicates photo-induced condensate breaking processes. (2) These transient spectra exhibit the characteristic SC lineshape with cusp peak at $2\Delta_{SC}$ (black

arrow), which is reproduced well by the MB theory (inset of Figure 5.2(a)). (3) Approaching the critical temperature from below, $\Delta R/R_{SC}$ quickly diminishes as the cusp at $2\Delta_{SC}$ shifts to lower frequencies (black arrows, Figure 5.2(a)). This SC gap temperature dependence is summarized in the top panel of Figure 5.2(b). We also compared the integrated reflectivity spectral weight associated with the SC states and the $\Delta R/R_{SC}$ amplitude at $t_{gate}$=4.4 ps. The strong correlation between the two at all temperatures (Figure 5.2(c)) and fluences (inset, Figure 5.4(b)) allows us to study the ultrafast pair-breaking dynamics by recording $\Delta R/R_{SC}$ as in Figure.5.1(d).

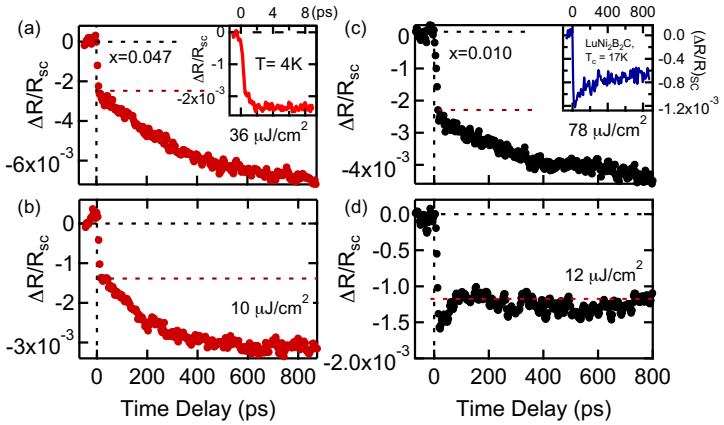


Figure 5.3 Ultrafast THz pump probe scan at different pump fluences for (a,b) $x$=0.047 and (c,d) $x$=0.1 samples. All traces taken in the superconducting state at T=4.1 K. Inset of (a): the initial dynamics. Inset of (c): The THz dynamics in $LuNi_2B_2C$ at pump fluence of 40 $\mu J/cm^2$.

Next we show the strong dependence of the non-equilibrium SC quench profile on pump fluence and doping. Figure 5.3(a) and 5.3(b) show the photoinduced $\Delta R/R_{SC}$ dynamics in the underdoped, $x$=0.047, sample and compare 36 $\mu J/cm^2$ and 10 $\mu J/cm^2$ pumping. Both excitations of the coupled SC/SDW ground state order show a sub-ps $\tau_{\text{Fast}}$ followed by a 100's ps $\tau_{\text{Slow}}$ SC quench process. Previous works in BCS and cuprate SCs have shown that the majority of the absorbed photon energy transfers to the phonon reservoir during the pulse (70). Hot phonons then deplete the condensate on a few-ps timescale (54; 58). This time interval becomes shorter (sub-ps) under the strong pumping used here, consistent with the inset of Figure 5.3(a). However, the slow ~800ps SC

quench under strong pumping is different from other superconductors. For comparison, the inset of Figure 5.3(c) shows the non-equilibrium pair breaking dynamics of the BCS superconductor $LuNi_2B_2C$. Unlike for the FeSCs, similar strong pumping of this SC exhibits single-step, sub-ps SC quenching, followed by slow *partial recovery* instead of further quench. This typical pair breaking temporal profile can be explained in terms of QP scattering with high energy phonons, followed by condensate recovery governed by phonon relaxation (bottleneck effect) (58). A comparison of the two SC systems indicates that an additional, remarkably slow and yet strong, SC quenching channel is present in the FeSCs. The continuing SC gap quench over many 100's of ps is "intrinsic" and cannot come from, e.g., heat diffusion. The latter would appear in both FeSC and BCS samples and would also differ between thin film (uniform excitation) and single crystal FeSC samples, which however show similar pre-bottleneck dynamics (supplementary).

Figures 5.3(c) and (d) show our results in the overdoped FeSC system ($x$=0.1),where there is no long-range SDW order in equilibrium. In this regime of the phase diagram, the quench temporal profile changes drastically with increasing pump fluence. While the slow SC quench is again seen at high fluences 78 $\mu J/cm^2$ (Figure 5.3(c)), at low pump fluences (12 $\mu J/cm^2$ in Figure 5.3(d)) the initial fast quench is followed by a partial recovery similar to the BCS sample (inset, Figure 5.3(c)). For the overdoped ground state without any SDW coherence, the slow SC quench channel only appears above a critical fluence, while in the underdoped regime with SC/SDW ground state it persists down to low fluences. Such a strong distinction in the temporal profile between sample dopings corroborates our assertion that the long-lived, continuing SC gap quench is "intrinsic" in FeSCs and differs from both BCS and cuprate SCs.

## 5.4 Theory Explanation: Formation of Photo-induced Excitonic State

The striking fluence and doping dependences of the FeSC condensate quench are seen more clearly in Figure 5.4(a) and 4(b). Here, the integrated spectral weight (SW), obtained from the peak-peak amplitude change $\Delta R/R_{SC}$ at $t_{gate}$=4.4 ps (inset, Figure 5.4(b)), is shown as function of pump fluence. Figure 5.4(a) compares the fluence dependence in the overdoped regime (no SDW

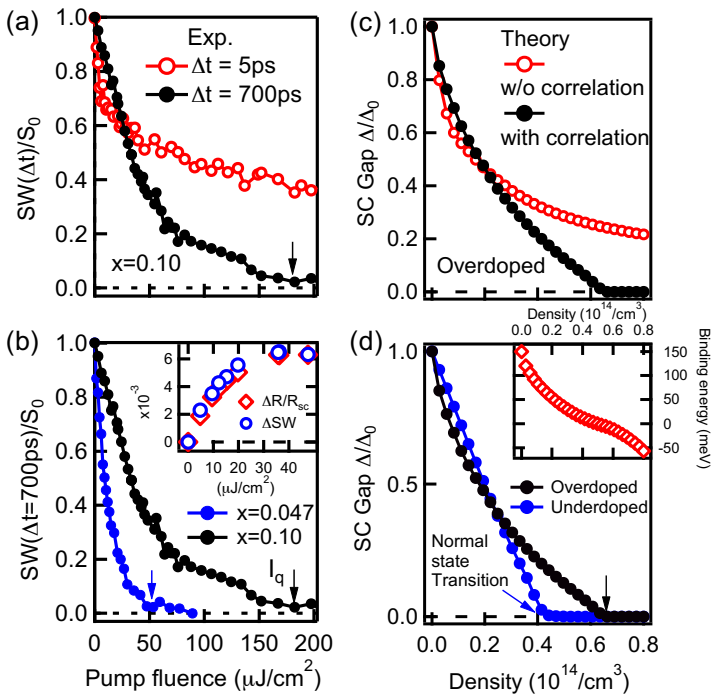


Figure 5.4 Measured fluence dependence of the integrated spectral weight (SW): (a) $x$=0.1 crystal at 5 ps (red) and 700 ps (black); (b) comparison of $x$=0.047 and $x$=0.1 samples at 700 ps. Inset: SW and $\Delta$R/R$_{SC}$ exhibit the same fluence dependence. (c) Theoretical modeling of the SC gap quench in the overdoped region as function of photoexcited QP density $\rho$, with (black line) or without (red line) inter-pocket excitonic correlation.The $y$-axis is normalized by the equilibrium SC gap $\Delta_0$. (d) Theoretical comparison of under- and over-doped regions for the photoinduced correlated SDW excitonic state. Inset: Excitonic energy $|E|$, Eq. (5.1), as function of $\rho$.

ground state coherence) between short 5 ps (red empty circle) and long 700 ps (black solid circle) time delays. The SC quench as function of photocarrier density is qualitatively different at short and long times and the two curves cross at ~25 $\mu$J/cm$^2$. At $\Delta t$=700 ps, we observe a transition from SC to normal state above a large critical pump fluence, I$q$=182 $\mu$J/cm$^2$. Such transition is not observed at 5ps, where the signal appears to saturate for high fluences. Figure 5.4(b) compares this SC-to-normal state transition at $\Delta t$=700ps between the under- and overdoped samples. In the underdoped regime with SC/SDW coherence ($x$=0.047), the transition occurs at much smaller critical pump fluence $\sim$ 50 $\mu$J/cm$^2$ than in the overdoped regime. Below we interpret these salient

experimental features based on build–up of excitonic correlation between the photoexcited $e$ and $h$ QPs.

The conventional Rotwarth-Taylor (RT) model (58; 59) describing QP interactions with hot bosons does not provide a consistent fit of our THz time–dependent data (supplementary). This model assumes that the hot bosons are distinct from the photoexcited QPs. Here, however, the same indistinguishable electrons participate in SC condensate, QP excitations, and inter–pocket $e$-$h$ pairs. The importance of fermionic correlations after coherence has decayed is well established in semiconductors, where calculations of exciton formation based on rate equations describing $e$ and $h$ QPs and excitons as distinct particles are inadequate (**?** ). Using a density matrix calculation of the QP dynamics arising from the strong inter–pocket interaction, here we describe the build–up of $e$–$h$ correlation after any SDW coherence has decayed (supplementary). An uncorrelated "plasma" state of $e$–$h$ QPs formed after initial cascade (46) creates hot QP populations of the disconnected $e$– and $h$–like Fermi sea pockets (Figure 5.1(b)) and evolves into a correlated many–QP state characterized by the two-particle density matrix (**?** ; 84). Slow formation of excitonic correlation between QPs is well established in semiconductors (**?** ).

We adopt the Hamiltonian of Refs. (82; 42), which in the mean-field approximation describes the essentials of competition between SC and SDW orders. Considering for simplicity one $e$ and one $h$ pocket, we first transform to the basis of Bogoliubov QPs with equilibrium SC and SDW coherence. Similar to semiconductors, here we assume an initial hot quasi-thermal distribution of uncorrelated QPs in both $e$ and $h$ pockets, formed after cascade relaxation (46) whose details are unimportant. The QP populations $n_{\mathbf{p}}$ evolve in time due to their residual interactions, which affect the low energy states. The e–h correlation is characterized by two-particle density matrices of the form $\langle X^{\dagger}X\rangle - \langle X^{\dagger}\rangle\langle X\rangle$, where $\langle X\rangle$ denotes the one-particle SDW coherence (82; 80). In this way we characterize the crucial properties of the quasi-stationary many–QP state formed after 100's of ps. This many–QP state is intermediate between uncorrelated $e$–$h$ plasma and spin–exciton many body state and is characterized by the amplitude $\phi_p$ given by the generalized Wannier equation

obtained from the equations of motion of $\langle X^\dagger X\rangle - \langle X^\dagger\rangle\langle X\rangle$ as in Refs. (84; **?** )(supplementary):

$$\left(\varepsilon_{\mathbf{p}}^{-} + \varepsilon_{\mathbf{p}}^{+}\right)\phi_{\mathbf{p}} - (1 - 2\,n_{\mathbf{p}})\sum_{\mathbf{k}} V_{\mathbf{k},\mathbf{p}}\phi_{\mathbf{k}} = E\,\phi_{\mathbf{p}}\,. \tag{5.1}$$

Here, $\varepsilon_{\mathbf{p}}^{-}$ and $\varepsilon_{\mathbf{p}}^{+}$ are the single–QP energies and $V_{\mathbf{k},\mathbf{p}}$ are the matrix elements describing the residual inter–pocket interaction. The energy eigenvalue $E$ describes corrections to the chemical potential as correlation builds up between QPs. $E$ depends on the total photoexcited QP density $\rho$ through the condition $\rho = \sum_{\mathbf{p}} n_{\mathbf{p}}$, where the QP distribution $n_{\mathbf{p}}$ is determined by (supplementary)

$$\left(n_{\mathbf{p}} - \frac{1}{2}\right)^2 + |\phi_{\mathbf{p}}|^2 = \frac{1}{4}. \tag{5.2}$$

The above equations, together with SC/SDW order parameter equations (supplementary), provide a self-consistent calculation of the quasi–stationary correlated many–QP state (85) and are analogous to the description of incoherent excitonic correlation build–up in semiconductors (**?** ) and the transition between Bose condensation and BCS superconductivity (83). Here we describe QP $e$–$h$ pair states, whose properties depend on the equilibrium SC and SDW coherence (81). This introduces a doping dependence that depends on the Fermi sea topology. Equation (5.1) interpolates between weak and strong coupling limits and can have both bound and unbound solutions, depending on QP density $\rho$, Pauli blocking effects, and inter–pocket interaction strength. With increasing $\rho$, the momentum dependence of the QP distribution $n_{\mathbf{p}}$ changes strongly due to its coupling with the QP pair amplitude $\phi_{\mathbf{p}}$. This, in turn, affects the Pauli blocking effects that quench the SC gap.

Figure 5.4(c) compares the calculated quasi-stationary SC gap with or without the excitonic correlation $\phi_{\mathbf{p}}$ as a function of total QP density $\rho$ (supplementary). The calculated SC gap for $\phi_p$=0 (red circles), which assumes uncorrelated photoexcited QPs, shows a fast decrease at low QP densities, which flattens (saturates) as $\rho$ increases further. This feature is in qualitative agreement with the measured fluence dependence of the SC gap at ps time delays (red circles, Figure 5.4(a)), where the standard BCS model with quasi–thermal QPs following initial relaxation is applicable ($\phi_p \approx 0$) (40).

With $\phi_p \neq 0$ developing when the interacting QPs form a metastable quasi–equilibrium state as indicated by our experiment, the distribution $n_{\mathbf{p}}$ changes drastically. In this state, our calculations show that the QP interactions, Eq. (5.1), lead to a complete quench of the SC gap at elevated $\rho$ (black curve in Figure 5.4(c)), with a non–thermal transition from SC to normal state above a critical pump fluence. This result is in qualitative agreement with the measured fluence dependence of the SC gap after 100's of ps (black circles, Figure 5.4(a)). It supports our claim that the experimentally observed qualitative difference in the SC gap fluence dependence between long and short times arises from the delayed formation of a correlated state among interacting laser–induced non–equilibrium QPs.

Figure 5.4(d) compares the calculated QP density dependence of the SC gap at long times between the underdoped (blue solid circle) and overdoped (black solid circle) regimes. The doping dependence of the critical pump fluence required for SC–to–normal state transition is in qualitative agreement with the experiment (compare to Figure 5.4(b)). While in the overdoped regime there is no SDW coherence, the equilibrium SDW coherence present in the underdoped regime results in SC-to-normal state transition at lower photoexcited QP densities. Such doping dependence of the residual $e$-$h$ correlations comes from the differences in the coherence between the overdoped and underdoped equilibrium states. Finally, the inset of Figure 5.4(d) shows the calculated energy eigenvalue $E$ per $e$–$h$ pair as a function of QP density $\rho$. At low $\rho$, we obtain a bound excitonic state, which however becomes unbound due to phase-space filling Pauli effects.

In conclusion, the ultrafast THz dynamics of FeSCs reveals a remarkably long-lived pre–bottleneck dynamics, i.e. a SC quench that continuous after many 100's of ps prior to SC recovery. Such delayed build–up of SC quench is observed in both single–crystal and thin–film samples and, together with its nonlinear fluence and doping dependence, provide evidence for the existence of a metastable many–QP state. These salient experimental features and differences between long and short times are consistent with our quantum kinetic calculation that underpins build–up of such quantum state due to inter–pocket QP interactions. The nonthermal control demonstrated here may be

used to access hidden density-wave phases and quantum criticality under the SC dome in high–$T_c$ superconductors.

# CHAPTER 6. LIGHTWAVE-DRIVEN GAPLESS SUPERCONDUCTIVITY AND FORBIDDEN QUANTUM BEATS BY TERAHERTZ SYMMETRY BREAKING

Light-induced supercurrents chart a path forward for electromagnetic design of emergent materials phases and collective modes for quantum engineering applications. However, controlled spatial-temporal modulation of the complex order parameter characterizing such non-equilibrium states remains elusive. Such ultrafast phase-amplitude modulation can manifest via high harmonic (HH) modes beyond those allowed by equilibrium symmetries. Here we drive moving condensate states via subcycle dynamical symmetry breaking achieved with nonlinear oscillating photocurrents. These non-equilibrium macroscopic quantum states with broken inversion symmetry are controlled via Cooper pair acceleration by asymmetric and multi-cycle terahertz photoexcitations. The observed supercurrent-carrying states evolve during a lightwave cycle and exhibit three distinguishing features: Anderson pseudo-spin precessions forbidden by equilibrium symmetry, strong HH coherent oscillations assisted by pairing, and long-lived gapless superfluidity with minimal condensate quench. Lightwave tuning of persistent photocurrents can be extended for quantum control of high-$T_C$ cuprates and topological matter, with implications on quantum gate and sensing functionalities.

## 6.1 Introduction

Ultrafast nonlinearity in quantum systems is emerging as a frontier for enabling laser-driven many-body correlation phenomena (14; 89; 22; 23; 88; 40; 87; 67; 25; 28; 78; 104). So far, strong coupling of superconductors (SC) to intense terahertz (THz) pulses has revealed, e.g., collective modes (40; 22; 23; 87; 88; 92) and a gapless quasiparticle (QP) metastable phase hidden beneath SC (67). A standard model for understanding ultrafast SC condensate coupling to an ac electric field, illustrated in Figure 1a, is Anderson pseudo–spin precession, $\vec{s}_k(t)$ (arrows). This precession

is driven by *even* nonlinear couplings, $O(\mathbf{A}^{2n})$, of the vector electromagnetic potential $\mathbf{A}(t)$, which are the only ones allowed by the equilibrium BCS symmetry (14; 89; 90; 93). Here we explore a different nonlinear mechanism, periodic and asymmetric acceleration of Cooper pair center-of-mass (CM) motion driven by phase-locked multi-cycle THz electric field pulses. We show that experimental manifestations of such lightwave acceleration of a macroscopic quantum state include strong odd (forbidden) Anderson pseudo–spin HH nonlinearities enabled by subcycle symmetry breaking. The latter result from transient changes in the pairing for sufficiently strong THz gauge fields corresponding to finite Cooper pair center of mass (CM) momentum. This coherent asymmetric THz field driving of condensate does not rely on resonant excitation of QPs or bandstructure details (89; 91), but rather on transient breaking of equilibrium inversion symmetry and nonlinear photocurrents. This is achieved by introducing a preferred direction parallel to the oscillating electric field, which leads to $(\mathbf{k}+\mathbf{p}_{\rm s}(t)\uparrow, -\mathbf{k}+\mathbf{p}_{\rm s}(t)\downarrow)$ Cooper pairs, with spatially-temporally modulated superfluid CM momentum $\mathbf{p}_{\rm s}(\mathbf{R},t)$ created during the pulse (Figure 1a, red line), via periodic acceleration of the SC condensate by the oscillating THz field and via spatial variations in the SC order parameter phase $\zeta$,

$$\mathbf{p}_{\rm s}(\mathbf{R},t) = -2e\mathbf{A}(\mathbf{R},t) + \nabla_{\mathbf{R}}\zeta(\mathbf{R},t) = 2e\int_{-\infty}^{t}\mathbf{E}_{\rm eff}(\mathbf{R},t')dt' \tag{6.1}$$

where 2e is the Cooper pair charge and $\mathbf{E}_{\rm eff}(\mathbf{R},t')$ (method, Eq.(3)) is the effective pulse that drives the light-induced CM motion. Furthermore, such gauge–invariant superfluid momentum can remain finite long after the pulse since THz driven nonlinear photocurrent sources and spatial variations determine an effective *asymmetric* oscillating electric field inside the SC during THz pulse propagation that satisfies the property $\int_{-\infty}^{\infty}{\rm d}\tau\,\mathbf{E}_{\rm eff}(\tau) \neq 0$ (94). Such effective pulse will drive persistent condensate flow if disorder is minimized in sufficiently clean superconductors.

We emphasize two smoking-gun signatures of the periodically driven, supercurrent-carrying macroscopic state: (1) As illustrated in Figure 1a, co-existence and interference (white dash arrows) in a pump—probe two-pulse experiment of quantum transport, $\mathbf{p}_s(t)$ (red lines), with even-order nonlinearity, $O(\mathbf{A}^{2n})$ (green lines), can result in new *forbidden* Anderson pseudo-spin modes due to dynamical symmetry breaking, e.g., coherent pseudo–spin oscillation (PSO) at $3\omega_{pump}$.

However, only even-order PSO nonlinearities have been considered so far, limited to $O(\mathbf{A}^2)$ at $2\omega_{pump}$ observed experimentally corresponding to a perturbative expansion (23); (2) in a moving condensate, $\vec{v}_s(t)$, the SC order parameter $\Delta_{SC}(t)$ is no longer equal to the QP excitation energy $E^{QP}_{min}(t) \approx \Delta_{SC}(t) - \mathbf{p}_F \cdot \vec{v}_s(t)$. To illustrate this, Figure 1b compares the QP dispersion between the equilibrium BCS state (left), with finite energy gap $2\Delta_{SC}$, and the current-carrying state (right) at critical Cooper pair velocity, $\vec{v}_s \cdot \mathbf{p}_F = \Delta_{SC}$. The latter state is *gapless* at $\mathbf{k}$ points with vanishing $E^{QP}_{min}$, i.e. it costs zero energy to excite QPs, although the order parameter $\Delta_{SC}(t)$ and superfluid density $n_s$(t) remain finite. A supercurrent-carrying gapless state is difficult to realize in equilibrium, due in part to heating of electric contacts in the presence of the large current and impurity scattering. Although the equilibrium gapless state has been inferred in tunneling spectroscopy of DC-biased SC nano-wires (95) and also induced as a Fulde-Ferrell-Larkin-Ovchinnikov (FFLO) state, coherent tuning of gapless superfluidity (44) is difficult by using these equilibrium methods. Here it is achieved by nonlinear lightwave acceleration of supercurrents (Figure 1a).

In this article, we drive a nonthermal transition from the equilibrium BCS state to a long-lived, supercurrent–carrying macroscopic state in a sufficiently clean $Nb_3Sn$. This is achieved by non-contact alternating current-bias using the sub-gap THz carrier wave of the light electric field (67; 78). The subcycle dynamical symmetry breaking manifests itself via the emergence of forbidden $3^{rd}$-order PSOs, interaction-enhanced strong $4^{th}$-order HH nonlinearities, and light–induced gapless superconductivity. Our results are consistent with the predictions of a quantum kinetic nonlinear calculation using a gauge–invariant density matrix.

## Forbidden Anderson pseudo–spin and strong HH oscillations

The pseudo–spin oscillations measured in a $Nb_3Sn$ film (97) (methods) are shown in Figure 1c. The SC state is driven by a $E_{\rm THz}$ =11.5 kV/cm sub-gap THz field with central frequency $\omega_{\rm pump}$ =0.5 THz (2.1 meV), well below the pair-breaking gap $2\Delta_{SC}$ =1.2 THz at 4.1 K. It is detected in a two-time, THz pump and THz probe experiment, by measuring the differential THz transmission $\Delta E/E_0$ as function of pump–probe time delay. The coherent dynamics reveals a

pronounced quantum beating superimposed on a slow amplitude change, which vanishes above the critical temperature $T_c$ ~16 K (inset). The origin of the oscillatory behavior of $\Delta E/E_0$ is demonstrated by its Fourier transformation shown in Figure 1d. Besides the conventional $2\omega_{\rm pump}$ mode (same as third harmonic generation, THG, in emission (23; 14), shown in supplementary), the spectrum displays *three new strong peaks*: (i) an inversion symmetry–forbidden, $3^{rd}$ harmonic PSO mode at $3\omega_{\rm pump}$, (ii) a strong $4^{th}$ harmonic PSO mode at $4\omega_{\rm pump}$, and (iii) a narrow $1^{st}$ order peak at the fundamental driving frequency, indicative of the build-up of a long-lived supercurrent (inset, Figure 1d). Odd-order PSO peaks are the hallmark for symmetry breaking, here induced by THz field-SC condensate coupling. Furthermore, the $4^{th}$–to–$2^{nd}$ order peak ratio is ~10%, 1000 times bigger than in the standard model (14), $1/12\pi eE/(2p_F\omega)^2$ ~$10^{-4}$.

Figs. 1e (time) and 1f (frequency) compare the experimental results to those of our gauge-invariant quantum kinetic theory with $\mathbf{p_s}(t) \neq 0$. By using an effective, slightly asymmetric sub–gap THz driving of the SC (red lines), we obtain both the forbidden mode at $3\omega_{\rm pump}$ and strong even harmonics, with a gigantic, interaction–enhanced, $4^{th}$–to–$2^{nd}$ order ratio ~10 %, comparable to that in the experiment. These HH peaks are vanishingly small in the linearized pseudospin (LPS) model (black lines). Note that the exact mechanism and details for generating $\mathbf{p_s}(t)$ do not affect the above identifications. We also compare to the theoretical results for symmetric THz driving (green lines), where $\mathbf{p}_s \approx 0$ after the THz pump, which suppresses the $3\omega_{\rm pump}$ mode (Figure 1f). These theoretical results indicate that the odd coherent PSOs are controlled by the THz pulse shape and SC phase spatial fluctuations, Eq.(1), while the even harmonic peak strength mostly depend on the pairing interaction and lightwave acceleration beyond the LPS model. These results underpin the interplay between subcycle dynamical symmetry breaking due to $\mathbf{p}_s(t)$ and interaction-enhanced HH nonlinearities in determining the light-driven SC ultrafast nonlinear dynamics.

The asymmetric and multi-cycle THz driving used here are critical for inducing non-adiabatically a moving condensate macroscopic state with forbidden Anderson pseudo-spin modes. Figure 2 compares quantum beating spectra obtained from coherent THz pump-THz probe dynamics driven by three different electric field waveforms of oscillation cycles and carrier frequency, Figs. 2a-2b, and

temporal asymmetry, Figure 2c, due to the nonlinear coupling effects. Specifically, in order to approximately evaluate the role of nonlinear asymmetric coupling, we compute the effective nonlinear pulse integral $\int_{-\infty}^{t} \mathrm{d}\tau\, \mathbf{E}_{\mathrm{eff}}(\tau)$ by inputing the THz pump pulse waveforms detected via electro-optic sampling in a <110> ZnTe crystal. Figure 2c clearly shows that the intense THz pulses used here as pump exhibit a non-zero integral of $\mathbf{E}_{\mathrm{eff}}(\tau)$, seen as a tilting of the temporal profile. In contrast, the weak probe THz pulse exhibits zero integral over time with negligible tilting (inset, Figure 2c). Note that a quantitative analysis of the gauge-invariant coupling of THz fields and superfluid momentum $\mathbf{p}_{\mathrm{s}}(t)$ need to also include longitudinal responses from spatial variations of the gap phase and chemical potential as seen in Eqs.(3) and (4) (method).

We point out four key observations when comparing the pump-probe responses to the three different pump pulses in Figs 2a and 2b. First, the 0.5 THz excitation clearly reveals $1^{st}$-$4^{th}$ PSO modes (Figure 2d), while the 1 THz excitation does not show $3^{rd}$ and $4^{th}$ order HH peaks (Figure 2e). Comparing the 0.5 THz (red) and 1 THz (blue) pump pulses, shown in Figure 2a, the former has comparable contribution to Anderson pseudo–spin precessions, i.e., $\mathbf{A}(t)^2 \propto E^2/\omega^2$, but higher asymmetry, seen as larger tilting of the time integral indicative of the nonlinear coupling of the electric field (Figure 2c). The 0.5 THz (red) pump pulse also has more oscillation cycles (Figure 2a), i.e., a sharper below-resonance pump spectrum (Figure 2b), while the 1 THz (blue) one tentds to excite larger QP populations due to spectral overlap and proximity to the SC gap shown in Figure 2b. Second, the single-cycle 1 THz pulse (gray, 47 kV/cm) shows a significantly broadened $2^{nd}$ PSO peak without other modes (Figure. 2f), which we attribute to the dephasing of resonantly excited quasiparticles absent for the multi-cycle (narrow band) 0.5 THz pulse (Figure 2b). The above comparison indicates that the symmetry breaking and HH modes are determined by the interplay of pulse asymmetric driving, pulse carrier frequency and oscillation cycles. The importance of more field cycles (sharper spectral width) and lower driving frequency (less dephasing with minimal QP excitations) is consistent with our observation that the 0.5 THz pulse driving (Figure 2a) is the most favorable for observing the nonlinear modes, e.g., it shows a stronger $2^{nd}$ PSO peak than even the $1^{st}$ order linear supercurrent peak (Figure 2d), unlike for the 1 THz pump (Figure 2e).

Third, the sharp $1^{st}$ order peaks seen for 0.5 and 1 THz pumping, which underpin condensate flow and, thereby, broken symmetry in Figs. 2d-2e, are absent in both a dirty limit NbN sample (inset, Figure 2e) and for the single-cycle 1 THz pump that excites large QPO populations (Figure 2f). Lastly, the simulated coherent THz *pump-probe* responses of the current-carrying quantum state (inset, Figure 2d) show excellent agreement to Figure 2, which corroborates our above assignments of the observed collective modes. We conclude that the ultrafast SC nonlinear response results from the interplay of two different photoinduced effects: lightwave nonlinear acceleration of a moving condensate state with finite momentum pairing and dephasing via photoexcited QP populations.

## Light-induced gapless superconductivity

The nonthermal transition from gapped BCS to gapless superfluid state driven by the asymmetric multi-cycle field $E_{1THz}$ pumping is demonstrated in Figs. 3a ($\sigma_1$) and 3b ($\sigma_2$). These figures show the dissipative and inductive nonlinear responses, respectively, after $\Delta t_{pp}$=100ps, which measure the QP excitation gap and SC order parameter ($n_s$). $\sigma_1$ reveals partial quench of the SC gap for low fields $E_{1THz}$ =34 (blue), 45 (magenta), 62 (black) and a transition to a gapless SC state at $\sim$ 78kV/cm (red diamond). The latter corresponds to fully filling the gap in $\sigma_1$, as seen by comparing $\sigma_1(\omega)$ with the normal state (gray line, Figure 3a). While the THz field quenches $E_{min}^{QP}$, a diverging $\sigma_2$ arises from the reactive SC coherence peak $n_s\delta(\omega = 0)$. Most intriguingly, despite the gapless conductivity demonstrated by $\sigma_1$, the quench of the SC order parameter and $n_s$ is minimal in Figure 3b. This is clearly seen from the similar divergence of the pump-induced (red diamond) and equilibrium (black dotted line) $\sigma_2$, which indicates observation of light–induced gapless superconductivity. Such gapless SC state with $n_s \neq 0$ can be driven by condensate flow $\mathbf{p}_s \neq 0$ and is distinct from previously known gapless QP states, realized after strong depletion of the condensate, $n_s \approx 0$. While such condensate quenching was achieved before by photoexcitation of large QP populations via broadband single-cycle pumping (67), the gapless SC state achieved here in a non-equilibrium supercurrent-carrying coherent state with minimally-quenched $n_s$, driven by nonlinear asymmetric photoexcitations via intense multi-cycle THz pulses. The excitation spectrum of such

quasi-stationary ordered state with finite Cooper pair velocity after 100ps is intuitively captured by Figure 1b. QP excitations moving against a critical condensate flow, $v_s \sim 3.15 \times 10^4$cm/s, are energetically favorable, but only at certain $\mathbf{k}$-points. This corresponds to populating $-\mathbf{k}_0 + \mathbf{p}_s \uparrow$ and $-\mathbf{k}_0 + \mathbf{p}_s \downarrow$ states with QPs after removing the Cooper pairs ($\mathbf{k}_0 + \mathbf{p}_s \uparrow$, $-\mathbf{k}_0 + \mathbf{p}_s \downarrow$) and ($-\mathbf{k}_0 + \mathbf{p}_s \uparrow$, $\mathbf{k}_0 + \mathbf{p}_s \downarrow$ from the condensate.

### Non-thermal control of the supercurrent-carrying quantum states

The nonthermal dynamics of the moving condensate states can exhibit much longer (∼100ps) rise times than for single-cycle pulse(67), which, as shown in Figs. 3c, strongly depends on the pulse temporal profile. This observation indicates a new tuning method for driving non-equilibrium protected quantum states. By comparing in Figure 3c the $\Delta E/E_0$ dynamics excited by three different THz pump waveforms (Figure 2a), we demonstrate control of the 100ps time evolution by tuning the intensity, field cycles and nonlinear asymmetry in the temporal profile of the driving THz field pulse. We compare first the time evolution for the two multi-cycle pulses, which are centered at 0.5 (red line, Figure 3c) or 1 THz (blue line, Figure 3c). These two pulses induce distinctly different temporal pathways (Figure 3c). First, the very early regime of coherent time evolution (marked as regime #1) displays pronounced PSOs, including symmetry-forbidden harmonics depending on the pulse shape. Second, we observe that the much longer temporal evolution well after the excitation pulse is controlled by the pulse shape (marked as regime #2). Third, the pulse energy required to reach the same non–equilibrium state after delayed timescales (marked as regime #3) differs by an order of magnitude between the two multi-cycle pulses: 12nJ vs. 130nJ for 0.5 and 1 THz pulses, respectively. Intriguingly, the most pronounced delayed build-up appears in the 0.5 THz pump trace (red line) with *much lower* pulse energy. Such slow 100ps dynamics coincides with the appearance of the forbidden Anderson pseudo-spin modes from asymmetric multi-cycle nonlinear THz field driving seen in Figure 2d. These distinguishing features clearly indicate nonthermal evolution of the discovered supercurrent-carrying state with minimal SC quench. For a macroscopic condensate flow (98; 99), the collective $\mathbf{p}_s(t)$ CM momentum of many Cooper pairs is "protected", e.g., against

phonon scattering (100), unlike for individual QPs. In contrast, a single-cycle broadband pulse centered at 1THz directly excites non-equilibrium QPs by the part of its spectrum above 2 $\Delta_{SC}$ (Figure 2b). Such QP populations quench $n_s$ (67), largely suppresses the coherent oscillations, and lead to very fast rise ∼1ps (gray line, Figure 3c). For such pulse spectrum, QP generation and dephasing dominate over condensed Cooper pair dynamics and damp the nonlinear modes (Figure 2f). Although low-field single-cycle pulsed excitation can also minimize the SC quench, the post-quench states in this case show sub-ps fast rise times during the pulse (inset, Figure 3c), a strongly broadened $2^{nd}$ PSO mode and no $1^{st}$ order supercurrent mode (Figure 2f).

A careful study of the complex conductivity ($\sigma_1(\omega, \Delta t_{pp})$, $\sigma_2(\omega, \Delta t_{pp})$) in Figs. 3d and 3e relates the delayed rise of -$\Delta E/E$ in regime #2 (Figure. 3c) to the filling of the QP excitation gap by additional spectral weight. By comparing the non–equilibrium $\sigma_1$ at 20ps and 100ps for our two multi-cycle pulses, we see that the initial gap filling continues with a pronounced delayed rise for pump pulse with $\omega_{pump}$=0.5 THz (Figure 3d). However, the slow rise becomes less obvious for $\omega_{pump}$=1 THz (Figure 3e), consistent with the respective $\Delta E/E$ dynamics in Figure 3c, as a faster component emerges. This faster dynamics dominates in the case of single-cycle 1THz pumping, as QP excitation dominates over lightwave acceleration, also evidenced by the absence of HH peaks. Unlike for $\sigma_1$, after multi–cycle pumping well below the SC gap, there is very small change in the condensate density $n_s$ measured by $\sigma_2(\omega)$ (Figs. 3d-3e).

For more quantitative analysis, we plot the QP density ($q$, red circle), extracted from the integrated $\sigma_1$, and the superfluid density ($p$, blue circle) extracted from the $\sigma_2$ divergence, as well as their sum ($\Sigma$, black symbol), as a function of $E_{THz}$ at 1 THz (inset, Figure 3b). It is clear that the quenched SC coherence peak $n_s\delta(\omega = 0)$ cannot account for the nearly doubled $\Sigma$, e.g., for $E_{THz}$=78kV/cm. The additional spectral weight during the current-carrying state evolution is consistent with quenching of the competing martensitic orders as discussed in Ref. (97). A spectral weight transfer mechanism has been also explored in ultrafast dynamics of competing spin density wave order (45; 97; 19; 103). In addition, Figure 3g shows the transient complex conductivity $\sigma_1(\omega, \Delta t_{pp})$ of the supercurrent-carrying state at time delays $\Delta t_{pp}$=-10–1000ps and

4.1 K with $E_{1THz}$ =109 kV/cm. The gapless $\sigma_1(\omega)$ with finite superfluid density still persists after $\Delta t_{pp}$=100ps, which again indicates a long-lived moving condensate well after the pulse. The superfluid momentum diminishes only after long, technologically relevant, nanosecond timescales, e.g., 750ps and 1000ps traces vs. -10 ps one (red shade), consistent with a persistent current with lifetime in the ns range.

## Gauge-invariant nonequilibrium density matrix simulations

To explore the pathways for nonlinear dynamics of a supercurrent-carrying coherent state, we solved the gauge-invariant density matrix nonlinear equations of motion outlined in the supplementary. These describe the interplay between Anderson pseudospin nonlinearity and SC quantum transport driven by lightwave acceleration. In this way, we describe the "initial condition" created by coherent time evolution (few ps) due to strong coupling of electromagnetic fields and its dependence on the driving pulse temporal profile. For this we extend previous studies of HHG and nonlinear photocurrent coherent control in non-superconducting systems (104; 105), as well as previous treatments of quantum transport effects in SCs (101; **?** ). Here we neglect the effects of non–thermal coupling to the martensitic order in order to focus on the most critical elements, i.e. THz light-induced condensate flow $\mathbf{p}_s(t)$ and spatial modulation of SC pairing. Figure 4a shows a slightly asymmetric sub–gap pump pulse $\mathbf{E}(t)$ with central $\hbar\omega_{pump}$=4.1 meV, which drives the time-dependent superfluid momentum $\mathbf{p}_s(t)$ shown in Figure 4b, corresponding to rapidly oscillating Cooper pair CM momentum. The latter determines the light–induced phase of the SC order parameter, whose amplitude $\Delta_{SC}(t)$,characterizing SC coherence and $n_s$, is shown in Fig 4c. While $\Delta_{SC}(t)$ decreases with $E_{THz}$, for finite $\mathbf{p}_s$ this coherence quench is more gradual than the closing of the QP excitation energy gap $E^{QP}_{min}$, shown in Figure 4d. This result is in qualitative agreement with the experimental findings in Figs. 3a-3b and demonstrates that the THz sub–gap pulse can drive non-adiabatically a gapless SC quantum phase with average $\Delta_{SC}$ >0 and $E^{QP}$ =0 only at certain $\mathbf{k}$–points.

With lightwave acceleration, we find three different regimes controlled by the pulse. For the lowest two pump fluences shown (purple and blue lines), both $\Delta_{SC}$ and $E_{min}^{QP}$ are finite after the pulse. While a gapless state is driven non-adiabatically during the pulse, the system does not stay there for low fields. With increasing $E_{THz}$, a transition to a gapless superfluid state, with $\Delta_{SC} > 0$ and $\mathrm{E}^{QP}$ =0, is observed after the pulse (green curve), consistent with the experiment. For very strong photoexcitation (pink curve), the system reaches a gapless QP state with $\Delta_{SC} = 0, E^{QP} = 0$, where the macroscopic coherence also vanishes. Figs. 4e-4g summarize the three different regimes, I–III, after the pulse, which create different initial conditions for delayed time evolution controlled by $E_{THz}(t)$. Figure 4e plots the field dependence of the supercurrent momentum $\mathbf{p}_s$ after the pulse and compares between symmetric (green curve) and slightly asymmetric (blue curve) effective pulse shapes. The acceleration of the Cooper pairs and odd-order HH nonlinearities critically depend on the THz pulse shape, not just its intensity (Figure 1f). We also compare the field dependence of $\Delta_{SC}$ (Figure 4f) and $E_{min}^{QP}$ (Figure 4g) after the pulse between the full gauge–invariant nonlinear theory with (green curve) or without (blue curve) $\mathbf{p}_s(t)$ after the pulse and the linearized (LPS) (black curve) or fully nonlinear (red curve) Anderson pseudo–spin models used before. The latter assume zero—momentum pairing ($\mathbf{k} \uparrow, -\mathbf{k} \downarrow$) and give $E_{min}^{QP} = \Delta_{SC}$. At high $\mathrm{E}_{THz}$, the fully nonlinear (red curve) pseudo–spin model predicts a gapless quantum state with $\Delta_{SC} \to 0$ (red curve). Unlike in our experiment, however, such gapless state has conductivity identical to that of the normal state (37). A symmetric pulse profile (green curves) gives $p_s(t) \neq 0$ only during the pulse. This approximation produces similar results to the nonlinear pseudospin model, but for much smaller $E_{THz}$, i.e. displays enhanced nonlinearity. Most intriguingly, light–induced gapless SC can be driven and controlled by a slightly asymmetric, effective pulse shape (blue curve). We obtain the required combination observed in the experiment after the pulse, $\mathbf{p_s} \neq 0$, $\Delta_{SC} > 0$, and $E_{min}^{QP} = 0$, for a range of $E_{THz}$ (shaded area, regime II), marked by two red arrows that highlight the different vanishing of $E_{min}^{QP}$ and $\Delta_{SC}$ for finite $p_s$.

## Conclusion

Our findings establish lightwave acceleration of supercurrents as a dynamical symmetry breaking principle for discovery of collective modes and emergent materials phases such as gapless superconductivity. We identify the important role of interference among various quantum pathways induced by subcycle nonlinear photocurrents and pairing interactions that are controllable by phase-locked THz pulse excitations.

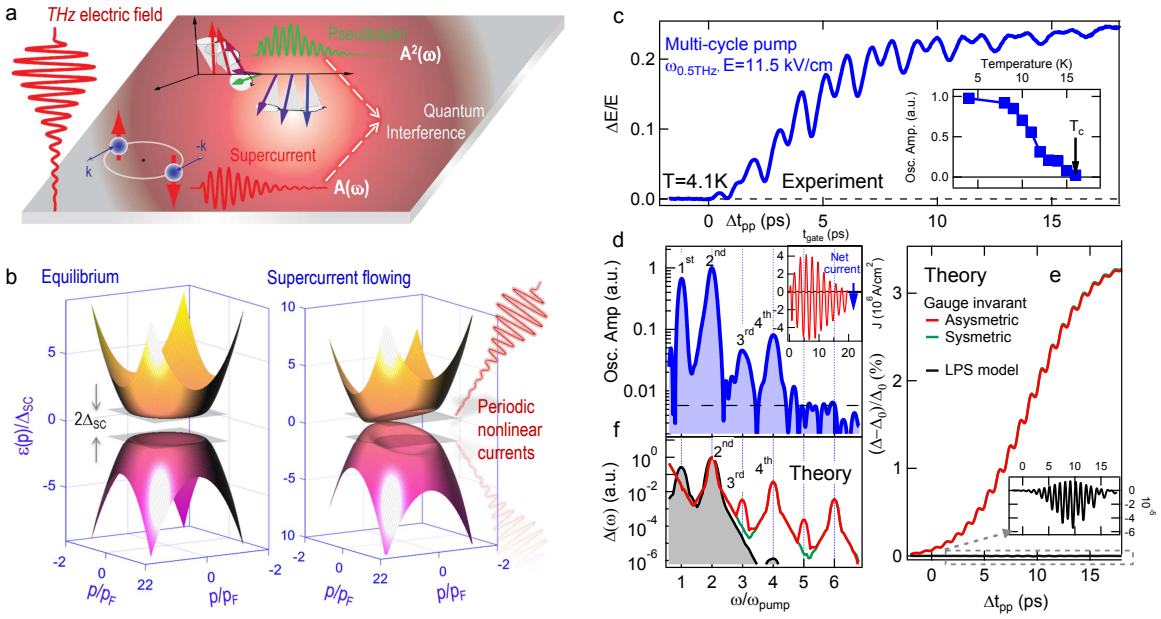


Figure 6.1 **Figure 6.1 Pseudo–spin coherent oscillations forbidden by the equilibrium symmetry and strong HHG nonlinearities.** (a) Experimental schematics. Quantum dynamics of Anderson pseudo–spins (arrows) in a *supercurrent–carrying* macroscopic state with time-dependent CM momentum pairing induced by an intense multi-cycle THz driving electric field. (b) QP energy dispersion of the fully-gapped equilibrium state (left) and the gapless current-carrying state with critical condensate flow $v_s \sim 3.15 \times 10^4$cm/s along x axis (right) in our $Nb_3Sn$ sample. Note that $\Delta_{SC}/E_F$ =0.4, instead of 0.002 in $Nb_3Sn$, is used to better visualize the partial gap closing (supplementary). (c) Pump induced change $\Delta E/E$ for narrow-band driving field centered at 0.5 THz (2.1 meV) shows pronounced quantum beats. Inset to (c): Oscillation amplitudes vanish at the critical temperature. (d) Quantum beat pump–probe experimental spectra showing PSO modes at 2 $\omega_{\rm pump}$, $3\omega_{\rm pump}$, $4\omega_{\rm pump}$, and THz–driven supercurrent at $\omega_{\rm pump}$, whose amplitudes are plotted in log scale to highlight the higher–order PSO harmonics. Inset: Simulated net supercurrent, marked by an arrow, produced by a multi-cycle THz pulse as in the experiment (a)-(b), driving a circuit model (supplementary). Simulated order parameter dynamics in time (e) and frequency (f) domains, obtained by using the gauge-invariant quantum kinetic theory summarized in the supplementary, with asymmetric (red) and symmetric (green) effective input THz pulses, and the LPS model (black). The amplitude of the forbidden $3\omega$ peak is enhanced by increasing asymmetric THz driving, while even PSO harmonics are less sensitive to this.

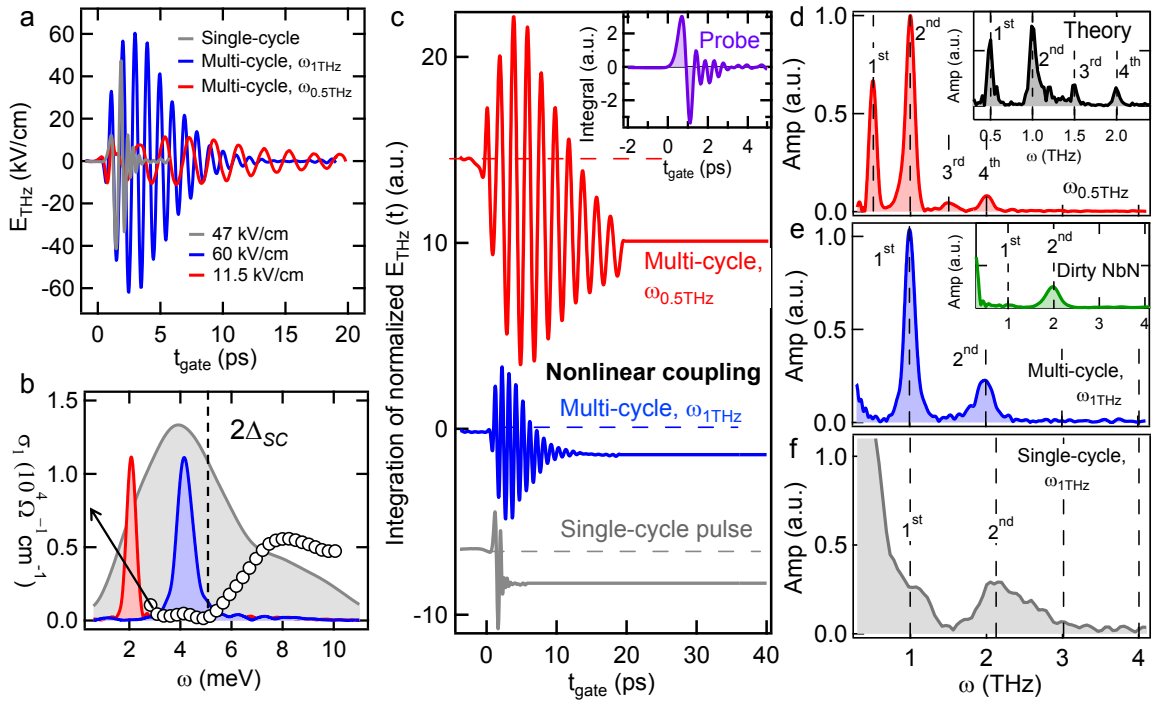


Figure 6.2 **Figure 6.2 Light–Driven Gapless Superconductivity.** (a) Three different THz temporal waveforms $E_{pump}(t)$ measured inside a nonlinear crystal: single–cycle pulse centered at 1 THz (gray) and multi-cycle pulses centered at 0.5 THz (red) and 1 THz (blue). Their spectra $E_{pump}(t)$ are plotted in (b) and compared to the static $\sigma_1(\omega)$ (empty circles) at 4.1K. (c) Effective THz field nonlinear coupling by integration $\int_{-\infty}^{t} d\tau \, \mathbf{E}_{eff}(\tau)$ using the normalized THz pump pulses measured inside a nonlinear crystal shows different tilting and oscillation cycles. Inset: integral of THz probe pulse. (d)-(f) Quantum beating spectra of experimentally measured coherent THz pump-probe dynamics of the supercurrent-carrying quantum state under the three different THz driving fields shown in (a). Even and odd order collective modes are marked by dashed lines. Inset to (d): The pump-probe spectrum, obtained from the simulated coherent $\Delta E/E$ dynamics using the multi-cycle 0.5 THz pump waveform in (a) (red line), exhibits collective modes fully consistent with the experiment (supplementary, Fig. S6). Inset to (e): PSO spectrum of a dirty limit NbN SC sample at 4.1K driven by the multi-cycle 1THz pulse in (a) (blue line) exhibits negligible supercurrent peak at the driving frequency.

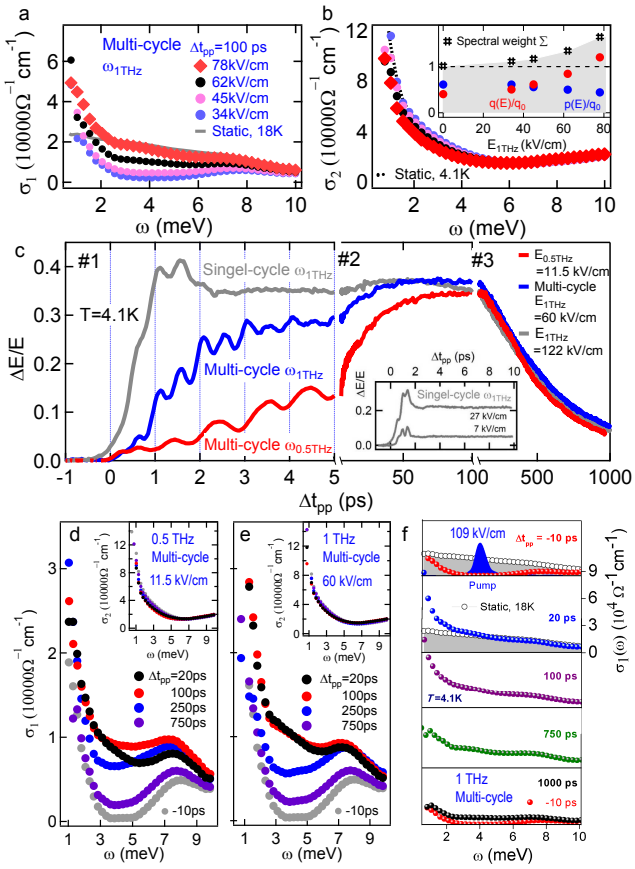


Figure 6.3 **Figure 6.3 Light–driven gapless superconductivity by non-thermal control of the supercurrent-carrying quantum states.** Real (a) and imaginary (b) parts of the THz-driven transient state conductivity spectra $\sigma_1(\omega)$ and $\sigma_2(\omega)$ at $\Delta t_{pp}$=100ps as function of driving field, compared to the static SC state at 4.1K (gray solid line) and the normal state (gray dash line) at 18K. Inset to (b): the QP density $q$ (red circles) was extracted by integrating $\sigma_1(\omega)$ spectral weight (SW) and the condensate density $p$ (blue circles) from the low–frequency divergence in $\sigma_2(\omega)$. $q_0$ denotes the normal state QP SW. $\Sigma$=$q/q_0 + p/q_0$ (black symbol) is larger than its normal state value of 1, which indicates a pump-induced extra SW inside the gap. (c) Temporal dynamics of $\Delta E/E$ under three different driving fields: multi-cycle 0.5 THz (red) and 1 THz (blue) and single-cycle (gray) pump centered at 1 THz. Inset: $\Delta E/E$ dynamics driven by single-cycle THz pump at E field 7kV/cm and 27kV/cm. (d) and (e): Post-driving $\sigma_1$ and $\sigma_2$ (insets) spectra at pump-probe delays from -10ps to 750ps in (c) for multi-cycle 0.5 THz (d) and 1 THz (e) pumping. The observed small change in $\sigma_2$ indicates that $\Delta E$ originates from the large pump induced change in $\sigma_1$, which arises from filling of the QP excitation energy gap due to long-lived supercurrent flow with finite order parameter and *minimal* quenching of condensate density. (f) Transient state conductivity spectra $\sigma_1(\omega)$ at $\Delta t_{pp}$ from -10ps to 1000ps under multi-cycle 1 THz pump with 109kV/cm peak electric field at 4.1K.

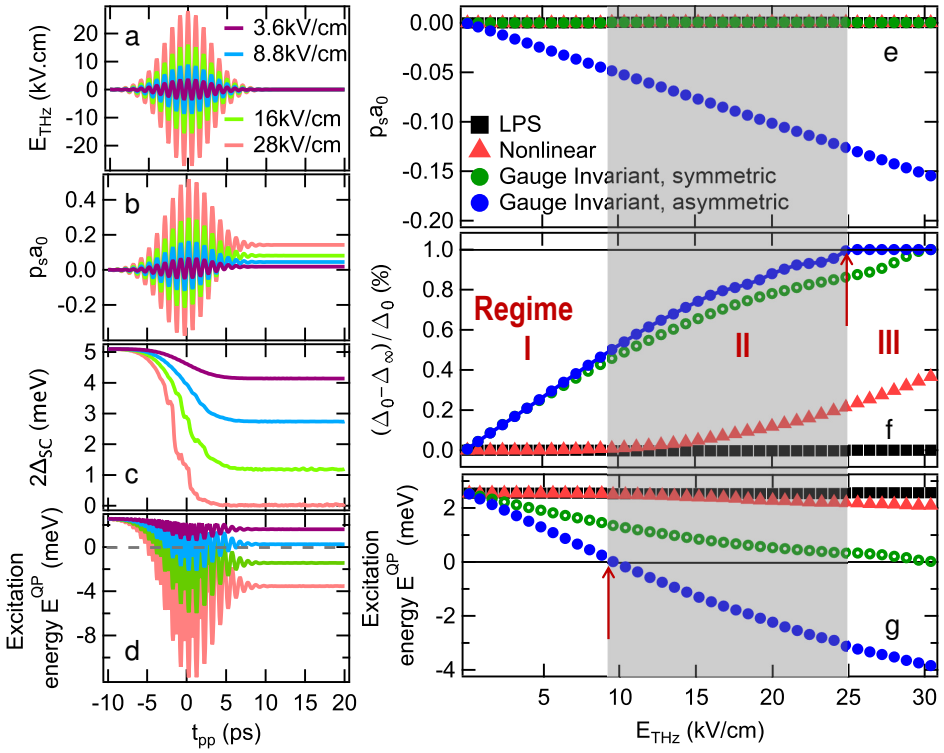


Figure 6.4 **Figure 6.4 Gauge-invariant quantum kinetic calculation of the density matrix for the periodically driven, supercurrent-carrying macroscopic state.** (a) The asymmetric THz waveform with peak E fields ranging from 3.6kV/cm to 28kV/cm centered at 1THz used in the theory simulation. (b)-(d) Temporal dynamics of condensate momentum $p_s a_0$ ($a_0$ denotes the lattice constant), SC order parameter $2\Delta_{SC}$ and excitation energy $E^{QP}$ calculated for the THz waveform in (a). (e)-(g) compare the simulation results for the state after the pulse obtained for the linear (black rectangle) and nonlinear (red triangle) Anderson pseudospin model to those using the full theory with symmetric (green circles) and asymmetric (blue circles) THz pump. The latter shows excellent agreement with the experimental results and allows access to three different regimes marked by red arrows by increasing the driving field: partial quench of $\Delta_{SC}$ and $E^{QP}$, gapless SC state with $\Delta_{SC} \neq 0$ and $E^{QP} = 0$, and gapless QP coherent state without SC.

# CHAPTER 7. FUTURE PLANS

The original motivation for my PhD study is to explore phase competition and quantum criticality in iron pnictide superconductors. Due to some technical issues, a simpler, more traditional BCS superconductor $Nb_3Sn$ becomes focus of my thesis (67; 97; 159; 150). Phase competition physics of s-wave superconductor $Nb_3Sn$ under resonant intense THz photo-excitation turns out to be a more complicated and intriguing problem than we expected. Single-cycle THz pump here, as a non-thermal, non-adiabatic quenching in analogy to parameter quench in cold atoms, serves as an ideal tool to explore quantum mechanism and quantum control of SC.

In addition to SC, we achieved an ultrafast non-thermal control of competing Martensitic transition by intense, single-cycle Terahertz (THz) pulses. It is manifested as light-induced, transient conductivity decrease due to a depletion of spectral weight near the Fermi surface $E_F$ that directly corresponds to the removal of $\Gamma_{12}$ band degeneracy. Such dynamic band splitting, indicative of enhancement of the Martensitic instability, is absent for high energy, thermal photoexcitations and persists up to a critical temperature at 100K, twice as large as the Martensitic transition $T_M$=48K in unexcited $Nb_3Sn$ samples. Together with first principle calculation, we attribute the transient increase in $T_M$ to the efficient THz tunning of the electronic states near $E_F$ and strong electron-phonon interaction, which gives rise to a photo-induced correlation gap and collective ordering above $T_M$.

We have obtained preliminary results from optimal doped $Ba(Fe_{1-x}Co_x)_2As_2$ film. Similar to $Nb_3Sn$, spin density wave competes with SC in iron pnictide compound. Again, we observe coherent peak builds up at low frequency when condensate is completely quenched, which proves the generality of our observation in Chapter 3. Anderson pseudo spin precession is excited under narrow band THz wave. Its amplitude is much more damped due to a dirty limit sample. A thorough study of iron pinctide SC at various doping would be an interesting topic in the future.

Ultrafast Terahertz pump-Terahertz (THz) probe spectroscopy also reveals very fast formation of electron-hole droplets (EHDs) in narrow band semiconductor InSb. Single cycle THz pulse non-thermally accelerates electron from valance to conduction band via impact ionization and inter-valley scattering, which forms long-lived indirect excitons. Above threshold density, THz induced excitons dissociate into electrons and holes, aggregate and form droplet state due to increased inter-exciton Coulomb interaction. EHDs state is characterized by enhanced THz conductivity, redshift exitonic peak and broad surface plasmon oscillation mode. Strikingly, formation time of THz induced EHDs state is one order of magnitude shorter than previous reports by optical photoexcitation above the bandgap.

In topological insulator $Bi_2Se_3$, we demonstrate the suppression of surface-to-bulk scattering by non-perturbatively driving coherent lattice vibrations above threshold electric field of a single-cycle, near resonant terahertz (THz) pulse (155). The distinct spectral-temporal characteristics obtained by a THz pump and THz probe method in $Bi_2Se_3$ reveals a marked crossover transition in the fluence-dependent, surface transport lifetime at the same threshold, absent in the bulk. This, together with theoretical simulation, identifies the unique role of spin-orbit interaction that reduces the phase space in the bulk bands available for scattering with Dirac fermions. Harnessing THz vibrational coherence demonstrated here provides a fundamental insight into the coherence-enabled, in additional to symmetry protected, quantum transport mechanisms, and imply their control for unprecedented topological and photonic functionalities and devices.

Previous paper has reported bandgap oscillation in perovskite organic semiconductor under THz radiation. With much higher E field strength in our setup, we observe THz driven quantum beats, symmetry controlled excitonic fine structure, and room temperature polaron coherence via a non-linear interaction process (156). It would be interesting to study the unique intense THz excitation of exciton in single-walled carbon nanotube (157) and Dirac carriers in single layer graphene. Second harmonic generation is used to analyze material symmetry of magnetic film samples (158).

# REFERENCES

[1] Rulliere, Claude. Femtosecond laser pulses. Springer Science+ Business Media, Incorporated, 2005.

[2] Spectra-Physics Millennia, Spitfire Ultrafast Laser Manual

[3] Lee, Yun-Shik. Principles of terahertz science and technology. Vol. 170. Springer Science and Business Media, 2009.

[4] Kampfrath, T., Tanaka, K. & Nelson, K.A. Resonant and nonresonant control over matter and light by intense terahertz transients, *Nat. Photonics* **7**, 680-690 (2013).

[5] Wikipedia, The Free Encyclopedia. Wikipedia, The Free Encyclopedia, 5 Jan. 2019. Web. 19 Jan. 2019.

[6] A. Velten, D. Wu, A. Jarabo, B. Masia, C. Barsi, C. Joshi, E. Lawson, M. Bawendi, D. Gutierrez, and R. Raskar, Femto-photography: capturing and visualizing the propagation of light. ACM Transactions on Graphics (ToG), 32(4), p.44 (2013)

[7] H. Hirori, A. Doi, F. Blanchard,and K. Tanaka. Single-cycle terahertz pulses with amplitudes exceeding 1 MV/cm generated by optical rectification in LiNbO 3. Applied Physics Letters, 98(9), p.091106 (2011).

[8] Matsunaga, R. & Shimano, R. Nonequilibrium BCS state dynamics induced by intense terahertz pulses in a superconducting NbN film. *Phys. Rev. Lett.* **109**, 187002 (2012).

[9] M. Born, E. Wolf, Principles of optics. Elsevier, (2013).

[10] M. Tinkham. Introduction to superconductivity. Courier Corporation, (2004).

[11] C. Kittel. Introduction to solid state physics. Vol. 8. New York: Wiley, (1976).

[12] Neil W. Ashcroft, and N. David Mermin. Solid state physics. Saunders college, Philadelphia, (1976).

[13] M. Dressel, and G. Grüner. Electrodynamics of solids: optical properties of electrons in matter (2002).

[14] Aoki, H. *et al.* Nonequilibrium dynamical mean-field theory and its applications. *Rev. Mod. Phys.* **86**, 779 (2014) and references therein.

[15] Langen, T. *et al.* Experimental observation of a generalized Gibbs ensemble. *Science* **348**, 207-211 (2015).

[16] Barankov, R. A. & Levitov, L. S. Synchronization in the BCS pairing dynamics as a critical phenomenon. *Phys. Rev. Lett.* **96**, 230403 (2006).

[17] Torchinsky, D. H. *et al.* Fluctuating charge-density waves in a cuprate superconductor. *Nat. Mater.* **12**, 387-391 (2013).

[18] Li, T. *et al.* Femtosecond switching of magnetism via strongly correlated spin-charge quantum excitations. *Nature* **496**, 69-73 (2013).

[19] Patz, A. *et al.* Ultrafast Observation of Critical Nematic Fluctuations and Giant Magnetoelastic Coupling in Iron Pnictides. *Nat. Commun.* **5**, 3229 (2014).

[20] Porer, M. *et al.* Non-thermal separation of electronic and structural orders in a persisting charge density wave. *Nat. Mater.* **13**, 857-861 (2014).

[21] Zhang, J. *et al.* Cooperative photoinduced metastable phase control in strained manganite films. *Nat. Mater.* **15**, 956-960 (2016).

[22] Matsunaga, R. *et al.* Higgs amplitude mode in the bcs superconductors $Nb_{1-x}Ti_xN$ induced by terahertz pulse excitation. *Phys. Rev. Lett.* **111**, 057002 (2013).

[23] Matsunaga, R. *et al.* Light-induced collective pseudospin precession resonating with Higgs mode in a superconductor. *Science* **345**, 1145-1149 (2014).

[24] Dienst, A. *et al.* Bi-directional ultrafast electric-field gating of interlayer charge transport in a cuprate superconductor. *Nat. Photonics.* **5**, 485-488 (2011).

[25] Fausti, D. *et al.* Light-Induced Superconductivity in a Stripe-Ordered Cuprate. *Science* **331**, 189-192 (2011).

[26] Broun, D.M., What lies beneath the dome? *Nature Physics* **4**, 170 (2008).

[27] Liu, M. *et al.* Terahertz-field-induced insulator-to-metal transition in vanadium dioxide metamaterial. *Nature* **487**, 345-348 (2012).

[28] Beck, M. *et al.* Transient increase of the energy gap of superconducting NbN thin films excited by resonant narrow-band terahertz pulses. *Phys. Rev. Lett.* **110**, 267003 (2013).

[29] Shirane, G. and Axe, J. D. Neutron Scattering Study of the Lattice-Dynamical Phase Transition in $Nb_3Sn$, *Phys. Rev. B* **4**, 2957 (1971).

[30] Bilbro, G. & McMillan, W. L. Theoretical model of superconductivity and the martensitic transformation in *A*15 compounds. *Phys. Rev. B* **14**, 1887-1892 (1976).

[31] Markiewicz, R. S. A survey of the Van Hove scenario for High Tc superconductivity with special emphasis on pseudogaps and striped phases. *J. Phys. Chem. Solids* **58**, 1179-1310 (1997).

[32] Escudero, R. & Morale, F. Point contact spectroscopy of Nb3Sn crystals: Evidence of a CDW gap related to the martensitic transition. *Solid State Commun* **150**, 715-719 (2010).

[33] Bhatt, R. N. Microscopic theory of the martensitic transition in A-15 compounds based on a three-dimensional band structure, *Phys. Rev. B* **16**, 1915-1932 (1977); Bhatt, R. N. and Lee, P. A., *Phys. Rev. B* **16**, 4288 (1977).

[34] Weber, W. & Mattheiss, L. F. Electronic structure of tetragonal $Nb_3Sn$. *Phys. Rev. B* **25**, 2270-2284 (1982) abd references therein.

[35] Sadigh, B. and Ozolins, V. Structural instability and electronic excitations in $Nb_3Sn$, *Phys. Rev. B* **57**, 2793 (1997).

[36] Owen, C. S. & Scalapino, D. J. Superconducting State under the Influence of External Dynamic Pair Breaking. *Phys. Rev. Lett.* **28**, 1559-1561 (1972).

[37] Chou, Y. Z. *et al.* Twisting Anderson pseudospins with light: Quench dynamics in terahertz-pumped BCS superconductors. *Phys. Rev. B* **95**, 104507 (2017).

[38] Stojchevska, L. *et al.* Ultrafast switching to a stable hidden topologically protected quantum state in an electronic crystal. *Science* **344**, 177-180 (2014).

[39] Lingos, P. C., Wang, J., and Perakis, I. E., Manipulating femtosecond spin-orbit torques with laser pulse sequences to control magnetic memory states and ringing, *Phys. Rev. B* **91**, 195203 (2015).

[40] Papenkort, T., Axt, V. M. & Kuhn, T. Coherent dynamics and pump-probe spectra of BCS superconductors. *Phys. Rev. B* **76**, 224522 (2007).

[41] Schnyder, Andreas P., Manske, Dirk, and Avella, Adolfo, Resonant generation of coherent phonons in a superconductor by ultrafast optical pump pulses, *Phys. Rev. B* **84**, 214513 (2011)

[42] Fernandes, R. M. & Schmalian, J. Transfer of optical spectral weight in magnetically ordered superconductors. *Phys. Rev. B* **82**, 014520 (2010).

[99] Moor, A., Volkov, P. A., Volkov, A. F. & Efetov, K. B. Dynamics of order parameters near stationary states in superconductors with a charge-density wave. *Phys. Rev. B* **90**, 024511 (2014).

[44] Yuzbashyan, E. A. & Dzero, M. Dynamical vanishing of the order parameter in a fermionic condensate. *Phys. Rev. Let.* **96**, 230404 (2006).

[45] Dzero, M., Khodas, M. & Levchenko, A. Amplitude modes and dynamic coexistence of competing orders in multicomponent superconductors. *Phys. Rev. B* **91**, 214505 (2015).

[46] M. Porer, *et al.* Non-thermal separation of electronic and structural orders in a persisting charge density wave, Nat. Mater. **13**, 857 (2014)

[47] M. Kataoka, Superconductivity and structural phase transition in A15 compounds. Journal of Physics C: Solid State Physics, **19**, 2939-2962 (1986).

[48] B. Sadigh and V. Ozoliņš, Structural instability and electronic excitations in $Nb_3Sn$. Phys. Rev. B **57**, 2793 (1998).

[49] J. K. Freericks, A. Y. Liu, A. Quandt, and J. Geerk, Nonconstant electronic density of states tunneling inversion for A15 superconductors: $Nb_3Sn$. Phys. Rev. B **65**, 224510 (2002).

[50] R. S. Markiewicz, A survey of the Van Hove scenario for high-Tc superconductivity with special emphasis on pseudogaps and striped phases. J Phys. Chem. Solids, **58**, 1179 (1997)

[51] T. Ekino, A. M. Gabovich, A. Sugimoto, Y. Sakai and J. Akimitsu, Superconductors–New Developments (DOI: 10.5772/58655), Chapter **4**, 55-72 (2015).

[52] T. P. Devereaux and R. Hackl, Inelastic light scattering from correlated electrons. Rev. Mod. Phys. **79**, 175 (pg. 202-205) (2007)

[53] J. Demsar *et al.*, Pair-Breaking and Superconducting State Recovery Dynamics in $MgB_2$ *Phys. Rev. Lett.* **91**, 267002 (2003).

[54] M. Beck *et al.* Energy-gap dynamics of superconducting NbN thin films studied by time-resolved terahertz spectroscopy. Phys. Rev. Lett. **107**, 177007 (2011).

[55] C. Giannetti *et al.* Ultrafast optical spectroscopy of strongly correlated materials and high-temperature superconductors: a non-equilibrium approach. Adv. in Phys., **65**, 58 (2016).

[56] M. Beyer *et al.* Photoinduced melting of superconductivity in the high- Tc superconductor $La_{2-x}Sr_xCuO_4$ probed by time-resolved optical and terahertz techniques. Phys. Rev. B., **84**, 019902 (2011).

[57] T. Mori, *et al.* Optical self-energy of superconducting Pb in the terahertz region. Physical Review B, **77** (17), 174515 (2008).

[58] V. V. Kabanov, J. Demsar, and D. Mihailovic, Kinetics of a superconductor excited with a femtosecond optical pulse. Phys. Rev. Lett. **95**, 147002 (2005).

[59] A. Rothwarf and B. N. Taylor, Measurement of recombination lifetimes in superconductors. Phys. Rev. Lett. **19**, 27 (1967).

[60] J. S. Kim, G. N. Tam, and G. R. Stewart, Universal scaling law for the condensation energy across a broad range of superconductor classes. Phys. Rev. B **92**, 224509 (2015).

[61] R. Zhang, P. Gao, X. Wang, and Y. Zhou, First-principles study on elastic and superconducting properties of $Nb_3Sn$ and $Nb_3Al$ under hydrostatic pressure. AIP Advances **5**, 107233 (2015).

[62] H. M. TuTuncu, G. P. Srivastava, S. Bagci, and S. Duman, Theoretical examination of whether phonon dispersion in $Nb_3Sn$ is anomalous. Phys. Rev. B **74**, 212506 (2006).

[63] E. L. Wolf et al., Tunneling and the electron-phonon-coupled superconductivity of $Nb_3$ Sn. Phys. Rev. B **22**, 1214 (1980).

[64] C. Geibel, H. Rietschel, A. Junod, M. Pelizzone, and J. Muller, Electronic properties, phonon densities of states and superconductivity in $Nb_{1-x}V_xN$. J. Phys. F **15**, 405 (1985).

[65] J. Kortus *et al.* Superconductivity of metallic boron in $MgB_2$. Phys. Rev. Lett. **86**.20, 4656 (2001).

[66] B. Z. Xu and S. P. Beckman, Quantum confinement induced band gaps in MgB2 nanosheets. 2D Mater. **3**.3, 031003 (2016).

[67] X. Yang, *et al.*, Terahertz-light quantum tuning of a metastable emergent phase hidden by superconductivity. Nature Materials, 17(7), p.586. (2018).

[68] Y. Kamihara, T. Watanabe, M. Hirano, and H. Hosono, Iron-based layered superconductor $LaO_{1-x}F_xFeAs$ (x= 0.05 0.12) with $T_c$= 26 K. J. Am. Chem. Soc. **130**, 3296 (2008).

[69] P. C. Canfield and S. L. Bud, Annu. FeAs-based superconductivity: a case study of the effects of transition metal doping on BaFe2As2. Rev. Condens. Phys **1**.1, 27-50 (2010).

[70] C. Giannetti, M. Capone, D. Fausti, M. Fabrizio, F. Parmigiani, and D. Mihailovic, Ultrafast optical spectroscopy of strongly correlated materials and high-temperature superconductors: a non-equilibrium approach. Advances in Physics **65**(2), pp.58-238. (2016).

[71] Mertelj, T., *et.al.*, Phys. Rev. Lett., **102**, 117002 (2009); Chia, E. E. M. *et.al.*, Phys. Rev. Lett., **104**, 027003 (2010); Torchinsky, *et.al.*, Phys. Rev. Lett., **105**, 027005 (2010).

[72] K. W. Kim, *et al.*, Ultrafast transient generation of spin-density-wave order in the normal state of BaFe 2 As 2 driven by coherent lattice vibrations. Nature Mat. **11**, 497 (2012).

[73] N. Ni, *et al.*, Effects of Co substitution on thermodynamic and transport properties and anisotropic $Hc_2$ in $Ba(Fe_{1-x}Co_x)_2As_2$ single crystals, Phys. Rev. B **78**, 214515 (2008).

[74] S. Nandi, *et al.*, Anomalous Suppression of the Orthorhombic Lattice Distortion in Superconducting $Ba(Fe_{1-x}Co_x)_2As_2$ Single Crystals. Phys. Rev. Lett. **104** (5), 057006 (2010).

[75] M. Kira and S. W. Koch. *Semiconductor Quantum Optics.* Cambridge University Press, 1st edition, (2011);

[86] K. Siantidis, V. M. Axt, and T. Kuhn. Dynamics of exciton formation for near band-gap excitations. Phys. Rev. B **65**, 035303 (2001).

[77] L. Luo, I. Chatzakis, A. Patz, and J. Wang, Ultrafast terahertz probes of interacting dark excitons in chirality-specific semiconducting single-walled carbon nanotubes. Phys. Rev. Lett. **114**,107402 (2015).

[78] L. Luo, *et.al.*, Broadband terahertz generation from metamaterials. Nat. Commun. **5**, 3055 (2014).

[79] I. Chatzakis, *et.al.*, Reversible modulation and ultrafast dynamics of terahertz resonances in strongly photoexcited metamaterials. Phys. Rev. B **86**, 125110 (2012).

[80] R. M. Fernandes and J. Schmalian, Competing order and nature of the pairing state in the iron pnictides. Phys. Rev. B **82**.1 014521 (2010).

[81] A. Bardasis and J. R. Schrieffer, Excitons and plasmons in superconductors. Phys. Rev. **121**, 1050 (1961).

[82] A. B. Vorontsov, M. G. Vavilov, and A. V. Chubukov, Superconductivity and spin-density waves in multiband metals. Phys. Rev. B **81**(17), p.174538. (2010).

[83] P. Nozieres and S, Schmitt-Rink, Bose condensation in an attractive fermion gas: From weak to strong coupling superconductivity. J. Low Temp. Phys. **59**, 195 (1985).

[84] H. W. Wyld and B. D. Fried, Quantum mechanical kinetic equations. Ann. Phys. **23**, 374 (1963).

[85] M. Mootz, M. Kira, and S. W. Koch, Pair-excitation energetics of highly correlated many-body states. New Journal of Physics **15**, 093040 (2013).

[86] K. Siantidis, V. M. Axt, and T. Kuhn. Dynamics of exciton formation for near band-gap excitations. Phys. Rev. B **65**, 035303 (2001).

[87] Rajasekaran, S. et al. Probing optically silent superfluid stripes in cuprates. *Science* **359**, 575 (2018).

[88] Nakamura, S. et al. Infrared activation of Higgs mode by supercurrent injection in a superconductor NbN. *arXiv* **1809**.10335 (2018)

[89] Cea, T. et al. Polarization dependence of the third-harmonic generation in multiband superconductors. *Phys. Rev. B* **97**.9, 094516 (2018).

[90] Mansarta, B. et al. Coupling of a high-energy excitation to superconducting quasiparticles in a cuprate from coherent charge fluctuation spectroscopy. *PNAS* **110**, 4539 (2018).

[91] Matsunaga, R. et al. Polarization-resolved terahertz third-harmonic generation in a single-crystal superconductor NbN: dominance of the Higgs mode beyond the BCS approximation. *Phys. Rev. B* **96**.2 020505 (2017).

[92] Giorgianni, F., Cea, T., Vicario, C., Hauri, C. P., Withanage, W. K., et al., Leggett mode controlled by light pulses, *Nat. Phys.* **110**, 267003 (2013).

[93] David Pekker and C.M. Varma, Amplitude/Higgs Modes in Condensed Matter Physics, *Annu. Rev. Condens. Matter Phys.* **6**, 269 (2015).

[94] Kozlov, V. et al. Generation of unipolar pulses from nonunipolar optical pulses in a nonlinear medium. *Phys. Rev. A* **84**, 023818 (2011)

[95] Anthore, A. et.al. Density of states in a superconductor carrying a supercurrent. *Phys. Rev. Let.* **90**.12 127001 (2003).

[96] Ruan, W. et al. Visualization of the periodic modulation of Cooper pairing in a cuprate superconductor. *Nature Physics* **1** (2018).

[97] Yang, X., et al. "Ultrafast nonthermal terahertz electrodynamics and possible quantum energy transfer in the Nb 3 Sn superconductor." Physical Review B **99**.9 094504 (2019).

[98] Semenov, A. V. et al. Coherent Excited States in Superconductors due to a Microwave Field. *Phys. Rev. Lett.* **117**, 047002 (2016).

[99] Moor, A. et al. Amplitude Higgs Mode and Admittance in Superconductors with a Moving Condensate. *Phys. Rev. Lett.* **118** 047001 (2017).

[100] Hansen, E.B. Infinite conductivity of ordinary and gapless superconductors. *Physica* **39**.2 271-292 (1968).

[101] M. J. Stephen, Transport Equations for Superconductors, *Phys. Rev.* **139**, A197 (1965).

[102] Yang, X. et al. Non-equilibrium pair breaking in $Ba(Fe_{1-x}Co_x)_2As_2$ superconductors:evidence for formation of photo-induced excitonic spin-density-wave state, *Phys. Rev. Lett.* **121**(26), p.267001 (2018).

[103] Patz, A. et al. Critical Speeding-up of non-equilibrium electronic relaxation near Nematic phase transition in unstrained $Ba(Fe_{1-x}Co_x)_2As_2$. *Phys. Rev. B* **95**, 165122 (2017)

[104] Reimann, J. *et al.* Subcycle observation of lightwave-driven Dirac currents in a topological surface band. *Nature*, in press (2018)

[105] Langer, F. et al. Lightwave valleytronics in a monolayer of tungsten diselenide. *Nature* **76** 557.7703 (2018).

[106] L. P. Gor'kov, Theory of the properties of superconductors with a *beta*-W structure. Inst. of Theoretical Physics, Moscow, **65**, 1658 (1973)

[107] R. N. Bhatt, and W. L. McMillan. Landau theory of the martensitic transition in A—15 compounds. Phys. Rev. B, **14**, 1007 (1976)

[108] G. Bilbro, and W. L. McMillan, Theoretical model of superconductivity and the martensitic transformation in A 15 compounds. Phys. Rev. B, **14**, 1887 (1976)

[109] R. N. Bhatt, Microscopic theory of the martensitic transition in A—15 compounds based on a three-dimensional band structure. Phys. Rev. B, **16**, 1915 (1977)

[110] M. Kataoka, Theory of the structural phase transition in A 15 compounds. Phys. Rev. B, **28**, 2800 (1983)

[111] B. Sadigh, and V. Ozoliņs. Structural instability and electronic excitations in $Nb_3Sn$ Phys. Rev. B, **57**, 2793 (1998)

[112] H. M. Tutuncu, G. P. Srivastava, S. Bagci, and S. Duman. Theoretical examination of whether phonon dispersion in Nb 3 Sn is anomalous. Phys. Rev. B **74**, 212506 (2006).

[113] A. T. Van Kessel, H. W. Myron, and F. M. Mueller. Electronic Structure of $Nb_3Sn$ Phys. Rev. Lett. **41**, 3. 181 (1978).

[114] L.F. Mattheiss, and W. Weber. Electronic structure of cubic V 3 Si and $Nb_3Sn$. Phys. Rev. B, **25**, 2248 (1982)

[115] P. E. Blochl, Projector augmented-wave method. Phys. Rev. B **50**, 17953 (1994)

[116] Greger, M., Kollar, M. & Vollhardt, D. Isosbestic Points: Theory and Applications *Phys. Rev. B* **87**, 195140 (2013) and references therein.

[117] Kindt, J. T. & Schmuttenmaer, C. A. Theory for determination of the low-frequency time-dependent response function in liquids using time-resolved terahertz pulse spectroscopy. *J. Chem. Phys.* **110**, 8589 (1999).

[118] Orenstein, J. & Dodge, J. S. Terahertz time-domain spectroscopy of transient metallic and superconducting states *Phys. Rev. B* **92**, 134507 (2015) and references therein.

[119] Kurihara, Y. Mixed collective modes in coexisting state of charge (spin) density wave and superconductivity. *Journal of the Physical Society of Japan* **52**, 542-548 (1983).

[120] K. Saha and I. Garate, Theory of bulk-surface coupling in topological insulator films. Phys. Rev. B **90**, 245418 (2014).

[121] C. X. Liu, X. L. Qi, H. J. Zhang, X. Dai, Z. Fang, and S. C. Zhang, Model Hamiltonian for topological insulators. Phys. Rev. B **82**, 045122 (2010).

[122] A. Togo and I. Tanaka, First principles phonon calculations in materials science. Scr. Mater. **108**, 1-5 (2015).

[123] G. Kresse and J. Furthmuller, Comput. Mater. Sci. **6**, 15 (1996).

[124] G. Kresse and J. Furthmuller, Efficient iterative schemes for ab initio total-energy calculations using a plane-wave basis set. Phys. Rev. B **54**, 11169 (1996).

[125] J. P. Perdew, K. Burke, and M. Ernzerhof, Generalized gradient approximation made simple. Phys. Rev. Lett. **77**, 3865 (1996).

[126] HJ Monkhorst , JD Pack. Special points for Brillouin-zone integrations. Physical review B. **15**; 13(12):5188 (1976).

[127] D. C. Mattis, , and J. Bardeen. Theory of the anomalous skin effect in normal and superconducting metals. Physical Review **111.2** (1958): 412.

[128] J. Demsar, *et al.* Photoinduced conductivity dynamics studies of MgB 2 thin films. International Journal of Modern Physics B. 17(18n20):3675-81 (2003).

[129] M Porer, *et al.* Non-thermal separation of electronic and structural orders in a persisting charge density wave. Nature materials, 13(9), p.857 (2014)

[130] M. Perpeet, *et al.* High-quality Nb 3 Sn thin films on sapphire prepared by tin vapor diffusion. Journal of applied physics, 82(10), 5021-5023 (1997).

[131] R. Kaindl, *et al.* Far-infrared optical conductivity gap in superconducting MgB 2 films. Physical review letters, 88(2), p.027003 (2001).

[132] S. A. Kuzmichev, T. E. Kuzmicheva, S. N. Tchesnokov, Determination of the electron-phonon coupling constants from the experimental temperature dependences of superconducting gaps in MgB 2. JETP Letters 99, 295 (2014).

[133] I. Mazin, V. P. Antropov, Electronic structure, electron–phonon coupling, and multiband effects in MgB2. Physica C: Superconductivity. Physica C **385**, 49 (2003).

[134] W. Weber, Lattice dynamics of transition-metal carbides. Phys. Rev. B 8, 5082 (1973).

[135] U. Haufe, G. Kerker, and K. H. Bennemann, Calculation of the superconducting transition temperature Tc for metals with phonon-anomalies. Solid State Commun. **17**, 321 (1975).

[136] J. Kortus, I. I. Mazin, K. D. Belashchenko, V. P. Antropov, and L. L. Boyer, Superconductivity of metallic boron in $MgB_2$. Phys. Rev. Lett. **86**(20), 4656 (2001).

[137] B. Z. Xu and S. P. Beckman, Quantum confinement induced band gaps in $MgB_2$ nanosheets. 2D Materials, 3(3), 031003 (2016)

[138] S. L. Budko, G. Lapertot, C. Petrovic, C. E. Cunningham, N. Anderson, and P. C. Canfield, Boron isotope effect in superconducting $MgB_2$. Phys. Rev. Lett. **86**(9), 1877 (2001).

[139] X. J. Chen, V. V. Struzhkin, S. Kung, H. K. Mao, and R. J. Hemley, Pressure-induced phonon frequency shifts in transition-metal nitrides. Phys. Rev. B **70**(1), 014501 (2004).

[140] L. J. Vieland and A. W. Wicklund, Specific heat of niobium-tin. Phys. Rev. **166**, 424 (1968).

[141] A. Junod, T. Jarlborg, and J. Muller, Heat-capacity analysis of a large number of A 15-type compounds. Phys. Rev. B 27, 1568 (1983).

[142] N. Barisic, *et al.* Electrodynamics of electron-doped iron pnictide superconductors: Normal-state properties. Physical Review B **82**.5 054518 (2010).

[143] A. Akbari, A. P. Schnyder, D. Manske, and I. Eremin, Theory of nonequilibrium dynamics of multiband superconductors. Europhysics Lett. **101**, 17002 (2013).

[144] P. M. R. Brydon and C. Timm, Spin excitations in the excitonic spin-density-wave state of the iron pnictides. Phys. Rev. B **80**(17), 1 (2009).

[145] B. Cheng, Anomalous gap-edge dissipation in disordered superconductors on the brink of localization. Physical Review B, **93**(18), p.180511 (2016).

[146] N. Harrison, et al. de Haas–van Alphen effect in the vortex state of $Nb_3Sn$. Physical Review B 50.6 (1994): 4208 (1994).

[147] Gurevich A. Theory of RF superconductivity for resonant cavities. Superconductor Science and Technology. 30(3):034004 (2017).

[148] Orlando TP, McNiff Jr EJ, Foner S, Beasley MR. Pauli limiting and the possibility of spin fluctuations in the A 15 superconductors. Physical Review Letters, 46(24), p.1598. (1981)

[149] G.W. Cullen, G. D. Cody, and J. P. McEvoy Jr. Field and angular dependence of critical currents in $Nb_3Sn$. Physical Review 132(2), p.577 (1963).

[150] Cui, T., *et al.* Impact of damping on superconducting gap oscillations induced by intense Terahertz pulses. arXiv preprint arXiv:1802.09711 (2019).

[151] Yu, T., & Wu, M. Gauge-invariant theory of quasiparticle and condensate dynamics in response to terahertz optical pulses in superconducting semiconductor quantum wells. I. s-wave superconductivity in the weak spin-orbit coupling limit. *Phys. Rev. B* **96**.15: 155311(2017).

[152] Nambu, Y., Quasi-particles and gauge invariance in the theory of superconductivity. *Physical Review* **648** 117.3 (1960).

[153] Stephen, M. J. Transport equations for superconductors. *Physical Review* **139**.1A A197 (1965).

[154] Tsuji, N. & Aoki, H. Theory of Anderson pseudospin resonance with Higgs mode in superconductors. *Phys. Rev. B* **92**.6 064508 (2015).

[155] Luo, L.,*et al.* "Ultrafast manipulation of topologically enhanced surface transport driven by mid-infrared and terahertz pulses in $Bi_2Se_3$." Nature communications 10.1 607 (2019).

[156] Liu, Z., *et al.* Single-Cycle Terahertz Driven Quantum Beats Reveal Symmetry-Selective Control of Excitonic Fine Structure in Perovskite. arXiv preprint arXiv:1905.12373 (2019).

[157] Luo, L., *et al.*. Anomalous variations of spectral linewidth in internal excitonic quantum transitions of ultrafast resonantly excited single-walled carbon nanotubes. Physical Review Materials, 3(2), p.026003 (2019).

[158] Herklotz, Andreas, et al. "Designing Morphotropic Phase Composition in BiFeO3." Nano letters (2019).

[159] X. Yang, *et al.* Lightwave-driven gapless superconductivity and forbidden quantum beats by terahertz symmetry breaking. Nature Photonics, 01 July (2019).

# APPENDIX A. ADDITIONAL MATERIALS: CHAPTER 3

## A.1 Two-time THz pump and THz probe spectroscopy of complex conductivity

Terahertz (THz) response functions such as the complex conductivity $\tilde{\sigma} = \sigma_1(\omega) + i\sigma_2(\omega)$ can be used to characterize the fundamental properties of correlated electronic states. They allow access to some key properties, e.g., the lifetime of low–frequency electronic excitations, scattering rates, electron–phonon and electron–impurity mass renormalization, and complex optical self-energy. The two-time THz pump and THz probe spectroscopy technique used here is a versatile tool for measuring the THz response functions both in– and out–of–equilibrium without excessive heating. We characterize the nonequilibrium post-quench states by measuring the complex conductivity $(\sigma_1(\omega, \Delta t_{pp}),\ \sigma_2(\omega, \Delta t_{pp}))$ as a function of pump-probe delay $\Delta t_{pp}$, as illustrated in Figure A.1. In this way we access electronic correlation and fluctuations in the post-quantum-quench states.

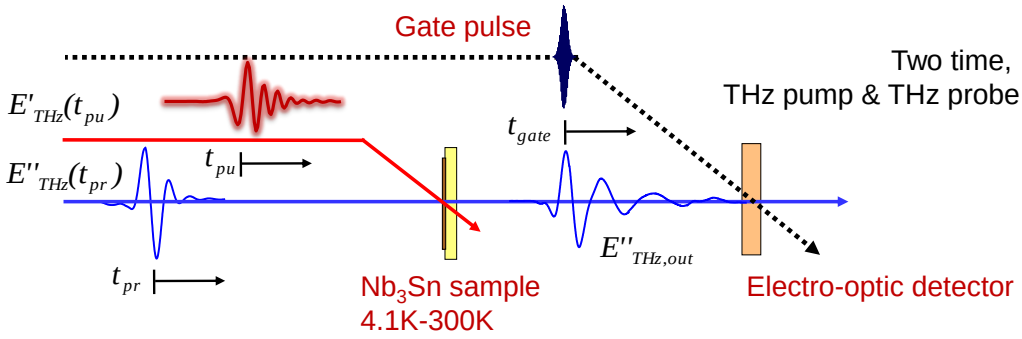


Figure A.1 A schematic of two-time, THz pump and THz probe spectroscopy of a $Nb_3Sn$ superconductor.

More subtleties of this type of analysis can be found in the literature, e.g., see Ref (118). One widely accepted conclusion relevant for this work is that the procedure used here is reliable for

describing out-of-equilibrium states and dynamics that last longer than the scattering time, i.e., $\Delta t_{pp} > \tau$. This applies well in our observation of the persisting quantum state.

## A.2 Thermodynamic properties and more characterizations of our sample

The equilibrium electrodynamic response in the vicinity of the SC gaps is obtained by time-domain THz spectroscopy shown in Figure 3.1(D) and (E) in the main text. Both the equilibrium gap size $\Delta_{SC}$ and the superfluid density $n_0$ are obtained from these THz spectra, shown as insets, and reduce to zero as the temperature approaches $T_c$. Specifically, the equilibrium 4.1 K traces exhibit a large, $1/\omega$ response in $\sigma_2$, which is a well–recognized feature of the SC condensate resulting from loss-free, yet reactive, bosons, and zero conductivity in $\sigma_1$ below 5.1 meV corresponding to twice the SC gap $\Delta_{SC}$. At the lowest frequencies <3 meV, a finite $\sigma_1$ results from intraband absorption of the thermally excited Bogoliubons, $|1,0\rangle$ and $|0,1\rangle$, of electron and hole excitations dressed by the BCS coherence $|\psi_{SC}\rangle$ of Cooper pairs $|1,1\rangle$. The above spectral shapes change in the normal state, as seen in the 16 K traces, in both $\sigma_2(\omega)$, which gradually decreases at low frequency, and in $\sigma_1(\omega)$, which shows zero gap. The equilibrium conductivity characterizes the relatively long mean field path, comparable to the coherent length, $l/\xi = \pi\tau\Delta_{SC}/\hbar \sim 1$, which is far from the dirty limit studied in previous THz experiments, as discussed in details in Section A6.

## A.3 Effective medium theory calculations

The observed, prethermalized quantum state is also well-distinguished from thermally mixed states (phase separation) as demonstrated in Figure A.3(A)-(B). For example, prior THz studies of dirty-limit BCS samples (8), using lower quench field than used here, identified a spatially mixed phase with finite superfluid density, which is in contrast to the conductivity of our measured full quench regime. For example, $\sigma_2(\omega)$ is entirely below the normal state spectra, as shown in the 446kV trace in Figure A.3 (solid red diamonds) and Figure 3.2(B) (#5 − #6). These is not expected for a statistical mixture of SC and normal state conductivities. Another significant difference lies in the $\sigma_1(\omega)$ spectra of our prethermalized quantum state (solid red diamonds, Figure A.3(A)),

which exceed the normal state spectra above $T_c$ near the Fermi surface (gray rectangles) and, thereby, result in ~10% of spectral weight in the range of 0-10 meV. This distinction highlights deviations from the prior experimental observations, which shows the similar spectral weight as normal state (8), and from predictions by the BCS quench model, which shows similar $\sigma_1(\omega)$ line shape as the normal state (37). Specifically, Figure A.3(A) and S3B presents an effective medium calculation (EMT) of the dielectric response of a spatially inhomogeneous state from phase separated patches consist of SC and normal states. Since the equilibrium conductivity of our cleaner sample cannot be described by the Mattis-Bardeen (MB) model used in prior studies of dirty limit superconductors (8; 28) we adopt the measured dielectric responses at the two boundaries, i.e., SC (gray circles) and normal states (gray rectangles), using the measured data in Figure 3.1(D) and (E). The EMT calculates the effective dielectric response of materials by evaluating the contribution from two composites that are spatially separated, e.g. the SC state and the normal state in type II superconductors. Assuming that the non-equilibrium state is a result of spatial inhomogeneity, the optical response should satisfy:

$$f\frac{\sigma_N(\omega)-\sigma_{eff}(\omega)}{g\sigma_N(\omega)+(1-g)\sigma_{eff}(\omega)}+(1-f)\frac{\sigma_S(\omega)-\sigma_{eff}(\omega)}{g\sigma_S(\omega)+(1-g)\sigma_{eff}(\omega)}=0 \tag{A.1}$$

where $\sigma_N(\omega)$, $\sigma_S(\omega)$ are the static conductivities of normal state (18K) and SC state (4K). The coefficient f describes the volume fraction of normal state in superconductor and g is the depolarization factor determined by the shape of the hot spots, which we assume to be 0.5. The coefficient f in post-quench phase is chosen to be 0.1 (pink circles), 0.5 (green circles) and 0.9 (blue circles). We emphasize two key differences between such spatially mixed states and the prethermalized quantum phase observed here. First, the additional coherent peaks in $\sigma_1(\omega)$ and the larger spectral weight $S(\omega)=\int \sigma_1 d\omega$ near the Fermi surface as compared to the thermalized states cannot be accounted for the sharp low frequency features and smaller $S(\omega)$ found for the mixed states (solid circles, Figure A.3(A), due to the residual of SC phases. Second, the spatially mixed state description again clearly fails to describe our data due to the requirement of simultaneously fitting both dielectric responses, $\sigma_1(\omega)$ and $\sigma_2(\omega)$. It is clearly visible that the post-quench spectra,

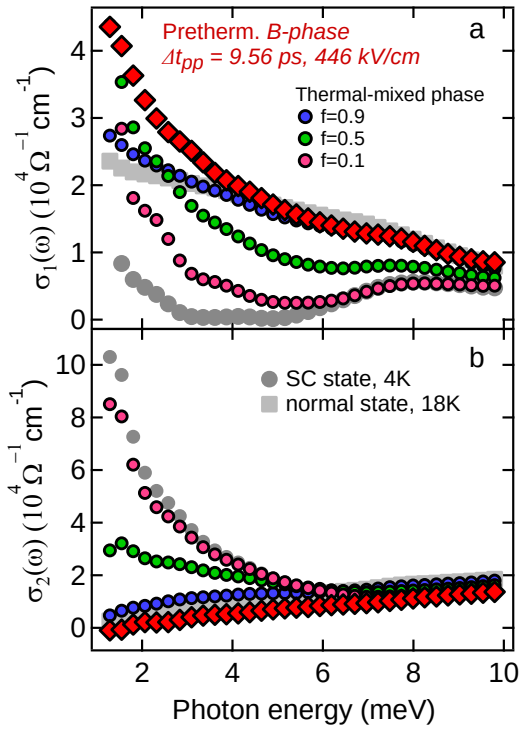


Figure A.2 Simulation of effective THz responses $\sigma_1$ (a) and $\sigma_2$ (b) for a spatially inhomogeneous phase of SC and metallic patches for different values of filling coefficient f=0.1 (pink), 0.5 (green) and 0.9 (blue). Shown together is the behaviors for the pre-thermalized, gapless quantum phase (red diamond) and static optical responses at 4.1K and 18K directly obtained in our measurement (gray diamond).

$\sigma_1(\omega)$ and $\sigma_2(\omega)$, have opposite dependence on parameter f which, in turn, cannot be simultaneously fitted by changing f.

## A.4 Frequency-dependent electric transport

The optical self-energy has been identified to be more effective than $\widetilde{\sigma}(\omega)$ itself for underpinning the exact nature of correlated electronic states. This self–energy can be regarded as a model–independent memory function in analogy to the way in which we analyze many-body interactions in the Green's function approach. Practically, it carries very similar information as the quasi-particle self-energy that is measured by, e.g., photoemission. The key difference is that the

forward electron scattering weights in such "THz" self-energy more than the backward scattering. Figure A.4 presents the complex optical self-energy $\Sigma(\omega, T)$ in terms of both frequency-dependent, momentum scattering rate $1/\tau(\omega)$ and electron-phonon mass renormalization $1+\lambda(\omega)$, which relate to the conductivity imaginary and real parts. These quantities are obtained as follows:

$$\frac{1}{\tau(\omega)} = \frac{\omega_{op}^2}{4\pi} \frac{\sigma_1}{\sigma_1^2 + \sigma_2^2} \tag{A.2}$$

and

$$1 + \lambda_{op}(\omega) = \frac{m_{op}^*(\omega)}{m} = \frac{\omega_{op}^2}{4\pi} \frac{\sigma_1}{\sigma_1^2 + \sigma_2^2} \frac{1}{\omega}. \tag{A.3}$$

Here, the plasma frequency $\omega_p$ is obtained by fitting the normal state conductivity spectra with Drude model, which gives the plasma frequency to be ~6.66eV

The superfluid density is obtained by sum rule:

$$\int_0^{+\infty} (\sigma_1^n(\omega) - \sigma_1^s(\omega))\, d\omega = \frac{\pi}{2} \frac{n_s e^2}{m}. \tag{A.4}$$

The superfluid density $n_s$ obtained from the sum rule agrees well with the extrapolated $\sigma_2^s(\omega)$ in the limit of $\omega \to 0$ in the superconducting state:

$$\frac{n_s(T)}{n} = (\frac{\omega_p^2}{4\pi})^{-1} \lim_{\omega \to 0} \omega \sigma_2. \tag{A.5}$$

Both methods give the number of superfluid over total carriers $n_s/n_0$ to be ~70%.

Next we discuss the results on the optical self-energy of the equilibrium state in Figure A.4(A) and (B). On the one hand, in the SC state, the $1/\tau_{op}(\omega)$ spectra in Figure A.4(B) clearly reveal the SC gap opening, which leads to significantly suppressed momentum scattering rate below $2\Delta_{SC}$ and reduces to zero at 4.1K. In the normal state, the elastic impurity scattering rate $1/\tau_{imp}$ is seen directly from the low frequency spectra, e.g., the 20K traces converge to a frequency– and temperature–independent constant ~7.7 meV smaller than in most noble metals. On the other hand, $m^*(\omega, T)/m_0$, shown in Figure A.4(A), in the SC state as $\omega \to 0$ approaches $n/n_s$, i.e., the ratio between the electron density n in the normal state and the superfluid density $n_s$. For example, $n/n_s(4.1K) = m^*(\omega = 0, 4.1K)/m_0$ ~1.34 indicates that ~75% of the total electrons participate in superfluidity. This is close to the value obtained from the optical sum rule in Eq.(12). Moreover,

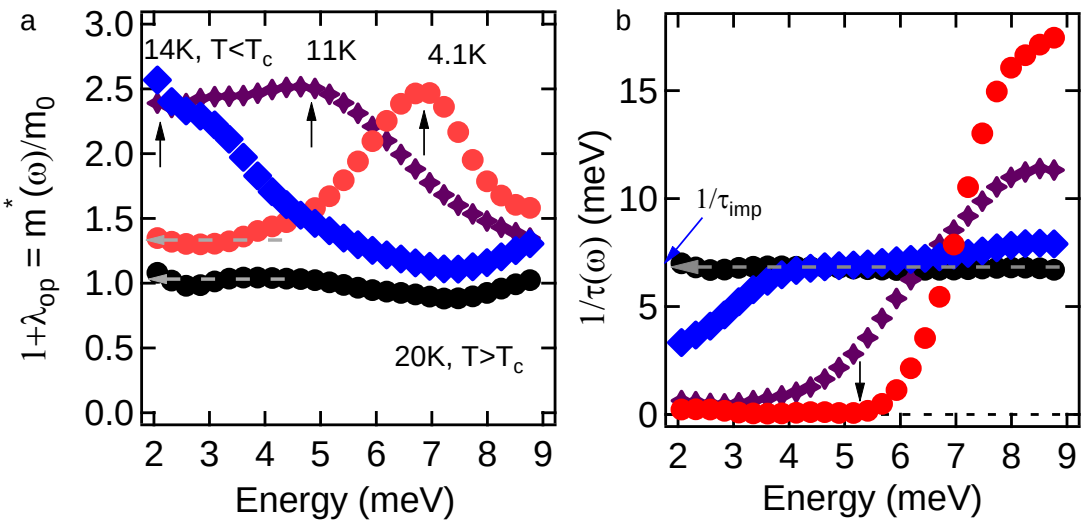


Figure A.3 The complex optical self-energy $\Sigma(\omega, T)$ in terms of both frequency-dependent, mass renormalization (a) $1+\lambda(\omega)$ and momentum scattering rate $1/\tau(\omega)$ (b) for various temperatures, 4K (red circles), 11K (purple star), 14K (blue diamond) and 20K (black circles).

sharp impurity peaks are absent in $1/\tau_{op}(\omega)$ and $1+\lambda(\omega)$ at $2\Delta_{SC}$. Both factors demonstrate much less impurity scattering in our high quality film samples than in those used in prior THz studies of BCS superconductors (28; 8; 22; 23).

The ratio of mean free path and coherent length to be $l/\xi = \pi\tau\Delta/\hbar$ is calculated ~1 in our sample, an order of magnitude larger than in other experiments reported in the literature, again indicative of very high film quality. Moreoever, note that here the complex conductivity and self-energy spectra are not described well by the Mattis-Bardeen formula commonly used for fitting dirty-limit superconductors.

Figure A.5 presents the mass renormalization $1 + \lambda(\omega)$ of the post-quench state for various time delays $\Delta t_{pp}$ of -10ps (green), 12ps (purple), 500ps (gray), 1ns (pink) at $E_{pump} = 620kV/cm$ at 4.1K (A) and 18K (B). They are comparable in size for the post-quench (solid circles) and equilibrium normal states that are more or less frequency independent. This confirms again the unique lineshape of $1/\tau(\omega)$ (Figure 3.2(D)) as a powerful probe of the post-quench quantum state

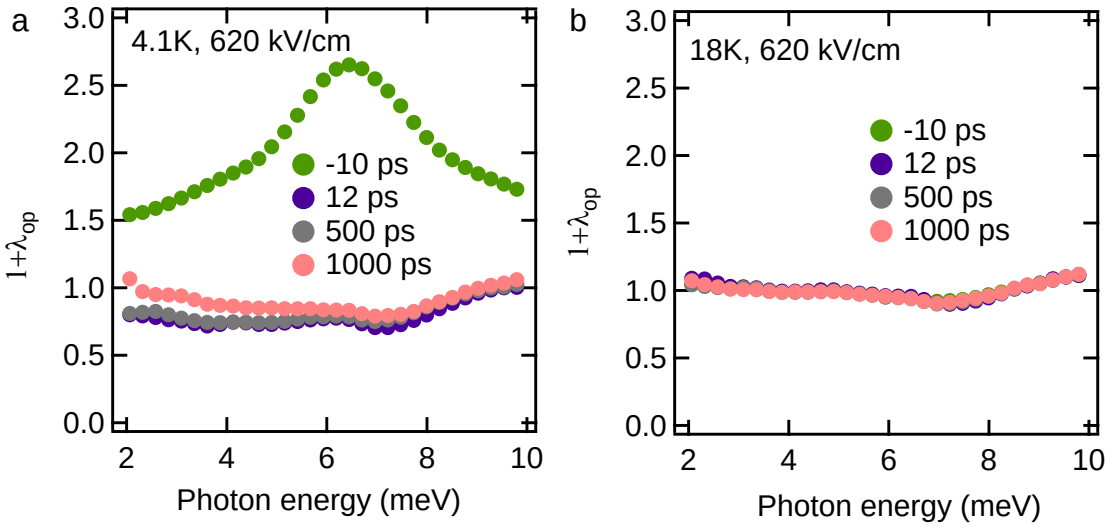


Figure A.4 **a**: Mass renormalization $1 + \lambda(\omega)$ of the post-quench state for various time delays $\Delta t_{pp}$ of -10ps (green), 12ps (purple), 500ps (gray), 1ns (pink) at $E_{pump}$=620kV/cm at 4.1K. **b**: The same spectral-temporal characteristics for the normal state at 18K.

below $T_c$. Moreover, $1 + \lambda(\omega)$ (Figure A.5(A)) shows no relaxation to the ground state even up 1 ns which corroborates of our claim that, at high quench $E_{THz} > E_{th}$, a much longer *many-ns* quasi-steady temporal regime emerges and dominates the energy relaxation and quasi-particle decay within less than 1 ns when close to the equilibrium state (Figure A.5(B)).

## A.5 Theoretical model of gapless conducting state

A strong THz pump pulse tuned close to the SC gap can deplete the SC condensate with minimal heating by exciting low energy quasi–particle populations. The spectral weight of the SC delta–function peak of $\sigma_1$ at $\omega = 0$, proportional to the superfluid density $n_s$, is then transfered to frequencies $0 < \omega \leq \Delta_{SC}$. Since the experiment indicates that the post–quench, prethermalization temporal regime with $\Delta_{SC}(t) = 0$ is characterized by an increase in the spectral weight of this low frequency region as compared to the normal state, this shows that the spectral weight of the condensate peak did not come exclusively from $\omega \leq 2\Delta_{SC}$. While the ultrafast quench of the

BCS SC gap can lead to a gapless state with finite coherence at early times, its conductivity line-shape remains similar to that of the normal state (37), while inelastic processes should lead to fast thermalization to a quasi–equilibrium state. Thus a simple BCS model does not explain the experimental observations. In our $Nb_3Sn$ superconductor studied here, the signatures of charge density wave order, shown in Figure A.2, are consistent with those reported that have been in the literature and may be attributed to three–dimensional Van Hove Singularities and saddle points predicted by bandstructure calculations (31; 33; 34). Therefore, we interpret our experimental results in terms of dynamical coexistence of superconducting, $\Delta_{SC}(t)$, and hidden CDW like order parameters, whose time–dependence is triggered by ultrafast THz quantum quench. For $\Delta_{SC} \ll \Delta_{CDW}$, such excitation will affect the two order parameter components differently, quenching $\Delta_{SC}(t)$ similar to a single–component BCS system while having a smaller effect on the much larger $\Delta_{CDW}(t)$ during very early time scales.

To interpret the experimental results, we use an extension of the one-dimensional electron model introduced by Bilbro and McMillan (30) to a three dimensional anisotropic electron band model. The latter accounts for the three-dimensional Van Hove singularities seen in bandstructure calculations (33; 34). Similar to Ref. (30), our model assumes that the Fermi surface consists of two regions: region 1 corresponds to momenta close to the Van–Hove singularities, where the Fermi surface shows nesting predicted by bandstructure calculations. This region favors the emergence of CDW order, which coexists with the SC order. On the other hand, only formation of SC order is possible in the rest of the Fermi surface, referred to as region 2.

Our model Hamiltonian describing the competition of SC order with CDW order in mean-field approximation is given by (30)

$$H = H_0 + H_{SC} + H_{CDW} + \frac{\Delta_{SC}^2}{V_{SC}} + \frac{\Delta_{CDW}^2}{V_{CDW}}. \tag{A.6}$$

In the above equation, the free Hamiltonian is

$$H_0 = \sum_{\mathbf{k},\sigma} \xi_{\mathbf{k}} c^{\dagger}_{\mathbf{k},\sigma} c_{\mathbf{k},\sigma} \tag{A.7}$$

where the operator $c^{\dagger}_{\mathbf{k},\sigma}$ creates an electron with crystal momentum $\hbar\mathbf{k}$ and spin $\sigma$. For simplicity, we assume that the Fermi surface close to the three-dimensional Van Hove singularities can be described by one hole and one electron pocket separated by wavevector $\mathbf{Q}$ (99). We approximate the dispersion close to the electron and hole pockets as

$$\xi_{\mathbf{k}} = -\xi_{1,0} + \sum_j \frac{\hbar^2 k_j^2}{2\, m_{j,1}} - \mu\,, \quad \xi_{\mathbf{k}+\mathbf{Q}} = \xi_{2,0} - \sum_j \frac{\hbar^2 k_j^2}{2\, m_{j,2}} - \mu \tag{A.8}$$

respectively, with chemical potential $\mu$, band-offsets $\xi_{n,0}$, and effective masses $m_{j,n}$ $(j = x, y, z)$ that depend on the details of the bandstructure. Here we do not consider such bandstructure details but simply point out that electron–hole asymmetry enhances the coexistence of SC with CDW order. The parameters used to introduce such electron–hole asymmetry here were $m_{x,1} = m_{y,1} = m_{z,1} = 1.3m_0$, where $m_0$ is the free electron mass, and $m_{x,2} = m_{y,2} = m_{z,2} = 2.0m_0$, with band-offsets $\xi_{1,0} = 0.095eV$ and $\xi_{2,0} = 0.125eV$ and chemical potential $\mu = 20.0meV$. The results are not very sensitive to this particular choice of parameters. Note that the band–offsets may change following laser excitation, due to non–equilibrium chemical potentials that differ between electron and hole, which leads to photoinduced changes in nesting and CDW correlation. The SC pairing interaction is given by

$$H_{SC} = -\sum_{\mathbf{k},\sigma} \left[\Delta_{SC}\, c^{\dagger}_{\mathbf{k},\uparrow} c^{\dagger}_{-\mathbf{k},\downarrow} + h.c.\right] \tag{A.9}$$

where the SC order parameter is

$$\Delta_{SC} = V_{SC} \sum_{\mathbf{k}} \langle c_{-\mathbf{k},\downarrow} c_{\mathbf{k},\uparrow} \rangle \tag{A.10}$$

and $V_{\mathrm{SC}}$ describes the strength of the interaction. The $\mathbf{k}$-sum includes the set $\mathcal{W}$ of wavevectors $\mathbf{k}$ in regions 1 and 2 with $|\xi_{\mathbf{k}}| \leq \hbar\omega_{\mathrm{C}}$, where $\omega_{\mathrm{C}}$ is the cut-off frequency. The CDW interaction has the form

$$H_{CDW} = -\sum_{\mathbf{k},\sigma} \left[\Delta_{CDW}\, c^{\dagger}_{\mathbf{k},\sigma} c_{\mathbf{k}+\mathbf{Q},\sigma} + h.c.\right] \tag{A.11}$$

where $\Delta_{\mathrm{CDW}}$ is the CDW order parameter with electronic and lattice contributions (119), which are proportional in quasi-equilibrium. Here, the $\mathbf{k}$-sum includes only the wavevectors of region 1.

The last term in Eq. (C.8) includes the lattice elastic energy and $V_{\rm CDW}$ depends on the lattice elastic constant.

We diagonalize the above Hamiltonian using a canonical transformation (30) and calculate the free energy $F =< H > -TS$ assuming a thermal distribution of quasi–particles. The details of the calculation will be given elsewhere. The quasiparticle excitation energies in the absence of perfect nesting are given by

$$E^2_{\pm,1,\mathbf{k}} = \frac{1}{2}\left[2\Delta^2_{SC} + 2\Delta^2_{CDW} + \xi^2_{\mathbf{k}} + \xi^2_{\mathbf{k+Q}} \pm (\xi_{\mathbf{k}} + \xi_{\mathbf{k+Q}})\sqrt{4\,\Delta^2_{CDW} + (\xi_{\mathbf{k}} - \xi_{\mathbf{k+Q}})^2}\right] ,$$

$$E^2_{\pm,2,\mathbf{k}} = \frac{1}{2}\left[2\Delta^2_{SC} + \xi^2_{\mathbf{k}} + \xi^2_{\mathbf{k+Q}} \pm (\xi^2_{\mathbf{k}} - \xi^2_{\mathbf{k+Q}})\right] , \tag{A.12}$$

in region 1 and 2, respectively. The free-energy density, shown in the main text, is given by

$$f(\Delta_{SC}, \Delta_{CDW}) = \frac{\Delta^2_{SC}}{V_{SC}} + \frac{\Delta^2_{CDW}}{V_{CDW}} - 2\,k_B\,T \sum_{\mathbf{k},a,l} log\left[2\,cosh\left(\frac{E_{a,l,\mathbf{k}}}{2\,k_B\,T}\right)\right] , \tag{A.13}$$

Here, the index $a$ describes the two quasi–particle branches $\pm$ at given $\mathbf{k}$ in the case of imperfect nesting, while $\bar{a}$ is defined as $\bar{a} = +$ for $a = -$ and $\bar{a} = -$ for $a = +$. The temperature-dependent energy gap equations follow from $\partial f(\Delta_{\rm SC}, \Delta_{\rm CDW})/\partial\Delta_{\rm SC} = \partial f(\Delta_{\rm SC}, \Delta_{\rm CDW})/\partial\Delta_{\rm CDW} = 0$:

$$\Delta_{\rm SC} = V_{SC} \sum_{\mathbf{k},a,l} \frac{\Delta_{SC}}{E_{a,l,\mathbf{k}}}\, tanh\left(\frac{E_{a,l,\mathbf{k}}}{2\,k_B\,T}\right) ,$$

$$\Delta_{CDW} = V_{CDW} \sum_{\mathbf{k},a} \frac{\Delta_{CDW}(E^2_{a,1,\mathbf{k}} - \Delta^2_{SC} + \xi_{\mathbf{k}}\xi_{\mathbf{k+Q}} - \Delta^2_{CDW})}{E_{a,1,\mathbf{k}}(E^2_{a,1,\mathbf{k}} - E^2_{\bar{a},1,\mathbf{k}})}\, tanh\left(\frac{E_{a,1,\mathbf{k}}}{2\,k_B\,T}\right) . \tag{A.14}$$

where $\Delta_{\rm CDW}$ is determined by $\mathbf{k}$–summation in region 1 and $\Delta_{\rm SC}$ depends on both regions. To compute the order parameters in equilibrium, we self-consistently solved the above coupled gap equations for given temperature $T$.

## A.6 Discussion on conductivity divergent behavior above threshold pumping field of prethermalization state

In this section, we like to make further discussions on the sharp turning up above the threshold (#4, #5 and #6) to a metastable QP phase (related to the feature in coherent $\sigma_1$ peak via

Kramers-Kronig) rather than to a residual condensate as in a SC/normal mixed state. Figure A.5 plots together the $\sigma_2$ of the post-quench states for three E fields below, at, and above the threshold $E_{th}$ (marked as #3, #4 and #5 as shown in the Figure 3.2(b) of the main text) where the prethermalization plateau is observed and the equilibrium $\sigma_2$ at five temperatures ranging from $T = 4K$ to $T = T_c = 16K$. We make our claims mainly based on three different observations:

1. The low frequency kink in $\sigma_2$ (at around 2-3 meV) is indeed present in the partial quench data, e.g., for the E-field #3 which is below $E_{th} = 256kV/cm$. As we pointed out in our previous response, this upturn in $\sigma_2$ is intimately connected to the sharp upturn in $\sigma_1$ at low frequencies (via Kramers-Kronig relation) which we clearly observe in our measured frequency range for such below-threshold fields. Our statement that this kink feature is associated with a metastable non-equilibrium state partially stems from our observation that such a kink frequency dependence of the non-equilibrium conductivity differs notably from the behavior of the equilibrium conductivity (at any temperature). In equilibrium, as shown in Figure 3.1 (full lines), $\sigma_2$ shows a smooth $1/\omega$ upturn towards low frequencies below $T_c$, on top of the broad, vanishing normal state curve (black line) measured at $T_c$=16K. Therefore we are very confident that this salient feature is not due to a simple residual condensate fraction present in part of the sample. This conclusion is further based on our analysis presented in Figure A.3, which excludes an inhomogeneous state with SC and normal regions, as acknowledged by the referee as well.

2. Even more critically, there is clear evidence, directly seen in Figure A.5, that the sharp upturn in the $\sigma_2$ spectra above the threshold, E field #4 and #5, cannot be assigned to the residual condensate either. Let's first focus on the post quench state at the threshold field (#4). $\sigma_2$ for #4 lies entirely below the normal state $\sigma_2$ (black line) down to ~2meV and then clearly shoots up much more dramatically at lower frequency, in a way that is not accounted by a residual condensate coherence at any temperature. For example, compare the above post-quench $\sigma_2$ lineshape with the static/equilibrium $\sigma_2$ (full lines). Although the latter does turn up due to the presence of a partial condensate, this upturn is much less sharp than the non-equilibrium feature towards lower frequency, especially at higher temperatures. For E field #3 below threshold, the low frequency

upturn could be accounted by the static 14K trace in a reasonable way. However, at threshold (#4), $\sigma_2$ exhibits a much sharper turning up below ~2meV as compared to that of the 14K and 15K (or lower T) static traces. Therefore a key conclusion that can safely be drawn from our data here is that the sharp upturn in $\sigma_2$ above the threshold cannot be accounted for by a simple $1/\omega$ increase due to the residual condensate coherence. For #5, our spectral range is not enough to resolve more data points of low frequency upturn, yet the trend is consistent with our argument above.

3. Finally, we want to point out that the metastability of the non-thermal post-quench state (for the strongest E field) follows even more directly from the time traces of $\Delta E/E_0$ presented in Figure 3.3 and does not rely exclusively on the above non-thermal behavior of $\sigma_2$. There, the time decay processes clearly show the emergence of the prethermalization plateau above $E_{th}$ (#4, #5 and #6), which differentiates the metastable QP quantum phase, with a distinctly long recovery, from the partial quench of the condensate, with distinctly shorter recovery times below the threshold. These different results put together clearly show that, even if the metastable state would show a kink feature at frequencies below our spectral detection range, this non-equilibrium state still clearly shows non-thermal decay features beyond equilibrium superconductivity. That's another reason why we attribute the sharp turning up above the threshold (#4, #5 and #6) to a metastable QP phase (related to the feature in coherent $\sigma_1$ peak via Kramers-Kronig) rather than to a residual condensate as in a SC/normal mixed state.

In summary, the main features of the metastable "non-thermal" post-quench state in Figure A.5 (or Figure 3.2 of the main text) and our interpretation are fully consistent. We note that this experimental observation is beyond the well-known phenomenology of a BCS quench scenario (as explained by Barankov, Levitov and others). Thus, our main goal here is to provide the original data that give the evidence for the existence of a metastable state and a first possible consistent description of the salient features that characterize such a state. We are fully aware that this state is worthy of further theoretical investigation that we hope that our manuscript will stimulate this (as pointed out nicely by Referee 2 as well).

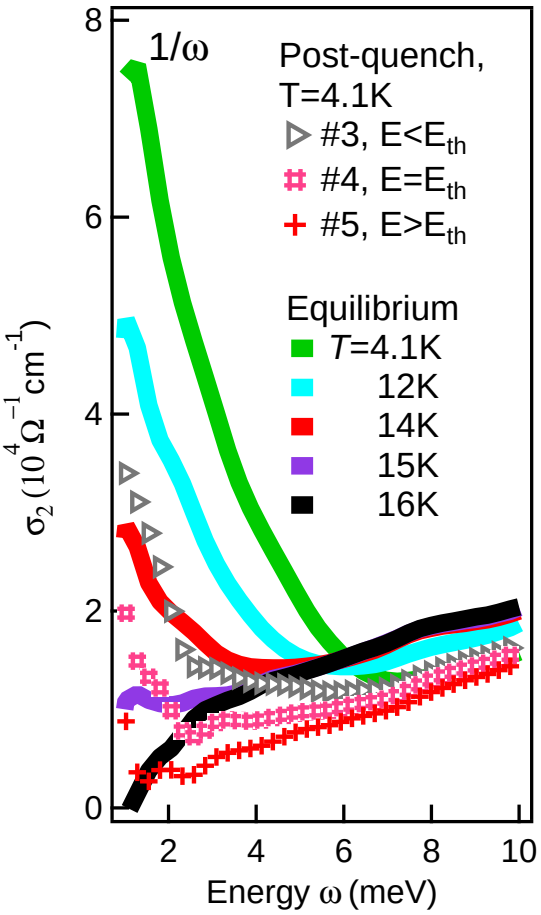


Figure A.5 The $\sigma_2$ of the post-quench states for three E fields below, at, and above the threshold $E_{th}$ (marked as $E_{\#3-\#5}$ as shown in the Figure 3.2b of the main text) and the equilibrium $\sigma_2$ at five temperatures ranging from T=4K to T=$T_c$.

# APPENDIX B. ADDITIONAL MATERIALS: CHAPTER 4

## B.1 Mattis-Bardeen Theorem Fitting

In this section, we simulate the static THz conductivity of $Nb_3Sn$ by Mattis-Bardeen (MB) model (127) used for type I, dirty limit superconductors. It has been used extensively in prior studies and successfully accounts for the measured THz electrodynamics in both $NbN$ (54; 8) and $MgB_2$ (128; 53) superconductors. Given the normal state conductivity $\sigma_1(\omega)$ at 16K, MB model reproduces THz response function of $Nb_3Sn$ at various temperatures plotted in Figure B.1.

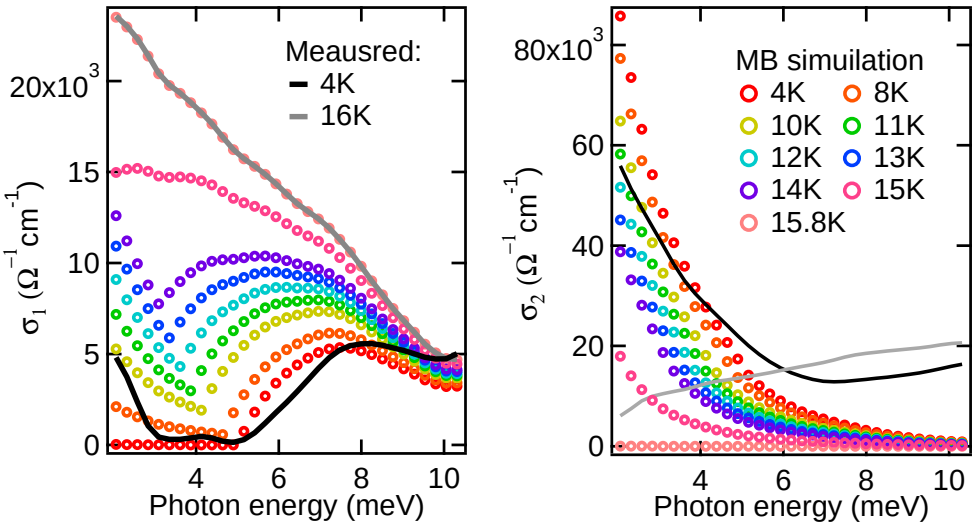


Figure B.1 Temperature dependent THz conductivity $\sigma_1(\omega)$ (left) and $\sigma_2(\omega)$ (right) at 4K, 16K compared to simulation done by Mattis-Bardeen theory

Simulation results present a clear deviation from experiment data in Figure 4.1(b)-(c) (main text). For example, simulated $\sigma_2(\omega)$ is much smaller than measured values at 15.5K, while showing larger divergence at 4K towards zero frequency. This comparison demonstrates that cleanness of superconductor sample is crucial for accounting the measured THz electrodynamics in the vicinity

of SC gap, which differentiates THz electrodynamics of cleaner $Nb_3Sn$ from prior THz results on dirty samples.

On the other hand, cleanness of sample has no influence on theoretical analysis of optical pump-probe dynamics presented here, since the RT model used does not consider electron-impurity scattering and sample cleanness (59; 58). In Table II. we can see that $Nb_3Sn$ is much cleaner than previously studied $NbN$ and $MgB_2$.

## B.2 THz Probing of Martensitic Phase

The correlation gap $\Delta_w$ associated with the Martensitic order inferred from scanning tunneling spectroscopy is ∼80 meV as a CDW-like feature which is out of the spectral window of our setup. There are also several other important reasons that make the Martensitic order relatively "blind" in the low frequency conductivity spectra.

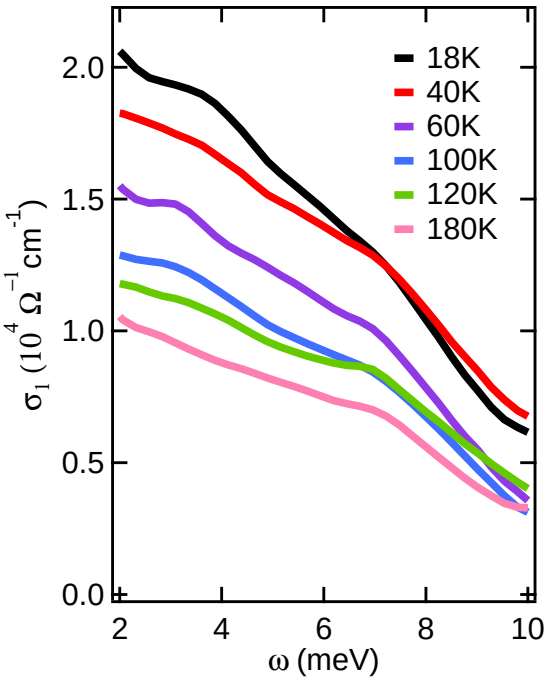


Figure B.2 Static THz conductivity $\sigma_1$ spectrum at temperature above $T_c$ from 18K to 180K.

First, unlike typical density wave orders where a significant spectra weight transfer , from low to high frequency develops in conjunction with establishment of the correlation gap, the Martensitic order represents a very subtle partial gapping of Fermi surface. Our data in Figure 4.2(c) (main text) measures this low frequency conductivity in $Nb_3Sn$ for the first time that allows the determination of a spectra weight change of less than 1% in the range of 1-10 meV. In contrast, materials with density wave orders typically produce more than 100% change which makes them clearly visible in low frequency conductivity, e.g., $TiSe_2$ (CDW) (129) and $BaFe_2As_2$ (SDW) ().

Second, temperature dependence of static optical conductivity in $Nb_3Sn$ is affected by two competing effects at elevated temperature: increased scattering rate and suppressed Martensitic gap $\Delta_w$. As shown in Figure B.2, spectral weight and slope of $\sigma_1(\omega)$ decreases simultaneously as temperature increases. Unfortunately, scattering rate increase is more significant than spectral weight transfer above SC critical temperature $T_c$, which results in a decrease of spectra weight in the 1-10 meV by thermal broadening with increasing lattice temperature, as shown in Figure B.2 . It is worth noting that such a decrease of the spectral weight at elevated temperatures is opposite to the strong density wave materials such as $TiSe_2$ (CDW) and $BaFe_2As_2$ (SDW) that show an increase of the spectral weight. Such thermal effect makes it difficult to underpin the suppression of $\Delta_w$ from the measured, static THz conductivity.

On the flip side, the above-mentioned difficulties show that the pump-probe measurement with superior signal-noise ratio represent a powerful method to probe study subtle change of Martensitic phase with a clear transition temperature at 47K (49; 32; 51; 52). The pump-induced increase of spectral weight indicates a distinct non-thermal ultrafast softening of the correlation gap since laser-induced heating will decrease the spectra weight after the pump. Here we demonstrate the first ultrafast measurement of the Martensitic order and non-thermal melting of its correlation gap by much lower frequency THz probe.

## B.3 Determination of Laser Energy Absorption

In our measurement we calculate 800nm energy absorption by Nb3Sn film at 4K by measuring the fs laser pulse transmission through sample. The pump fluence is set to $4\mu J/cm^2$, same as the saturation fluence in inset of Figure 4.4(C). The experiment data is shown in Table I.

Table B.1 Laser power transmission measurement results.

| **800nm, 35fs pulse** | Total | **Transmission** |
|---|---|---|
| Laser Power | 4mW | 0.451mW |

Since $Nb_3Sn$ film thickness (20nm) is much smaller than penetration depth 64-93nm (148; 130), we can use the following way it to calculate absorbed laser energy ratio. The absorption coefficient of $Nb_3Sn$ is:

$$\alpha = \frac{2}{\delta_0} = \frac{1}{40} nm^{-1} \tag{B.1}$$

by using penetration depth $\delta_0 = 80nm$. According to Lambert-Beer's law:

$$\alpha = -\frac{1}{I}\frac{dI}{dr} \tag{B.2}$$

we can get laser energy transmission through sample as:

$$I_{out}/I_{in} = e^{-\alpha d_s} = 0.61 \tag{B.3}$$

where $d_s = 20nm$ is the sample thickness and $I_{in}$, $I_{out}$ are the laser fluences penetrating in/out from the sample. THe absorbed energy density $I_{abs}$ is:

$$I_{abs}/I_{in} = (I_{in} - I_{out})/I_{out} = 0.64 \tag{B.4}$$

From this ratio, we can calculate energy absorption $P_{abs} = 0.288mW$, which takes up around 7.2% of the total laser energy shining on the sample. Considering double reflection by sapphire substrate, around 90% of absorbed energy is actually from initial laser excitation. Although there are other details to make the accurate determination of energy absorption rate in experiment, like coherent

transmission within film samples, the above estimation is similar to prior references (128) and should be at the same order of accurate values. Since our sample thickness $d_s << \delta_0$, penetration depth can't be determined accurately in experiment. Instead, we measure light transmission and use penetration depth reported in previous references here. It is slightly different from (54), which determines penetration depth of NbN film at thickness $\sim \delta_0$ in experiment.

By assuming uniform excitation within $Nb_3Sn$ film, the average laser absorption energy density at saturation fluence $I_{pump}$ is:

$$\begin{aligned} U_{abs} &= 90\% \times 7.2\% \times I_{pump}/d_s \\ &= 0.1302 J/cm^3 = 5768.8 mJ/mol \end{aligned} \tag{B.5}$$

where $d_s = 20nm$ is the sample thickness. Light energy deposition into sample matches BCS condensation energy $U = 4757 mJ/cm^3$ quite well (60). This corroborates our analysis and the quantum limit energy transfer picture in $Nb_3Sn$ superconductor.

Such measurement also demonstrates that Martensitic phase has ignorable influence on Cooper pair breaking process, since it is greatly suppressed below $T_c$ by the establishment of superconductivity.

## B.4 Determination of Laser Energy Absorption

Here we estimate 800nm energy absorption by $Nb_3Sn$ film by measuring the fs laser pulse transmission and reflection at 4K. Pump fluence is set to $4\mu J/cm^2$, same as the saturation fluence in inset of Fig.4(c) (main text). The experiment data is shown in Table I and the laser reflection, transmission by different surface is shown in Fig. B.3.

Table B.2 Laser power transmission measurement results.

| | Total $I_{total}$ | Transmission $I_t$ | Reflection $I_r$ |
|---|---|---|---|
| Sample | 4.00mW | 0.62mW | 3.06mW |
| Ratio ($/I_{total}$) | | $T = 15.5\%$ | $R = 76.5\%$ |

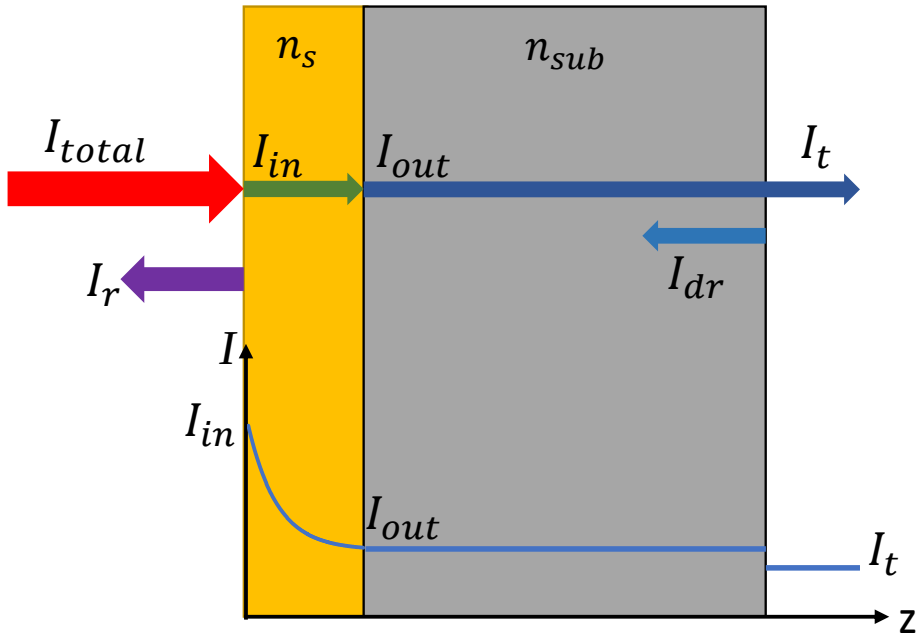


Figure B.3 Laser energy transmission through 20nm $Nb_3Sn$ film on 1mm sapphire substrate. $I_{total}$: total laser fluence used to excite sample; $I_{in}$, $I_{out}$: laser fluence penetrating in and out from the film; $I_r$: film reflection; $I_t$: laser transmission through substrate; $I_{dr}$: double reflection by back surface of substrate.

Substrate transmission ratio is:

$$T_{sub} = \frac{I_t}{I_{out}} = 1 - (\frac{n_{sub} - 1}{n_{sub} + 1})^2 = 92.4\% \tag{B.6}$$

in which optical index of sapphire substrate $n_{sub} = 1.76$ at 800nm. From $T_s$ we can estimate that $I_{dr}/I_{total} = T \cdot (1 - T_{sub})/T_{sub} = 1.27\%$.

It is worth noting that measurement in Table I includes multiply laser reflection from substrate, as shown in the Fig. B.3. To simplify the calculation, we assume all double reflection energy by substrate is completely reabsorbed by sample. Since it only takes only 1.27% of total energy, such assumption has little influence on final results. However, this secondary energy absorption should be excluded from our estimation since "Quantum limit" energy transfer only refers to the initial fs

excitation. Laser transmission from film to substrate is:

$$T_s = I_{out}/I_{total} = T/T_{sub} = 16.8\% \tag{B.7}$$

Laser energy absorption ratio by $Nb_3Sn$ is:

$$A = 1 - \frac{I_r}{I_{total}} - \frac{I_{out}}{I_{total}} = 1 - R - T_s = 6.7\% \tag{B.8}$$

The average laser absorption energy density at saturation fluence $I_{pump}$ is:

$$\begin{aligned} U_{abs} &= 6.7\% \times I_{pump}/d_s \\ &= 0.13467 J/cm^3 = 5967 mJ/mol \end{aligned} \tag{B.9}$$

where $d_s = 20nm$ is the sample thickness. Light energy deposition into sample matches well with BCS condensation energy $U_{BCS} = 4757 mJ/mol$ (60). This analysis is consistent with (54) and corroborates the "Quantum limit" energy transfer process in $Nb_3Sn$ superconductor.

Since sample thickness is much smaller than wavelength, multiply reflections and coherent light propagation have to be considered. From $R$ and $T_s$, we can extract $Nb_3Sn$ complex optical index $n_s$. The penetration depth for 800nm light is:

$$\delta = \frac{c}{\omega \, \mathrm{Im}(n_s)} = 26.7nm \tag{B.10}$$

which is at the same order of values reported in (130; 148).

## B.5 Rothwarf-Taylor Model Analysis

The Cooper pair breaking (CPB) dynamics by high energy photons can be quantitatively analyzed using RT model. Prior experimental studies are summarized in Table II as comparison to our work. The fitting procedure is descried below.

### B.5.1 Step.1: Fitting of the pump-probe dynamics.

In the low photoexcitation limit, the pump-probe signal Q is proportional to the photoexcitation quasi-particle (QP) density n(t) (53; 58) which is described by the RT model:

Table B.3 Comparison of Optical Pump-THz Probe Experiment on $NbN$, $MgB_2$ and $Nb_3Sn$ Superconductor

| **Sample** | $NbN$ (54) | $MgB_2$ (53), (131) | $Nb_3Sn$ |
|---|---|---|---|
| Transport Lifetime | $246cm^{-1}$=22fs | 37meV=18fs | 8.27meV=80fs |
| Photoexcitation Pulse Duration | 50fs | 150fs | 35fs |
| Electron-Phonon Coupling $\lambda$ | 1.1 | 0.7-0.9 | 2 |
| p | ∼9% | ∼6% | ∼0.33% |

$$Q \propto n(t) = \frac{1}{R}[-0.25\beta - \frac{\beta}{2\tau} + \frac{\beta}{\tau}\frac{1}{1 - Kexp(-\frac{t}{\tau/\beta})}] \tag{B.11}$$

The fitting parameters are $\{R, \beta, (\frac{\tau}{\beta})_i, K_i\}$, where $R$ and $\beta$ are the common parameters for all pump fluence, $\frac{\tau}{\beta}$ and $K$ are fluence dependent. Through fitting the pump-probe dynamics at different fluence (Figure 4.4(a)), we can extract $K$ and $\frac{\tau}{\beta}$ as the function of fluence (Figure 4.4(b)-(c)). Meanwhile, in this step, we can obtain $R^* \sim 10^4$ (a constant times R) and $\beta \sim 1.1$.

### B.5.2 Step.2: Fitting of $\frac{\tau}{\beta}$ and $K$ vs. fluence.

The following relations are used in our fitting of $\frac{\tau}{\beta}$ and $K$:

$$\tau^{-1} = \sqrt{\frac{1}{4} + \frac{2R}{\beta}(2N_0 + n_0)} \tag{B.12}$$

$$K = \frac{(\frac{4Rn_0}{\beta} + 1) - 2\tau^{-1}}{(\frac{4Rn_0}{\beta} + 1) + 2\tau^{-1}} \tag{B.13}$$

where $n_0 = p\Omega/\Delta$ and $N_0 = (1-p)\Omega/\Delta$ are initial density of QPs and high frequency phonons (HFP) right after optical pump. p is the portion of photoexcitation energy $\Omega$ that initially goes to QPs.

Here we convert laser fluence $\mu J/cm^2$ to $\mu eV$/unit cell. We know that $Nb_3Sn$ has a cubic $Pm-3n$ structure with 2 formula units in the unit cell and lattice constant $a = 5.28\mathring{A}$. As we discussed above, laser energy absorption matches well with BCS condensation energy in $Nb_3Sn$. We can obtain the conversion relation: $1\mu J/cm^2 \sim 24.531\mu eV/$ unit cell.

The best fit was obtained when $p = 0.2\%$, giving $R = 105$ and $\beta = 1.0$, consistent with the value from the first step. Figure 4.4(d) is plotted in the way that a series of fitting were performed by fixing p and optimizing $R$ and $\beta$. The mean squared error (MSE) represents the difference between fitted values of $K$, $\frac{\tau}{\beta}$ and the targets (i.e. fitting parameters obtained in step 1 and plotted in Figure 4.4 (b) and (c)):

$$MSE = \sum_i \{(K^i_{fit} - K^i_{tar})^2 + [(\frac{\tau}{\beta})^i_{fit} - (\frac{\tau}{\beta})^i_{tar}]^2\} \tag{B.14}$$

Here we briefly discuss about fitting accuracy of RT model. Photoexcitation energy $\Omega$ and SC gap $\Delta$ can be measured in experiment. Since $\tau^{-1}$ and $K$ are fluence dependent parameter as function of $\{R, \beta, N_0, n_0\}$, while $\{N_0, n_0\}$ is calculated from $\{p, \Omega, \Delta\}$, $\tau^{-1}$ and $K$ are ultimately determined by two sets of parameters: fluence independent $\{R, \beta, p\}$ and photoexcitation energy $\Omega$. Since fitted pump-probe dynamics in Fig. 4.4(a) contains hundreds of data points at each fluence, unique set of $\{R, \beta, p\}$ can be obtained at very high accuracy.

### B.5.3 Further discussion on the fitting parameters

To understand the difference in the fitted values of $\beta$ (i.e. CPB probability by adsorption of HFP) and $R$ (i.e. bare QP recombination rate) in different systems, we further computed $\beta/R$ in $MgB_2$, $NbN$ and $Nb_3Sn$ as it has the dimensionality of concentration and can be expressed in terms of material intrinsic properties:

$$\frac{\beta}{R} = \frac{N(0)^2 \pi \omega_D^3}{18 \nu \Delta} \tag{B.15}$$

where $N(0)$ is the electronic density of states (DOS) per unit cell, $\omega_D$ is the Debye energy, $\nu$ is the number of atomes per unit cell, $\Delta$ is the superconducting gap.

The calculated results and other key parameters of different materials ($MgB_2$, $NbN$, and $Nb_3Sn$) are summarized in Table III (Supplementary). Fitted $\beta/R$ shows a decent agreement with calculated values by Eq.(10). We found that $\beta/R$ in $Nb_3Sn$ is much larger (more than 10 times) than the other two systems, which is attributed to the much larger DOS at the Fermi level.

Assuming that the absorbed optical energy exceeds the condensation energy by a factor of 10, this will not change the best value of $p = 0.2\%$ and $\beta = 1.0$ but will give R$\sim$10.5 which produce unphysical result for $\beta/R \sim 0.095$. Therefore this cannot be the correct scenario for Nb3Sn. Such fitting results, together with experiment measurement of laser energy absorption are consistent with previous studies on BCS SCs such as NbN, whose 800nm energy absorption have been shown to match BCS condensation energy quite well. RT model analysis again confirms the "Quanutum-limit" energy transfer in $Nb_3Sn$ superconductor.

The different fitting parameters for $Nb_3Sn$ can be readily observed in pump-probe traces. After fs photoexcitation, $Nb_3Sn$ reaches the saturation QPs density at much shorter time compared to NbN and $MgB_2$. Quantitatively, at optical fluence corresponding to 10% pair breaking, $Nb_3Sn$ takes 4ps to reach the peak of QPs density, an order of magnitude faster than NbN (20ps) (54) and $MgB_2$ (40ps) (53). Such behavior is consistent with the much larger pair breaking probability $\beta$ in $Nb_3Sn$ from fitting.

Table B.4 Comparison of the key parameters among $NbN$, $MgB_2$ and $Nb_3Sn$ Superconductor

| **Sample** | $MgB_2$ (53) | $NbN$ (54) | $Nb_3Sn$ |
|---|---|---|---|
| $T_c$ | $\sim$39K | $\sim$15K | $\sim$16K |
| $\lambda$ | 0.7$\sim$0.9 (132; 133) | 1$\sim$1.2 (134; 135) | 1.8$\pm$0.15 (63) |
| SC gap $\Delta$ | $\Delta_1 = 2.2meV$ $\Delta_2 = 7.2meV$ | $\Delta = 3.07meV$ | $\Delta = 2.55meV$ |
| N(0) (spin cell eV)$^{-1}$ | 0.7 (136; 137) | 0.88 (54) | 11.4 (61) |
| $\omega_D$ | 0.064eV (750K) (138) | 0.31eV(363K) (139) | 0.02eV(230K) (140; 141) |
| p | 6% | 9% | $\sim$0.3% |
| R (ps$^{-1}$ unit cell$^{-1}$) | 100$\pm$30 | 160$\pm$20 | 105$\pm$10 |
| $\beta$ (ps$^{-1}$) | 1/(15$\pm$2) | 1/(6$\pm$1) | 0.99 |
| Rising time | $\sim$40ps | $\sim$20ps | $\sim$4ps |
| $\beta/R$ from fitting (unit cell$^{-1}$) | 0.00067 | 0.001 | 0.0095 |
| $\beta/R$ from eq.(10) (unit cell$^{-1}$) | 0.001 | 0.0007 | 0.0089 |

### B.5.4 Energy absorption influence on the fitting results

The above fitting results is obtained under the condition that laser energy absorption is approximate to BCS condensation energy $\Omega \sim U_{BCS}$. Varying $\Omega$ only modifies the best fitting result of

$R$, while it has no influence on $p = 0.2\%$ and $\beta = 1.0$. Assuming that the optical energy absorption is $\Omega \sim 10U_{BCS}$, this will give R$\sim$10.5 and produces unphysical result for $\beta/R \sim 0.095$, which is 10 times larger than the result given by Eq. 10. Therefore this cannot be the correct scenario for $Nb_3Sn$. On the other hand, $\beta/R$ shows a very good agreement with Eq.10 for $Nb_3Sn$, NbN and $MgB_2$, when 800nm energy absorption matches well with BCS condensation energy. With $p = 0.2\%$ and $\Omega \sim U_{BCS}$, RT model analysis again confirms the "Quantum-limit" energy transfer picture in $Nb_3Sn$ superconductor within fs excitation.

## B.6 "One Photon-One Cooper Pair" Quantum Limit Energy Transfer

The non-equilibrium Cooper pair breaking (CPB) responses in the superconducting state after fs optical excitation may be roughly divided into several temporally overlapping stages: (1) quantum non-thermal regime during the optical pulse photoexcitation less than 10s of fs. This initial temporal regime is not directly resolved experimentally, but sets up the initial condition for the better understood ps dynamics that is directly observed in the present experiment. There is no microscopic theory yet to fully account for this initial regime, which in our A15 system involves coherence and non-thermal populations of both electrons and phonons. Indeed, the optical phonon condensation in the SC ground state below the Martensitic transition temperature is perturbed by the photoexcitation process, leading to photoinduced electron-phonon dynamics. It is premature to base our analysis of the experimentally observed non-thermal features that depend on the initial condition on direct comparison with a microscopic non-equilibrium theory. Since femtosecond pulses are shorter than the characteristic time scales of non-thermal SC dynamics, we choose a phenomenological approach based on the "standard RT model" used to interpret the ps dynamics in most SC experiments up to now. The portion of absorbed energy that initially goes into quasi-particles (QP) excitations without lattice excitation is denoted as $p = p_0$, while the rest excites phonon populations both during and after pair-breaking. We thus characterize phenomenologically the initial condition that triggers subsequently the incoherent dynamics after the pulse. (2) Pre-bottleneck regime that accounts for the formation dynamics of the phonon

bottleneck. Here the CPB kinetics can be based on the Rothwarf-Taylor (RT) model, which has been extensively and successfully applied in various SC systems and can be derived microscopically within a Markovia quasi-adiabatic approximation. Previous works have shown that the majority of the absorbed photon energy $(1 - p_0)$ subsequently transfers to the phonon reservoir as high frequency phonons (HFPs) and then continues to break Cooper pairs after the photoexcitations. (3) Bottleneck recovery regime. The first two regimes are the focus on this paper.

We emphasize two points to reach our conclusions. (1) The portion of absorbed energy, $p$, to break Cooper pairs compared to total energy absorption can be directly obtained from Rothwarf-Taylor (RT) model simulations of the measured and better resolved ps data without further assumption or measurement at fs time scales. We did not claim to have directly resolved this 10's fs regime here since it is technically challenging for our setup. On the other hand, this very early 10's fs temporal regime creates the initial condition that triggers subsequently the incoherent pair breaking after the pulse (100's fs). We refer to it as pre-bottleneck regime immediately after or during the optical pulse (10's fs). What we claim here, based on hard evidence extracted from our high quality data by following the same exact analysis as for most previous SC experiments, is that, although the 10's fs regime is not directly accessed in our and other experiments, it is still possible to determine $p = p_0$ from high signal-to-noise-ratio data obtained during the longer, 100's fs pre-bottleneck time regime. In our case, the extracted $p$ from the RT model applied during ps timescales is 0.33%, same as $2\Delta/(\hbar\omega)$ determined by SC gap and photoexcitation energy. Thus, one high energy photon $\hbar\omega$ basically breaks one low energy Cooper pair $2\Delta$ during the coherent excitations of optical pulse (the quantum SC quench regime) accompanied by phonon excitation. We refer the observation of one photon-to-one pair, non-resonant energy transfer during the fs optical excitations as quantum energy transfer. (2) In $Nb_3Sn$, $p$ is two orders of magnitude smaller than in $NbN$, $MgB_2$, as shown in Table III (supplementary), which provides the much needed comparisons between these samples that was absent in the SC literature. (3) Our data indicates that phonon emission is much more efficient during the QP de-coherence and population build-up immediately after and during the pulse ~30 fs. This is consistent with enhanced e-phonon coupling in $Nb_3Sn$

and the optical phonon condensation in the ground state below the Martensitic transition that differentiates A15 from other simpler SCs. Note, however, that the exact microscopic dynamics of quantum quench of superconductivity and build-up of QP population immediately after fs pulse is still lacking. There are neither experimental results like ours nor theoretical discussions in this regime.

Our result will motivate the development of such non-equilibrium quantum quench dynamics of a strongly coupled e-lattice system with optical phonon condensation in the ground state. While we could speculate about the non-equilibrium dynamics of electron-phonon interactions in the coherent and very early non-thermal regimes, we did not attempt this here. Rather, we presented experimental evidence about an unusual "initial condition" based on fits of our data at later times using the conventional RT model also used to interpret the other experiments in the SC systems without Martensitic transition that we compare with the A15 SCs during similar timescales.

# APPENDIX C. ADDITIONAL MATERIALS: CHAPTER 5

## C.1 Experiment Setup

Optical pump-Terahertz (THz) probe ultrafast spectroscopy setup is driven by 1KHz Ti-Sapphire regenerative amplifier. Single-crystalline $Ba(Fe_{1-x}Co_x)_2As_2$ with cobalt substitutions of x=0.047 and 0.1 is mounted at 45 degrees to the incident light in liquid He-flow cryostat and cooled down to 4K. Sample is excited by 800nm, 35fs pump pulse to non-equilibrium transient state. Phase-locked THz probe is generated by optical rectification through 1mm thick ZnTe crystal. By scanning delay of gate pulse $t_{gate}$, reflected THz E field oscillation is measured in time domain through EO sampling. Only center part of 8mm diameter optical pump is used to ensure uniform excitation. Beam diameter of optical pump, THz probe on sample are 2.9mm, 2.5mm respectively. Ultrafast dynamics of the system is obtained by scanning the relative time delay $t_{pp}$ between pump and probe.

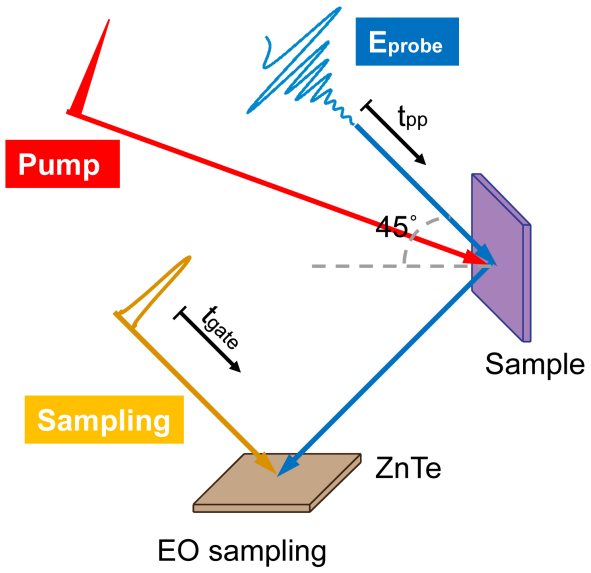


Figure C.1 Experiment scheme of optical pump-THz probe measurement.

## C.2 THz Response Simulation of Superconductivity by Mattis-Bardeen Theory

Due to the difficulty of extracting THz conductivity from reflection measurement, we simulate the THz response of superconductivity by Mattis-Bardeen theory and compare the results to measured THz spectrum.

We assume a Drude response of $Ba(Fe_{1-x}Co_x)_2As_2$ at normal state, with plasma frequency $\omega_p/(2\pi c) = 12000cm^{-1}$ and scattering rate $1/\tau = 3 \times 10^{13}s^{-1}$ (142). Despite the slightly different $\omega_p$ and $1/\tau$ of various cobalt doping samples, simulation results are not sensitive to the choice of Drude parameters. According to Drude model expression, we can generate optical conductivity $\tilde{\sigma}(\omega) = \sigma_1(\omega) + i\sigma_2(\omega)$ at normal state as:

$$\sigma_1^N(\omega) = \frac{\omega_P^2\tau}{4\pi}\frac{1}{1+(\omega\tau)^2} \tag{C.1}$$

$$\sigma_2^N(\omega) = \frac{\omega_P^2\tau}{4\pi}\frac{\omega\tau}{1+(\omega\tau)^2} \tag{C.2}$$

where $\sigma_1^N$ and $\sigma_2^N$ are real and imaginary part of optical conductivity at normal state.

Mattis-Bardeen theory describes the low frequency conductivity of dirty limit superconductor (127). Given the SC gap $\Delta$ and temperature $T$, conductivity ratio between SC and normal state can be calculated by the following integral. When $\hbar\omega/\Delta < 2$, we have:

$$\begin{aligned}
\frac{\sigma_1^{SC}(\omega)}{\sigma_1^N(\omega)} &= \frac{2}{\hbar\omega}\int_{\Delta}^{+\infty}\frac{E^2+\Delta^2+\hbar\omega E}{(E^2-\Delta^2)((E+\hbar\omega)^2-\Delta^2)}\cdot \\
&\qquad [f(E,T)-f(E+\hbar\omega,T)]dE, \\
\frac{\sigma_2^{SC}(\omega)}{\sigma_1^N(\omega)} &= \frac{1}{\hbar\omega}\int_{\Delta-\hbar\omega}^{\Delta}\frac{E^2+\Delta^2+\hbar\omega E}{(E^2-\Delta^2)((E+\hbar\omega)^2-\Delta^2)}\cdot \\
&\qquad [1-2f(E+\hbar\omega,T)]dE,
\end{aligned} \tag{C.3}$$

And when $\hbar\omega/\Delta \geq 2$, we get:

$$\frac{\sigma_1^{SC}(\omega)}{\sigma_1^{N}(\omega)} = \frac{2}{\hbar\omega}\int_{\Delta}^{+\infty} \frac{E^2+\Delta^2+\hbar\omega E}{(E^2-\Delta^2)((E+\hbar\omega)^2-\Delta^2)}\cdot [f(E,T)-f(E+\hbar\omega,T)]dE + \frac{1}{\hbar\omega}\int_{\Delta-\hbar\omega}^{-\Delta} \frac{E^2+\Delta^2+\hbar\omega E}{(E^2-\Delta^2)((E+\hbar\omega)^2-\Delta^2)}\cdot [1-2f(E+\hbar\omega,T)]dE, \tag{C.4}$$

$$\frac{\sigma_2^{SC}(\omega)}{\sigma_1^{N}(\omega)} = \frac{1}{\hbar\omega}\int_{\Delta-\hbar\omega}^{\Delta} \frac{E^2+\Delta^2+\hbar\omega E}{(E^2-\Delta^2)((E+\hbar\omega)^2-\Delta^2)}\cdot [1-2f(E+\hbar\omega,T)]dE,$$

in which $\omega$ is photon energy, $f(E,T)$ is the Fermi-Dirac distribution function. $\sigma_1^{SC}$ and $\sigma_2^{SC}$ are real and imaginary part of conductivity at SC state as function of $\omega$ and $T$. Here we reproduce the full response function at both normal and SC state.

By knowing $\sigma_1(\omega)$, $\sigma_2(\omega)$, complex optical index of the material is:

$$\tilde{N}(\omega) = \sqrt{\tilde{\epsilon}(\omega)} = \sqrt{1+i\frac{4\pi}{\omega}\tilde{\sigma}(\omega)} \tag{C.5}$$

THz reflection spectrum of materials at 45 degrees at polarization parallel to sample plane can be simulated by Fresnel equation:

$$\tilde{r}_{\parallel} = \frac{\tilde{E}_r(\omega)}{\tilde{E}_{in}(\omega)} = \frac{\tilde{N}^2\cos\phi - \mu_1(\tilde{N}^2-\sin^2\phi)^{1/2}}{\tilde{N}^2\cos\phi + \mu_1(\tilde{N}^2-\sin^2\phi)^{1/2}} \tag{C.6}$$

in which permeability $\mu_1 = 1$ for optical frequency and $\phi = \pi/4$ is the incident angle.Given the incident THz wave $\tilde{E}_{in}(\omega)$, we are able to compute complex reflected THz spectrum at normal $\tilde{E}_r^N(\omega)$ and SC state $\tilde{E}_r^{SC}(\omega)$. In experiment, $\tilde{E}_{in}(\omega)$ is the complex spectrum obtained from time domain incident THz wave $E_{in}(t)$ by Fourier transform. In reference measurement, $E_{in}(t)$ is recorded by placing a 100% reflector like gold mirrors at the sample position.

The ratio $\tilde{E}_r^{SC}(\omega)/\tilde{E}_r^{N}(\omega)$ is plotted in Fig. 5.1(c). By inverse Fourier transform, we can get reflected THz waveform $E_r^N(t)$ and $E_r^{SC}(t)$ in time domain.

In the simulation of transient THz reflection after photoexcitation, we assume that optical pump completely quenches SC condensate within penetration depth around 100nm. Considering the

penetration depth mismatch between THz and optical light, Fresnel equation is replaced by transfer matrix of stratified medium (9). Similarily, $E_r^{PP}(t)$ is reproduced conductivity spectrum at SC and normal state $\tilde{\sigma}^{SC}(\omega)$ and $\tilde{\sigma}^{N}(\omega)$. Pump induced change is calculated by $\Delta E_r(t) = E_r^{PP}(t) - E_r^{SC}(t)$. Inset of Fig. 5.2(a) shows the spectrum of pump induced change $\Delta E_r(\omega)$ after Fourier transform. Pump induced change $\Delta E_r$ is more than two orders of magnitude smaller than $E_{in}$

## C.3 Optical conductivity extraction from THz reflection measurement

The extraction of optical conductivity is essentially the reverse of simulation procedure discussed in the previous section. Despite great similarities, extracting optical conductivity from THz reflection proves more challenging than transmission measurement. In the experiment, complex reflection ratio is measured, which is function of $\tilde{\sigma}(\omega)$.

$$\tilde{r}_{\parallel} = \frac{\tilde{E}_r(\omega)}{\tilde{E}_{in}(\omega)} \sim f(\tilde{\sigma}(\omega)) \tag{C.7}$$

Various algorithm can be used to solve for $\tilde{\sigma}(\omega)$ from $\tilde{r}_{\parallel}$.

First challenge originates from reference measurement. To achieve high accuracy, reflection surface of reference has to exactly match sample surface, which is extremely difficult in experiment. Few $\mu m$ deviation of reflection plane greatly modifies both phase and amplitude of $\tilde{r}$, leading to large errors in $\tilde{\sigma}(\omega)$ spectrum, and even unrealistic results.

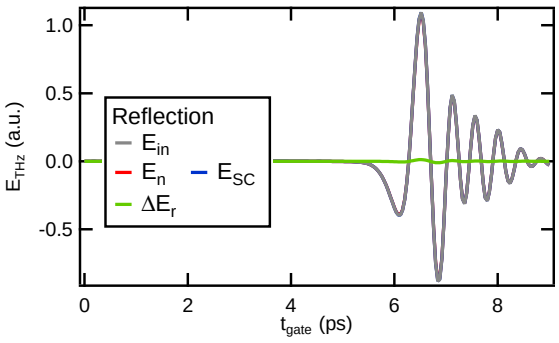


Figure C.2 Simulated THz time domain measurement of SC $E_{SC}(t)$ (blue) and normal state $E_N(t)$ (red) in reflection geometry under incident wave $E_{in}(t)$ (grey). $\Delta E_r(t)$ in green line is the difference between $E_N(t)$ and $E_{SC}(t)$.

Second problem is related to sample we studied here, iron pnictide superconductor. In our study, $Ba(Fe_{1-x}Co_x)_2As_2$ has reflection close to 100% across $T_c$. Efficient extraction, on the other hand, requires significant difference between reference and sample measurement. Simulated static THz reflection is shown in Figure C.3, in which $E_{in}$, $E_r^{SC}$ and $E_r^N$ overlaps with each other. This proves, on the other hand, that the ultrafast pump-probe measurement with much higher sensitivity is a powerful tool to study quantum dynamics and phase competition physics.

## C.4 Comparison of SC Quench Dynamics Between Thin Film and Single–Crystal Samples

Figure C.1 shows our optical pump-THz probe measurement on a thin film optimally doped $Ba(Fe_xCo_{1-x})_2As_2$ sample. Sample thickness is 60 nm, which is below the penetration depth of both 1.55 eV and THz frequency light. This guarantees the uniform excitation of the entire sample probed by the transmitted THz wave. By comparing the fluence dependence of $\Delta E/E$ between the single crystal and thin film samples, we find a striking similarity that confirms the robust microscopic origin of the observed very slow SC quench and long–lived non–equilibrium state as well as the different fluence dependence between short and long times. In addition, in the thin film sample, we were able to extract the frequency dependence of the THz conductivity in a transmission measurement, which we plotted in the insets of Figure C.1. We compare the long time conductivity following SC quench above fluence threshold with the normal state conductivity and find that they are identical. The pump-induced changes measured in the thin film sample as a function of fluence clearly show a crossing between the curves at short and long times, at a fluence of $4\mu J/cm^2$. Above this fluence, the SC order parameter at long times (350ps) is smaller than the order parameter at short times (30ps). This behavior of the thin film sample is very similar to one measured in the single crystal sample, Figure 5.4(a) in the main text. The fact that very different thin film and bulk samples show the same behavior excludes an alternative explanation of our results in terms of penetration depth mismatch or heat diffusion. Also, as shown in the inset (bottom left) the pump-probe signal disappears above Tc, which correlates the observed nontrivial

pump-induced dynamics with the superconductivity. The static (equilibrium) conductivity (top right) below Tc shows a $1/\omega$ peak in $\sigma_2$ and a suppressed $\sigma_1$ below the SC gap, consistent with the existence of a SC condensate delta-function peak at zero frequency. Figure C.1 displays very similar spectral features in $\sigma_1$ and $\sigma_2$ between the normal and post-pump states at 350ps. This result indicates that, after long times, the SC condensate can be quenched non–thermally above a fluence threshold, as predicted by our theory when the effect of e-h correlations among the QPs is included. On the other hand, the measured SC condensate remains finite at short times ~30 ps at all fluences, consistent with BCS behavior and uncorrelated photoexcited QP populations.

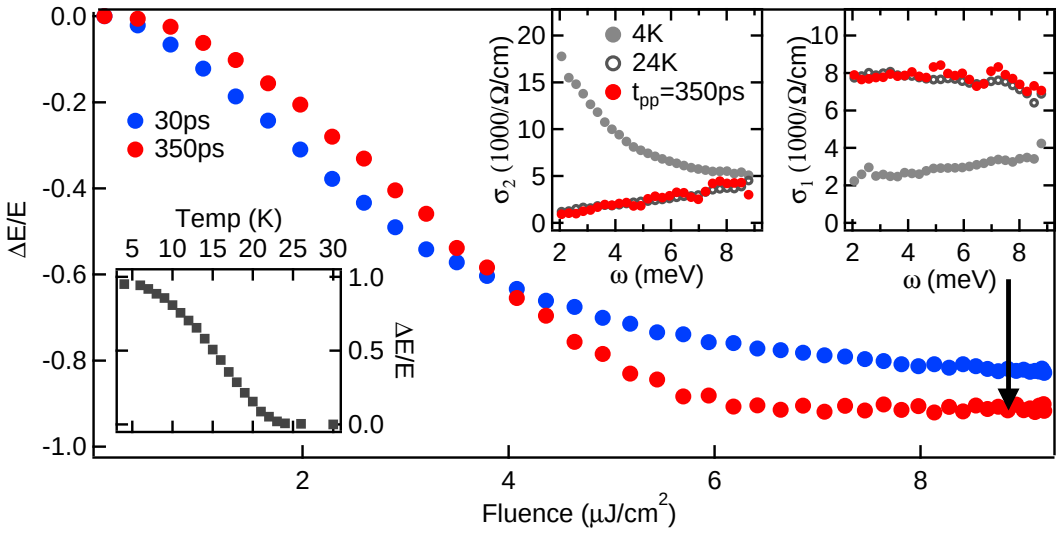


Figure C.3 THz measurement of a 60nm thin film optimal doped $Ba(Fe_xCo_{1-x})_2As_2$ at short (30ps) and long (350ps) times after 1.55eV, 40fs photoexcitation. Inset (bottom): pump-probe signals at various temperatures disappear above Tc at 22K. Inset (top): static and time-resolved complex conductivity at 4K, 24K and non-equilibrium state at 350ps after pump.

## C.5 Many-body Theory of Excitonic SDW Correlation Formation

### Hamiltonian

In this section we provide a brief overview of our microscopic theory, with full details and further calculations to be presented elsewhere. We use the simplest model Hamiltonian believed to give a good qualitative description of the competition between SC and SDW order in the iron pnictides (42; 82):

$$H = H_0 + H_\Delta + H_{\rm m}\,. \tag{C.8}$$

The non-interacting part of the Hamiltonian describes the $e$ and $h$ Fermi sea pockets predicted by the bandstructure:

$$H_0 = \sum_{\mathbf{k},\sigma}[\xi_{\rm c}(\mathbf{k})c^\dagger_{\mathbf{k},\sigma}c_{\mathbf{k},\sigma} + \xi_{\rm f}(\mathbf{k})f^\dagger_{\mathbf{k},\sigma}f_{\mathbf{k},\sigma}]\,. \tag{C.9}$$

We include only one circular hole-like band at the $\Gamma$-point, with dispersion $\xi_{\rm c}(\mathbf{k}) = \xi_{\rm c,0} - \frac{\hbar^2k^2}{2m_{\rm c}} - \mu$, and one elliptical electron-like band with dispersion $\xi_{\rm f}(\mathbf{k}) = \frac{\hbar^2k_x^2}{2m_{{\rm f}_x}} + \frac{\hbar^2k_y^2}{2m_{{\rm f}_y}} - \xi_{\rm f,0} - \mu$ close to the $\mathbf{Q}_0 = (\pi,0)/(0,\pi)$ pocket (42; 82). These electron and hole energy dispersions are determined by effective masses $m_{\rm c/f}$, energy offsets $\xi_{\rm c/f,0}$, and chemical potential $\mu$. The operators $f^\dagger_{\mathbf{k},\sigma}$ ($c^\dagger_{\mathbf{k},\sigma}$) create a carrier with crystal momentum $\hbar(\mathbf{k}-\mathbf{Q}_0)$ ($\hbar\mathbf{k}$) and spin $\sigma$ in the electron-like band near $\mathbf{Q}_0$ (hole-like band close to the $\Gamma$-point). The SC pairing interaction (42) is given by

$$H_\Delta = V_{\rm SC}\sum_{\mathbf{k},\mathbf{k}'}\left[c^\dagger_{\mathbf{k},\uparrow}c^\dagger_{-\mathbf{k},\downarrow}f_{-\mathbf{k}',\downarrow}f_{\mathbf{k}',\uparrow} + {\rm h.c.}\right]\,, \tag{C.10}$$

with interaction magnitude $V_{\rm SC}$. Here we only include the pair hopping between the two pockets (42; 82), which is believed to be the dominant interaction producing $s^{+-}$ SC pairing (143). Besides this SC interaction, the low energy properties depend on the magnetic interaction in the SDW channel (42)

$$\begin{aligned} H_{\rm m} &= -\frac{V_{\rm m}}{2}\sum_{\mathbf{k},\mathbf{p},\mathbf{q}} S^\dagger_z(\mathbf{p},\mathbf{q})S_z(\mathbf{k},\mathbf{q})\,, \\ S_z(\mathbf{k},\mathbf{q}) &= \sum_\sigma \sigma\, c^\dagger_{\mathbf{k},\sigma}f_{\mathbf{k}+\mathbf{q},\sigma}\,, \end{aligned} \tag{C.11}$$

where $V_{\rm m}$ describes the strength of the magnetic interaction. For simplicity we neglect the coupling to phonons.

**Ground-state configuration**

Following previous works, the equilibrium SC properties can be described by treating the above Hamiltonian Eq.(C.8) in the mean-field approximation (42; 82):

$$H_{\Delta}^{\rm MF} = -\sum_{\mathbf{k}\in\mathcal{W}} \left[\Delta_{\rm c} c_{-\mathbf{k},\downarrow} c_{\mathbf{k},\uparrow} + \Delta_{\rm f} f_{-\mathbf{k},\downarrow} f_{\mathbf{k},\uparrow} + \text{h.c.}\right] , \tag{C.12}$$

where the SC order parameters $\Delta_{\rm c}$ and $\Delta_{\rm f}$ are given by (42)

$$\begin{aligned} \Delta_{\rm c} &= -V_{\rm SC} \sum_{\mathbf{p}\in\mathcal{W}} \langle f_{-\mathbf{p},\downarrow} f_{\mathbf{p},\uparrow}\rangle , \\ \Delta_{\rm f} &= -V_{\rm SC} \sum_{\mathbf{p}\in\mathcal{W}} \langle c_{-\mathbf{p},\downarrow} c_{\mathbf{p},\uparrow}\rangle . \end{aligned} \tag{C.13}$$

The sums in Eq.(C.13) only include the set $\mathcal{W}$ of wavevectors $\mathbf{k}$ with $|\xi_\lambda(\mathbf{k})| \leq \hbar\omega_{\rm C}$, where $\omega_{\rm C}$ is the cut-off frequency. Hartree-Fock decoupling of the magnetic interaction Eq.(C.11) gives (42)

$$H_{\rm m}^{\rm MF} = -\sum_{\mathbf{k},\sigma} \sigma \left[M\, f_{\mathbf{k}+\mathbf{q},\sigma}^{\dagger} c_{\mathbf{k},\sigma} + M\, c_{\mathbf{k},\sigma}^{\dagger} f_{\mathbf{k}+\mathbf{q},\sigma}\right] \tag{C.14}$$

with SDW order parameter (42)

$$M = \frac{V_{\rm m}}{2} \sum_{\mathbf{k},\sigma} \sigma \langle c_{\mathbf{k},\sigma}^{\dagger} f_{\mathbf{k}+\mathbf{q},\sigma}\rangle \tag{C.15}$$

assumed to be polarized in the $z$-direction (144). The SDW order is assumed for simplicity to form with a single momentum $\mathbf{Q} = \mathbf{Q}_0 + \mathbf{q}$ between the electron and hole pockets, which becomes commensurate for $\mathbf{q} = 0$. We only include this momentum in our calculations here. The mean-field Hamiltonian $H^{\rm MF} = H_0 + H_{\rm SC}^{\rm MF} + H_{\rm m}^{\rm MF}$ is diagonalized exactly, yielding the self-consistent temperature–dependent SC and SDW gap equations that characterize the thermal equilibrium state (42):

$$\begin{aligned} \Delta_\lambda &= -\frac{V_{\rm SC}}{S} \sum_{\mathbf{k},j} K_{\mathbf{k},j}^{\lambda} \tanh\left(\frac{E_{j,\mathbf{k}}}{2\,k_{\rm B}T}\right) , \\ M &= \frac{V_{\rm m}}{S} \sum_{\mathbf{k},j} K_{\mathbf{k},j}^{\rm m} \tanh\left(\frac{E_{j,\mathbf{k}}}{2\,k_{\rm B}T}\right) , \end{aligned} \tag{C.16}$$

with kernels

$$K^{\lambda}_{\mathbf{k},j} = \frac{\Delta_{\bar{\lambda}}(E^2_{j,\mathbf{k}} - \Delta^2_{\lambda} - \xi^2_{\lambda,\mathbf{k}}) + M^2\Delta_{\lambda}}{2\,E_{j,\mathbf{k}}(E^2_{j,\mathbf{k}} - E^2_{\bar{j},\mathbf{k}})}\,,$$
$$K^{\mathrm{m}}_{\mathbf{k},j} = \frac{M\,(E^2_{j,\mathbf{k}} + \Delta_{\mathrm{c}}\Delta_{\mathrm{f}} + \xi_{\mathrm{c},\mathbf{k}}\xi_{\mathrm{f},\mathbf{k}} - M^2)}{2\,E_{j,\mathbf{k}}(E^2_{j,\mathbf{k}} - E^2_{\bar{j},\mathbf{k}})}\,,$$

$$\bar{\lambda} = \begin{cases} \mathrm{c} & \text{if } \lambda = \mathrm{f} \\ \mathrm{f} & \text{if } \lambda = \mathrm{c} \end{cases}$$

$$\bar{j} = \begin{cases} 1 & \text{if } j = 2 \\ 2 & \text{if } j = 1 \end{cases}$$

and excitation energies

$$\left(E_{(j=1,2),\mathbf{k}}\right)^2 = \frac{1}{2}\left(\Gamma_{\mathbf{k}} \pm \sqrt{\Gamma^2_{\mathbf{k}} + \Omega_{\mathbf{k}} + \tilde{\Omega}_{\mathbf{k}}}\right)\,,$$
$$\Gamma_{\mathbf{k}} = 2\,M^2 + \Delta^2_{\mathrm{c}} + \Delta^2_{\mathrm{f}} + \xi^2_{\mathrm{c}}(\mathbf{k}) + \xi^2_{\mathrm{f}}(\mathbf{k}+\mathbf{q})\,,$$
$$\Omega_{\mathbf{k}} = -4\left(\xi^2_{\mathrm{c}}(\mathbf{k}) + \Delta^2_{\mathrm{c}}\right)\left(\xi^2_{\mathrm{f}}(\mathbf{k}+\mathbf{q}) + \Delta^2_{\mathrm{f}}\right)\,,$$
$$\tilde{\Omega}_{\mathbf{k}} = 8\,M^2\left(\Delta_{\mathrm{c}}\Delta_{\mathrm{f}} + \xi_{\mathrm{c}}(\mathbf{k})\xi_{\mathrm{f}}(\mathbf{k}+\mathbf{q}) - \frac{M^2}{2}\right)\,. \tag{C.17}$$

To compute the equilibrium state, we solved the above mean-field gap equations self-consistently for given equilibrium chemical potential $\mu$ determined by the level $x$ of Co doping. While the above equations may also be used to describe a quasi–thermal photoinduced state characterized by time–dependent temperature and chemical potential, the main effects of interest here come from non–thermal deviations from such quasi–thermal state, which occur prior to thermalization of the photoexcited QPs between the Fermi sea pockets.

**Non-thermal dynamics**

To study the photo-excited incoherent dynamics that govern our experiment, we first introduce a basis of Bogoliubov QPs, defined by the transformation

$$
\begin{aligned}
c_{\mathbf{k},\uparrow} &= u_{\mathbf{k}}\alpha^{\dagger}_{\mathbf{k}} - v_{\mathbf{k}}\beta_{\mathbf{k}} + \bar{u}_{\mathbf{k}}\gamma^{\dagger}_{\mathbf{k}} + \bar{v}_{\mathbf{k}}\delta_{\mathbf{k}}\,, \\
c^{\dagger}_{-\mathbf{k},\downarrow} &= v_{\mathbf{k}}\alpha^{\dagger}_{\mathbf{k}} + u_{\mathbf{k}}\beta_{\mathbf{k}} + \bar{v}_{\mathbf{k}}\gamma^{\dagger}_{\mathbf{k}} - \bar{u}_{\mathbf{k}}\delta_{\mathbf{k}}\,, \\
f_{\mathbf{k}+\mathbf{q},\uparrow} &= w_{\mathbf{k}}\alpha^{\dagger}_{\mathbf{k}} + x_{\mathbf{k}}\beta_{\mathbf{k}} + \bar{w}_{\mathbf{k}}\gamma^{\dagger}_{\mathbf{k}} - \bar{x}_{\mathbf{k}}\delta_{\mathbf{k}}\,, \\
f^{\dagger}_{-\mathbf{k}-\mathbf{q},\downarrow} &= x_{\mathbf{k}}\alpha^{\dagger}_{\mathbf{k}} - w_{\mathbf{k}}\beta_{\mathbf{k}} + \bar{x}_{\mathbf{k}}\gamma^{\dagger}_{\mathbf{k}} + \bar{w}_{\mathbf{k}}\delta_{\mathbf{k}}\,.
\end{aligned}
\tag{C.18}
$$

Here, $u_{\mathbf{k}}$, $v_{\mathbf{k}}$, $w_{\mathbf{k}}$, $x_{\mathbf{k}}$, $\bar{u}_{\mathbf{k}}$, $\bar{v}_{\mathbf{k}}$, $\bar{w}_{\mathbf{k}}$, and $\bar{x}_{\mathbf{k}}$ are coherence factors that depend on the instantaneous SC and SDW order parameters. We include for simplicity only a single momentum $\mathbf{q}$ in $H_{\Delta}$ and $H_{\mathrm{m}}$ as discussed above. Since we are interested in SDW excitonic state formation, we consider the full inter–pocket SDW interaction Eq. (C.11) without factorization, which introduces relaxation driven by the inter–band interaction. On the other hand, the SC interaction is treated within the mean-field approximation for simplicity.

Substituting Eq.(C.18) into the above Hamiltonian and eliminating the off–diagonal quadratic contributions, we transform the Hamiltonian in the QP basis for given order parameters $\Delta_{\mathrm{c}}$, $\Delta_{\mathrm{f}}$ and $M$:

$$
\begin{aligned}
H_{\mathrm{BCS}} &= H_0 + H^{\mathrm{MF}}_{\Delta} \\
&= \sum_{\mathbf{k}} \left[ R^{-}_{\mathbf{k}} \left( \alpha^{\dagger}_{\mathbf{k}}\alpha_{\mathbf{k}} + \beta^{\dagger}_{\mathbf{k}}\beta_{\mathbf{k}} \right) + R^{+}_{\mathbf{k}} \left( \gamma^{\dagger}_{\mathbf{k}}\gamma_{\mathbf{k}} + \delta^{\dagger}_{\mathbf{k}}\delta_{\mathbf{k}} \right) \right],
\end{aligned}
\tag{C.19}
$$

where we introduced

$$
\begin{aligned}
R^{-}_{\mathbf{k}} &= \xi_{\mathrm{c}}(\mathbf{k}) \left( v^2_{\mathbf{k}} - u^2_{\mathbf{k}} \right) + \xi_{\mathrm{f}}(\mathbf{k}+\mathbf{q}) \left( x^2_{\mathbf{k}} - w^2_{\mathbf{k}} \right) \\
&\quad - 2 \left( u_{\mathbf{k}} v_{\mathbf{k}} \Delta_{\mathrm{c}} + x_{\mathbf{k}} w_{\mathbf{k}} \Delta_{\mathrm{f}} \right), \\
R^{+}_{\mathbf{k}} &= \xi_{\mathrm{c}}(\mathbf{k}) \left( \bar{v}^2_{\mathbf{k}} - \bar{u}^2_{\mathbf{k}} \right) + \xi_{\mathrm{f}}(\mathbf{k}+\mathbf{q}) \left( \bar{x}^2_{\mathbf{k}} - \bar{w}^2_{\mathbf{k}} \right) \\
&\quad - 2 \left( \bar{u}_{\mathbf{k}} \bar{v}_{\mathbf{k}} \Delta_{\mathrm{c}} + \bar{x}_{\mathbf{k}} \bar{w}_{\mathbf{k}} \Delta_{\mathrm{f}} \right).
\end{aligned}
\tag{C.20}
$$

and

$$
\begin{aligned}
H_{\mathrm{m}} = -\frac{V_{\mathrm{m}}}{2} \sum_{\mathbf{k},\mathbf{p}} \Big[ & 2\, l_{\mathbf{k}} m_{\mathbf{p}} \left( \alpha_{\mathbf{p}}^{\dagger} \alpha_{\mathbf{p}} + \beta_{\mathbf{p}}^{\dagger} \beta_{\mathbf{p}} \right) \\
& + 2\, l_{\mathbf{k}} p_{\mathbf{p}} \left( \gamma_{\mathbf{p}}^{\dagger} \gamma_{\mathbf{p}} + \delta_{\mathbf{p}}^{\dagger} \delta_{\mathbf{p}} \right) \\
& + m_{\mathbf{k}} m_{\mathbf{p}} \left( \alpha_{\mathbf{p}}^{\dagger} \alpha_{\mathbf{p}} + \beta_{\mathbf{p}}^{\dagger} \beta_{\mathbf{p}} \right) \left( \alpha_{\mathbf{k}}^{\dagger} \alpha_{\mathbf{k}} + \beta_{\mathbf{k}}^{\dagger} \beta_{\mathbf{k}} \right) \\
& + p_{\mathbf{k}} p_{\mathbf{p}} \left( \gamma_{\mathbf{p}}^{\dagger} \gamma_{\mathbf{p}} + \delta_{\mathbf{p}}^{\dagger} \delta_{\mathbf{p}} \right) \left( \gamma_{\mathbf{k}}^{\dagger} \gamma_{\mathbf{k}} + \delta_{\mathbf{k}}^{\dagger} \delta_{\mathbf{k}} \right) \\
& + p_{\mathbf{k}} m_{\mathbf{p}} \left( \alpha_{\mathbf{p}}^{\dagger} \alpha_{\mathbf{p}} + \beta_{\mathbf{p}}^{\dagger} \beta_{\mathbf{p}} \right) \left( \gamma_{\mathbf{k}}^{\dagger} \gamma_{\mathbf{k}} + \delta_{\mathbf{k}}^{\dagger} \delta_{\mathbf{k}} \right) \\
& + \left( r_{\mathbf{k}} r_{\mathbf{p}} + s_{\mathbf{k}} s_{\mathbf{p}} \right) \tilde{S}_z^{\dagger}(\mathbf{p}) \tilde{S}(\mathbf{k}) \\
& + \left( \bar{r}_{\mathbf{k}} \bar{r}_{\mathbf{p}} + \bar{s}_{\mathbf{k}} \bar{s}_{\mathbf{p}} \right) \bar{S}_z^{\dagger}(\mathbf{p}) \bar{S}(\mathbf{k}) \Big]
\end{aligned}
\tag{C.21}
$$

with coherence factors

$$
\begin{aligned}
& l_{\mathbf{k}} = 2 \left( u_{\mathbf{k}} w_{\mathbf{k}} + \bar{u}_{\mathbf{k}} \bar{w}_{\mathbf{k}} \right) , \quad m_{\mathbf{k}} = \left( u_{\mathbf{k}} w_{\mathbf{k}} + v_{\mathbf{k}} x_{\mathbf{k}} \right) , \\
& p_{\mathbf{k}} = \left( \bar{u}_{\mathbf{k}} \bar{w}_{\mathbf{k}} + \bar{v}_{\mathbf{k}} \bar{x}_{\mathbf{k}} \right) , r_{\mathbf{k}} = v_{\mathbf{k}} \bar{w}_{\mathbf{k}} + \bar{v}_{\mathbf{k}} w_{\mathbf{k}} , \\
& s_{\mathbf{k}} = \left( \bar{u}_{\mathbf{k}} x_{\mathbf{k}} + \bar{x}_{\mathbf{k}} u_{\mathbf{k}} \right) , \quad \bar{r}_{\mathbf{k}} = \bar{v}_{\mathbf{k}} x_{\mathbf{k}} + u_{\mathbf{k}} \bar{w}_{\mathbf{k}} , \\
& \bar{s}_{\mathbf{k}} = v_{\mathbf{k}} \bar{x}_{\mathbf{k}} + \bar{u}_{\mathbf{k}} w_{\mathbf{k}} .
\end{aligned}
\tag{C.22}
$$

The last two lines in Equation (C.21) describe the deviations from the mean field Hamiltonian and involve four QP operators (two pairs of QPs). The collective effects in the SDW channel are described by the QP pair operators

$$
\tilde{S}_z(\mathbf{k}) = \beta_{\mathbf{k}} \gamma_{\mathbf{k}} + \alpha_{\mathbf{k}} \delta_{\mathbf{k}} , \quad \bar{S}_z(\mathbf{k}) = \beta_{\mathbf{k}}^{\dagger} \delta_{\mathbf{k}} - \alpha_{\mathbf{k}}^{\dagger} \gamma_{\mathbf{k}} . \tag{C.23}
$$

Since we are interested in long timescales after dephasing of any coherences among QPs, we only keep the QP number–conserving terms in Eqs. (C.19) and (C.21) and neglect any photoinduced coherence among QPs, $\langle \tilde{S}_z(\mathbf{k}) \rangle = \langle \bar{S}_z(\mathbf{k}) \rangle = 0$. The transformation of the SC and SDW gap

equations in the QP basis then yields

$$\Delta_{\rm c} = -V_{\rm SC}\sum_{\mathbf{k}}\Big[u_{\mathbf{k}}v_{\mathbf{k}}\left(1-n^{\alpha}_{\mathbf{k}}-n^{\beta}_{\mathbf{k}}\right)$$
$$+\bar{u}_{\mathbf{k}}\bar{v}_{\mathbf{k}}\left(1-n^{\gamma}_{\mathbf{k}}-n^{\delta}_{\mathbf{k}}\right)\Big]\,,$$
$$\Delta_{\rm f} = -V_{\rm SC}\sum_{\mathbf{k}}\Big[w_{\mathbf{k}}x_{\mathbf{k}}\left(1-n^{\alpha}_{\mathbf{k}}-n^{\beta}_{\mathbf{k}}\right)$$
$$+\bar{w}_{\mathbf{k}}\bar{x}_{\mathbf{k}}\left(1-n^{\gamma}_{\mathbf{k}}-n^{\delta}_{\mathbf{k}}\right)\Big]\,,$$
$$M = -\frac{V_{\rm m}}{2}\sum_{\mathbf{k}}\left[2\,l_{\mathbf{k}}-m_{\mathbf{k}}\left(n^{\alpha}_{\mathbf{k}}+n^{\beta}_{\mathbf{k}}\right)-p_{\mathbf{k}}\left(n^{\gamma}_{\mathbf{k}}+n^{\delta}_{\mathbf{k}}\right)\right]\,, \tag{C.24}$$

where we introduced the QP distributions

$$n^{\alpha}_{\mathbf{k}} = \langle\alpha^{\dagger}_{\mathbf{k}}\alpha_{\mathbf{k}}\rangle\,,\quad n^{\beta}_{\mathbf{k}} = \langle\beta^{\dagger}_{\mathbf{k}}\beta_{\mathbf{k}}\rangle\,,\quad n^{\gamma}_{\mathbf{k}} = \langle\gamma^{\dagger}_{\mathbf{k}}\gamma_{\mathbf{k}}\rangle\,,$$
$$n^{\delta}_{\mathbf{k}} = \langle\delta^{\dagger}_{\mathbf{k}}\delta_{\mathbf{k}}\rangle\,. \tag{C.25}$$

As in the simple BCS theory, the excitation of QP populations quenches both the SC and the SDW order parameters. We simplify the problem by assuming that, after the initial sub–ps QP relaxation, the QP distributions are all similar for high frequency optical pump excitation at ∼1.5eV: $n^{\alpha}_{\mathbf{k}} \approx n^{\beta}_{\mathbf{k}} \equiv n^{\alpha\beta}_{\mathbf{k}}$ and $n^{\gamma}_{\mathbf{k}} \approx n^{\delta}_{\mathbf{k}} \equiv n^{\gamma\delta}_{\mathbf{k}}$. The time evolution of the SC and SDW order parameters monitored by the THz probe is determined by the time evolution of the above QP populations, which we describe by deriving equations of motion using the full above Hamiltonian. The scattering processes determined by $H_m$ lead to QP relaxation described by

$$\frac{\partial}{\partial t}n^{\alpha\beta}_{\mathbf{p}} = \frac{V_{\rm m}}{\hbar}{\rm Im}\sum_{\mathbf{k}}\Big[\left(r_{\mathbf{k}}r_{\mathbf{p}}+s_{\mathbf{k}}s_{\mathbf{p}}\right)C^{\mathbf{k},\mathbf{p}}_{\rm SDW,1}$$
$$+\left(\bar{r}_{\mathbf{k}}\bar{r}_{\mathbf{p}}+\bar{s}_{\mathbf{k}}\bar{s}_{\mathbf{p}}\right)C^{\mathbf{k},\mathbf{p}}_{\rm SDW,2}\Big]\,,$$
$$\frac{\partial}{\partial t}n^{\gamma\delta}_{\mathbf{p}} = \frac{V_{\rm m}}{\hbar}{\rm Im}\sum_{\mathbf{k}}\Big[\left(r_{\mathbf{k}}r_{\mathbf{p}}+s_{\mathbf{k}}s_{\mathbf{p}}\right)C^{\mathbf{k},\mathbf{p}}_{\rm SDW,1}$$
$$-\left(\bar{r}_{\mathbf{k}}\bar{r}_{\mathbf{p}}+\bar{s}_{\mathbf{k}}\bar{s}_{\mathbf{p}}\right)C^{\mathbf{k},\mathbf{p}}_{\rm SDW,2}\Big]\,. \tag{C.26}$$

The higher density matrices $C_{SDW}$ that appear on the right-hand side of the above equations involve four QP operators and are defined after subtracting all factorizable contributions by using

a cluster-expansion as in (**?** ):

$$C^{\mathbf{p},\mathbf{k}}_{\mathrm{SDW},1} = \Delta\langle \tilde{S}^{\dagger}_{z}(\mathbf{k})\tilde{S}_{z}(\mathbf{p})\rangle\,, \quad C^{\mathbf{p},\mathbf{k}}_{\mathrm{SDW},2} = \Delta\langle \bar{S}^{\dagger}_{z}(\mathbf{k})\bar{S}_{z}(\mathbf{p})\rangle\,. \tag{C.27}$$

For $C_{SDW}$=0 we recover the mean-field results, while the four–QP density matrices describe correlation build–up and scattering among QPs. Such processes modify the QP distributions as compared to mean field, which leads to time–dependent SC order parameter quench. The equations of motion of $C_{SDW}$ describe the time evolution of correlations among the photoexcited QPs and are derived similar to Ref. (**?** ):

$$\begin{aligned}
\mathrm{i}\hbar\frac{\partial}{\partial t}C^{\mathbf{p},\mathbf{k}}_{\mathrm{SDW},1} &= \left(\varepsilon^{-}_{\mathbf{p}} + \varepsilon^{+}_{\mathbf{p}} - \varepsilon^{-}_{\mathbf{k}} - \varepsilon^{+}_{\mathbf{k}}\right) C^{\mathbf{p},\mathbf{k}}_{\mathrm{SDW},1} + S^{\mathbf{p},\mathbf{k}}_{1} \\
&+ 2\,V_{\mathrm{m}}\left(1 - n^{\alpha\beta}_{\mathbf{k}} - n^{\gamma\delta}_{\mathbf{k}}\right)\sum_{\mathbf{l}}\left(r_{\mathbf{k}}r_{\mathbf{l}} + s_{\mathbf{k}}s_{\mathbf{l}}\right) C^{\mathbf{p},\mathbf{l}}_{\mathrm{SDW},1} \\
&- 2\,V_{\mathrm{m}}\left(1 - n^{\alpha\beta}_{\mathbf{k}} - n^{\gamma\delta}_{\mathbf{k}}\right)\sum_{\mathbf{l}}\left(r_{\mathbf{p}}r_{\mathbf{l}} + s_{\mathbf{p}}s_{\mathbf{l}}\right) C^{\mathbf{l},\mathbf{k}}_{\mathrm{SDW},1} \\
&+ D^{\mathbf{p},\mathbf{k}}_{1} + T^{\mathbf{p},\mathbf{k}}_{1}\,,
\end{aligned} \tag{C.28}$$

$$\begin{aligned}
\mathrm{i}\hbar\frac{\partial}{\partial t}C^{\mathbf{p},\mathbf{k}}_{\mathrm{SDW},2} &= \left(\varepsilon^{-}_{\mathbf{p}} - \varepsilon^{+}_{\mathbf{p}} - \varepsilon^{-}_{\mathbf{k}} + \varepsilon^{+}_{\mathbf{k}}\right) C^{\mathbf{p},\mathbf{k}}_{\mathrm{SDW},2} + S^{\mathbf{p},\mathbf{k}}_{2} \\
&+ 2\,V_{\mathrm{m}}\left(n^{\alpha\beta}_{\mathbf{k}} - n^{\gamma\delta}_{\mathbf{k}}\right)\sum_{\mathbf{l}}\left(\bar{r}_{\mathbf{k}}\bar{r}_{\mathbf{l}} + \bar{s}_{\mathbf{k}}\bar{s}_{\mathbf{l}}\right) C^{\mathbf{p},\mathbf{l}}_{\mathrm{SDW},2} \\
&- 2\,V_{\mathrm{m}}\left(n^{\alpha\beta}_{\mathbf{k}} - n^{\gamma\delta}_{\mathbf{k}}\right)\sum_{\mathbf{l}}\left(\bar{r}_{\mathbf{p}}\bar{r}_{\mathbf{l}} + \bar{s}_{\mathbf{p}}\bar{s}_{\mathbf{l}}\right) C^{\mathbf{l},\mathbf{k}}_{\mathrm{SDW},2} \\
&+ D^{\mathbf{p},\mathbf{k}}_{2} + T^{\mathbf{p},\mathbf{k}}_{2}\,,
\end{aligned} \tag{C.29}$$

where the QP energies are given by

$$\begin{aligned}
\varepsilon^{-}_{\mathbf{k}} &= \xi_{\mathrm{c}}(\mathbf{k})\left(v^{2}_{\mathbf{k}} - u^{2}_{\mathbf{k}}\right) + \xi_{\mathrm{f}}(\mathbf{k}+\mathbf{q})\left(x^{2}_{\mathbf{k}} - w^{2}_{\mathbf{k}}\right) \\
&- 2\left(u_{\mathbf{k}}v_{\mathbf{k}}\Delta_{\mathrm{c}} + x_{\mathbf{k}}w_{\mathbf{k}}\Delta_{\mathrm{f}}\right) - 2\left(u_{\mathbf{k}}w_{\mathbf{k}} + v_{\mathbf{k}}x_{\mathbf{k}}\right)M\,, \\
\varepsilon^{+}_{\mathbf{k}} &= \xi_{\mathrm{c}}(\mathbf{k})\left(\bar{v}^{2}_{\mathbf{k}} - \bar{u}^{2}_{\mathbf{k}}\right) + \xi_{\mathrm{f}}(\mathbf{k}+\mathbf{q})\left(\bar{x}^{2}_{\mathbf{k}} - \bar{w}^{2}_{\mathbf{k}}\right) \\
&- 2\left(\bar{u}_{\mathbf{k}}\bar{v}_{\mathbf{k}}\Delta_{\mathrm{c}} + \bar{x}_{\mathbf{k}}\bar{w}_{\mathbf{k}}\Delta_{\mathrm{f}}\right) - 2\left(\bar{u}_{\mathbf{k}}\bar{w}_{\mathbf{k}} + \bar{v}_{\mathbf{k}}\bar{x}_{\mathbf{k}}\right)M\,.
\end{aligned} \tag{C.30}$$

The usual scattering among individual QPs is described by the source terms

$$S_1^{\mathbf{p},\mathbf{k}} = \frac{4\,V_{\rm m}}{S}\,(r_{\mathbf{k}} r_{\mathbf{p}} + s_{\mathbf{k}} s_{\mathbf{p}})\,\Big[n_{\mathbf{p}}^{\alpha\beta} n_{\mathbf{p}}^{\gamma\delta}(1-n_{\mathbf{k}}^{\alpha\beta})(1-n_{\mathbf{k}}^{\gamma\delta}) - n_{\mathbf{k}}^{\alpha\beta} n_{\mathbf{k}}^{\gamma\delta}(1-n_{\mathbf{p}}^{\alpha\beta})(1-n_{\mathbf{p}}^{\gamma\delta})\Big]\,, \tag{C.31}$$

$$S_2^{\mathbf{p},\mathbf{k}} = \frac{4\,V_{\rm m}}{S}\,(\bar{r}_{\mathbf{k}} \bar{r}_{\mathbf{p}} + \bar{s}_{\mathbf{k}} \bar{s}_{\mathbf{p}})\,\Big[n_{\mathbf{k}}^{\alpha\beta} n_{\mathbf{p}}^{\gamma\delta}(1-n_{\mathbf{p}}^{\alpha\beta})(1-n_{\mathbf{k}}^{\gamma\delta}) - n_{\mathbf{k}}^{\alpha\beta} n_{\mathbf{p}}^{\gamma\delta}(1-n_{\mathbf{p}}^{\alpha\beta})(1-n_{\mathbf{k}}^{\gamma\delta})\Big]\,. \tag{C.32}$$

$S_{1,2}^{\mathbf{p},\mathbf{k}}$ have the typical form describing Boltzmann scattering with in- and out-scattering contributions. The first line in Eqs. (C.28) and (C.29) describe relaxation among individual quasi–particles within the Born approximation, without any excitonic correlation. Such perturbative Born scattering approximation does not change the behavior at long 100's ps times.

The next two lines on the rhs of Eqs. (C.28) and (C.29) give the most important contributions here. As soon as non–thermal QP populations are excited in the $e$ and $h$ Fermi sea pockets, $S^{\mathbf{p},\mathbf{k}} \neq 0$ and the above equations describe screening build–up and formation of spin–excitons among the laser-induced QPs. Renormalization of the QP energies and screening-type effects are described by the remaining two-particle contributions $D_{1,2}^{\mathbf{p},\mathbf{k}}$. The coupling to three-particle correlations, $T_{1,2}^{\mathbf{p},\mathbf{k}}$, introduces relaxation of the SDW excitonic correlation.

$C_{\rm SDW,2}^{\mathbf{p},\mathbf{k}}$ is mostly significant in the strong excitation regime, as it requires an appreciable imbalance between QP distributions such that $(n_{\mathbf{k}}^{\alpha\beta} - n_{\mathbf{k}}^{\gamma\delta})$ is non-vanishing. In contrast, $C_{\rm SDW,1}^{\mathbf{p},\mathbf{k}}$ becomes large already at low QP densities. Here we assume that high–frequency pump excitation results in similar nonthermal densities of $\alpha$-, $\beta$- and $\gamma$-, $\delta$- QPs, so we neglect $C_{\rm SDW,2}^{\mathbf{p},\mathbf{k}}$. More details on the full theory will be presented elsewhere.

**Generalized Wannier Equation for Describing the Excitonic Correlation**

Following an initial temporal regime of ultrafast SC gap quenching, the QP distributions $n_{\mathbf{k}}^{\alpha\beta}$ and $n_{\mathbf{k}}^{\gamma\delta}$ change adiabatically with time, so we seek stationary solutions of Eq. (C.28). The form of these equations of motion suggests the transformation of the SDW correlation $C_{\rm SDW,1}^{\mathbf{p},\mathbf{k}}$ into an

excitonic basis (**?** ) defined by the wavefunction $\phi^{\rm r}_{\nu,\mathbf{q}}$. The latter is given by the generalized Wannier equation

$$\left(\varepsilon^{-}_{\mathbf{p}}+\varepsilon^{+}_{\mathbf{p}}\right)\phi^{\rm r}_{\nu}(\mathbf{p})-\left(1-n^{\alpha\beta}_{\mathbf{p}}-n^{\gamma\delta}_{\mathbf{p}}\right)\sum_{\mathbf{k}}V_{\mathbf{k},\mathbf{p}}\phi^{\rm r}_{\nu}(\mathbf{k})$$
$$=E_{\nu}\,\phi^{\rm r}_{\nu}(\mathbf{p})\,, \tag{C.33}$$

where the Coulomb matrix element depends on the QP coherence factors:

$$V_{\mathbf{k},\mathbf{p}}=2\,V_{\rm m}\left[\left(\bar{u}_{\mathbf{k}}x_{\mathbf{k}}+\bar{x}_{\mathbf{k}}u_{\mathbf{k}}\right)\left(\bar{u}_{\mathbf{p}}x_{\mathbf{p}}+\bar{x}_{\mathbf{p}}u_{\mathbf{p}}\right)\right.$$
$$\left.+\left(v_{\mathbf{k}}\bar{w}_{\mathbf{k}}+\bar{v}_{\mathbf{k}}w_{\mathbf{k}}\right)\left(v_{\mathbf{p}}\bar{w}_{\mathbf{p}}+\bar{v}_{\mathbf{p}}w_{\mathbf{p}}\right)\right]\,. \tag{C.34}$$

It is then convenient to introduce the excitonic operator

$$X_{\nu}=\sum_{\mathbf{p}}\phi^{\rm l*}_{\nu}(\mathbf{p})\tilde{S}_{z}(\mathbf{p}). \tag{C.35}$$

Unlike for phonons, the commutation relations of this composite exciton operator have non-bosonic corrections due to Phase Space Filling arising from the fermionic character of the QPs involved. By transforming from uncorrelated QPs to the excitonic basis

$$\tilde{S}_{z}(\mathbf{p})=\sum_{\nu}\phi^{\rm r}_{\nu}(\mathbf{p})X_{\nu} \tag{C.36}$$

we describe the correlations of interest in terms of the above-defined spin-excitons:

$$C^{\mathbf{p},\mathbf{k}}_{\rm SDW,1}=\sum_{\nu,\nu'}\left[\phi^{\rm r}_{\nu}(\mathbf{k})\right]^{\star}\phi^{\rm r}_{\nu'}(\mathbf{p})\,\Delta\langle X^{\dagger}_{\nu}X_{\nu'}\rangle\,,$$
$$\Delta\langle X^{\dagger}_{\nu}X_{\nu'}\rangle=\sum_{\mathbf{k},\mathbf{p}}\phi^{\rm l}_{\nu}(\mathbf{k})\left[\phi^{\rm l}_{\nu'}(\mathbf{p})\right]^{\star}C^{\mathbf{p},\mathbf{k}}_{\rm SDW,1}\,. \tag{C.37}$$

The coupling of the QP distributions to the excitonic amplitude in Eq. (C.33) yields a non-hermitian eigenvalue problem, so we obtain left- and right-handed eigenfunctions $\phi^{\rm r,l}_{\nu,\mathbf{q}}$. These describe both bound and scattering solutions, where the latter correspond to unbound QP pairs whose properties are modified by the magnetic interaction. The above wavefunctions satisfy the orthogonality and completeness relations

$$\sum_{\mathbf{p}}\left[\phi^{\rm l}_{\nu}(\mathbf{p})\right]^{\star}\phi^{\rm r}_{\nu'}(\mathbf{p})=\delta_{\nu,\nu'}\,,\quad\sum_{\nu}\left[\phi^{\rm l}_{\nu}(\mathbf{p})\right]^{\star}\phi^{\rm r}_{\nu}(\mathbf{p}')=\delta_{\mathbf{p},\mathbf{p}'}\,. \tag{C.38}$$

To simplify the problem for our purposes here, we assume relaxation to the lowest spin–exciton state $\phi_{\mathbf{p}} \equiv \phi^{\mathrm{r}}_{\nu=0}(\mathbf{p})$ and only retain this contribution to Eq. (C.37). As a result,

$$C^{\mathbf{p},\mathbf{k}}_{\mathrm{SDW},1} = \phi^{\star}_{\mathbf{p}}\phi_{\mathbf{k}}\,, \tag{C.39}$$

where we have absorbed $\Delta\langle X^{\dagger}_{\nu=0}X_{\nu=0}\rangle$ into $\phi_{\mathbf{p}}$.

In the incoherent long–time regime and for $C^{\mathbf{p},\mathbf{k}}_{\mathrm{SDW},1}$ dominating over $C^{\mathbf{p},\mathbf{k}}_{\mathrm{SDW},2}$, we obtain Eq. (5.2) from an exact relation between the traces of the corresponding density matrices. The coupled Eqs. (5.2) and (C.33), together with the order parameter equations (C.24) and coherent factor expressions, yield a self-consistent calculation of the many-body state defined by $(\phi_{\mathbf{p}}, n_{\mathbf{p}}, \Delta_{\mathrm{c}}, \Delta_{\mathrm{f}}, M)$. This result corresponds to an adiabatic solution of the equations of motion and describes the non-equilibrium state reached after formation/buildup of SDW correlation and before the system thermalizes via scattering across the Fermi sea pockets.

**Numerical Calculations**

In our numerical calculations presented in Figure 5.4, we first computed the thermal ground state configuration by solving the SDW and SC gap equations (C.16) self-consistently for a given doping level. We then solved Eqs. (5.1) and (5.2) together with the order parameter equations iteratively until convergence was reached. The energy eigenvalue $E$ determines the total QP density $\rho = 1/S\sum_{\mathbf{k}} n_{\mathbf{k}}$ and thus corresponds to excitonic corrections to the chemical potential. In all numerical calculations we used typical parameters of $\mathrm{Ba}(\mathrm{Fe}_{1-x}\mathrm{Co}_x)_2\mathrm{As}_2$, which yield a good qualitative agreement with the experimentally observed doping dependence of the SC and SDW orders (42). To model the photoinduced initial condition immediately after the initial phonon–induced ultrafast SC gap quench following photocarrier relaxation, we assume that the excited QPs have relaxed into the different pockets and describe their distributions for simplicity by Fermi–Dirac distributions

$$\begin{aligned} n^{\alpha,\beta}_{\mathbf{k}} &= \frac{1}{1+\exp\left(\varepsilon^{-}_{\mathbf{k}}/k_{\mathrm{B}}T_{\alpha,\beta}\right)}\,, \\ n^{\gamma,\delta}_{\mathbf{k}} &= \frac{1}{1+\exp\left(\varepsilon^{+}_{\mathbf{k}}/k_{\mathrm{B}}T_{\gamma,\delta}\right)} \end{aligned} \tag{C.40}$$

which determine the initial condition to our time–dependent calculation. The temperatures $T_{\alpha,\beta}$ and $T_{\gamma,\delta}$ are obtained from the total QP densities

$$\rho_{\alpha,\beta} = \frac{1}{S}\sum_{\mathbf{k}} n_{\mathbf{k}}^{\alpha,\beta}\,, \quad \rho_{\gamma,\delta} = \frac{1}{S}\sum_{\mathbf{k}} n_{\mathbf{k}}^{\gamma,\delta}\,. \tag{C.41}$$

In the actual calculations presented here, $T_{\alpha,\beta}$ and $T_{\gamma,\delta}$ were chosen such that the total densities of the different QPs are the same, i. e. $\rho \equiv \rho_{\alpha,\beta} = \rho_{\gamma,\delta}$. However, our conclusions do not depend on how we describe the initial QP distributions, which form following relaxation of the photocarriers from high energy energy states populated by the pump that are not well known.

## C.6 Build–up of Excitonic Correlation

SDW order implies $e$–$h$ coherence between different Fermi sea pockets. In the SC ground state, such coherences are nonzero only in the underdoped regime. In contrast, they vanish in the overdoped regime. They are described by the off–diagonal elements of the one–particle density matrix, which deviate from their equilibrium values immediately after laser excitation. However, they relax within few ps or sooner, similar to the dynamics of the photoexcited excitonic coherent amplitudes in semiconductors (optical polarization dephasing).

In semiconductors, excitonic coherence $\langle X\rangle$ characterizes a quantum superposition of electron and hole states. Excitonic coherence $\langle X\rangle$ must be distinguished from incoherent excitonic correlation characterized by two-particle density matrices of the form $\langle X^\dagger X\rangle - \langle X^\dagger\rangle\langle X\rangle$ (**?** ). Such "excitonic fluctuations" are of main interest here, induced by inter–pocket $e$–$h$ interactions.

Since for high energy pump excitation the populations of the low energy $e$–$h$ eigenstates that depend strongly on the interactions are initially small relative to the population of the higher energy continuum states, excitonic correlation among QPs will build up with time after relaxation to lower energies. $\langle X^\dagger X\rangle$ does not require an $e$–$h$ coherent superposition, only residual interactions among excited QPs. Our experiment shows the existence of a long-lived metastable SC state with quenched SC gap, which is consistent with QP populations that have not yet relaxed back to equilibrium after 100's of ps. We argue that the existence of Fermi sea pockets with large momentum difference may be responsible for this long lifetime, which allows QP correlation to build–up.

Similar to the standard RT model, many calculations of excitonic correlation formation in semiconductors use three-particle models, where electrons, holes, and excitons are treated as distinct QPs. These models are based on rate or Boltzmann equations for distinct populations of fermionic QPs ($e$'s and $h$'s) and bosons (excitons). In semiconductors, it is known that multi-particle rate equations similar to the RT model are inadequate to describe the experimental observations (**?** ; 86). Discrepancies arise because excitons are not perfect bosons and phase space filling effects are important. While the RT model considers bosons that are distinct from the SC QPs, the main nonlinearities of interest here come from additional fermionic correlations when the same indistinguishable electrons participate in SC condensate, uncorrelated QPs, and correlated $e$–$h$ excitations. The importance of excitonic correlation build–up in ultrafast pump–probe experiments during the incoherent non–thermal temporal regime is well established in semiconductors but not observed in multi-band SCs up to now. Inter–pocket interaction between QPs leads to formation of a quasi–stationary correlated $e$–$h$ state after some time, characterized by the build–up of $\langle X^{\dagger}X\rangle$ while $\langle X\rangle$ decays back to equilibrium (85).

# APPENDIX D. ADDITIONAL MATERIALS: CHAPTER 6

## D.1 Equilibrium THz electrodynamics in $Nb_3Sn$

The real and imaginary parts of the conductivity, $\sigma_1(\omega)$ and $\sigma_2(\omega)$, measure the dissipative and inductive responses of the studied material, respectively, as shown in Fig.S1. At 4K, the SC state shows a vanishing $\sigma_1(\omega)$ below $2\Delta = 5.1meV$ and a divergent $\sigma_2(\omega)$ towards zero frequency. The $\sigma_1(\omega)$ signals at low frequencies below 3 meV originates from intraband absorption of thermally excited Bogoliubov quasi-particles, while the residual condensate density $n_s$ is proportional to the divergence of $\sigma_2(\omega)$. All these features are replaced by a response of weakly interacting QPs above 16K, i.e. above $T_c$.

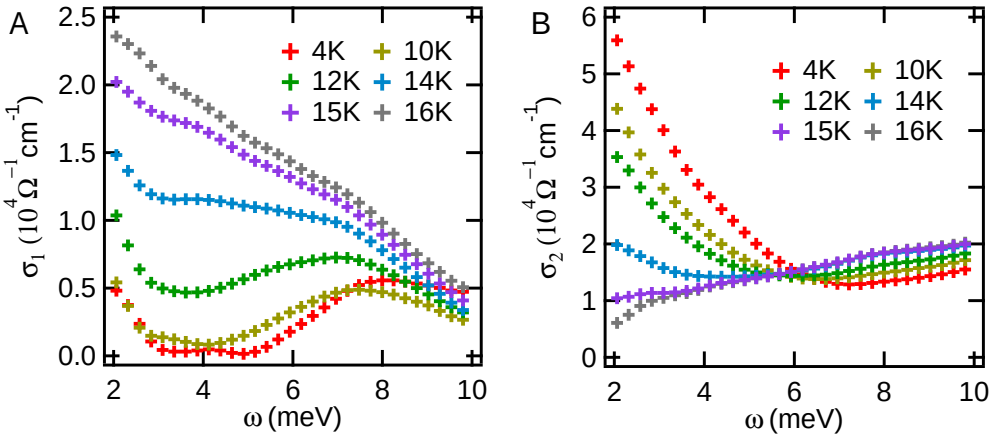


Figure D.1 Static THz conductivity spectra of (A) $\sigma_1(\omega, T)$ and (B) $\sigma_2(\omega, T)$ from 4K to 16K.

By fitting the normal state $\sigma_1(\omega)$ and $\sigma_2(\omega)$ simultaneously with the Drude model, we obtain a plasma frequency of $\omega_p$=1.24eV and a scattering time $h/\tau$=8.27meV for our $Nb_3Sn$ film.We obtain the carrier density $n$ from plasma frequency:

$$\omega_p = \left(\frac{4\pi ne}{m}\right)^{\frac{1}{2}} \tag{D.1}$$

We get $n = 1.11 \times 10^{21} cm^{-3}$. $m$ and $e$ represent the electron mass and charge. We obtain Fermi vector $k_F$ and Fermi velocity $v_F$ as following:

$$k_F = \sqrt[3]{3\pi^2 n} = 3.2 \times 10^7 cm^{-1} = 0.32 \mathring{A}^{-1} \tag{D.2}$$

$$v_F = \frac{\hbar k_F}{m} = 0.369 \times 10^8 cm/s \tag{D.3}$$

These values are consistent with a similar calculation based on $Nb_3Sn$ lattice structure.

## D.2 A classical circuit model analysis of the THz pump-induced supercurrent

The light-driven supercurrent in $Nb_3Sn$ superconductor can be obtained using an intuitive circuit model with inputs such as the experimentally measured THz pulses. The THz field is represented by a pulsed voltage source $V_s(t)$, calculated by using the THz driving E-field penetrating into the sample, $E_{in}$, and the pump beam diameter $d_p$: $V_s = E_{in} \cdot d_p$. $E_{in}$ can be estimated by using the optical index of the sample $n_s$ and the pump E field $E_0$ as:

$$E_{in} \sim E_0 \cdot \frac{2}{1 - n_s} = 0.01 E_0 \tag{D.4}$$

From the static measurement in Fig. S1, the optical index $n$ is around 200, which gives $E_{in} \sim 1.1 kV/cm$.

The impedance of the sample is calculated from the static conductivity spectrum as:

$$Z_{total} = Y_{total}^{-1} = (\sigma_1 \frac{S}{d} + i\sigma_2 \frac{S}{d})^{-1} \tag{D.5}$$

where $S = d_p \cdot t_s$ is the cross section area of current flow. $t_s = 20nm$ is the sample film thickness. The sample impedance in Fig. S2 manifests as inductance linearly increasing with frequency and negligible resistance below $2\Delta_{SC}$, as for an ideal inductor. With such simplifications, the THz pulse induced super-current is simulated by a circuit that consists of a perfect inductor in series with a very small resistor under pulsed power supply, as shown in Fig. S3. The supercurrent flow in the circuit is obtained by solving the time dependent differential equation:

$$V_s(t) = L \cdot \frac{\partial I(t)}{\partial t} + I(t) \cdot R \tag{D.6}$$

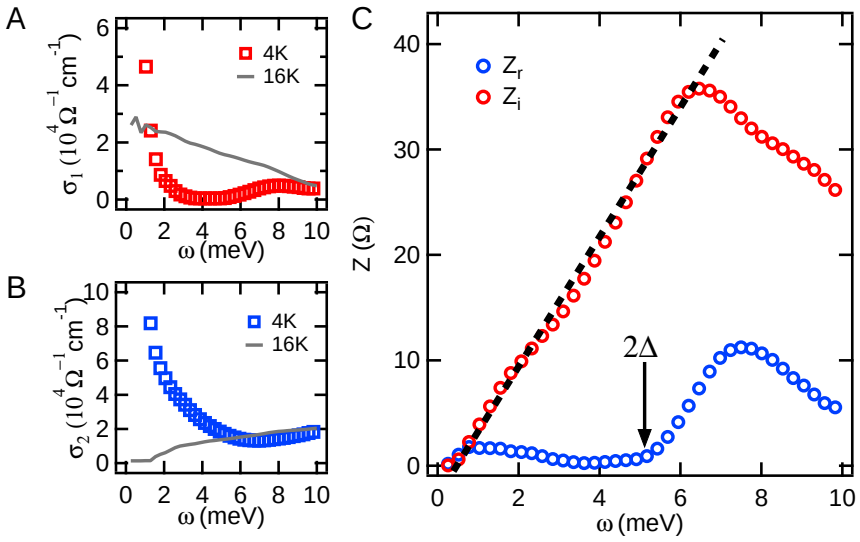


Figure D.2 (A) and (B) Real and imaginary of the optical conductivity $\sigma_1(\omega)$, $\sigma_2(\omega)$ at 4K and 16K. (C) Material impedance calculated by using the sample geometry, pump beam size and Terahertz conductivity in (A) and (B).

Fig. S4 shows the current $I(t)$ obtained from this simulation. During the excitation, the current is dominated by the inductive response that is delayed by $\pi$ compared to the applied voltage. After excitation, the DC current persists for hundreds of ps for the asymmetric effective THz pump field shown in Fig. 3f (main text). However, a DC current is absent in the simulation when using a symmetric Gaussian excitation waveform with similar pulse energy, center frequency and bandwidth. A residual current driven by a pulsed voltage source can be understood as follows. Due to the asymmetric nonlinear coupling, finite energy is stored into the inductor during the

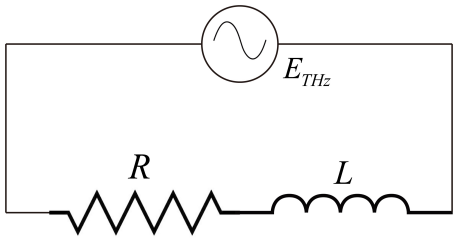


Figure D.3 Circuit model for THz-induced supercurrent in $Nb_3Sn$.

excitation and is slowly dissipated via the very small resistor when $V_s = 0$. This simple toy model successfully reproduces the THz induced DC supercurrent required for a gapless SC state and symmetry breaking for observing the forbidden pseudo-spin modes.

We compare the residual current to the gapless SC current and the SC critical current in the following section. The minimum velocity and current required to achieve the gapless SC state are $v_{gl} = \Delta_{SC}/p_F = 1.09 \times 10^5 cm/s$ and $J_{gl} = en_s v_{gl} = 9.73 \times 10^6 A/cm^2$. The superfluid density $n_s = 5.58 \times 10^{20} cm^{-3}$ is obtained by fitting the low frequency $\sigma_2(\omega)$ with $1/\omega$ divergence.

Table D.1 Material properties of $Nb_3Sn$.

| Upper critical field $H_{c2}$ | coherent length $\xi$ | penetration depth $\lambda$ | GL parameter $\kappa$ |
|---|---|---|---|
| 26-30T | 3.2nm | 64nm | 20 |

The SC critical current in our film sample is calculated from the critical magnetic field. From the material properties of $Nb_3Sn$ listed in Table 1 (148), we calculate the GL parameter $\kappa = \lambda/\xi = 20$ and thermodynamic critical field $H_c = H_{c2}/(\sqrt{2}\kappa) \sim 1T$. Due to reduced magnetization in thin film samples, the critical field is enhanced by more than 10 times:

$$H_{c\|} = \sqrt{12} H_c \lambda / t_s = 11T \tag{D.7}$$

The critical current of the $Nb_3Sn$ bulk crystal is reported around $10^6 A/cm^2$ (149). Since $J_c \propto H_c$, it is a reasonable estimation that $J_{c\|}$ in the measured $Nb_3Sn$ film sample is around $1.1 \times 10^7 A/cm^2$, which is slightly larger than $v_{gl}$ as expected. From the simulation results shown in Fig.S4, the current during the excitation is dominated by the inductive response $J_{ind} = \sigma_2 \cdot E_{in} \sim 2.6 \times 10^7 A/cm^2$, which is two-orders of magnitude higher than the conductive part $J_{con} = \sigma_1 \cdot E_{in} \sim 4.4 \times 10^5 A/cm^2$. However, note that such high frequency currents cannot effectively quench the condensate. The post-pulse DC current $J_{post}$ is around $2.7 \times 10^6 A/cm^2$, of the same order as $J_{gl}$ but smaller than critical current $J_c$. We conclude that our sample and excitation conditions satisfy the requirements for observing light-induced SC and forbidden modes predicted by our theory. However, an accurate determination of $J_{post}$, considering the complicated physical processes like

the ultrafast nonlinear response, phase competition, impurity scattering, etc is beyond the scope of this crude model.

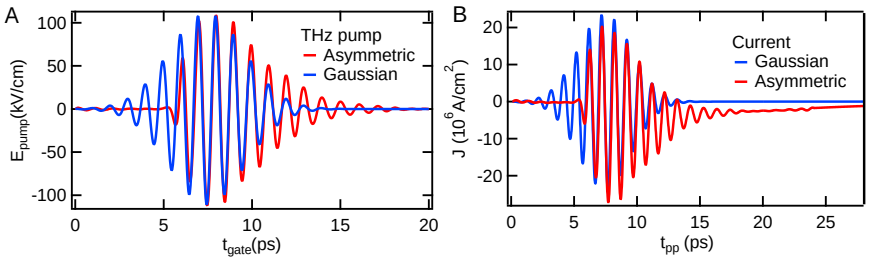


Figure D.4 (A) Asymmetric (red) and symmetric (blue) THz drivings. (B) Corresponding supercurrent produced by the toy model.

## D.3 A quasi-equilibrium picture of the gapless superconducting state (Fig. 6.1b, main text)

BCS theory predicts a possible gapless SC state of a current carrying moving condensate. Such state has vanishing pair breaking energy at certain momenta while it retains macroscopic quantum coherence and perfect conductivity. Under a finite DC current, the energy dispersion is shifted by momentum $q$, leading to an anisotropic excitation energy $E_k \approx E_k^0 + \vec{p_k} \cdot \vec{v_s}$ where $E_k^0 = \sqrt{(p_k^2/2m - E_F)^2 + \Delta_{SC}^2}$. A condensate moving against a current has minimum excitation energy $E_{min} = \Delta_{SC} - p_F \cdot v_s$, at certain k points. At critical gapless speed $v_{gl} = \Delta_{SC}/p_F$, the pair breaking energy drops to zero at these k-points, thus realizing a *gapless superconductivity* state. Fig. 1b (main text) plots QP energy dispersion of the fully-gapped equilibrium state (left) and the gapless current-carrying state with critical condensate flow $v_s$ along x axis (right) with parameters of our $Nb_3Sn$ samples described in prior sections. Please note that a much bigger value of $\Delta_{SC}/E_F$ =0.4, instead of 0.002 in $Nb_3Sn$, is used to better illustrate the gap closing effect in Fig. 1b (main text). Realization of this state has proved to be challenging in equilibrium for experiment: the speed of the moving condensate needs to be carefully set at a value right in-between the minimum speed $v_{gl}$ required for gapless superconductivity and the condensate speed $v_c$ at critical current density

$J_c$. A self-consistent solution of BCS theory shows that $v_{gl}$ is at most 1-2% percent below $v_c$ in clean-limit SCs. The experimental realization of a supercurrent-carrying phase also needs to avoid heating of electric contacts and scattering. In dirty-limit SCs,the Meissner state may break down with increasing current or magnetic field before establishing this gapless state. Here we implement a non-equilibrium manipulation scheme and coherent control of the Cooper pair momentum in real time to succeed in driving long-lived gapless superconductivity up to 100's ps timescales in a sufficiently clean sample. The subcycle dynamical symmetry breaking leads to the discovery of forbidden $3^{rd}$-order PSOs, Coulomb-enhanced strong $4^{th}$-order HHG nonlinearities, and drives a long-lived *gapless superconductivity* state that is coherently controlled by the THz pulsed field shape and amplitude. These are reproduced by a quantum kinetic nonlinear calculation of the gauge–invariant density matrix for $\mathbf{p_s}(t) \neq 0$ without perturbative susceptibility expansions.

## D.4 Third harmonic generation (THG) in $Nb_3Sn$

In this section, we present the known third harmonic generation (THG) obtained from the 2nd order pseudospin oscillations in our sample. A standard working principle for understanding the quantum dynamics of a SC condensate coupled to an ac electric field, illustrated in Fig. 1a of the main text, is Anderson pseudo–spin precession, $\vec{s}_k(t)$ (arrows). This precession is driven by quadratic coupling, $O(\mathbf{A}^2)$ (green lines), between $\vec{s}_k$ and the vector electromagnetic field potential $\mathbf{A}(t)$:

$$\frac{d\vec{s}_k}{dt} = 2\mathbf{B}_k(\mathbf{A}(t), \Delta_{SC}) \times \vec{s}_k. \tag{D.8}$$

The pseudo-magnetic field $\mathbf{B}_k$ has two components: (1) z-component $\mathbf{B}_k^z(t) = (\varepsilon_{\mathbf{k}-\frac{e}{c}\mathbf{A}} + \varepsilon_{-\mathbf{k}-\frac{e}{c}\mathbf{A}})/2$, which determines the coupling of the THz field $\mathbf{A}(t)$ and depends on the electronic band dispersion $\varepsilon_{\mathbf{k}}$; (2) perpendicular component $\mathbf{B}_k^{\perp}(t)$, which is determined by the SC off–diagonal coherence $\Delta_{SC}$ and its nonlinear modification by THz ultrafast excitation and periodic drive. Such a *forced linear harmonic oscillator* model predicts coherent pseudo–spin oscillations (PSO) in THz pump-probe signals, expected, at leading order, to occur at a frequency double that of the pump field, $2\omega_{pump}$. This contribution is linear in $B^z = O(\mathbf{A}^2)$ and gives rise to third harmonic generation (THG)

observed in single-pulse, nonlinear emission measurements. In addition, the equilibrium symmetry of the SC state implies that all odd–order nonlinear responses to the coherent coupling of the THz electric field, i.e., O($\mathbf{A}^{2n-1}$) (n=1,2...), must vanish, including the linear (O($\mathbf{A}$)) response. For example, a coherent PSO at three times the driving field frequency, $3\omega_{pump}$, to be distinguished from the THG emission, is forbidden by the symmetry of the BCS state, which consists of Cooper pairs with zero momentum.

In Fig. S5, the optical gate pulse samples THz pump emission through $Nb_3Sn$ film *without* the presence of probe pulse. In contrast to the THz pump-probe method discussed above, this essentially measures the quasi-equilibrium response. A $3\omega$ THG component is observed in the emission spectrum, which can originate from SC amplitude fluctuations and/or Cooper pair excitations $4\omega$ and $5\omega$ emission components from the 3rd and 4th order pseudospin oscillations are below experimental sensitivity of the emission spectra yet, they are clearly observable in the THz pump-probe measurement with higher sensitivity and less scattering as discussed in the next section. Here the nonlinearity merges with the background of strong additional scattering contributions. It is not practically possible to see the second harmonic peak, which is only 0.5 THz away from the fundamental, in such single-pulse experiment. It is there but masked by the main scattering peak as compared to pump-probe.

### D.5 Single-pulse emission vs. THz pump-probe

The forbidden and HH peaks are much harder to see in a linear or nonlinear emission experiment with single pump beam, i.e., quasi-CW incoherent responses. This is the case in both from the theoretical and experimental points of view. On the one hand, the emission signal is a mixture of linear and nonlinear responses, where the former masks the latter, as already known from semiconductors. There, it was necessary to isolate the nonlinear effects in order to discover the new physics. In addition, the large THz pump scattering background here masks the important effects but has nothing to do with the current. In strong contrast, the two-pulse coherent pump-probe responses measured here accomplish the following: (1) subtract the detrimental linear background

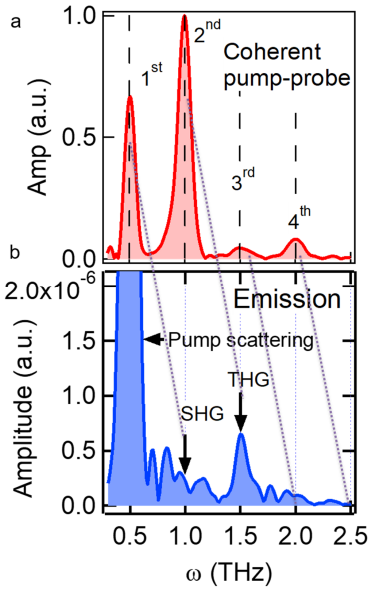


Figure D.5 Pseudo-spin coherent oscillation spectra in pump-probe (a) and pump emission measurements (b) using narrow band THz pump centered at 0.5THz through $Nb_3Sn$ film at 4K.

by comparing pump on and off; and (2) two-pulse pump-probe signals are coherent and directional, arising from interference in third order responses of two pulses. Therefore, these are cleaner experiments similar to semiconductors, unlike for the third order responses measured with a single pulse. This is well established in studies of coherent ultrafast dynamics of excitons in semiconductors, where e.g. the new signals in the phase matching directions come from quantum interference of two pulses and are much cleaner than in SHG and THG harmonic generation with single pulse.

In order to further substantiate the above statements from pure theory in the ideal case, we directly simulated the dynamics (Fig. S6a) and spectrum (Figs. S6c and S6e) of the total current $j_{tot}$, i.e. emission, and the corresponding dynamics (Fig. S6b) and spectrum of the pump-probe response

(Figs. S6d and S6f) using experimental pulses in Fig. S8. To obtain the pump-probe response, we computed the transmitted E-field of pump+probe pulse, $E_{pp}(t,\tau)$, as function of electro-optical sampling time t and pump-probe delay tau, as well as the transmitted electric field resulting from the probe pulse, $E_{probe}(t)$, and the pump pulse, $E_{pump}(t,\tau)$, alone. The nonlinear pump-probe response is then defined in our calculation as $E_{NL}$ =$E_{pump-probe}$-$E_{pump}$-$E_{probe}$. $E_{NL}/E_{probe}$ is plotted at fixed gate time t as function of pump-probe delay $\tau$. The emission shows only one peak at the pump frequency $\omega_L$ due to the direct pump scattering given the scale presented, while the pump-probe response shows all collective peaks at $1^{st}$-$4^{th}$ harmonics, fully consistent with the experiment for the same pulse temporal profile. These further establish a direct connection between experiment and theory that fully support the proposed picture of discovering the supercurrent moving quantum state.

### D.6 Effective asymmetric multi-cycle THz pump pulses

In the gauge invariant quantum kinetic theory simulation discussed below and in the main text, we study the effects of strong and asymmetric THz pulse photoexcitation and the effects of superfluid momentum $\mathbf{p}_s(t)$, which dynamically breaks the symmetry of the BCS state. Please note the effective driving asymmetry is determined by THz-induced nonlinear photocurrent sources and spatial variations inside the SC during THz pulse propagation instead of free space THz waveform. Our calculation predicts the strong nonlinearities and describes the physical picture. For the input to our theory, we define the asymmetry of an effective input pulse with electric field $\mathbf{E}_{\rm eff}$ as $\eta = \int_{-\infty}^{\infty} {\rm d}t\, E(t)/E(\omega=\omega_{\rm L}) = E(\omega=0)/E(\omega={\rm L})$ where $E(\omega)$ is the Fourier transformation of $E(t)$. In this way, $\eta = 0$ for a symmetric pulse driving, while an asymmetric pulse driving is characterized by $\eta \neq 0$. The 0.5 THz (1.0 THz) multi-cycle experimental and theoretical pulses have an asymmetry of $\eta = 0.03$ ($\eta = 0.02$), as shown in Fig. S7. As discussed in Fig. 2c (main text), in order to approximately evaluate the role of nonlinear asymmetric coupling in experiment, the effective nonlinear pulse integral $\int_{-\infty}^{t} {\rm d}\tau\, \mathbf{E}_{\rm eff}(\tau)$ is computed by inputing the THz pump pulse waveforms detected via electro-optic sampling in a <110> ZnTe crystal. To check whether the

theoretical results depend on the details of the asymmetry used, we have tried different functional forms for the input asymmetric pulse. The calculations show that the results for high-harmonic generation as well as the non-equilibrium state after the pulse are qualitatively similar for different asymmetric pulse shapes, as long as $\eta$ of the pulses is the same. This indicates that the theoretical results are robust and do not critically depend on the specific choice of functional form of the pulse, but only on its asymmetry. They arise from dynamical symmetry breaking due to the introduction of a preferred direction by the Cooper pair momentum, which can persist after the pulse due to asymmetric driving-induced photocurrents. A quantitative modeling of the gauge-invariant coupling of THz fields and superfluid momentum $\mathbf{p}_s(t)$ need to include longitudinal responses from spatial variations of the gap phase and chemical potential as seen in Eqs.(3) and (4) (method), which will be explored elsewhere.

### D.7 Multi-cycle vs. single-cycle pumping

The mechanism of light absorption in the material depends on the details of the pulse shape. In more detail, the part of the pulse in frequency domain above $2\Delta$ excites non-equilibrium quasiparticle populations, while the portion below the gap drives time-dependent inductive currents. In general, these two effects coexist in a strongly time-dependent system. To model the THz-driven current, one has to take into account the strong time-dependence of the THz pulse and not just its intensity as in an equilibrium calculation. For this purpose, we have developed the time-dependent density matrix equation of motion theory, which takes both effects into account while satisfying gauge invariance. As a result, both effects mentioned above contribute to the SC quench by the THz pulse, which leads to a significant increase in the total nonlinearity and modifies simple quantum quench results. In addition, the theory shows that sufficient lightwave acceleration of the macroscopic Cooper pair state along a specific direction results in zero QP excitation energy in specific $\mathbf{k}$-points, even if the frequency is below the equilibrium energy gap.

Although the low-field single-cycle pulse excitations in Ref. (67) can also be used to minimize the condensate quench, the post-quench states in this case still show the same very fast rise times

during the pulse, as shown in the inset of Fig. 3c, even down to 7 kV/cm. The slow 100ps rise time observed for the current-carrying state is not so much dependent on the excitation gap and its quenching. It depends on the collective Cooper pair momentum in a moving condensate quantum state, which makes the latter robust against scattering. The latter momentum depends on the pulse asymmetry and not just on the pump intensity. All behaviors with single-cycle pulse pumping are very different from the post-quench multi-cycle, supercurrent-carrying states observed. This result is important, as it shows a path for driving non-equilibrium protected quantum states.

The differences in the conductivity are not as striking as in the dynamics. The similarities however are perfectly understandable, since the single-cycle pulse has broadband spectral components that will give mixed responses, with some signatures of gapless SC in the conductivity. However, that is only one of the features of the post-quench states and is not the dominant one. The direct photon transitions exciting quasiparticles by quickly depleting the condensate clearly dominate the sub-ps dynamics observed during the pulse in Ref. (67). This is distinctly different from the supercurrent-flowing state observed here, which continues to evolve after the pulse and also leads to new HH peaks. Therefore, only the multi-cycle sub-gap driven, supercurrent-carrying states allow us to truly identify the existence of a gapless SC phase under minimal quenching of condensate density. This also demonstrates why the pulse shape controls ∼100ps dynamics. Note that any state with substantial condensate quench, such as the one observed in Ref. (67), will appear to be "gapless", e.g., the single-cycle quench at E field = 120 kV/cm and 155 kV/cm. However, this is different from, e.g., 0.5 THz pumping (Figs. 3a and 3b) at E field = 78 kV/cm. There, the non–equilibrium state is gapless, as seen by comparing $\sigma_1$ with the normal state equilibrium lineshape (gray line), despite a minimal light-induced change in the diverging $\sigma_2$, i.e. minimum change of condensate density but full quench of the SC gap. We also stress the difference between energy gap in the excitation spectrum (E) and order parameter ($\Delta_{SC}$) of a quantum state. Clearly, the energy gap is not enough to characterize the properties of a quantum state, e.g SC is gap plus Meissner effect. Here we distinguish between two different gapless non-equilibrium states with different order parameters: almost zero in Ref. (67) and large in the supercurrent-carrying state here,

as seen from several experimental features (HH modes, $\sigma_2$ divergence...). Clearly, these two states are different. We also demonstrate this with our theoretical model, which distinguishes between two different gapless regimes, II and III, based on the order parameter.

## D.8 Gauge-invariant nonequilibrium SC theory

In this section, we briefly present our gauge-invariant density matrix approach used to illustrate control of non-equilibrium SC dynamics via THz-light-induced super-currents. We start from the microscopic spatial-dependent Bogoliubov–de Gennes mean-field model for $s$-wave superconductors (151)

$$H = \sum_{\sigma} \int \mathrm{d}^3\mathbf{x}\, \psi_\sigma^\dagger(\mathbf{x}) \left[\xi(\mathbf{p} + e\mathbf{A}(\mathbf{x},t)) - \mu - e\phi(\mathbf{x},t)\right] \psi_\sigma(\mathbf{x}) \\ - \int \mathrm{d}^3\mathbf{x} \left[\Delta(\mathbf{x})\psi_\uparrow^\dagger(\mathbf{x})\psi_\downarrow^\dagger(\mathbf{x}) + \mathrm{h.c.}\right] . \tag{D.9}$$

Here $\psi_\sigma^\dagger(\mathbf{x})$ and $\psi_\sigma(\mathbf{x})$ are the Fermionic creation and annihilation field operators with spin index $\sigma$, $\mathbf{p} = -\mathrm{i}\nabla_{\mathbf{x}}$ is the momentum operator, $\xi(\mathbf{p})$ defines the single-particle energy dispersion, and $\mu$ is the chemical potential. To describe the coupling to the electromagnetic field we use the minimal (Peierls) substitution $\xi(\mathbf{p}) \to \xi(\mathbf{p} + e\mathbf{A}(\mathbf{x},t))$ where $\mathbf{A}(\mathbf{x},t)$ denotes the vector potential while $\phi(\mathbf{x},t)$ is the scalar potential. The SC pairing is described by second part of Hamiltonian (D.9) where

$$\Delta(\mathbf{x}) = |\Delta| \mathrm{e}^{\mathrm{i}\zeta(\mathrm{x})} = V_{\mathrm{SC}} \langle \psi_\downarrow(\mathbf{x}) \psi_\uparrow(\mathbf{x}) \rangle \,, \tag{D.10}$$

is the complex spatially- and time-dependent SC order parameter with SC pairing interaction strength $V_{\mathrm{SC}}$ and SC gap phase $\zeta(\mathrm{x})$.

A gauge invariant SC theory requires gauge-invariance of the Hamiltonian (D.9) under the gauge transformation (152)

$$\Psi(\mathbf{x}) \;\to\; \mathrm{e}^{\mathrm{i}\sigma_3 \Lambda(\mathbf{x})/2} \Psi(\mathbf{x}) \,, \tag{D.11}$$

where $\Psi(\mathbf{x}) = (\psi_\uparrow(\mathbf{x}), \psi_\downarrow^\dagger(\mathbf{x}))^T$ is the field operator in Nambu space and $\sigma_3 = \begin{pmatrix} 1 & 0 \\ 0 & -1 \end{pmatrix}$. This is fulfilled when vector potential, scalar potential, and SC gap phase transform via

$$\mathbf{A}(\mathbf{x}) \;\to\; \mathbf{A}(\mathbf{x}) + \frac{1}{2e}\nabla\Lambda(\mathbf{x})\,, \quad \phi(\mathbf{x}) \;\to\; \phi(\mathbf{x}) - \frac{1}{2e}\frac{\partial}{\partial t}\Lambda(\mathbf{x})\,, \quad \zeta(\mathbf{x}) \;\to\; \zeta(\mathbf{x}) + \Lambda(\mathbf{x})\,. \tag{D.12}$$

To obtain a gauge-invariant description of the non-equilibrium SC dynamics, we introduce center-of-mass and relative coordinates $\mathbf{R} = (\mathbf{x} + \mathbf{x}')/2$ and $\mathbf{r} = \mathbf{x} - \mathbf{x}'$. We then transform system's density matrix $\rho(\mathbf{x}, \mathbf{x}') = \langle \Psi(\mathbf{x})^\dagger \Psi(\mathbf{x}') \rangle$ using the transformation (151; 153)

$$\tilde{\rho}(\mathbf{r}, \mathbf{R}) = \exp\left[-\mathrm{i}e \int_0^{\frac{1}{2}} \mathrm{d}\lambda\, \mathbf{A}(\mathbf{R} + \lambda\,\mathbf{r}, t) \cdot \mathbf{r}\,\sigma_3\right] \rho(\mathbf{r}, \mathbf{R}) \exp\left[-\mathrm{i}e \int_{-\frac{1}{2}}^{0} \mathrm{d}\lambda\, \mathbf{A}(\mathbf{R} + \lambda\,\mathbf{r}, t) \cdot \mathbf{r}\,\sigma_3\right] \tag{D.13}$$

where $\rho(\mathbf{r}, \mathbf{R}) = \langle \Psi^\dagger(\mathbf{R} + \frac{\mathbf{r}}{2}) \Psi(\mathbf{R} - \frac{\mathbf{r}}{2}) \rangle$. By applying the gauge transformation (D.11), the density matrix $\tilde{\rho}(\mathbf{r}, \mathbf{R})$ transforms as (151)

$$\tilde{\rho}(\mathbf{r}, \mathbf{R}) \;\to\; \exp\left[\mathrm{i}\sigma_3 \Lambda(\mathbf{R})/2\right] \tilde{\rho}(\mathbf{r}, \mathbf{R}) \exp\left[-\mathrm{i}\sigma_3 \Lambda(\mathbf{R})/2\right]\,. \tag{D.14}$$

The dynamics of the transformed density matrix is then derived by using the Heisenberg equation of motion technique. The details of the derivation will be published elsewhere. To simplify the problem, we choose the gauge, $\Lambda(\mathbf{x}) = -\zeta(\mathbf{x})$, where the phase $\zeta(\mathbf{x})$ of the SC gap is eliminated and assume homogenous excitation conditions by neglecting the $\mathbf{R}$-dependence of vector and scalar potential. After transforming to momentum space, we obtain the gauge-invariant Bloch equations (151; 153)

$$\begin{aligned}
\mathrm{i}\frac{\partial}{\partial t}\tilde{\rho}_{1,1}(\mathbf{k}) &= -\mathrm{i}\,e\,\mathbf{E}(t) \cdot \nabla_{\mathbf{k}} \tilde{\rho}_{1,1}(\mathbf{k}) + |\Delta|\left[\tilde{\rho}_{1,2}(\mathbf{k} - \mathbf{p}_\mathrm{S}) - \tilde{\rho}_{2,1}(\mathbf{k} - \mathbf{p}_\mathrm{S})\right]\,, \\
\mathrm{i}\frac{\partial}{\partial t}\tilde{\rho}_{2,2}(\mathbf{k}) &= \mathrm{i}\,e\,\mathbf{E}(t) \cdot \nabla_{\mathbf{k}} \tilde{\rho}_{2,2}(\mathbf{k}) - |\Delta|\left[\tilde{\rho}_{1,2}(\mathbf{k} + \mathbf{p}_\mathrm{S}) - \tilde{\rho}_{2,1}(\mathbf{k} + \mathbf{p}_\mathrm{S})\right]\,, \\
\mathrm{i}\frac{\partial}{\partial t}\tilde{\rho}_{1,2}(\mathbf{k}) &= \left[\xi(\mathbf{k} - \mathbf{p}_\mathrm{S}) + \xi(-\mathbf{k} - \mathbf{p}_\mathrm{S}) - 2\,\mu_\mathrm{eff}\right]\tilde{\rho}_{1,2}(\mathbf{k}) - |\Delta|\left[\tilde{\rho}_{2,2}(\mathbf{k} + \mathbf{p}_\mathrm{S}) - \tilde{\rho}_{1,1}(\mathbf{k} - \mathbf{p}_\mathrm{S})\right]\,.
\end{aligned} \tag{D.15}$$

which describe quantum transport in BCS superconductors. Here we introduced the homogeneous gauge-invariant superfluid momentum and effective chemical potential

$$\mathbf{p}_\mathrm{s} = -e\mathbf{A}\,, \quad \mu_\mathrm{eff} = \mu + e\,\phi\,. \tag{D.16}$$

The superfluid momentum yields center-of-mass acceleration of Cooper pairs, $\frac{\partial}{\partial t}\mathbf{p}_s = e\,\mathbf{E}(t)$, such that the inversion symmetry of electron ($\tilde{\rho}_{1,1}$) and hole densities ($\tilde{\rho}_{2,2}$) is broken. In the equations of motion (D.15) it leads to quantum transport terms like $\mathrm{i}\,e\mathbf{E}(t)\cdot\nabla_{\mathbf{k}}\tilde{\rho}_{1,1}(\mathbf{k}+\mathbf{p}_\mathrm{S})$ which are absent in the pseudo-spin model description as discussed below (154; 37). The time-dependent effective chemical potential describes the dynamics of the condensate. In our calculation it is determined by the conservation of the total charge $N = \sum_{\mathbf{k}}[\tilde{\rho}_{1,1}(\mathbf{k}) + 1 - \tilde{\rho}_{2,2}(\mathbf{k})]$ (151) which is generally not fulfilled in the mean-field description of superconductivity. This way the condensate responds simultaneously to the QP dynamics.

In our calculations we use the square lattice nearest-neighbor tight-binding dispersion $\xi(\mathbf{k}) = -2\,J[\cos(k_x\,a) + \cos(k_y\,a)]$ with nearest-neighbor hopping strength $J > 0$ and lattice constant $a$. We assume half-filling case by setting $\mu = 0$. The kinetic term in the equations of motion (D.15) is expanded up to $\mathbf{p}_s^2$ order, $\xi(\mathbf{k}-\mathbf{p}_\mathrm{S}) + \xi(\mathbf{k}+\mathbf{p}_\mathrm{S}) = 2\,\xi(\mathbf{k}) + 2\,J\,a\cos(k_x\,a)\mathbf{p}_s^2 + \mathcal{O}(\mathbf{p}_s^4)$, where the electric field $\mathbf{E} = E\,\mathbf{e}_x$ is chosen to be polarized along the $x$-direction. As initial state we use a BCS ground state with SC gap $2\Delta = 5.2$ meV. We then excite the superconductor with an electric field

$$\mathbf{E}(t) = \mathbf{E}_0\,\mathbf{e}_x\,(\cos(\omega_L\,t) + \kappa)/(1+\kappa)\exp[-t^2/(2\,\sigma_t^2)] \tag{D.17}$$

where $\mathbf{E}_0$ is the strength, $\omega_L$ denotes the center frequency, and $\sigma_t$ defines the duration of the applied THz light field. The temporal asymmetry of the pulse is controlled by the parameter $\kappa$ which thus determines the strength of $\mathbf{p}_s$ after the pulse.

**Quasi-particle excitation energy**

As we illustrate in Fig. 1d in the main text, the presence of a superconducting velocity $\mathbf{v}_\mathrm{S}$ results in a tilt of the quasi-particle energy spectrum. More precisely, in the presence of the supercurrent the energy spectra of quasi-electrons (+) and quasi-holes (-) are approximately given by $E_{\mathbf{k},\pm} = \pm\mathbf{k}\cdot\mathbf{v}_\mathrm{S}/2 + \sqrt{(\xi(\mathbf{k})-\mu)^2 + |\Delta|^2}$. One can see that the QP excitation energy and the SC order parameter differ in the presence of superfluid velocity and acceleration of the macroscopic electronic state. Depending on the size of $\mathbf{v}_\mathrm{S}$, some of the electrons near the Fermi surface of spin-

up and -down states cannot form Cooper pairs anymore. In general, one can distinguish between two cases: (I) For $|\mathbf{k}\cdot\mathbf{v}_S/2| < \sqrt{(\xi(\mathbf{k})-\mu)^2+|\Delta|^2}$, both quasi-electron and –hole energies remain positive-valued within the entire momentum range, so that all electrons near the Fermi surface can still form Cooper pairs. As a result, the rigid Cooper pair condensate moves as a whole with velocity $\mathbf{v}_S$. (II) For $|\mathbf{k}\cdot\mathbf{v}_S/2| > \sqrt{(\xi(\mathbf{k})-\mu)^2+|\Delta|^2}$ , the quasi-electron or quasi-hole excitation energy can become zero for some $\mathbf{k}$-values, i. e. the QP energy gap closes at specific wavevectors and the macroscopic state becomes partially gapped with finite order parameter. Then the Cooper pairs are broken for such wavevector values, while the Cooper pairs with $E_{\mathbf{k},\pm} > 0$ remain unbroken (condensed). In this situation, the $\mathbf{k}$-space near the Fermi surface can be divided into two regions, analogous to a Fulde-Ferrell-Larkin-Ovchinnikov (FFLO) state: pairing and depairing regions. The latter is characterized by a gapless quasiparticle spectrum, i.e., it costs zero energy to excite QPs for such wavevectors. In Fig. 4d and g in the main text we plot the dynamics and fluence dependence of the minimum of $E_{\mathbf{k},\pm}$ within the complete $\mathbf{k}$-space, which allows us to monitor the non-equilibrium transition from a gapped SC state to a gapless state with macroscopic coherence similar to the FFLO state. If the minimum of $E_{\mathbf{k},\pm}$ after THz light-induced SC gap quench is positive-valued, the system is in a quenched but still gapped SC state, while the system reaches a gapless SC state as soon as $E_{\mathbf{k},\pm}$ becomes zero for some $\mathbf{k}$-values, where QPs can be now excited due to light-wave acceleration.

**High-harmonics generation vs. Higgs mode**

Our theory predicts two effects: First, the amplitude oscillations of the SC order parameter observable during the pulse in Fig. 1e correspond to high harmonics generation. The symmetric pulse produces only even harmonics, while an asymmetric pulse yields both even and forbidden odd harmonics, due to the THz-light induced inversion symmetry breaking via overall acceleration of the macroscopic state along a preferred direction. Second, in contrast, the oscillations of the SC order parameter observable after the pulse are a result of the photo-excited Higgs mode. Both symmetric and asymmetric pulses excite the Higgs mode, which depends on the magnitude of the light-induced

SC order parameter quench. Qualitatively, the frequency of the Higgs mode is $\omega_{\text{Higgs}} = 2\Delta_\infty/\hbar$ where $\Delta_\infty$ is the quenched order parameter amplitude value, which $|\Delta(t)|$ asymptotically reaches after the THz-light induced quench. In general, the asymmetric pulse produces a stronger quench of the SC order parameter (Fig. 4f) at a given electric field amplitude, which results in different Higgs frequencies for symmetric and asymmetric pulses. The stronger quench of the SC gap with an asymmetric pulse is the result of the light-induced nonlinear supercurrent but for different reasons than the forbidden modes. As discussed above, in the presence of a superconducting velocity $\mathbf{v}_S$, the energies of quasi-electrons and quasi-holes can become zero for some $\mathbf{k}$-values. As a result, the excitation spectrum is gapless at certain points and the Cooper pairs are broken for such $\mathbf{k}$-points, which yields a reduction of the SC coherence and thus the SC order parameter as compared to the excitation with a symmetric pump pulse. This enhances the Higgs oscillations after the pulse. In general, the Higgs mode is not so easily detectable in experiments because it cannot be probed by linear-response-type measurements. In addition, the observation of the Higgs mode in time-resolved experiments requires very clean samples with large enough dephasing times, which complicates the detection.

### D.9 Interference between quantum transport and pseudo-spin precession

The emergence of forbidden harmonics reflects the sensitivity of high harmonic generation to dynamical symmetry breaking, which is realized in our experiment via light-wave acceleration of the Cooper-pair condensate. This introduces a preferred direction that changes the symmetry of the macroscopic state. To systematically describe light-wave driven dynamical symmetry breaking and its interplay with the conventional Anderson pseudo-spin precession, we have developed the microscopic gauge-invariant density matrix theory without perturbative susceptibility expansions, discussed above. Our theory combines nonlinear Anderson pseudo–spin dynamics with nonlinear light-wave acceleration of the Cooper-pair condensate. The latter is absent in the pseudo-spin precession model which is the standard theory for understanding the quantum dynamics of a SC condensate coupled to an ac electric field. Both nonlinear quantum transport as well as nonlin-

ear pseudo-spin precession contribute to the generation of the high harmonics in the equations of motion presented in Eq. (D.15): Nonlinear quantum transport originates from driving terms of the form $\mathbf{E}(t) \cdot \nabla_{\mathbf{k}} \tilde{\rho}(\mathbf{k})$ while Anderson pseudo–spin dynamics is described by terms of the form $|\Delta(t)| \tilde{\rho}(\mathbf{k} \pm \mathbf{p}_{\mathrm{S}})$, modified by the lightwave acceleration here, in addition to the usual light–matter coupling contribution $\propto \mathbf{p}_{\mathrm{S}}^2$. There is clearly an interplay between quantum transport and Anderson pseudo-spin precession, which is described consistently by our theory that maintains gauge invariance and avoids uncontrolled perturbative expansions of the displaced populations of a moving condensate. The quantum transport terms induce a center-of-mass momentum of the Cooper pairs, with inversion-symmetry breaking due to the finite $\mathbf{p}_{\mathrm{S}}$ that introduces a preferred direction. The pseudo-spin precession terms lead to pseudo-spin oscillations modified by the quantum transport and center-of-mass acceleration that changes the phase of the macroscopic wavefunction. In general, the nonlinear quantum transport contributions alone lead to high harmonic generation, as long as an accelerated Cooper-pair condensate is present with a finite SC order parameter. These nonlinearities have not been adequately addressed so far and are absent in the normal state. To determine the exact interplay, we note that Anderson pseudo-spin precession requires a sufficiently non-parabolic bandstructure, and is more sensitive to the bandstructure of individual materials as compared to the lightwave acceleration. Quantum transport and pseudo-spin precession nonlinear contributions thus non-trivially interfere during the photo-excitation process in a way that depends on the bandstructure and both contribute to the generation of the high harmonics.

To understand the origin of high-harmonic generation in more detail, we have expanded the density matrix in orders of the pump laser center frequency, $\tilde{\rho}(\mathbf{k}) = \sum_N \tilde{\rho}^{(N\omega_{\mathrm{L}})}(\mathbf{k})$, where $\tilde{\rho}^{(N\omega_{\mathrm{L}})}(\mathbf{k})$ is the $N$-th order response of the density matrix. For a symmetric one-color pump pulse, we find that $\tilde{\rho}_{2,1}^{((2N+1)\omega_{\mathrm{L}})}(\mathbf{k}) = 0$ while $\tilde{\rho}_{1,1}^{((2N+1)\omega_{\mathrm{L}})}(\mathbf{k}) = \tilde{\rho}_{2,2}^{((2N+1)\omega_{\mathrm{L}})}(\mathbf{k})$ such that the transient THz response or SC order parameter $\Delta = \sum_N \Delta^{(N\omega_{\mathrm{L}})} = V_{\mathrm{SC}} \sum_N \sum_{\mathbf{k}} \tilde{\rho}_{2,1}^{(N\omega_{\mathrm{L}})}(\mathbf{k})$ shows only even harmonics. This is similar to all previous theoretical descriptions of the coherent dynamics. The situation changes, however, when the system is excited with an asymmetric pump pulse, due to ligh-wave acceleration of Cooper pairs. Such a pulse induces a finite center-of-mass momentum of the Cooper pairs,

which, importantly, persists after the pulse. As a result, equilibrium inversion symmetry of the system is broken, such that forbidden high harmonics should be expected to emerge. This can be understood by viewing the asymmetric pulse as a two-color pulse, where one pulse oscillates at the laser's center frequency $\omega_{\mathrm{L}}$ while the second one has frequency peak close to $\omega = 0$. The dynamical interference of these two frequency components, clearly seen in the experimental pulse, in the quantum transport terms as well as in the pseudo-spin precession contributions leads to the generation of equilibrium-forbidden odd harmonics, in addition to the even harmonics discussed before, since now both $\tilde{\rho}_{2,1}^{((2N+1)\omega_{\mathrm{L}})}(\mathbf{k}) \neq 0$ and $\tilde{\rho}_{1,1}^{((2N+1)\omega_{\mathrm{L}})}(\mathbf{k}) \neq \tilde{\rho}_{2,2}^{((2N+1)\omega_{\mathrm{L}})}(\mathbf{k})$. This is somewhat analogous to two-color pulse experiments on inversion-symmetric samples, where the interference of the two frequencies breaks the equilibrium inversion symmetry and even and odd harmonics become observable. The ratios between even and odd harmonics is controllable in our model by adjusting the asymmetry of the applied pump pulse, while the ratios between different even harmonics also depend on the details of the bandstructure. Our numerical calculation in the time domain puts the above analysis on a quantitative basis and identifies the importance of the new nonlinearities introduced by lightwave acceleration of a condensate along a preferred direction for strong linearly polarized THz electric field.

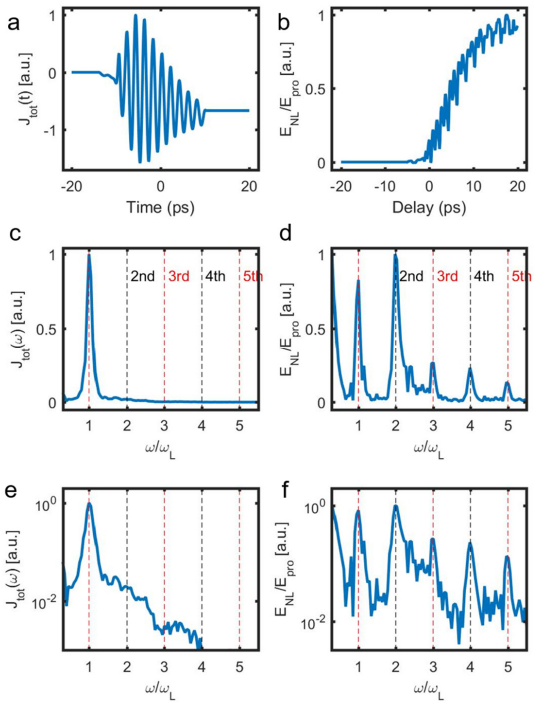


Figure D.6 (a)-(b) Dynamics of total current and THz pump-probe response. The corresponding spectra are plotted in (c)-(d) ((e)-(f)) in linear (semi-logarithmic) scale.

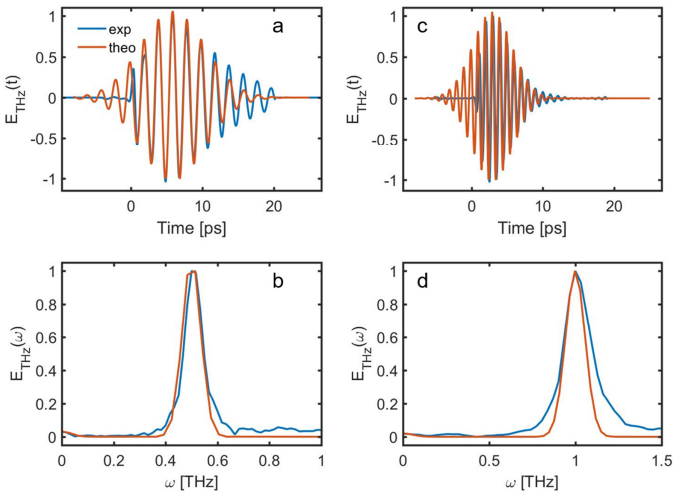


Figure D.7 Asymmetry of the experimental and theoretical pulses. The dynamics of (a) 0.5THz and (b) 1.0THz experimental (blue line) and theoretical (red line) pump pulses are shown. The corresponding spectra are plotted in (c) and (d). The asymmetry of 0.5THz and 1.0THz pulses are 3% and 2% (see text for details).